NASA SP-193

EVALUATION OF MOTION-DEGRADED IMAGES

A seminar held in
CAMBRIDGE, MASSACHUSETTS
DECEMBER 3-5, 1968

NATIONAL AERONAUTICS AND SPACE ADMINISTRATION

NASA SP–193

EVALUATION OF MOTION-DEGRADED IMAGES

The proceedings of
a seminar held in Cambridge, Massachusetts,
December 3–5, 1968, and sponsored by
the NASA Electronics Research Center

Scientific and Technical Information Division
OFFICE OF TECHNOLOGY UTILIZATION 1969
NATIONAL AERONAUTICS AND SPACE ADMINISTRATION
Washington, D.C.

Seminar Chairman

Max R. Nagel
Optics and Microwave Research Laboratory
NASA Electronics Research Center
Cambridge, Massachusetts

Session Chairmen

F. Dow Smith
Itek Corporation
Lexington, Massachusetts

Joseph W. Goodman
Applied Electronics Laboratory
Stanford University
Palo Alto, California

Brian J. Thompson
Department of Optics
University of Rochester
Rochester, New York

NASA Sponsorship

Lester C. Van Atta
Assistant Director
NASA Electronics Research Center
Cambridge, Massachusetts

For sale by the Superintendent of Documents
U.S. Government Printing Office, Washington, D.C. 20402
Price $2.00
Library of Congress Catalog Card Number 75–600852

FOREWORD

The necessity of dealing with motion-degraded images has been with us for a long time. As new problems have arisen, the science and technology for dealing with them have advanced. In recent years, aerospace applications have created requirements for the ultimate in undistorted imaging under novel operating conditions. Thus the field remains a dynamic one, calling for a gathering where experts can discuss the state-of-the-art in relation to its current applications.

It is our hope that this purpose has been served by the Seminar on Evaluation of Motion-Degraded Images. Acting for the National Aeronautics and Space Administration, the Electronics Research Center has been honored to host this seminar. The center accepts the responsibility to disseminate the information presented at the seminar, not only by assembly of the present report, but by any other means at its disposal.

LESTER C. VAN ATTA

Page intentionally left blank

Page intentionally left blank

CONTENTS

SESSION I, F. Dow Smith, *Chairman*

SESSION II, F. Dow Smith, *Chairman*

SESSION III, Joseph W. Goodman, *Chairman*

SESSION IV, BRIAN J. THOMPSON, *Chairman*

OPENING REMARKS

GENE A. VACCA
NASA Office of Advanced Research and Technology

Although the value of imaging is well recognized by NASA and its Office of Advanced Research and Technology, there has been relatively little direct research and development support in the specific area to be discussed by this seminar. There are several reasons for this: One is that we never have enough money to do all the things that we would like to do. Another is that this kind of activity has been characteristically related to flight missions and flight projects. For example, motion compensation is intimately related, and more or less mechanically connected, to the spacecraft; this makes it a rather difficult thing to do apart from a flight mission. Another reason is that there has been a relatively large effort in this field supported by the Department of Defense, in order to carry out its responsibilities for surveillance, reconnaissance, and other intelligence activities.

Although the agenda of the meeting seems to cover practically every aspect of its topic, one area which I think may not be considered—but one that we at NASA Headquarters have to be responsive to—is that of cost effectiveness. Cost effectiveness, of course, is not just the cost of doing things. Certainly anyone in this room can calculate relatively easily the cost of doing any of the things that he proposes to do: He can estimate the man-hours, the materials, and other items of that type. But far more difficult to calculate is the value of what he does, particularly in the kind of subject that we are dealing with in this seminar. How much is it worth to correct or improve a picture? We do not have any measures for the value of such a correction or improvement and, because it is difficult to determine this value, it has again been difficult to find R&D support in this field.

There is no quick and easy answer to the question of calculating the value of image compensation, correcting images, and improving images, but there is perhaps one approach that might be worth considering. It is based on the old cliche of "a picture being equal to a thousand words." Although there is argument over whether it is 1000 or 10 000 words, one can make a simple calculation that indicates it is even greater than the latter.

By applying some of the space philosophy that we have developed in recent years, one can translate an image into numbers; that is, one can digitize it. Assuming a rather modest resolution of a particular picture of 500 vertical and 500 horizontal lines—which is not even as good as commercial television—a picture divided into that number of elements would give 250 000 picture elements.

Assume we want to categorize the picture by 63 scales of grey. We also assume, and we know, that 63 grey scales can be digitized with a 6-bit digital code. To describe this picture would then require 6 bits times 250 000—or about 1½ million bits. This is the procedure used to calculate the channel capacity required to transmit that picture. Roughly, therefore, ½ million bits are required to describe digitally a picture of modest resolution.

Now, if we use English—and assume that there are about 26 characters in the English alphabet—we can use a 5-bit digital code to represent any letter we wish. Then, if we assume that, on the average, there are seven letters in each word, we can digitize each word with 35 bits. So if we have a 1½-million-bit picture, we divide 35 into 1½ million, which gives roughly 50 000 words in our picture. Considering the information contained in each one of the elements in the picture and determining the value of the presence of each element—whether it is useful or useless, whether it is a good bit or a bad bit—this approach might show a way to quantify the value of image improvement. Of course, this is a gross simplification that does not treat the intellectual interpretation, but that is an entirely different subject.

To give another quantitative indication of the value of visual and pictorial information, let us look at the consumer, the human being. In his brain and nervous system, he has about 10^{10} neurons that use the kind of information we are to discuss at this seminar.

Any information comes to the ultimate user, the brain, through the five basic categories of transducers that we possess: sight, smell, taste, touch, and hearing. These five transducer categories are connected to the 10 billion neurons through 3 million information channels. Surprisingly, two-thirds, or 2 million, of these channels connect the two eyes to the brain. The other 1 million are shared by the remainder of the senses. This gives a somewhat quantitative indication of the importance of visual information, even though we have always been intuitively aware of the fact that sight is our most dominant sense.

In conclusion, I would again like to encourage you to give some thought to the value of the imaging improvements that you are going to discuss at this meeting and to think of ways we might be able to quantify potential improvements in images and pictures.

INTRODUCTION

MAX R. NAGEL
NASA Electronics Research Center, Cambridge, Mass.

It would be unusual if anyone who sees the glamorous pictures of the Earth, moon, or Mars in our newspapers, magazines, and books, or who sees them on the walls of the offices, hallways, and laboratories, would not be led to think that photography must be the least troublesome area of the entire space effort.

Unfortunately the impression obtained from walking through office corridors or glancing through magazines is quite misleading. A person simply does not hang bad pictures on walls or advertise failures without necessity. Actually, throughout the history of space photography in the United States or abroad and within and outside the NASA effort, extensive failures have occurred. It is true that much publicity has been given to the malfunctioning camera sequencer that spoiled 50 percent of the photographic output of Lunar Orbiter I. The press also noted that Lunar Orbiter III had stopped taking photographs 11 hours before the planned time. The complete fact is, however, that almost all major space photographic projects have initially had technical difficulties and problems.

The accompanying illustrations offer what seems to be a fairly representative sampling of less-than-perfect results of some such space photographic programs. Figure 1, taken in 1959 from one of the earliest spacephoto experiments aboard Explorer VI, shows a well-washed-out picture of a cloud field over the Pacific Ocean. Figure 2 is a section of one Ranger VII photograph taken shortly before the impact of the craft on the lunar surface in 1964. Figure 3 shows photographs of a dust sampler placed against the window of a Gemini space capsule and taken with a hand-held camera; in figure 4 there are clippings from a film looking through the window of the Gemini XI spacecraft, and figure 5 is a picture from the Lunar Orbiter I mission. An example of ground-based degraded photography is given in figure 6, which is the atmospherically degraded picture of the Pegasus micrometeorite research satellite taken with the Air Force sky surveillance telescope in Cloud-

FIGURE 1.—Cloud field over the Pacific Ocean. Photograph taken by Explorer VI, August 14, 1959. (Courtesy of the Editor, TRW Space Log, Redondo Beach, Calif.)

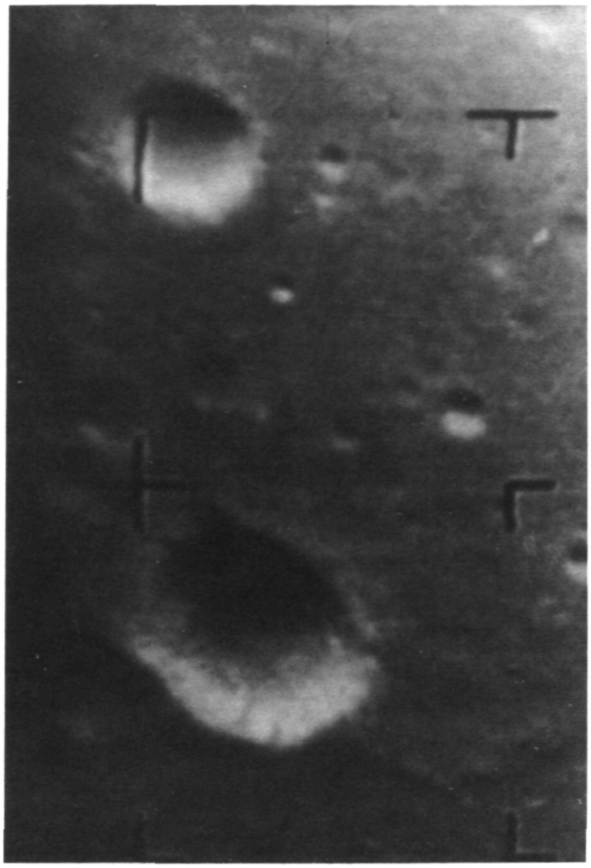

FIGURE 2.—Section from a photograph of the lunar surface, made by Ranger VII from 25 miles above the surface on July 31, 1964.

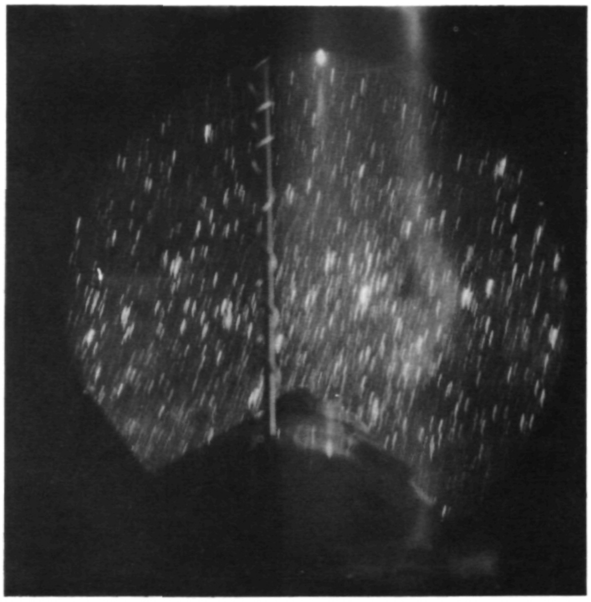

FIGURE 3.—Photograph taken of dust samples at the window of a Gemini space capsule taken with a handheld camera.

croft, New Mexico. Finally, in order to show that image blurs are indeed an international problem, figure 7 gives a reproduction of the first, heavily retouched photograph of the backside of the moon made by the Russians from Lunik III in 1959.

In the context of our seminar, it is now significant that the degradations in all of these pictures have been caused primarily by image motion. It is not difficult to find such motion-degraded photographs. In fact, except for blemishes introduced by electronic transmission anomalies, motion degradations are the most frequent, and at the same time the most damaging form of deficiency likely to appear in images relating to the exploration of space and the universe. This is so because there are many more possibilities that motion blurs will occur than for any other kind of defect.

Failures such as these can be caused by malfunction of the photographic apparatus itself, by the influence of the environment, or by the human factors involved. In other cases, they may be a consequence of built-in deficiencies of the entire spacecraft or simply of the operational situation at the instant when a picture is taken.

In particular the failures may be caused by vibration from closeby machinery, the spinning or tumbling of the spacecraft, the jerking of the camera by the hand of an astronaut who cannot steady himself properly in a gravitationless environment, or even by the click of the camera shutter. Failures may also occur when photographs are taken with large focal length cameras and without image motion compensation at high speeds from low altitudes as during both Lunar Orbiter experiments. Finally on the ground the rapidly fluctuating index of refraction of the atmosphere makes the image jump rapidly in the image plane of telescopes and cameras, thus imposing most severe limitations in the activities of astronomers, tracking technicians, and sky observers. In fact, the design specifications for large

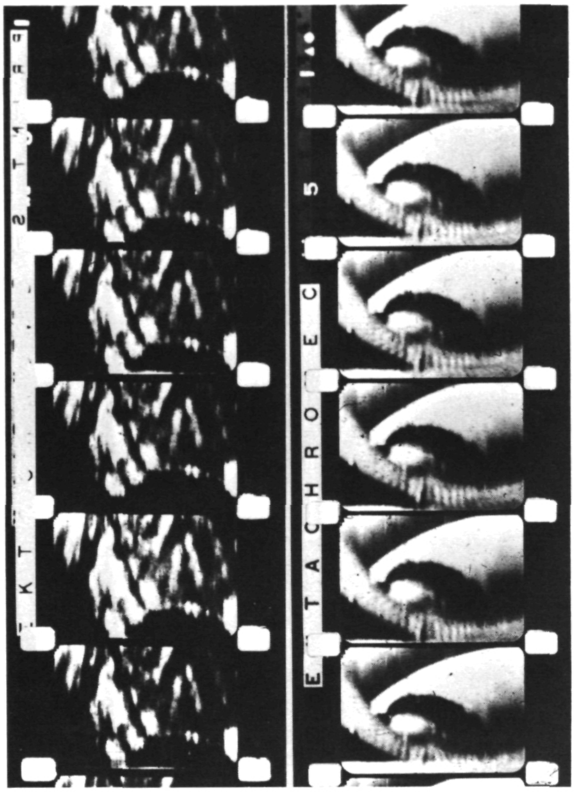

FIGURE 4.—Clippings from a 16mm film made during the flight of Gemini XI.

FIGURE 6.—Picture of the Pegasus micrometeorite research satellite taken with the Air Force telescope in Cloudcroft, N.M.

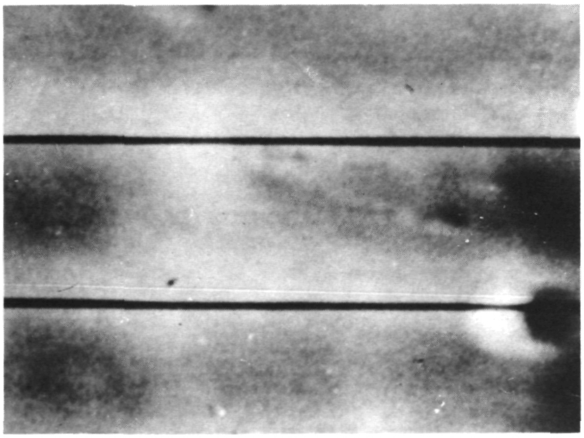

FIGURE 5.—Enlargement of a photograph made with the high resolution camera aboard Lunar Orbiter I.

→

FIGURE 7.—Backside of the moon. One of three pictures taken from Lunik III, 1959.

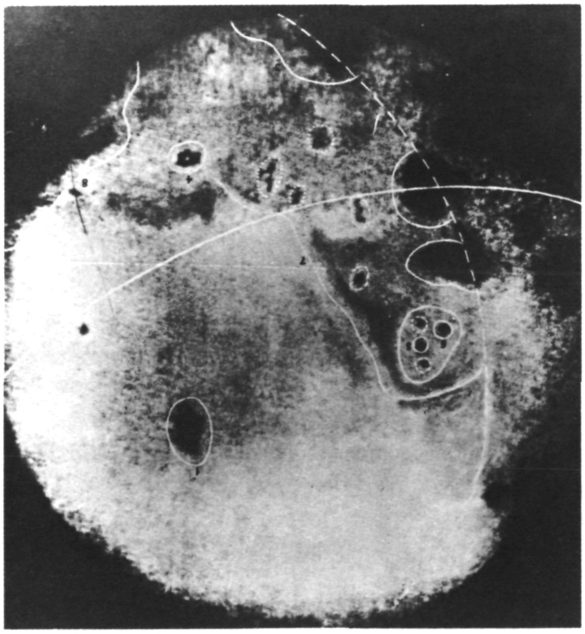

ground-based astronomical telescopes reflect the realization that, atmospheric "seeing" conditions, not the technology, determine the quality currently obtainable in optical imagery.

In addition to being the most frequent and devastating image degradation, the motion blur is also the most difficult one to deal with, once it is present. Even defocussing smears—which are infrequent in space flight situations, as fixed-focus cameras are predominant—are more amenable to modern image processing techniques, and problems of faulty exposure can often be solved by rather conventional printing methods. Motion degradation in imagery has therefore become one of the important areas of concern in space photography and astronomy.

Motion degradation is likely to become more important in the years to come when, in 1969 and 1973, we will again take cameras to the Moon, to Mars, and beyond and when programs such as the Earth resources survey program will get underway. The merits of other information notwithstanding, the immediacy of the impact of a picture on the human mind certainly makes television and photography two of the most important parts, if not the most important ones, of our future space programs.

From another point of view, the 22 pictures produced during the 1964 Mariner IV flight to Mars represent an asset of immeasurable scientific value. Conversely, any bit of information unnecessarily left buried in smears and blurs is just as great a loss in scientific knowledge. At the same time it is also a loss in effort and dollars. Calculated in proportion to the number of transmitted bits alone, the cost for the Mars pictures, for example, amounts to about $5 million. Quite possibly the actual cost may be closer to $10 million. Obviously, all means must therefore be explored to protect an investment of this magnitude in the austere years ahead for the space program. We just cannot afford to lose $10 million of our precious research funds to the undeniable and immutable possibility of a defunct camera shutter.

This seminar has primarily been called to discuss the state of the art and the progress made in the development of techniques for the *post facto* removal of motion degradations from photographic imagery, including specifically also degradations induced by the turbulence of the atmosphere. We have already seen impressive results of such techniques and are confident that both time and funds spent for such development will yield handsome returns and an effective insurance of the large national investment in the photographic programs in space and on the ground. This is so even though few of us will share the view of that visitor to NASA some time ago who, when shown a series of "before-and-after" photos, blurted out with the suggestion that it might soon be time now to sell his stock in the company that makes NASA's image motion compensation equipment! Rather, it seems appropriate to leave room also for the consideration of methods by which image motion is eliminated even before it affects the image on the film, of techniques for the retrieval of the geometry and photometry of images from motion-degraded photographs, and of studies on the phenomena generally observable within a motion-degraded photograph. Finally we have invited our speakers specifically to address themselves also to the aspect of shortcomings and practical limitations of the modern image evaluation techniques. We hope thereby to find a direction for the needs and planning of future work in a field that holds great promises, indeed, for many of NASA's projects in the next decade.

In conclusion, it is the privilege of the seminar chairman to thank the management of NASA's Electronics Research Center for permission to hold the seminar and for making available the necessary facilities and for providing administrative help. In particular, special thanks are due Lester C. Van Atta, who not only presented the proposal of the seminar to the ERC Management Council but also followed up with a sizable contribution from the special projects fund. Finally, the chairman wishes to express his appreciation for the work done, and still remaining, by the many people behind the scenes, and especially to Robert W. Galligan and Mary L. Leonard, without whose devotion to the project and efficient assistance throughout the past three months this seminar would have been entirely impossible.

7

Session I

ANALYSIS AND EVALUATION OF MOTION-DEGRADED PHOTOGRAPHY

F. Dow Smith, *Chairman*
Itek Corporation
Lexington, Mass.

Page intentionally left blank

Page intentionally left blank

THE INFLUENCE OF IMAGE MOTION ON THE PHOTOGRAPHIC IMAGE

ROLAND V. SHACK

University of Arizona
Tucson, Ariz.

ABSTRACT

The theory of photographic image formation in the presence of image motion was developed for the general case of the extended object, using Fourier transform theory. The assumptions and conditions under which this approach is valid were discussed in some detail, and it was shown that it is often possible to treat the effect of image motion as an additional stage of image formation having its own transfer function and spread function contributing to the total degradation of the image. The special cases of linear and simple harmonic image motion were discussed in some detail, the latter especially for the case where there are at the most only a few periods in the exposure time. An approximation for small degradations was then described which makes it much easier to consider the consequences of combined image motions. The variation of image motion across the field of a photograph was also discussed, especially with regard to the possibility of correcting for it either before or after the photograph is made.

Page intentionally left blank

Page intentionally left blank

THE PRECISION OF EDGE ANALYSIS APPLIED TO THE EVALUATION OF MOTION-DEGRADED IMAGES*

MELVIN J. MAZUROWSKI AND ROBERT E. KINZLY
Cornell Aeronautical Laboratory, Inc.
Buffalo, N.Y.

The evaluation of amount and type of motion degradation is desirable in assessment of operational performance of optical systems and in the design of image enhancement techniques. Since test charts are not usually available in the image format, alternative techniques such as edge gradient analysis are frequently employed. Such techniques are not without error due to nonlinear film response, film granularity, instrumentation effects, etc. An analysis of a single edge trace is usually not sufficient to evaluate the system transfer function, let alone determine quantitative information about the presence of motion degradations.

In the process of evaluating the quality of the Lunar Orbiter photography, the precision of the edge analysis techniques in evaluating the system modulation transfer function was studied in detail. These results are used to determine the probability that motion degradations can be evaluated as a function of the number of edge traces used in the analysis and the magnitude of the motion degradation.

In addition, edge gradient techniques were used to assess the image motion compensation capability of the Lunar Orbiter photographic system in actual operation and preflight laboratory testing. An oblique high resolution photograph, taken during the Lunar Orbiter II mission, can be expected to exhibit different degrees of compensation with format position. Eleven areas in the format of the photograph were selected, appropriate edges scanned, and values of the resolution at the lunar surface determined. The resolutions compared favorably with those values expected for each of the areas in the format depending upon the distance of each area from the point at which the IMC detector was aimed.

A laboratory test of the operation of the IMC system for the primary and backup photo subsystems for the Orbiter V mission was made. In this test, photographs were obtained of a checkerboard test pattern driven past the optical system on a belt moving at controlled speeds ranging from 37.5 milliradians per second down to 3 milliradians per second. Edge gradient analysis made on the recorded edges of the checkerboard pattern clearly shows the motion-degrading effects between images obtained with the IMC operating and with it off.

The enhancement of imagery usually requires some knowledge of the amount of degradation introduced into the image by the optical system. This degradation is represented by the optical transfer function (OTF) of the imaging system. Generally, one must rely upon an analysis of the information content in the image to evaluate quantitatively the OTF. The technique most frequently employed is that of edge gradient analysis. In this technique, an edge or series of edges are selected in the image format and scanned using a microdensitometer. If required, the resulting edge traces are corrected for any nonlinear photometric response such as the Hurter-Driffield response of photographic film.

---

*Part of this work was supported by NASA Langley Research Center.

The resulting edge traces can then be differentiated, Fourier transformed, and normalized to determine the optical transfer function.

Since the imagery consists of both signal and noise components, the evaluation must employ statistical estimation procedures. When a significant portion of the noise power in the image is outside the spatial frequency band occupied by the signal, simple low pass filtering can be used to smooth the noisy edge trace before it is processed to evaluate the OTF. On the other hand, if a significant amount of noise power remains within the signal band, more sophisticated techniques may be required for processing the data to remove this noise. The most direct method for removing some portion of this noise is to have the edge trace smoothed from visual examination.

In spite of these techniques for reducing noise power, in some cases a significant amount of noise may remain in the edge trace and produce an error in the estimation of the OTF. In a study of image evaluation techniques applied to the Lunar Orbiter spacecraft (ref. 1), we observed that one had to resort to additional estimation procedures to evaluate the modulus of the optical transfer function which is usually referred to as the modulation transfer function (MTF). We averaged the individual modulation transfer functions determined from several parallel edges in proximity in the image format. As a result we obtained, in addition to the MTF, an estimate of the precision of the analysis technique when applied to the Lunar Orbiter photography. The precision was measured as the standard deviation between the various measurements of the MTF as a function of spatial frequency. This information is used in this paper to assess the applicability of edge gradient analysis to the evaluation of motion-degraded images.

MTF ESTIMATION BY ENSEMBLE AVERAGING

The method of ensemble averaging, in which individual modulation transfer functions are determined using k different edges from the same area in the image format and the average value of the individual measurements used as an estimate of the true modulation transfer function, has recently been studied (ref. 2). It has been shown that at the spatial frequencies where the true MTF diminishes, the residual noise in the edge trace introduces significant errors in the determination of the modulation transfer function and that these errors do not diminish with the acquisition of more edge traces.

Assuming that the optical transfer function for the imaging system in its normal operation is real and therefore equal to the nominal modulation transfer function, $\tau(\nu)$, the individually measured modulation transfer functions can be written as

$$\tau_j(\nu)=\left|\tau(\nu)+n_j(\nu)e^{i\phi_j(\nu)}\right|_{j=1,2,\ldots,k} \tag{1}$$

where $n_j(\nu)$ and $\phi_j(\nu)$ represent the modulus and phase introduced in the Fourier transfer due to the residual noise present in the jth edge trace. Since this equation represents a nonlinear transformation between $\tau(\nu)$ and $\tau_j(\nu)$ the average MTF,

$$\hat{\tau}(\nu)=\frac{1}{k}\sum_{j=1}^{k}\tau_j(\nu) \tag{2}$$

is not equivalent to the modulus of the average optical transfer function. If $\tau(\nu)$ is allowed to vanish in equation (1), the estimator described by equation (2) approaches the expected value of the modulus of the residual noise. Thus an error or positive bias is introduced into the measured modulation transfer function so that it is progressively greater than the true modulation transfer function as spatial frequency increases; that is,

$$\hat{\tau}(\nu)=\tau(\nu)+\epsilon(\nu) \tag{3}$$

The point where the error, $\epsilon(\nu)$, becomes significant depends upon the magnitude of the residual noise in the normalized edge traces and can be expected to vary depending upon the optical system which produces the imagery.

The modulation transfer function for both the medium resolution and high resolution imaging systems were measured using this ensemble averaging technique on the Lunar

Orbiter II photography. For each system, the MTF was measured once on a frame at the beginning of a mission and once on a frame near the end of a mission. There was no apparent difference in the MTF in the beginning and end of the mission and the individual measurements were combined and averaged to determine the MTF for the entire mission. The results obtained for the high resolution imaging system of Orbiter II are shown in figure 1. The 95 percent confidence interval for the average MTF was determined in the conventional manner, assuming that the individual deviations are normally distributed. The data shown by the squares in the figure represent the modulation transfer function determined from preflight calibration data. There is excellent agreement between our measurements and these data at spatial frequencies below 60 lines/mm. Above this frequency, however, measured MTF is biased above the true value. In the case of the Lunar Orbiter imaging system, therefore, the error function introduced by the ensemble averaging method becomes significant in the spatial frequency region of 50 to 60 lines/mm.

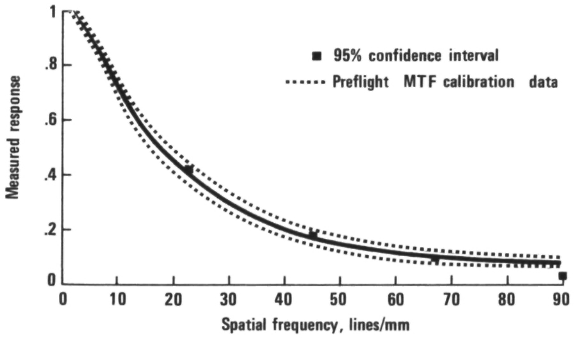

FIGURE 1.—Measured MTF for the Lunar Orbiter II high resolution imaging system.

We are now ready to consider the problem of the detection of additional degradation in the imagery over and above that introduced by the nominal MTF of the optical system. Specifically, we would like to consider how the observed precision of the ensemble averaging technique would have affected our ability to detect uniform image motion due to poor IMC performance in the Lunar Orbiter imaging system.

DETECTION OF MOTION DEGRADATIONS

How much additional degradation must be introduced into the image in order to be able to detect it from the measured value of the modulation transfer function, assuming that the modulation transfer function of the system for its normal operation is known (nominal MTF)? In practice we would subtract the measured MTF from the nominal MTF and inquire whether the observed difference is significant enough to state that additional degradation has been introduced into the imagery. Specifically, we will examine the problem of the detection of uniform image motion whose MTF is given by

$$\tau_D(\nu)=\left|\frac{\sin(\pi\nu x_0)}{\pi\nu x_0}\right| \tag{4}$$

The measured transfer function, following the form of equation (3), is

$$\hat{\tau}(\nu)=\tau(\nu)\tau_D(\nu)+\epsilon(\nu) \tag{5}$$

where the function $\epsilon(\nu)$ represents the bias error in the average measurement.

One distinguishing feature of the transfer function for uniform image motion is the fact that it possesses nulls at equally spaced intervals in spatial frequency. We note, however, that due to the presence of the error function, $\epsilon(\nu)$, that the measured value of the MTF, $\hat{\tau}(\nu)$, will not approach zero at these spatial frequencies and, we can use the zero locations of the motion degradation as an indication of the presence of degradation in the imagery only when the residual noise in the edge trace is small enough that ensemble averaging is not required. Instead, we pose the question as a statistical test of the significance of the difference between the known normal modulation transfer function and the measured modulation transfer function at a given spatial frequency, assuming that the deviations in the measurements are normally distributed. Since we know that the measured modulation transfer function will be less than the nominal modulation transfer function, if any additional degradation is present we can use a one-sided T-test to test the significance of the difference between the nominal and measured transfer functions, that is, the difference between the two transfer functions must be large enough to satisfy the following inequality

$$\frac{\tau(\nu)-\hat{\tau}(\nu)}{s(\nu)} > \frac{t_{1-\alpha}}{\sqrt{k}} \qquad (6)$$

where $t_{1-\alpha}$ is the percentile of the T-distribution at significance level α. If we assume that we make our test at a spatial frequency where $\epsilon(\nu) << \tau(\nu)\tau_D(\nu)$, we can simplify this expression by employing equation (5), neglecting $\epsilon(\nu)$ and the test becomes

$$1-\tau_D(\nu) > \frac{s(\nu)}{\tau(\nu)}\frac{t_{1-\alpha}}{\sqrt{k}} \qquad (7)$$

From this expression, we can see that the ratio of the observed standard deviation to the known nominal transfer function determines the number of samples required to be able to detect a given amount of degradation at a particular level of significance. The value of the ratio of $s(\nu)/\tau(\nu)$ presented in figure 2 was determined from the data obtained in evaluating the Lunar Orbiter II photography. The dashed curve is the ratio of the observed standard deviation to the nominal MTF for the high resolution system determined from preflight calibration data. The solid curves were determined using the measured MTF. The rounding of the ratio at spatial frequencies above 40 lines/mm in the data for the high resolution system is due to the error inherent in the ensemble average estimation method. In the case of the medium resolution data, the rounding off is not as evident because the nominal MTF does not decrease as rapidly for that system.

Using the dashed curve, the number of measurements required to detect 10, 12.5, 16.7 and 25 microns of image motion at levels of significance of 90, 95, and 99 percent were evaluated. Some of the results are presented in figures 3 and 4. Figure 3 shows the number of measurements required to detect 10 microns of linear motion on the spacecraft film of Lunar Orbiter II as a function of the spatial frequency at which the test is conducted. The one-meter resolution limit of this sytem is equivalent to 13 microns on the spacecraft film and therefore the magnitude of the motion is slightly under the resolution limit. In establishing the one-sided

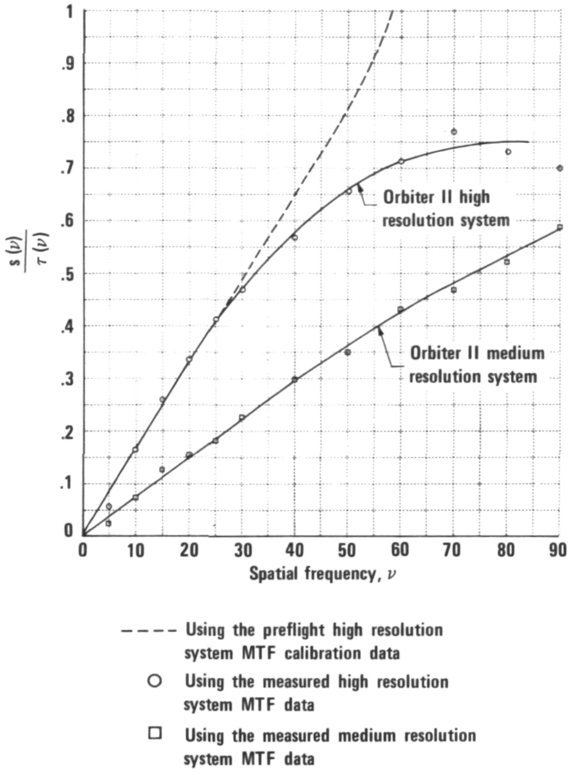

FIGURE 2.—Ratio of standard deviation to nominal MTF for Lunar Orbiter II.

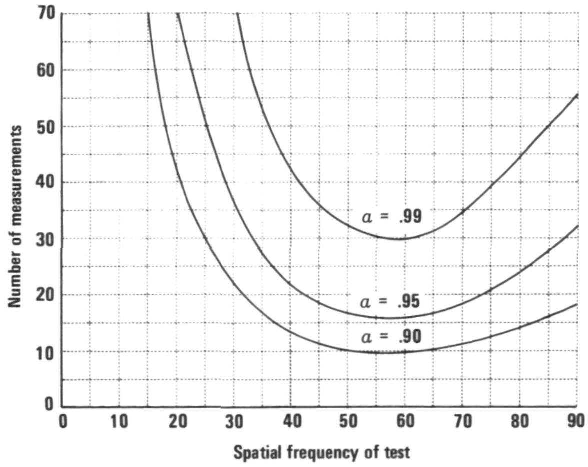

FIGURE 3.—Number of edge traces required to detect 10 microns of linear motion degradation in the Lunar Orbiter II high resolution imagery at the 0.90, 0.95, and 0.99 significance levels.

T-test, it will be recalled that we assume that the test was made in a region where $\epsilon(\nu)$ could be neglected compared to the product $\tau(\nu)\tau_D(\nu)$ and in the case of the high resolution system, this would correspond to spatial frequencies less than 50 lines/mm for 10 microns of image motion. If 20 to 25 edge traces are employed in determining the modulation transfer function, a significant deviation of the measured transfer function from a normal transfer function would occur in the spatial frequency band of 30 to 50 lines/mm and that 90 percent of such deviations would be attributed to traditional degradation motions in the imagery rather than the precision of the estimation method. Figure 4 shows the number of edge traces required to detect various amounts of linear motion degradation at the 0.95 significance level. As the magnitude of the motion increases, the product $\tau(\nu)\tau_D(\nu)$ decreases thus forcing us to further restrict the upper bound of the region where the test is applicable. This is compensated for by the decrease in the number of measurements required at the low spatial frequencies which allows the lower bound of the test region to be reduced simultaneously. By the time the magnitude of the motion is about two resolution elements (25 microns), 20 edge measurements provide more than enough information to detect the additional degradation in the spatial frequency band of 5 to 20 lines/mm.

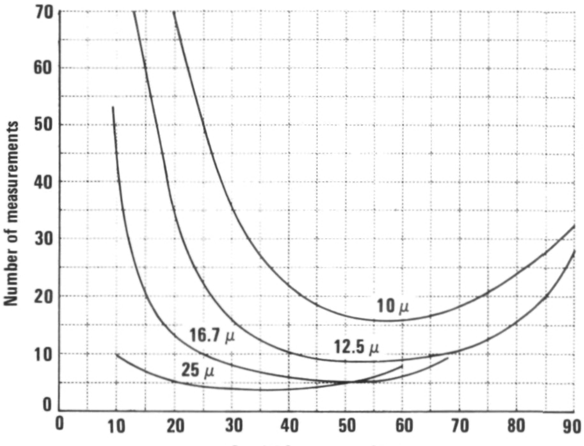

FIGURE 4.—Number of edge traces required to detect 10, 12.5, 16.7, and 25 microns of linear motion degradation in the Lunar Orbiter II high resolution imagery at the 0.95 significance level.

Although the results presented here are based upon the precision of estimating the modulation transfer function of the Lunar Orbiter imaging system and therefore are dependent upon the residual noise in the edge traces obtained in analyzing that imagery, similar results are to be expected in the case of other types of imaging systems. It also should be pointed out that when a significant deviation is observed between the nominal modulation transfer function and the measured modulation transfer function, there is no guarantee that this deviation is due to the degradation of linear motion alone but may include other types of degradation such as vibration and atmospheric effects.

APPLICATIONS

The MTF evaluation techniques were used to assess the image motion compensation capabilities of the Lunar Orbiter photographic system in two practical cases: (1) involving the actual operation of the system and (2) to analyze data obtained in preflight laboratory testing.

To utilize the Lunar Orbiter imaging system to obtain higher-resolution convergence stereo photographs, the spacecraft had to photograph the area of interest on two subsequent orbits obtaining nearly vertical photographs from one orbit and an oblique photograph from the other orbit. For oblique photography, the operation of the image motion compensation system is rendered less effective than for vertical photography since increasing the angle between optic axis of the camera system and the nadir produces varying amounts of motion compensation across the image format. In addition, the V/H sensor, which is aimed at a point ahead of the area covered by the high resolution photographic frame, senses a lower relative velocity than would exist anywhere within the image format of the high resolution frame. Consequently, the observed resolution should vary across such an oblique photographic frame and be greater than the nominal one-meter resolution limit of the vertical photography.

To determine the magnitude of this effect,

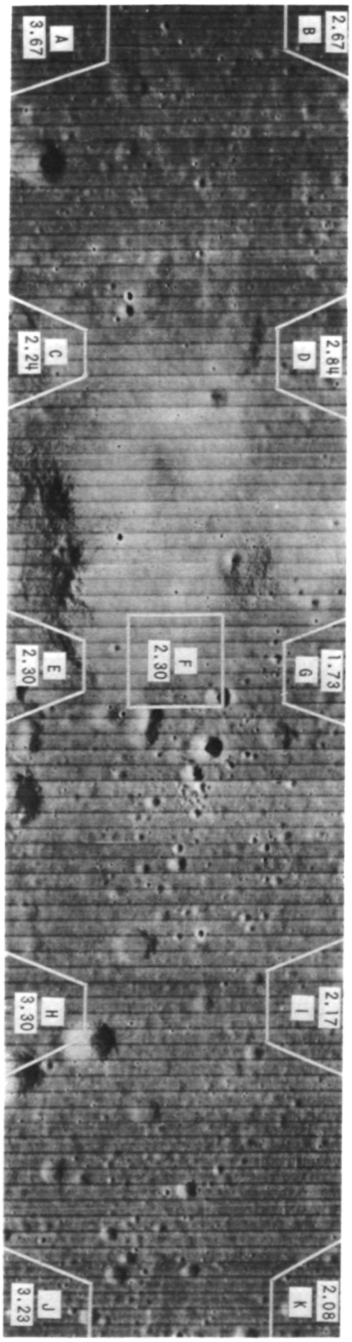

FIGURE 5.—Assessment of the ground resolution in oblique high resolution number 26 from Lunar Orbiter II. The numbers indicate resolution in meters on the lunar surface. The nominal resolution would be 1 meter at the center of the format without motion degradations.

an oblique high resolution frame from Mission II was analyzed. Sixty-one edges were selected from high resolution frame number 26 from 11 different areas in the image format and an evaluation of the imaging system modulation transfer function within each of the areas was performed. The ground resolution was determined for each of the 11 areas by noting the frequency at which the MTF decreases to 9 percent and converting this value to meters of resolution in a lunar surface. The 9 percent point was selected to be consistent with the point at which the preflight calibration of Lunar Orbiter II indicated a ground resolution of one meter on the lunar surface. The high resolution photograph with the areas sampled and the corresponding ground resolutions obtained, is shown in figure 5. The V/H sensor was aimed, in this case, just above area *G* resulting in the most effective motion compensation near that area of the format. The ground resolution can be seen to deteriorate as the distance from area *G* increases. In addition to the reduction in resolution due to the lack of motion compensation, the effect of the off-axis resolution of the camera lens can also be noted to cause an additional decrease in the resolution as the distance from the center of the photograph increases.

In the second application, a comparative evaluation was made of the image motion compensation at low V/H ratios for both the primary and backup photo subsystems for Lunar Orbiter V mission. During the operation of Lunar Orbiter IV, it appeared that when the image motion compensation system was operated at low values of V/H (less than 3 milliradians per second), the image quality was less than the quality achieved with the IMC off. It was felt that at low V/H ratios, the operation of the IMC system may have introduced more degradation (possibly due to vibration) in the quality of a photograph than would the image motion if the IMC were left off.

To determine the optimum range of operation for the image motion compensation system for Lunar Orbiter V, a series of tests were conducted in which both the primary and backup photo subsystems were used to generate test films. A checkerboard pattern on a moving belt was photographed by each system with the belt being driven to simulate image motion rates of 3, 4, 6, 8, and 37.5 milliradians per second. At each rate, a photograph was obtained with the IMC operating and with the IMC turned off. Typical examples of imagery obtained are shown in figure 6.

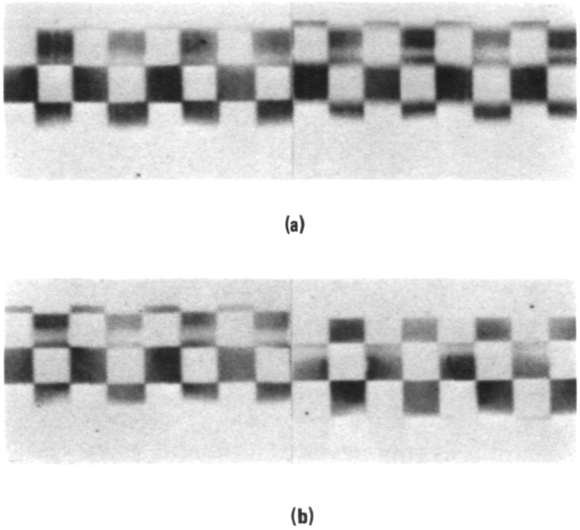

FIGURE 6.—Checkerboard test pattern images. Images on the left were obtained with motion compensation and those on the right without motion compensation. (a) V/H rate of 37.5 milliradians/sec.; (b) V/H rate of 8 milliradians/sec.

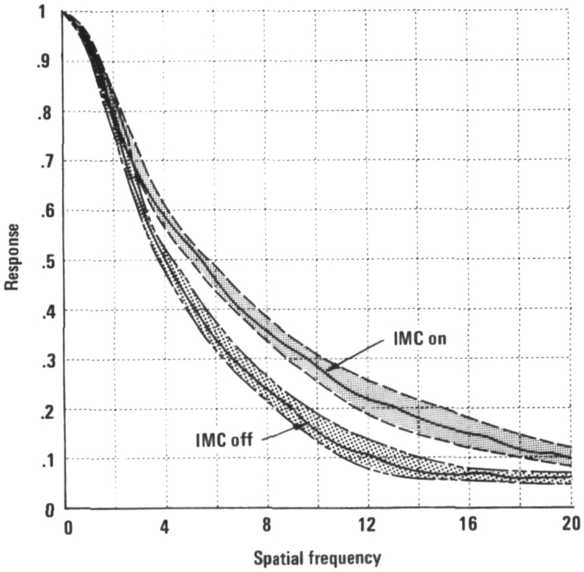

FIGURE 7.—Measured MTF with and without image motion compensation at a V/H rate of 3 milliradians/sec.

An analysis of the effectiveness of the IMC system was conducted by making several edge traces from the checkerboard pattern in the direction of motion and determining the modulation transfer function for each of the recorded images. Approximately five edge traces were analyzed from each of the photographs of the test pattern. The inherent resolution due to the quality of the checkerboard pattern (that is, its sharpness) was only on the order of 20 lines/mm; however, this resolution is still sufficient to enable the effect of the IMC operation at the lowest V/H ratio to be determined. This result is illustrated in figure 7 where the modulation transfer functions, including the 65 percent confidence intervals, are plotted for the system with the IMC system operating (upper curve) and with the IMC sytem off for an image motion rate of 3 milliradians per second. The motion transfer function for this image motion rate has its first zero value at 13.7 lines/mm. The technique of MTF estimation by ensemble averaging, while necessary to determine whether a significant difference exists between the transfer functions obtained with the IMC on and the IMC off, has clearly masked the appearance of a cusp at 13.7 lines/mm. If we divide the mean value obtained for the motion degraded MTF in figure 7 (IMC off) by the mean value of the undegraded MTF in figure 7 (IMC on), we can obtain an estimate of the degrading effect of the motion itself as shown in figure 8. Comparing this to the actual image-motion transfer function also shown in figure 8, an increasing positive bias can be noted in the estimate beginning at about 6 lines/mm and becoming approximately constant beyond the first "zero." Despite the significant bias, the estimated degrading effect of the motion does exhibit a minimum at approximately 14 lines/mm yielding a fairly accurate determination of the amount of image motion responsible for the degradation. The value of spatial frequency at which the bias becomes significant (i.e., about 6 lines/mm) corresponds to the frequency at which the effect of the residual noise in the edge traces influences the precision of the

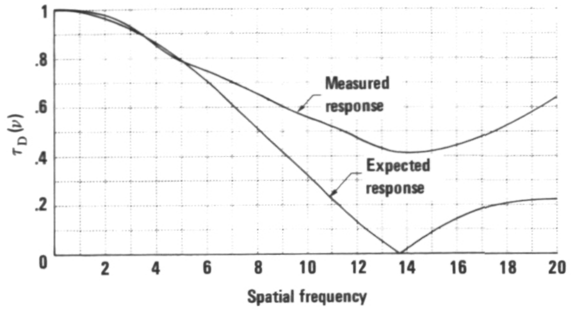

FIGURE 8.—Ratio of the measured MTF data in fig. 6 compared to the corresponding image motion transfer function.

ensemble averaging technique and corresponds to the spatial frequency where the transfer function being estimated decreases to approximately 1/3.

CONCLUSIONS

The technique of MTF estimation by ensemble averaging is biased, particularly at the spatial frequencies where the true MTF becomes small, less than 0.3 in the case of the Lunar Orbiter imagery. The amount of the bias depends upon the residual noise level in the individual edge traces. This error precludes the use of the zero locations of the motion degradations as an indication of their presence in the imagery. However, if a sufficient number of edge traces are employed in computing the average MTF, a significant difference between it and the known nominal MTF will exist in some band of spatial frequencies and the presence of additional degradation can be detected. The spatial frequency band and the required number of edge traces depend upon the magnitude of the degradation, as well as the residual noise level. In the case of the Lunar Orbiter, motion degradations whose magnitude is equal or greater than a resolution element would have been detected if they had existed in the imagery.

REFERENCES

1. KINZLY, R. E.; MAZUROWSKI, M. J.; and HOLLADAY, T. M.: Image Evaluation and Its Application to Lunar Orbiter. Appl. Opt., vol. 7, no. 8, Aug. 1968, p. 1577.
2. BLACKMAN, E. S.: Effects of Noise on the Determination of Photographic System Modulation Transfer Functions. Photo. Sci. and Eng., vol. 12, no. 5, Sept.–Oct. 1968, p. 244.

ON THE DENSITOMETRIC STRUCTURE OF MOTION-BLURRED EDGE TRACES IN UNDEREXPOSED PHOTOGRAPHS AND ITS EFFECT ON IMAGE-ANALYSIS PROCEDURE

MAX R. NAGEL
NASA Electronics Research Center
Cambridge, Massachusetts

This paper concerns photographic anomalies, which can be observed within the image traces contained in a heavily motion-degraded photograph, that are caused by the photometric structure of the projected image, the sensitometric properties of the photographic material, and, in some cases, by the photographic apparatus. In particular, the case of underexposure is considered. The results of laboratory experiments on the subject will be shown and discussed.

It appears that the amount of blur present in the underexposed photograph of an object depends on the luminance of the object and its background and that it can be influenced by the developing process. All other conditions being equal, images of the same object can produce different amounts of blur depending on their location in the image plane and on the mechanical characteristics of the shutter used. The amount of motion blur in the forward edge of an image can be different from that in the aft edge. In general, the distribution of the density within the image trace is subject to a modified version of reciprocity law failure.

We are concerned here with a number of photographic-sensitometric phenomena that can be observed in heavily motion-blurred photographs and which, either by themselves or in the interplay with other factors—introduced, for example, by the photographic apparatus—influence the results of the photogrammetric exploitation of such photographs. Some of these phenomena have been reported in earlier publications, several of them almost 30 years ago (refs. 1 through 3), but now appear to deserve renewed attention in the context of studies involving motion blur simulation, design and manufacture of spatial filters for image restoration, and the development of techniques for digital processing of motion-blurred images. In some of these applications, they determine the validity or practical limitation of such work.

In particular the considerations will refer to the case of a rapidly moving bright object photographed against a dark, and therefore underexposed background, when at the same time the image motion amounts to a substantial percentage of the dimension of the object. The dark background situation provides for good contrast in a photograph and is therefore often deliberately created in laboratory and field studies (e.g., on disintegrating ballistic objects) or while photographically tracking spaceborne vehicles or debris through a turbulent atmosphere, and during space photographic missions covering high-contrast lunar or planetary surface features at high angular speeds.

For the purposes of this report, motion-induced degradation is understood to appear in the form of motion blur only, and motion blur itself will be defined as the manifestation of image motion on a photographic film. Under the conditions assumed above, the amount of motion blur is given by the length of the recorded image trace of a moving edge.

BASIC EXPERIMENTS

When in the cases mentioned, object distances and dimensions were to be determined, the direct measurement of the length or photometric structure of the photographic image trace often gave obviously wrong results. Ordinarily it would be expected that, under the influence of an image motion s, an image with a stationary dimension l in the photograph would result in an image trace of length $L=l+s$. In fact, however, the dimension of the recorded image trace of the object itself is often smaller than given by image size and amount of image motion alone. At the same time, the distances between image traces were found to be larger than those given by the simple arithmetics. A series of experiments was therefore conducted to study the pertinent phenomena.

Figure 1 shows the basic experiment and its result. The object photographed, shown in the left half of the figure, was a white circular sector on a black background. The 135° sector was rotated about its apex at a constant speed and photographed using an accurately calibrated camera shutter. The angular path length of the image during the exposure time was determined to be about 86°. As expected, the central portion of the negative, called the core, which is characterized by a constant maximum density, extends over an angle of approximately 49°. Therefore, the first-order assumption would have been that in the photographic negative, shown on the right, the nominal length of recorded image trace would be $49° + (2 \times 86°) = 221°$ as indicated by the outermost heavy dashed radii. To the unaided eye, however, the boundaries of the image trace appeared in the negative at the faint radii inside these nominal limits, while the boundaries given by the density .1 above fog (which, for evaluation purposes, was adopted as the "practical" limit of the image trace) occurred at the innermost radii with the crosses indicating points of actual measurement. In the case shown, the visible length of the image trace was found to be 203°, and its practical one 180°, corresponding to a visible motion blur of 77° and a practical one of 65.5°. Accordingly, no less than 10 percent of the image motion was left unrecorded in the process.

Obviously these results can be accounted for by the sensitometric properties of the film used. Only where the exposure is great enough can a noticeable image density above the fog noise be produced. This threshold exposure is not reached, however, within the extreme forward and aft portions of the image trace. There, the moving image exposes the film for only a very short time, thus causing the observed shortening of the image trace.

Clearly, therefore, the amount of motion

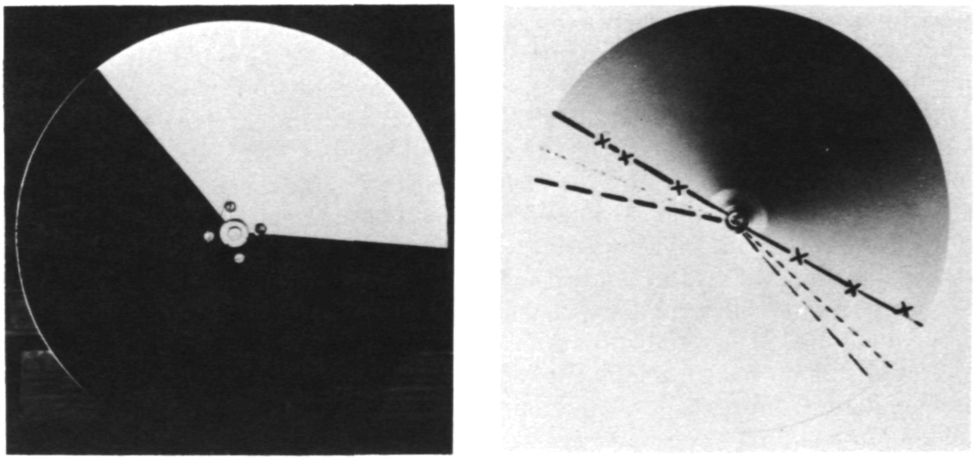

FIGURE 1.—Basic experiment demonstrating suppression of image motion. Object used at left, and negative obtained at right. The radii indicate the dimensions of the nominal, visible, and practical boundaries of motion blur.

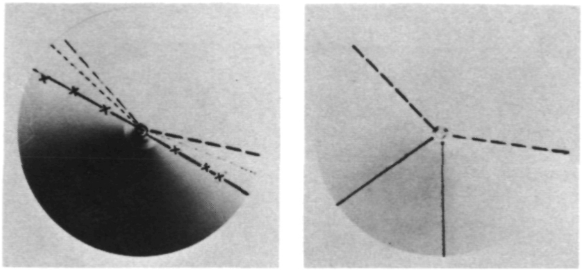

FIGURE 2.—Suppression of motion blur by underdevelopment. The right negative is developed for a shorter time than the left negative. The radii indicate the location where the negative density is 0.1 above fog.

blur appearing in a photograph is subject to all sensitometric factors and thus, also among others, to the development conditions. This is confirmed in figure 2 where, under otherwise equal experimental conditions, the negative at the right has been developed for a shorter time than the one on the left. Here again the 0.1 above fog "practical" trace limits have been indicated and show a considerable increase of the unrecorded portion of the image trace.

Perhaps of greater significance is the dependence of the motion blur on the photometric properties of the object. The left part of figure 3 shows the object used in a demonstration of that dependency, and the right part shows the negative resulting from it. The unrecorded part of the image trace diminishes distinctly and the motion blur is augmented when the object radiance increases. The analyst who intends to determine true stationary image dimensions from motion-blurred negatives must therefore carefully observe the possibility of unrecorded image motion and, in any particular case, look for an opportunity to find the full amount of image motion.

One such possibility presents itself from the microdensitometric study of image details located on a background of finite radiance. This is demonstrated in figure 4, where the same solid white object sector is now superimposed on a series of "background" rings of varying radiance. As before, the nominal and the practical boundaries of the image trace are indicated, and, as must be expected, the difference between the amounts of image motion and motion blur diminishes, indeed, with the increasing background brightness. The difference disappears if the exposure inflicted on the film by the background equals or exceeds the threshold exposure of the film. This is the case in the outermost ring where the radiance of the brightest background is almost as great as that of the object proper.

Obviously, therefore, the best way to determine the total image motion is to measure it directly from an image trace superimposed on a homogenous background of a brightness

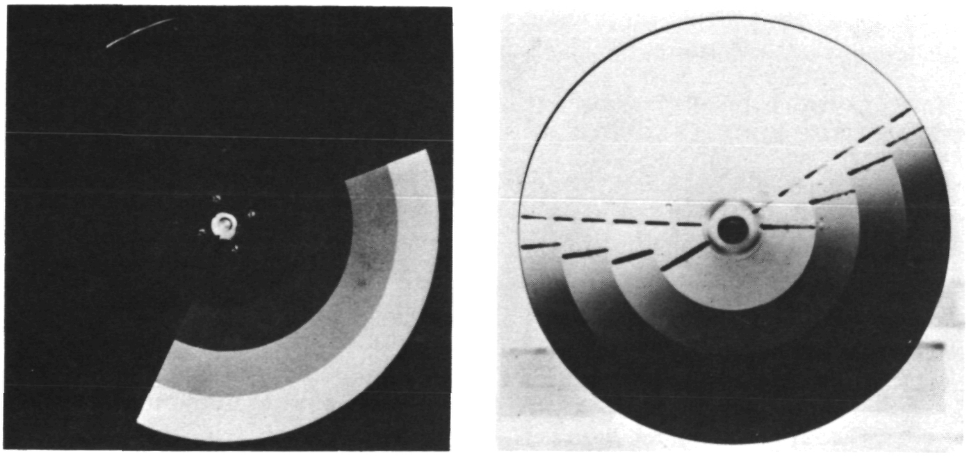

FIGURE 3.—Dependency of motion blur on the photometric properties of the object. Object at left, and negative obtained at right. The radii indicate location where the negative density is 0.1 above fog.

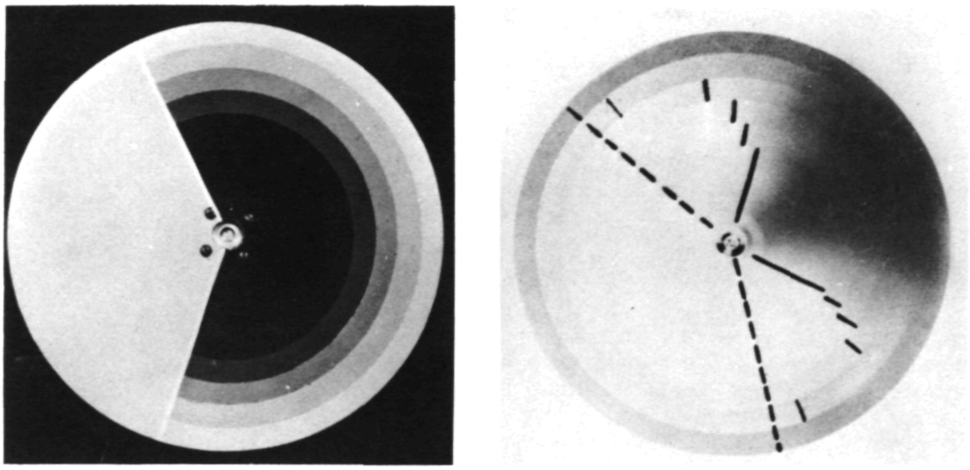

FIGURE 4.—Dependency of motion blur on the background density. Object at left, and negative obtained at right. The radii indicate location where the density is 0.1 above fog.

that by itself suffices to lift the resulting exposure above the threshold level of the film.

Because real-life photography commonly contains randomly distributed images and backgrounds of varying luminance, the results of the foregoing experiments justify the question of how far current spatial filtering techniques are able to restore a motion-blurred image. Under the conditions of the experiments—dark backgrounds and heavy image motion superimposed on relatively large images—the point spread function can vary significantly from point to point of an image field. Obviously, therefore, a simple spatial filter will not necessarily reconstruct the original geometry or photometry in all sections of the field.

PHOTOMETRIC RELATIONSHIPS BETWEEN THE FORWARD AND AFT EDGE TRACES OF AN IMAGE

While the basic effect underlying the phenomena shown in the foregoing illustrations is easily explained through the interplay of sensitometric and geometric optical factors, the further implications will best be deduced by examining the process by which the density distribution on the film is generated. For this purpose, refer to the upper part of figure 5 and assume that the sharp image of a homogenously radiating object produces on the film an irradiance $I(t)$ which is a function of the time t. This image moves at a constant speed over the film in the direction of increasing x. The dimension of the image on the film, in the direction of motion, is l. The terms "forward" and "aft" refer to the direction of the image motion as indicated in the figure.

At the beginning of the exposure, the aft edge of the image rests for a short time dt at a point $x=x_0$ and imparts over the length l a small exposure $dE=I(t)\ dt$, which in the illustration is indicated by the height of the bottom "parcel" of exposure. During the next time interval, the image moves toward the right by a distance $dx=vdt$ and imparts another parcel of exposure which now, because of the changing irradiance, has a height different from the previous one. This process continues until, at the end of the exposure time T, the image has traveled a distance $s=vT$ and, in the core of the image trace, the exposure $E_{\max}$ has been reached. The combined heights of all parcels above any point x constitute the exposure $E(x)$ in that point.

Plotting $E(x)$ in the conventional manner in the lower part of the figure and indicating a threshold exposure $E(\tau)$ at which the film develops a minimal noticeable density above its fog (or noise) level, this presentation graphically confirms the phenomena demonstrated in figures 1 through 4. It also yields directly the basic relationship between the exposure distributions in

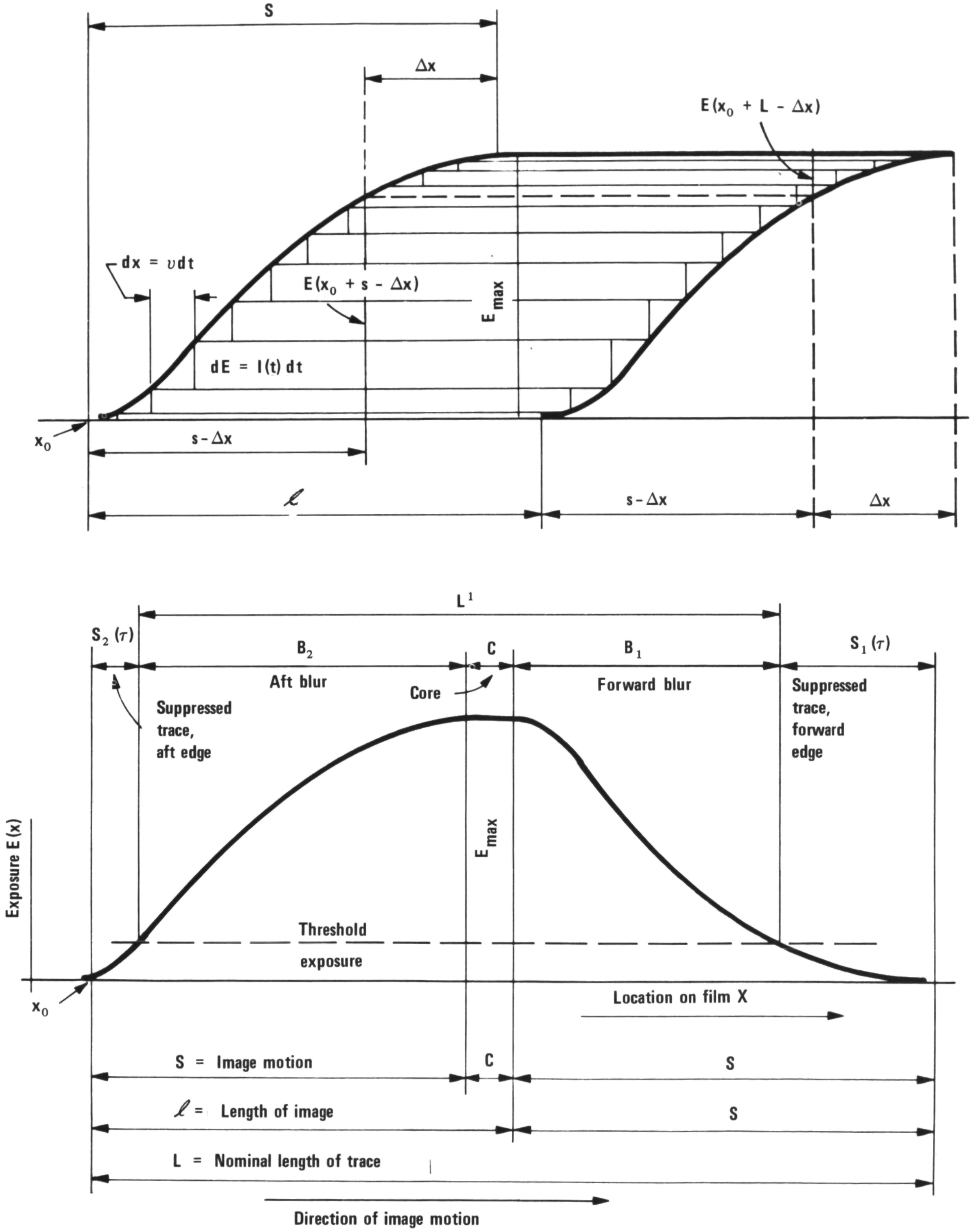

FIGURE 5.—Illustration demonstrating the generation of the density distribution within the image trace of a moving object. A defective camera shutter producing asymmetric motion blurs B_1 and B_2 is assumed.

the image traces of the front and aft edges of the object:

$$E(x_0+L-\Delta x)=E_{\max}-E(x_0+s-\Delta x) \quad (1)$$

where $E(x)$ is the exposure in any point x within the region of the aft edge, or $x_0 \leq x \leq x_0+s$, respectively. This relationship is experimentally significant, because the reference points $x=x_0+s$ and $x=x_0+L-s$ are often fairly accurately measurable as the beginning and end of the core section of the trace where the density is constant. This fact, together with equation 1, in many cases permits the reconstruction of both the geometry and the exposure distribution within the entire image trace. Notably this also includes those portions that superficially seem to have been lost in the subthreshold fog noise of the film. This is so because, according to equation 1, the subthreshold exposures in the image trace of one edge reappear in the trace of the other edge in the form of differences between $E_{\max}$ and the exposures producing the densities in the vicinity of the trace core.

Therefore, if the characteristic curve of the film is known, the subthreshold exposures, and the geometry of the entire image trace can be determined by measuring the location of the points with matching exposures. The only other requirements connected with this procedure are that the total exposure time T must be greater than 2 times the threshold exposure time τ and that, indeed, the geometric dimensions and image motions involved are large enough to permit meaningful measurement. Once the image motion s has been determined from the image of one object, the lengths l of all images are given by $l=c+s$, where c, the length of the core portion, can be measured directly from the photographic negative.

Another relationship derivable immediately from figure 5 is that existing between the spatial exposure gradient $g(x)=dE(x)/dx$ at the point x within the two edge traces of an image. It is $g(x)=-g(x+l)$, which again is valid for $x_0 \leq x \leq x_0+s$. However, the utility of this equation for the experimental determination of the dimension l is limited because gradients often change little over considerable distances within an edge trace and also because, even if it does vary, the same gradient recurs in different parts of the same edge trace.

Finally it is also $g(x)=I(t)/v$. In some cases, where both the image velocity and the H and D graphs of the film are given, this equation might be useful in determining the radiance versus time dependency of extended light sources in the measurement of shutter characteristics or the like.

MOTION BLUR ASYMMETRY

An interesting and seldom recognized image motion phenomenon is the possibility of asymmetric motion blur, i.e., the possibility that the motion blur in the forward and aft edges of the same image can assume different amounts. Because motion blur asymmetry affects not only the direct exploitation of unprocessed motion-blurred photographs and because it can also introduce a directional dependency into spatial filters used for motion blur removal, a more detailed consideration of this effect is appropriate.

Motion blur asymmetry is quite common, for example, when the object adjoins backgrounds of differing radiance. It is quite explicit also in the experiment underlying figure 4, where the white sector is in fact an object bordering on such backgrounds. Accordingly the amount of motion blur is greater in those parts of the edge trace that are superimposed on the brighter background.

Asymmetric motion blur, however, can also result irrespective of the photometric properties of the background, when the image illuminance changes during the exposure in a manner asymmetric in relation to the midpoint of the exposure time T. This is quite frequently the case, for instance, under the influence of the opening and closing lens shutter, or because the flash bulb intensity or the object radiance change during the exposure of the film. In figure 5, for which the conditions for a defective shutter were adopted intentionally, the amount b_1 of recorded motion blur turned out to be considerably smaller than the corresponding amount of motion blur b_2 in the aft edge trace. Since in both edge traces the image motion s is equal, the reverse relationship applies to the respective amounts of suppressed image motion $s_1 (\tau)$ and $s_2 (\tau)$.

In an experiment designed to demonstrate asymmetric motion blur, the image of a white rectangle on a black background was projected on a film moving uniformly at a known speed and exposed by means of a flash bulb. The results of the experiment are shown in figure 6. The oscilloscope trace of the heavily unsymmetric time versus intensity function of the flash bulb is in the upper part of the figure, the negative resulting from the exposure is in the middle, and its densitometric record is in the lower part. The direction of increasing time is indicated, as well as the extent of the core portion of the image. The difference of the image blurs in the two edge traces are quite distinct and, in fact, amount to about 45 percent of the smaller blur.

Reciprocity Law Failure

An important factor influencing the density distribution and the analytical properties within an image trace is the reciprocity law failure, short RLF, of the film. The RLF characterizes the response of a film to a given amount of exposure $E = I \times t$ as a function of the time within which it is delivered to the film. This effect is illustrated in figure 7 where the H and D curves of a commercial film have been plotted for a variety of exposure times between 100 and 1/4000 sec.

In the context of this study, it is pertinent to note here that the individual curves in the figure are the result of the internationally standardized test procedure according to which the variation of exposure is accomplished by an intensity scale, i.e., by maintaining a constant exposure time T and changing the illuminance on the sample by means of a density wedge.

Within the image trace of a moving edge, however, the exposure time changes from point to point. It is zero at the extreme ends of the trace and increases toward the inside proportionally with the distance from the ends. Only the core portion of the image trace is exposed through the entire exposure period T.

A different characteristic curve of the kind shown in figure 7 applies therefore to each point within the image trace outside the core; when, during the exposure both image velocity and illuminance remain constant, the exposures within the image trace are arranged in the manner of a linear time scale. This case is frequently approximated when modern between-lens shutters and long exposure times are used.

Figure 8 illustrates the effect of the differing exposure arrangements—intensity scale versus time scale—on the same commercial film to which the characteristic curves in figure 7 apply. For figure 8 it has been assumed that

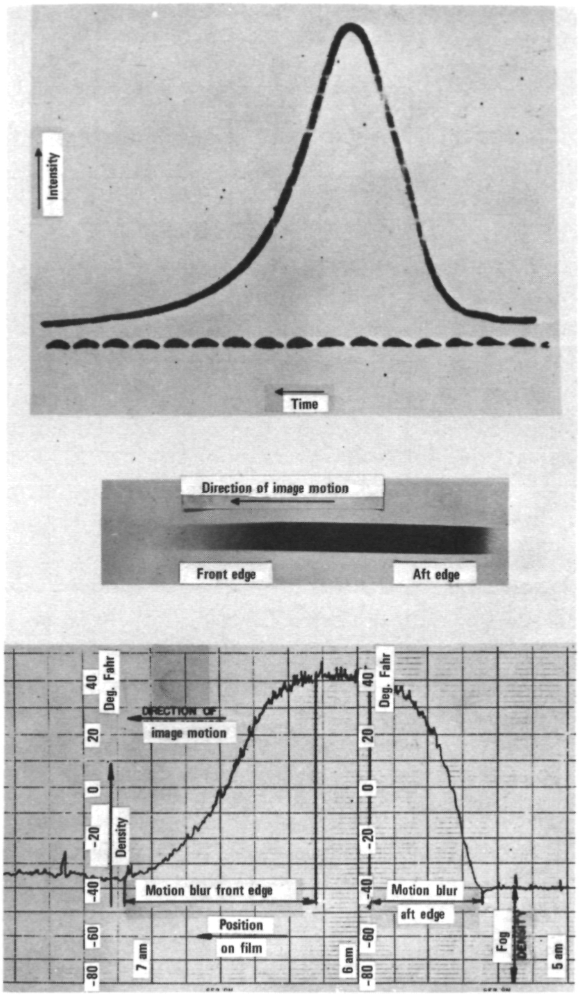

FIGURE 6.—Demonstration of asymmetric motion blur. The object is a white rectangle projected in a fast moving film. Upper part: intensity versus time characteristic of flash bulb used; center: negative obtained; lower part: microdensitometer trace.

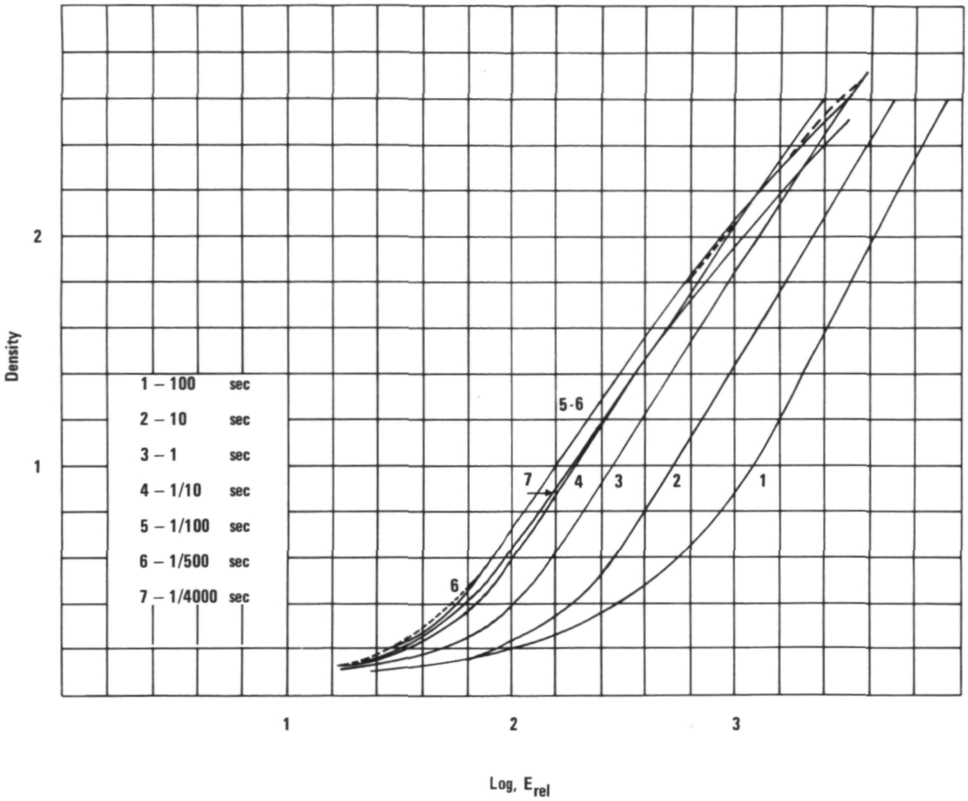

FIGURE 7.—Characteristic curves of a commercial film for different exposure times, illustrating reciprocity law failure.

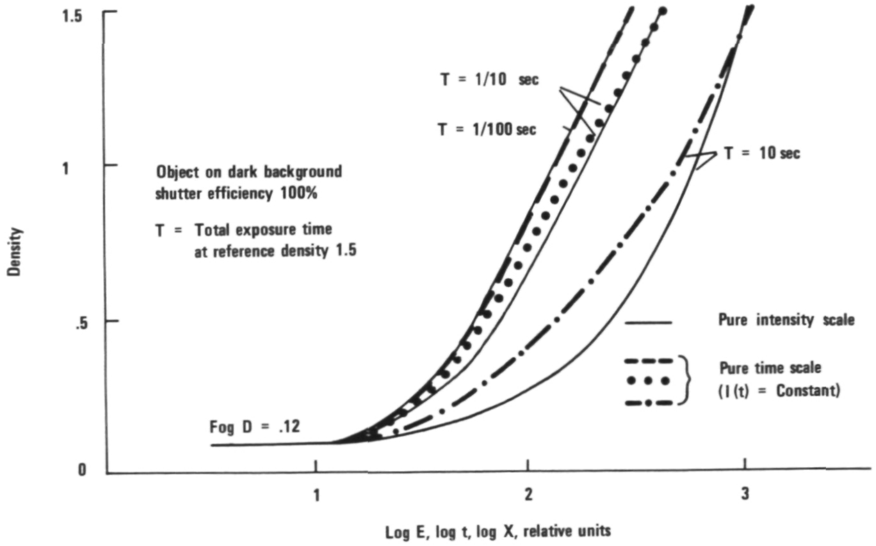

FIGURE 8.—Characteristic curves for exposure times 10, 1/10, and 1/100 sec for the film in figure 7, showing densities obtained under conditions of pure time scale and pure intensity scale if maximum density is 1.5.

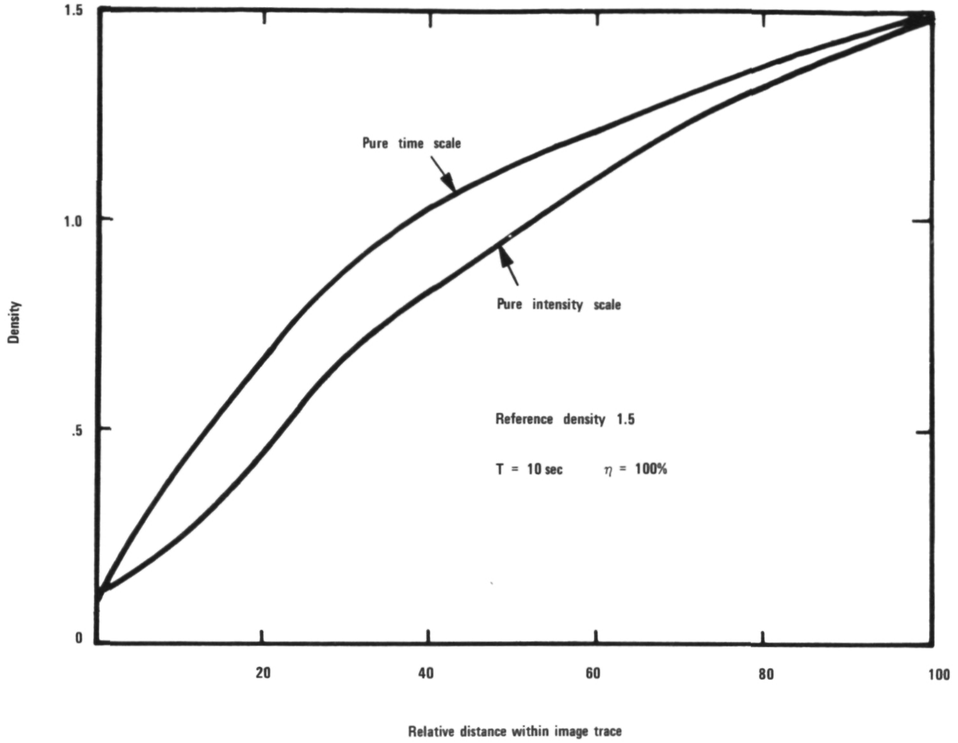

FIGURE 9.—Density distribution within the image trace of a moving edge for pure intensity scale and pure time scale exposure, assuming film characteristics shown in figure 8, $T=10$ sec.

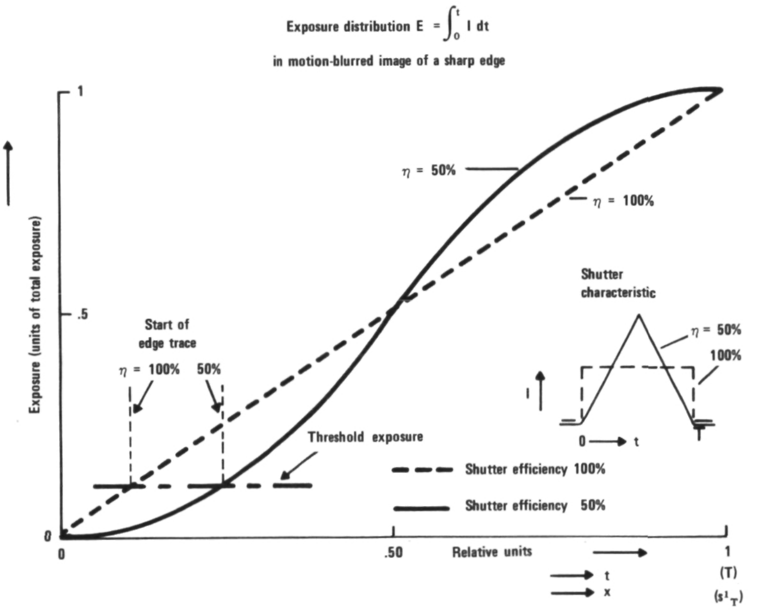

FIGURE 10.—Exposure distribution in the image trace of a moving edge at shutter efficiencies of 50 and 100 percent.

the same limiting reference density 1.5 has to be reached at three exposure times—10, 1/10, and 1/100 sec. The solid lines indicate the lesser densities obtained when an intensity scale—fixed exposure time, varying illuminance—is used, which is the manner of exposure on which commercial film data are based. The broken or dotted graphs show the same relationship when a time scale—fixed illumination, varying exposure time—applies. This latter condition corresponds to that in the image trace of a moving edge.

For the two long exposure times, the increase in densities resulting from the moving edge situation is distinct, while at 1/100 sec the point of maximum film system efficiency has already been passed. In the latter case, the densities resulting from the time scale situation are therefore slightly smaller. At still smaller exposure times, the decrease would here be more pronounced. When the data in figure 8 are used to show the effect of the RLF on the density structure of the image trace of a moving edge, then figure 9 results. Here, density distributions are plotted considering the two cases of the pure time and intensity scales, respectively, for an exposure time of 10 sec.

The significance of the variations of densities distribution or, in general, of the reciprocity law failure reaches into several aspects of image processing and image evaluation. Obviously it is not permissible *per se* to refer to characteristic curves obtained in the standardized intensity scale of exposures when image illuminance versus time functions are to be photometrically derived from edge trace densities, when motion blurs are simulated for filtering studies, or when moving images are employed to generate pregiven density distributions by way of film motion control or by programed shutter speed modulation.* Also, in the determination of image dimensions from motion-blurred photographs, the amount of unrecorded image motion $s(\tau)$ may turn out either to be too small or too great if, in the process, time-scale exposures were confused with the intensity scale exposures customarily quoted in commercial data sheets.

Some relief, or even more confusion, may lie in the fact that usually neither a pure time scale nor a pure intensity scale prevails in the image traces, because the illuminance changes during the exposure time as the camera shutter opens and closes, the flash bulb burns off, etc. In this most common case, a "mixed" scale results. The following graphs illustrate some effects that can be expected when the camera shutter is considered a part of the system.

Figure 10 shows the exposure versus time characteristics of two idealized shutters having efficiencies of 100 and 50 percent. The figure also indicates the displacement of the start of the image trace under the influence of the motion shutter efficiency. In the case shown, the blur is greater, and the suppressed part of the image motion is smaller, when the shutter efficiency is high. However, it is interesting to note that at large relative thresholds, or underexposure, this relationship reverses because of the rapid increase in the shutter opening around the midpoint of the exposure time; a high shutter efficiency is then associated with a motion blur *smaller* than that resulting from a low efficiency.

Figure 11 shows the density distribution that can be expected when the two shutters from figure 10 would be used in conjunction with the same film, again under the conditions that the object is bright enough to produce in either case a maximum density of 1.5. The dashed distribution, resulting under the assumption of a pure intensity scale, has been included to indicate the nature of the errors introduced if the RLF is neglected. The area enclosed by the two solid graphs indicates the possible variations in the density distributions which may occur under the assumed conditions, when conventional shutters of sound design and performance are used. Defective or speed-modulated shutters may, of course, cause efficiencies below 0.5 and may deform the distributions further.

OFF-AXIS MOTION BLUR

Even more complexities may be introduced into the image evaluation procedure when the images travel away from the center of the image

---

*See O. Bryngdahl and A. W. Lohmann, "Compensation of Motion Blur by Shutter Modulation," p. 189.

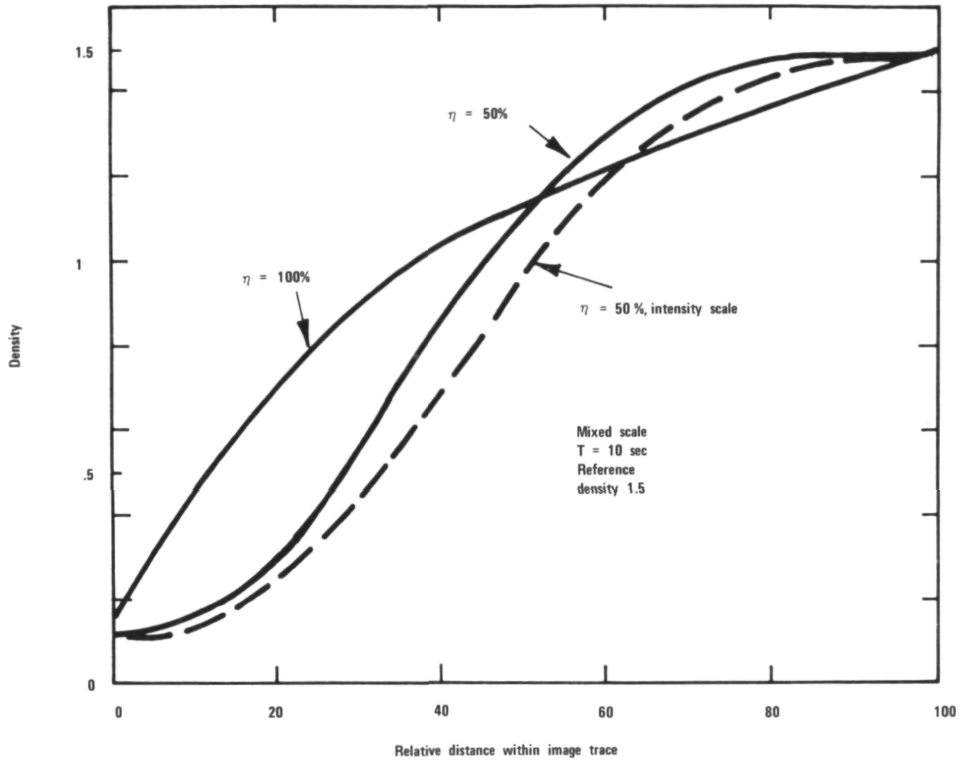

FIGURE 11.—Density distribution in the image trace of a moving edge, mixed scale, using exposure distribution of figure 10.

field. One would first expect such complications from the variation of illumination in the image plane that is caused by the $\cos^4 \phi$ law of illuminance.

That this type of variation cannot always be neglected is shown by figures 12 and 13, which illustrate a real-life case for a wide-angle (90°) reconnaissance lens; figure 12 shows the measured illuminance in the image field, and figure 13 the resulting density distributions to be expected in the image traces of the same rapidly moving object, when its image is centered at four different locations within the field of the lens. The latter illustration assumes the case of the same commercial film as before and a reference density of 1.5 for the center of the field. The general decrease of density can be seen in the figures along with that of the length of the visible image trace that occurs when the objects move toward the edges of the field. It is even more noticeable when the minimum detectable density difference deteriorates under the influence of film noise and densitometer performance. In the case shown, the expected suppression of image motion would range from about 1 percent for the center to well over 20 percent for the corners of the frame.

In the context of off-axis motion blur evaluation, another example may finally be mentioned of a possible, but fortunately infrequent, source of error that was uncovered during a rather thorough test of the between-lens shutter of a reconnaissance camera by means of high-speed photography. The arrangement used permitted photographing the opening and closing of the shutter on a continuous filmstrip, simultaneously as seen from its axis and as seen from two opposite directions about 45° from the axis.

The rather surprising result for a between-lens shutter is illustrated in figure 14 which shows the three sequences of pictures obtained at a rate of about 5000/sec for a nominal exposure time of the tested shutter of 1/50 sec.

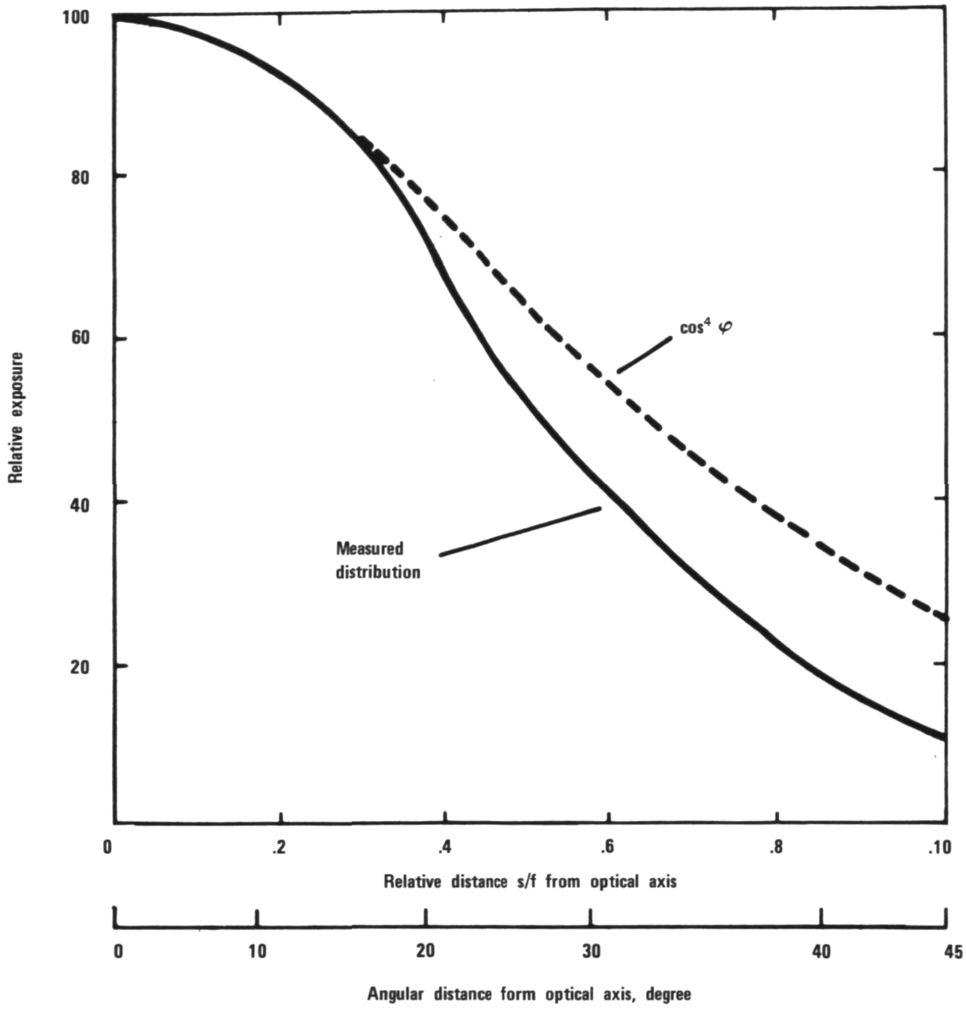

FIGURE 12.—Illuminance distribution in the image plane of a wide-angle reconnaissance lens.

The single pictures are separated from each other only at both ends of the sequences, that is, during the opening and closing of the shutter. In the center portion of each sequence (during the dwell period of the exposure cycle), the pictures merge into each other. The vignetting effect, as well as the perspective foreshortening of the lens image that accounts for one factor cos ϕ in the cos^4 ϕ law, is evident in the variations of the lens images in the three sequences: round in the center and oval in the sideview.

The phenomenon of interest here, however, is that the shutter appears to close at different times when seen from different angles. In the case shown, the mutual deviation of exposure times for the two outward directions amounted to no less than 2×10^{-3} sec or 10 percent of the nominal exposure time. Obviously, therefore, the exposure times can be a function of the viewing direction, and the length of the recorded image trace may even differ locally within the image plane of the camera by virtue of the shutter alone.

The reason for this effect lies in the design of the particular shutter tested. It turned out that the shutter blades were mounted with a spacing of a fraction of 1mm from each other. Therefore, as figure 15 indicates, at certain

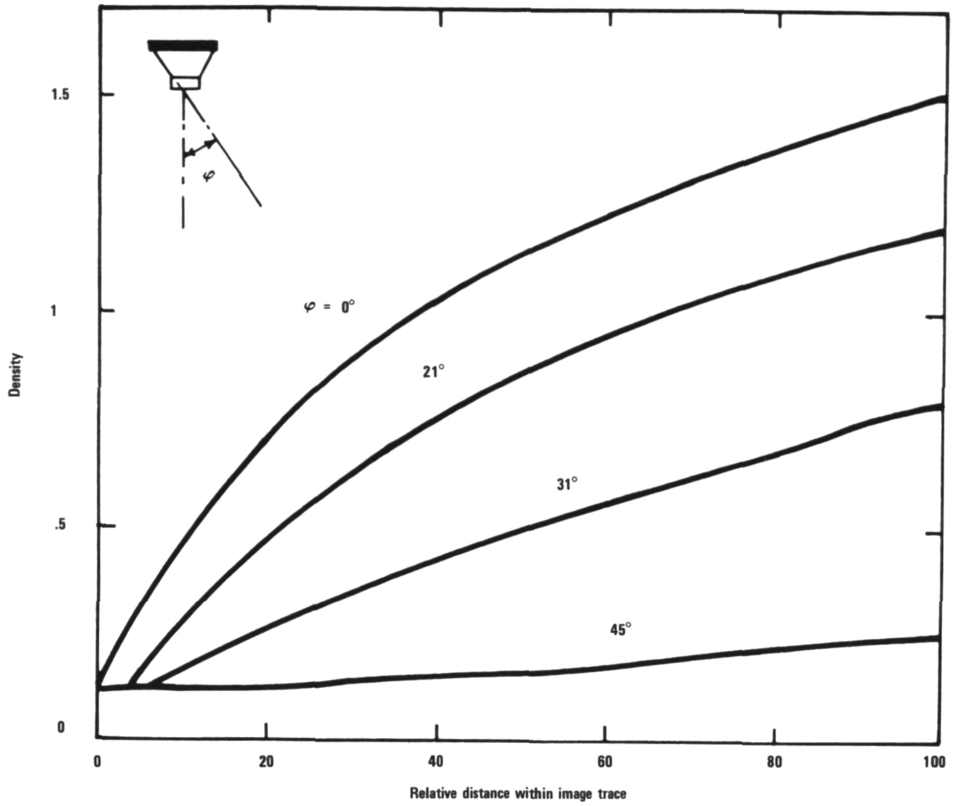

FIGURE 13.—Density distributions in the image trace of a moving edge in four different locations within the image field of the lens in figure 12.

blade situations during the opening-closing cycles the light could reach some parts of the image plane while it was still blocked from reaching others. Although the effect is easily explained, its quantitative variation within the image plane is complex, and no attempt was made to determine its distribution. The difference in exposure time is insignificant sensitometrically. In its interplay with image motion and other error sources, however, it may well influence the outcome of photogrammetric exploitation. Certainly it adds to the tribulations of a photoanalyst who may have placed his confidence in a camera designed for war and field situations and fabricated by a world-renowned manufacturer.

CONCLUSION

Following are the principal conclusions to be drawn from this study:

(1) The motion blur is not necessarily a complete record of the underlying image motion.

(2) Removal of that blur will not necessarily restore the true geometry or photometry of the original image.

(3) The length of the recorded image trace may change with the location of the image, with the luminance of the object, with the photometric conditions in its vicinity, and with the sensitometric properties of the film. All these factors must be taken into account before one image trace or spread function is used as a standard for reconstructing the images of other details, even if these images are located within the same photograph.

(4) The same is true for the relationship between the forward and aft edges of the same image. This may introduce a directional factor into the spatial filters used for image restoration,

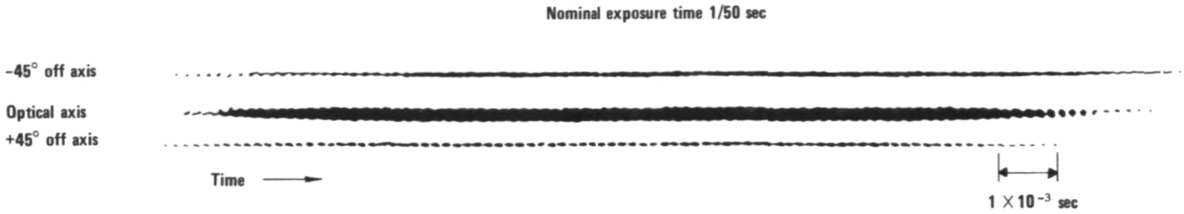

FIGURE 14.—High-speed photographic test of a camera shutter seen from three locations of the image plane. The exposure times vary in different parts of the image field.

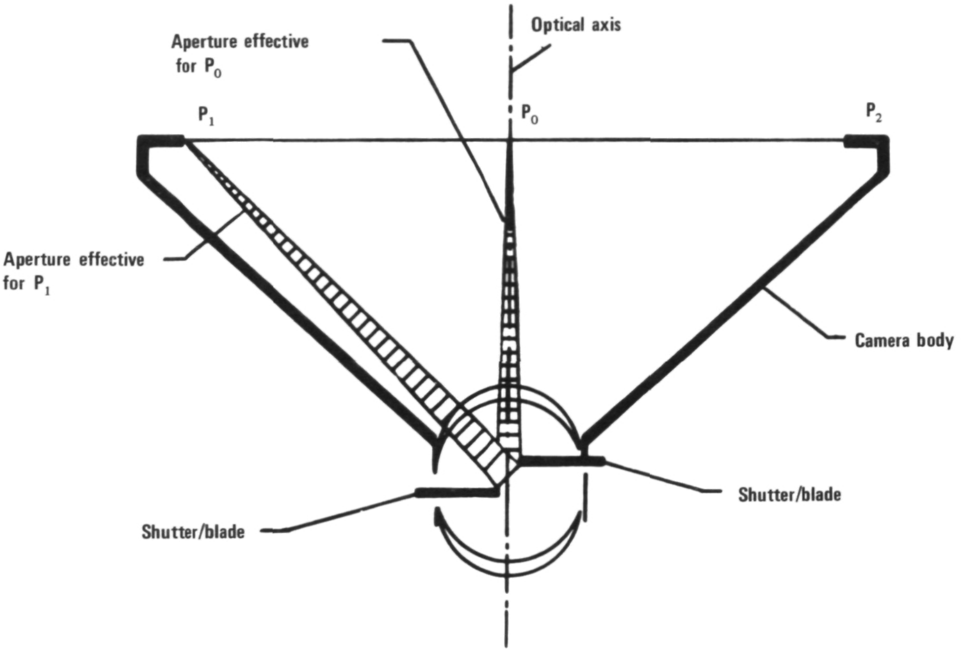

FIGURE 15.—Explanation for phenomenon shown in figure 14, showing effect of spacing between shutter blades.

even when only straight-line image motion is involved.

(5) The photometric structure of the image trace of a moving edge is primarily determined by a time scale or mixed time-intensity scale arrangement of exposures.

(6) The optical and mechanical characteristics of the photographic apparatus play an important part in the distribution of the motion blur in a photograph and the densitometric structure of an image trace.

It should be mentioned finally that overexposure affects motion blurs in a way quite similar to underexposure. This aspect will, however, be the subject of a future study.

REFERENCES

1. NAGEL, M. R.: Remarks on the Definition of "Motion Blur." Bemerkungen zur Definition der Bewegungsunschärfe. Photogr. Korresp., vol. 74, no. 12, 1938, pp. 193–194.
2. NAGEL, M. R.: Experiments on the Motion Blur as a Function of Negative Density. Versuche über die Abhängigkeit der Bewegungsunschärfe von der Negativschwärzung. Zs. f. wiss. Photogr., vol. 38, nos. 9 and 10, 1939, pp. 181–209.

3. Nagel, M. R.: Asymmetric Motion Blur in the Photographic Image of Fast-Moving Objects. Proceedings of the 7th International Congress on High-Speed Photography, 1965. (Reviewed in Journal SMPTE, vol. 75, 1966, p. 371.)
4. Harris, J. L.: Image Evaluation and Restoration. J.O.S.A., vol. 56, 1966, pp. 569–574.
5. Anon: A Study of Lunar Orbiter Photographic Evaluation. Cornell Aeronautical Laboratory, Report No. VS–2182—D–2, May 20, 1966.
6. Brown, B. R.; and Lohmann, A. W.: Complex Spatial Filtering with Binary Masks. Appl. Optics, vol. 5, 1966, pp. 967–969.
7. Mueller, P. F.; and Reynolds, J. G. O.: Image Restoration by Removal of Random-Media Degradations. J.O.S.A., vol. 57, 1967, pp. 1338–1344.
8. Kinzly, R. E.; Haas, R. C.; and Roetling, P. S.: Designing Filters for Image Processing to Recover Detail. Presented to SPIE Seminar on Image Information Recovery (Philadelphia), Oct. 1968.
9. Horner, J. L.; and Rycus, M. J.: Restoration of Linearly Smeared Transparencies. Presented to SPIE Seminar on Image Information Recovery (Philadelphia), Oct. 1968.
10. Considine, P. S.: Image Processing with In-Line Optical Systems. Presented to SPIE Seminar on Image Information Recovery (Philadelphia), Oct. 1968.

Page intentionally left blank

Page intentionally left blank

EFFECT OF IMAGE RESOLUTION AND CONTRAST ON TARGET DETECTION AND IDENTIFICATION

SHELDON MACLEOD AND JOHN J. MAIER
Rome Air Development Center
Griffiss Air Force Base, N.Y.

The amount of useful intelligence extracted from aerial photography by image interpreters is dependent upon many factors. One of these is obviously the quality of the imagery he is viewing. A number of behavioral studies have been performed to evaluate this type of relationship; i.e., the dependency of measures of interpreter performance upon image contrast, sharpness, resolution or granularity. Investigations of this type have been reported by Jennings (ref. 1), Roetling (ref. 2), Brainard (ref. 3), and Scott (ref. 4).

The objective of this study was to explore the joint effects of two of these indices, resolution and contrast, upon four types of interpreter performance measures.

The selection of resolution as an experimental factor alines this study with the theme of the present conference, since along with aberration and focus of the camera's lens system and the type of film selected, uncontrolled image motion is a principal operational determinant of photographic resolution.

EXPERIMENTAL PROCEDURE

Sixteen vertical panchromatic aerial scenes of different ICBM missile sites provided the content of the test images. These were displayed on 70mm positive frame transparencies at a scale of about 1:5000. Thirteen of these sites were Minutemen, the rest were Titans. An enlarged example of a site is shown in figure 1.

Each of these images was subjected to experimental modification* as follows:

A positive master was processed such that the product of its gamma and the gamma of the camera original was unity. This master was then printed in a modified contact printer, the spread function of the printer illumination being controlled by a rotating mask technique.

Image resolution was varied by introducing spacers between the master and print material. The gamma of the print was kept at unity. Image resolution was determined by an edge gradient analysis from which normalized modulation transfer functions (MTF) were derived. Specifically, resolution was defined by the MTF as the limiting spatial frequency where exposure modulation approached the eye modulation threshold (at 0.022 modulation).

Image contrast was varied by pre-exposing the print before the test transparency was produced. Constant average density was maintained and the amount of contrast reduction defined in terms of conventional sensitometry as the exposure modulation (EM) factor

$$\mathrm{EM}=\frac{E_{\max}-\mathrm{E}_{\min}}{E_{\max}+\mathrm{E}_{\min}}$$

Based on the above specifications, an experimental matrix (table I) of 70mm positive

---

*This modification was carried out by the Perkin-Elmer Corporation under contract to RADC (AF30 (602)-4007).

FIGURE 1.—Typical missile site used in interpretation test.

test transparencies at 4×4 resolution-versus-contrast (RC) levels was produced.

The absolute values inserted in this matrix were selected on the basis of a pilot test to provide suitable anchor points for bridging a wide range of performance measures, i.e., images representing corner cells *A* and *P* in table 1 were preselected to represent, respectively, about 25 and 75 percent correct detections of those missile site components detectable on a high resolution blowup, while the images in corner cells *M* and *D* were designed to provide about 50 percent correct detections of the components.

These expected performance levels were based on preliminary judgments of five experienced interpreters. They were instructed to avoid reporting as detectable any object belonging in the site but not actually imaged. Each of the missile sites was processed according to the 16 RC quality levels depicted in table I yielding a total of 256 experimental test images.

Sixteen experienced military interpreters selected as test subjects. Since a number of these had little experience with missile site analysis, all were given a four-hour intensive training program on Titan and Minuteman components to decrease subject variability and help peak their proficiency for the experimental task. This training consisted of a special teaching machine program* in addition to a detailed review of

---

*Prepared and presented by Raytheon/Autometric Corp., Alexandria, Virginia.

TABLE I.—*Experimental Matrix of Resolutions—Contrast Values*

Contrast	Resolution (cycles per mm)			
Exposure modulation factor	32	16	12	6
.80	A	B	C	D
.59	E	F	G	H
.37	I	J	K	L
.29	M	N	O	P

site diagrams and images provided by the test monitor.

Following this training each interpreter was tested on 16 of the 256 images. In every case he sampled one of each missile site at one of each RC level. No subject, however, viewed the same site or RC level twice. This type of design balanced out subject differences both across scenes and RC conditions.

Table II summarizes the experimental assignment of images to each interpreter. The targets are denoted by number, the RC values by capital letter (each letter represents the same RC value indicated in table I), and the subject by small letters.

Each subject's assigned images were presented to him in a random temporal order. The subject viewed the test transparencies on a Richards light table in a sound-proof booth. He was also given standard measurement and magnification aids (Zoom 90). His task required that he carefully search each photograph and report all visible components against a numbered list of objects. This list represented all militarily significant components discernible in all the images by two experienced interpreters (viewing a high resolution blowup of each image and using an appropriate missile key). Three types of components were included: (1) Permanent components such as security fences and power poles; (2) temporary components such as construction materials and generator units; and (3) vehicles such as trucks and tractors. The actual number of these components contained in any one site varied between nine and 50.

If the interpreter decided that an anomaly on the film was one of the listed components but was too degraded to be assigned its correct label, he merely recorded it, along with its photographic coordinates (determined by a grid over

TABLE II.—*Experimental Assignment of Test Imagery*

RC conditions	Targets															
	1	2	3	4	5	6	7	8	9	10	11	12	13	14	15	16
A	a	b	c	d	e	f	g	h	i	j	k	l	m	n	o	p
B	p	a	b	c	d	e	f	g	h	i	j	k	l	m	n	o
C	o	p	a	b	c	d	e	f	g	h	i	j	k	l	m	n
D	n	o	p	a	b	c	d	e	f	g	h	i	j	k	l	m
E	m	n	o	p	a	b	c	d	e	f	g	h	i	j	k	l
F	l	m	n	o	p	a	b	c	d	e	f	g	h	i	j	k
G	k	l	m	n	o	p	a	b	c	d	e	f	g	h	i	j
H	j	k	l	m	n	o	p	a	b	c	d	e	f	g	h	i
I	i	j	k	l	m	n	o	p	a	b	c	d	e	f	g	h
J	h	i	j	k	l	m	n	o	p	a	b	c	d	e	f	g
K	g	h	i	j	k	l	m	n	o	p	a	b	c	d	e	f
L	f	g	h	i	j	k	l	m	n	o	p	a	b	c	d	e
M	e	f	g	h	i	j	k	l	m	n	o	p	a	b	c	d
N	d	e	f	g	h	i	j	k	l	m	n	o	p	a	b	c
O	c	d	e	f	g	h	i	j	k	l	m	n	o	p	a	b
P	b	c	d	e	f	g	h	i	j	k	l	m	n	o	p	a

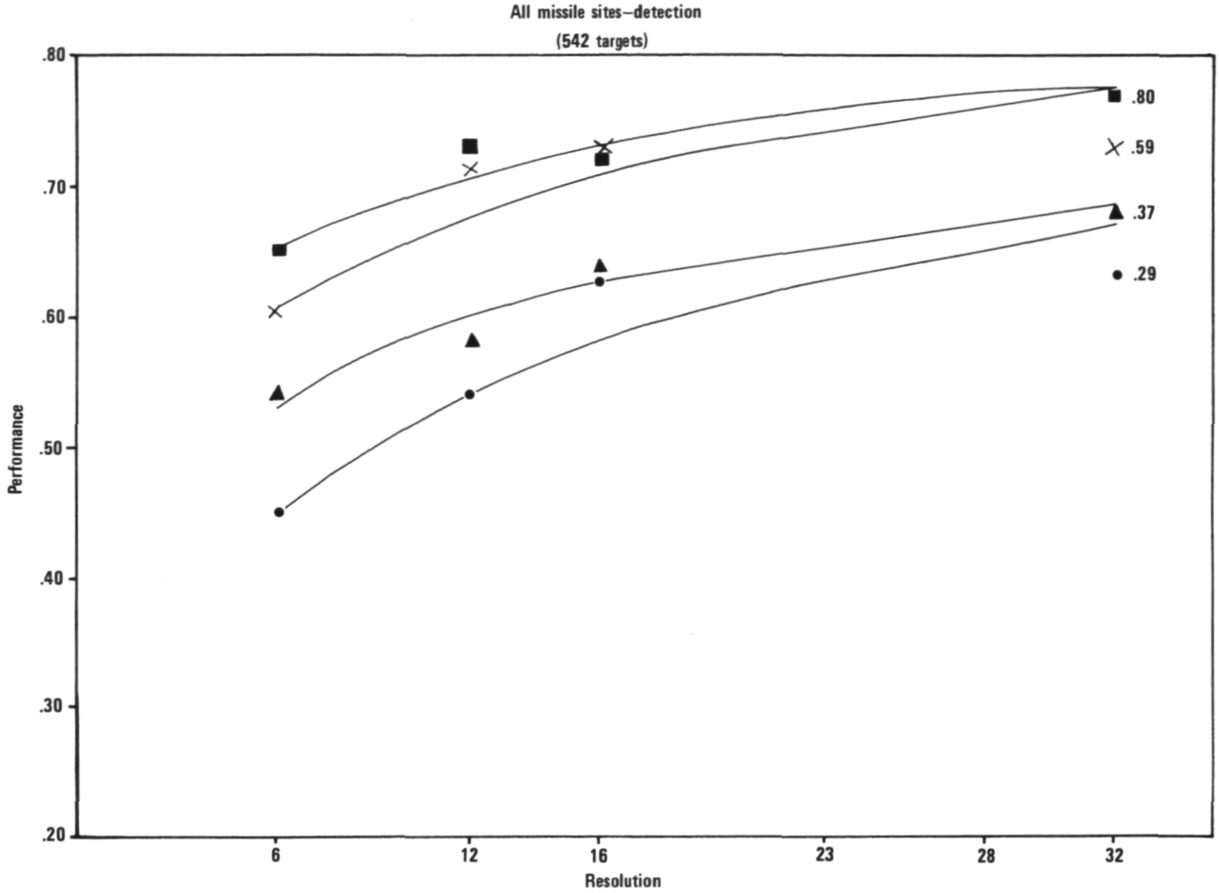

FIGURE 2.—Curvilinear relationships between detection c ompleteness and resolution plotted at each contrast level.

lay) as a detection. However, if he could also label it, he included its identifying number. Subjects were instructed to proceed from image to image in the predesignated order while attempting to record their detections and identifications as completely and accurately as possible.

Four kinds of performance measures were derived for each subject on each image.

(1) Detection completeness: This was the percentage of correctly located anomalies with respect to the total number of components found in the list which pertained to the image in question.

(2) Identification completeness: This was a similar percentage of correctly located and labeled items.

(3) Detection accuracy: This was the percentage of correct detections with respect to the total number of attempted detections and identifications.

(4) Identification accuracy: This was the percentage of correctly labeled items with respect to the total number of attempted detections and identifications.

Notice that the completeness measures reflect errors of omission while the accuracy measures reveal errors of commission (i.e., either false alarms or misidentifications).

EXPERIMENTAL FINDINGS

Figure 2 shows four curvilinear relationships between detection completeness and resolution plotted at each contrast level. The curves are logarithmic functions and have been fitted by the method of least squares to the 16 RC data points. Each RC datum is a cumulative

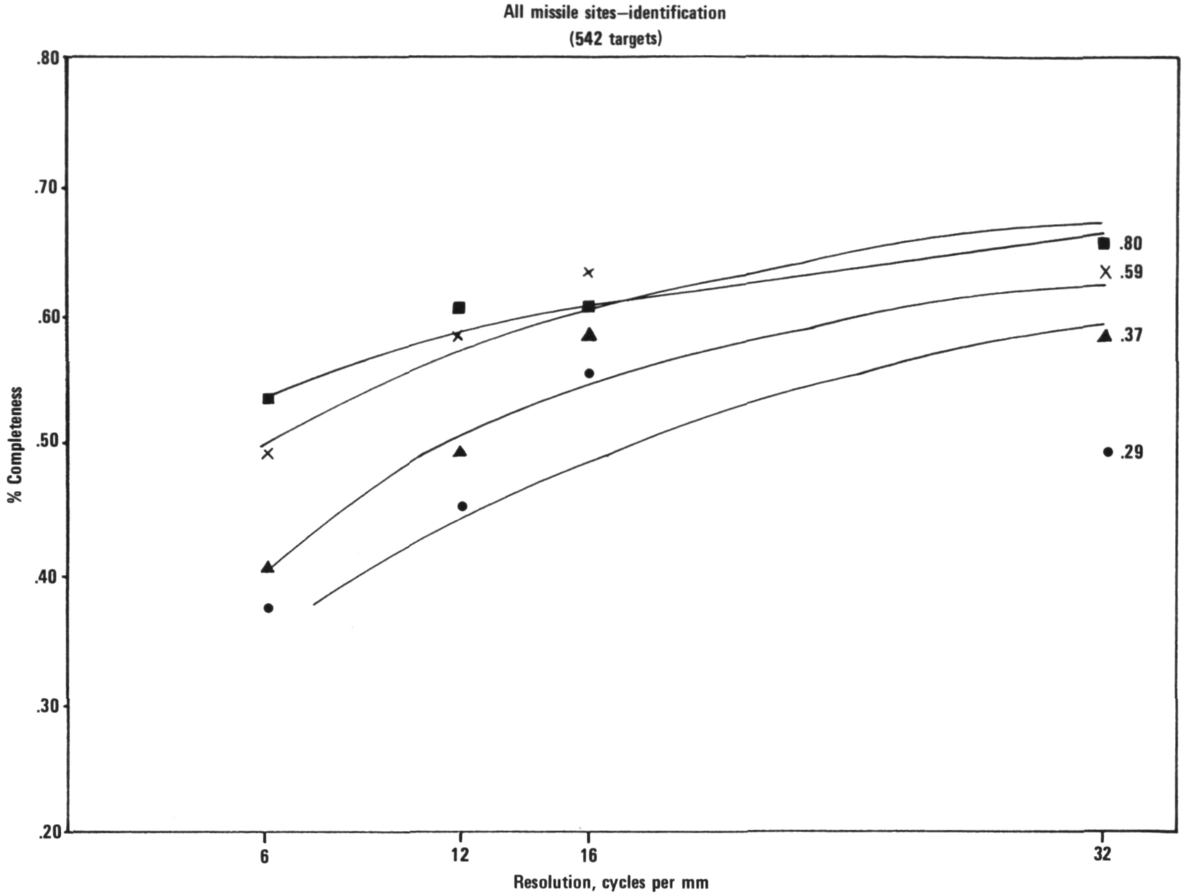

FIGURE 3.—Shows similar relationships when identification completeness is plotted against resolution.

percentage incorporating responses of all subjects on all missile sites.

The data of figure 2 exhibit the following trends: (1) Performance for each curve is described by an increasing logarithmic function of resolution; (2) the effect of resolution is reduced (the curves have less curvature) at the two higher levels of contrast; and (3) the uppermost curve appears to be approaching an asymptote of about 80 percent under the conditions of this study. This represents a limit beyond which higher quality imagery would not improve performance.

A replot of figure 2 with contrast along the base line and the four resolution values as parameters (though not shown here) yields parallel trends: (1) Logarithmic curves remain reasonable fits for the data; (2) the effect of contrast diminishes at the two upper resolution levels; and (3) the upper resolution curve approaches a limit of about 80 percent completeness.

The above type of parallelism suggests that there is little interaction between resolution and contrast, although the effect of either variable upon performance appears significant. This observation is borne out by a two-way analysis of variance which shows the main effects of resolution and contrast to be highly significant (with *F* ratios beyond the 0.01 level) while the effects of CR interaction are not.

Figure 3 shows similar relationships when identification completeness is plotted against resolution at the four contrast levels. Note that the data are again fitted by logarithmic curves

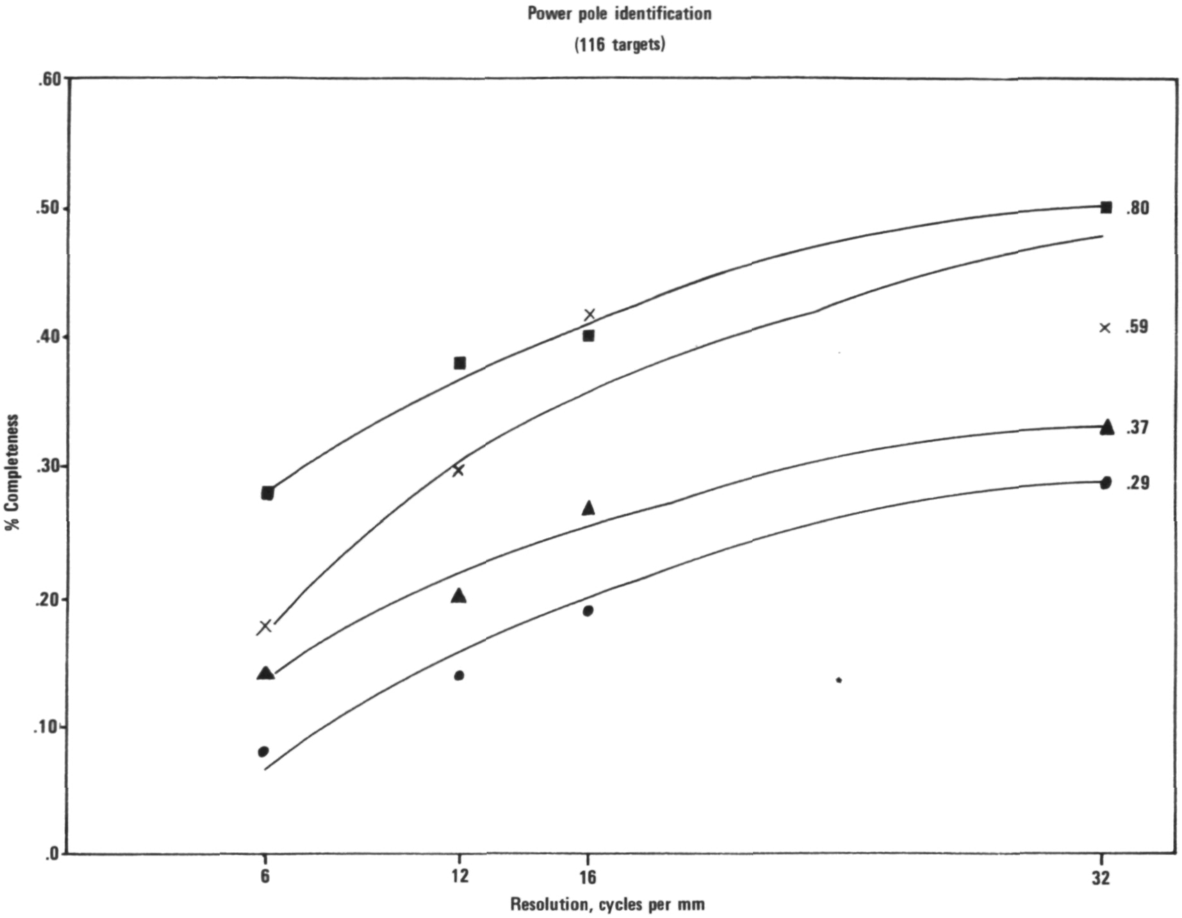

FIGURE 4.—Identification completeness of 116 power poles represented in various images.

which at the two higher contrast levels are approaching an upper limit of about 70 percent completeness. This 10 percent difference, as compared with the curves of figure 2, is relatively constant for all four functions and is due to the more exacting performance measure of identification. Otherwise, all the trends noted for figure 2 also apply in this case. The *F* ratios associated with effects of contrast and resolution are highly significant and their interaction is again insignificant.

Performance levels for the two accuracy measures (detection and identification) showed no definable relationship to either resolution or contrast. Hence, the percentage of correct to the total attempted responses is independent of both resolution and contrast.

A somewhat different type of analysis is illustrated in figure 4. The function here pertains to the identification-completeness of 116 power poles represented in various images. Again, logarithmic fits are a reasonable description of the curvilinear relationships between performance and resolution. These curves can be used to predict the identifiability of this type of component at the various RC levels.

The ground diameter of this target (viewed vertically) is about 1.5 feet making it one of the smaller objects contained in the imagery. Larger objects such as automobiles (with a long dimension of about 15 feet) are identified at an average completeness level of about 60 percent at all RC levels. Hence, under the conditions of this study, such a target is sufficiently large to be unaffected by image quality. The steepness and separation of the curves for the power poles (fig. 4) can be explained by the importance of shadow-to-image identification. At lower RC levels where the shadow is lost, performance drops to about 10 percent.

In conclusion we believe this data will contribute to a more precise understanding of how motion degradation can affect the availability of photographic reconnaissance information. One problem confronting this type of research concerns agreed-upon operational definitions of image quality so that all investigators refer to the same type of measurement and physical indices in discussing data of this type.

REFERENCES

1. MEEKER, F. B.; and PROWER, G. A.: Ground Resolution Study. RADC–TDR–63–224, 1963.
2. ROETLING, P. G.; HAMMELL, H. B.; and HOLLADAY, T. M.: Quality Categorization of Aerial Reconnaissance Photography. RADC–TDR–63–279, 1963.
3. BRAINARD, R. W.; SADACCA, R. M.; LOPEZ, L. J.; AND ORMSTEIN, T. N.: Development and Evaluation of a Catalogue Technique for Measuring Image Quality. APRO Technical Research Report 1150, 1966.
4. SCOTT, F.: The Search for a Summary Measure of Image Quality—A Progress Report, Photographic Science and Engineering. Vol. 12, no. 3, May–June 1968, pp. 154–164.

Page intentionally left blank

Page intentionally left blank

Session II

IMAGE MOTION SENSING AND COMPENSATION

F. Dow Smith, *Chairman*
Itek Corporation
Lexington, Massachusetts

351-160 O—69——4

Page intentionally left blank

Page intentionally left blank

PREDICTION AND COMPENSATION OF LINEAR IMAGE MOTIONS IN AERIAL CAMERAS

EARLE B. BROWN
The Perkin-Elmer Corporation
Norwalk, Conn.

Image motions in aerial cameras of any type arise from two causes: apparent ground motion and camera rotation. General equations are given for each variety of motion for a camera pointed in any direction, including the differential motions resulting from errors in pointing.

The five image motion patterns which can appear in the focal plane are named and described and the conditions for their occurrence are identified.

Tables of the coefficients for ground motion in the flight direction for the sixteen possible pointing sequences around three orthogonal vehicle axes have been given in a published paper (ref. 1).

GEOMETRY AND NOMENCLATURE

Figure 1 shows the geometry and nomenclature adopted. Two coordinate systems are involved: the camera coordinate system, XYZ, in which the coordinates of a point in the focal plane are (x_f,y_f,z_f), where $z_f=f$ (the focal length), and the ground coordinate system $X'Y'Z'$. Both have their origin at the entrance pupil of the camera.

The coordinates of a ground point in the ground coordinate system are (x_g',y_g',z_g'), where $z_g'=-H$ (the altitude), and its coordinates in the camera system are x_g,y_g,z_g.

A point in the focal plane (x_f,y_f,z_f) is related to its conjugate ground point (x_g,y_g,z_g) by a projective transformation. The ground system coordinates of a ground point (x_g',y_g',z_g') are related to its camera system coordinates (x_g,y_g,z_g) by a successive rotation of the ground coordinate system through a combination of the angles θ (Z-axis rotation, or yaw), β (Y-axis rotation, or roll), and ϕ (X-axis rotation, or pitch).

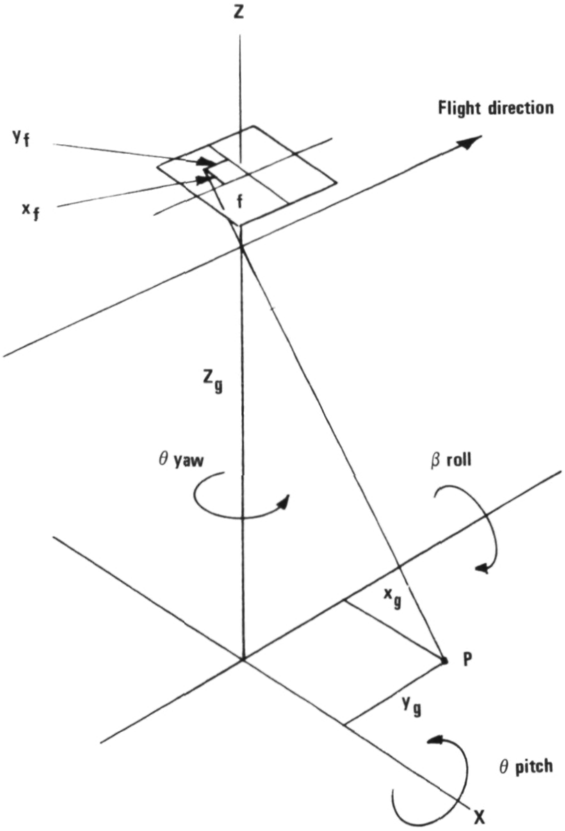

FIGURE 1.—Geometrical conventions.

The positive directions of the coordinate axes and of the rotations of the ground coordinate system, are shown in figure 1. It is important to note that the signs of the rotational angles should be reversed if the rotation is assigned to the camera. For example, a clockwise rotation of the camera about the Y-axis would be called negative.

THE IMAGE MOTION EQUATIONS

The equations for image motion in the focal plane, expressed in terms of linear velocity as a function of focal plane position (the velocity in the X-[transverse] and Y-[longitudinal] directions being given separately), are as follows:

Motion due to apparent ground motion—

$$s_x=\frac{V}{H}\left[af+bx_f+cy_f+d\frac{x_f^2}{f}+e\frac{x_fy_f}{f}\right] \tag{1}$$

$$s_y=\frac{V}{H}\left[gf+jx_f+ky_f+e\frac{y_f^2}{f}+d\frac{x_fy_f}{f}\right] \tag{2}$$

where V is the apparent ground velocity and H is the altitude.

Motion due to rotational velocity in the angle α—

$$s_x=\left[Af+Cy_f+D\frac{x_f^2}{f}+E\frac{x_fy_f}{f}\right]\dot{\alpha} \tag{3}$$

$$s_y=\left[Gf+jx_f+E\frac{y_f^2}{f}+D\frac{x_fy_f}{f}\right]\dot{\alpha} \tag{4}$$

Note on units.—The dimensions of s_x and s_y are length per unit time and f, x_f and y_f have the dimension of length, and are in millimeters, inches or feet, as desired. The velocities then have the equivalent units. The apparent ground velocity, V, has the dimensions of length per unit time, and is expressed usually in feet per second. H should have the same length unit as V; hence V/H is in radians per unit time (usually seconds). The image motion velocities will have the same time unit as V. Rotational velocity, $\dot{\alpha}$ is in radians per unit of time (use the same time unit as for V). All of the coefficients are trigonometric functions of the pointing angles, so that their units are not of concern.

Image motions resulting from errors in pointing are readily obtained by differentiation of equations (1) and (2) to obtain

$$\delta s_x=\frac{V}{H}\left[a'f+b'x_f+c'y_f+d'\frac{x_f^2}{f}+e'\frac{x_fy_f}{f}\right]\delta\alpha \tag{1a}$$

$$\delta s_y=\frac{V}{H}\left[g'f+j'x_f+k'y_f+e'\frac{y_f^2}{f}+d'\frac{x_fy_f}{f}\right]\delta\alpha \tag{2a}$$

where $\delta\alpha$ is the pointing error about a given coordinate axis ($\delta\phi$, $\delta\beta$ or $\delta\theta$), and $a'=\partial a/\partial\alpha$, $b'=\partial b/\partial\alpha$, etc. Since the derivatives of the coefficients are readily written for a particular case, it has not been considered useful to tabulate them separately, there being 66 sets of them for the 16 cases, two conditions and three axes.

Tables of the coefficients for image motion for ground motion in the negative flight direction for the sixteen possible pointing sequences around three orthogonal vehicle axes have been published (ref. 1).

IMAGE MOTION PATTERNS

Equations (1) through (4) describe five distinct image motion patterns in each direction. These patterns are illustrated in figure 2, and have been given the descriptive names shown in table I.

The reason for the choices of names is evident from the illustrations. It is interesting to note that the coefficients for image drift and trapezoidal motion are the same for both directions but are interchanged.

CONDITIONS FOR THE OCCURRENCE OF IMAGE MOTION PATTERNS

For any camera pointed through finite angles about three axes, all patterns of image motion appear as a result of ground motion. The patterns which appear as a result of camera rotations depend on the pointing sequence adopted, and the patterns which appear for various two-axis cases* are shown in figure 3. Change in magnification does not occur for rotational motion for any case.

---

*For apparent ground motion in the negative flight direction.

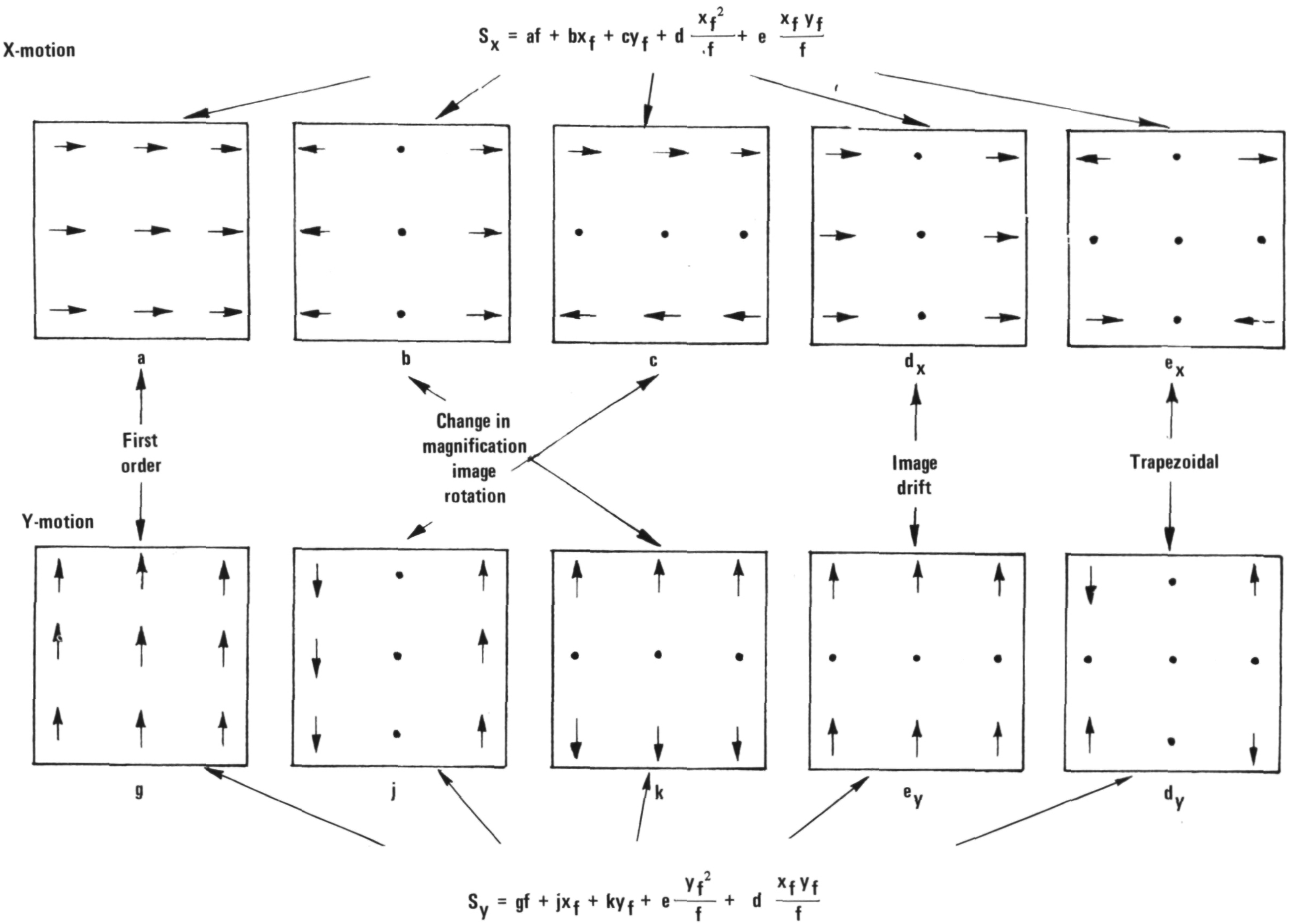

FIGURE 2.—Image motion patterns.

TABLE I.—*Names of Patterns Shown in Figure 2*

Variable	Coefficients	Name
X-Direction motions (s_x)		
f	a, A	First order motion
x_f	b	Change in magnification
y_f	c, C	Image rotation
x_f^2/f	d, D	Image drift
$x_f y_f/f$	e, E	Trapezoidal motion
Y-Direction motions (s_y)		
f	g, G	First order motion
x_f	j, J	Image rotation
y_f	k	Change in magnification
y_f^2/f	e, E	Image drift
$x_f y_f/f$	d, D	Trapezoidal motion

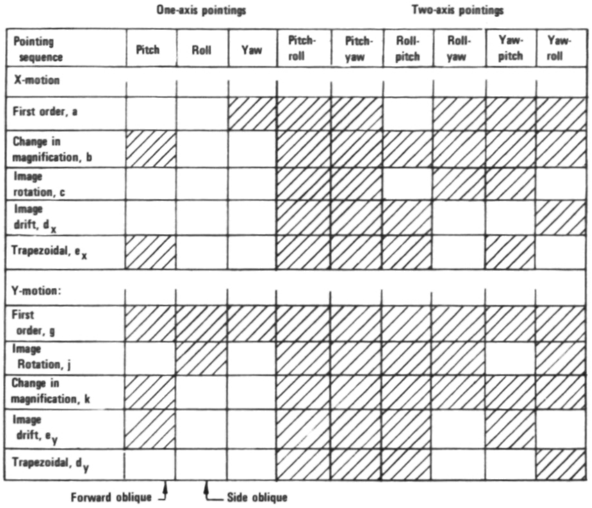

	One-axis pointings			Two-axis pointings					
Pointing sequence	Pitch	Roll	Yaw	Pitch-roll	Pitch-yaw	Roll-pitch	Roll-yaw	Yaw-pitch	Yaw-roll
X-motion									
First order, a			▨	▨	▨		▨	▨	▨
Change in magnification, b	▨			▨	▨	▨	▨	▨	▨
Image rotation, c				▨	▨		▨	▨	
Image drift, d_x				▨	▨	▨			▨
Trapezoidal, e_x	▨			▨	▨	▨		▨	
Y-motion:									
First order, g	▨	▨	▨	▨	▨	▨	▨	▨	▨
Image Rotation, j		▨		▨	▨	▨	▨		▨
Change in magnification, k	▨			▨	▨	▨	▨	▨	▨
Image drift, e_y	▨			▨	▨	▨		▨	
Trapezoidal, d_y				▨	▨	▨			▨

FIGURE 3.—Conditions for appearance of image motion patterns.

COMPENSATION

Specific types of aerial cameras are identifiable in terms of the pointing angles involved and the range of values of the focal plane coordinates that apply. In framing cameras, the format has finite extension in both x and y directions; in strip and panoramic cameras, one of the focal plane coordinates is substantially zero, since the format is a slit. In vertical cameras, all of the pointing angles are nominally zero; for side or forward oblique cameras, either roll or pitch has a finite value; for the transverse panoramic camera, roll is a time variable. Zero values for some of the pointing angles and/or focal plane coordinates result in some of the image motion patterns vanishing. The five fundamental types of aerial cameras and the motion patterns which appear in them are shown in table II.

In general, any camera which has pointing components about all three of the coordinate axes exhibits image motions of all five types. There are a few special cases where *some* of the five patterns are absent in one of the focal plane directions.

Except for unusual cases of extreme pointing angles, the first-order motion (first term in the equation) dominates, and for ordinary situations its source is reflected vehicle forward motion. This motion, being uniform over the format, is readily compensated by moving the film in the focal plane at an appropriate constant rate during the exposure. In the case of scanning cameras, such as panoramics, the image motion due to the scan dominates.

For other terms in the equations, the motions are functions of focal plane position, and when their magnitude is sufficient to require compensation, relatively complex techniques have to be employed. Complete compensation can be achieved by film motion in the focal plane in two orthogonal directions, synchronized with a spot scan of the format. In most situations, this is too complex and requires too long a framing time to be practicable. Usually, however, some of the terms are sufficiently small that they can be ignored, and then simplified

TABLE II.—*The Five Fundamental Types of Aerial Cameras and Their Motion Patterns*

Camera type	Equation terms with finite values	
	Intrack	Crosstrack
Vertical frame	1	----------
Side oblique frame	1, 3	----------
Forward oblique frame	1, 2, 4	3, 5
Vertical strip	1	----------
Vertical panoramic	1	----------

approaches are feasible—for example, a slit scan of the focal plane, together with rotational and linear film motion.

MATHEMATICAL PROCEDURE

Image Motion Due to Ground Motion

Referring to figure 1, which shows the two coordinate systems (camera and ground, with common origin at the camera entrance pupil) in coincidence for a vertical camera, it is seen that the projective relation between a ground point, P (x_g, y_g, z_g) and its conjugate in the camera focal plane (x_f, y_f, z_f) is given by

$$x_f = fx_g/z_g$$

$$y_f = fy_g/z_g$$

$$z_f = f \tag{5}$$

If the ground point has a velocity component, then the image point will have velocity components, and

$$s_x = \dot{x}_f = f\,\frac{z_g\dot{x}_g - x_g\dot{z}_g}{z_g^2} \tag{6}$$

$$s_y = \dot{y}_f = f\,\frac{z_g\dot{y}_g - y_g\dot{z}_g}{z_g^2} \tag{7}$$

Substitution from equation (5) gives

$$s_x = \frac{f\dot{x}_g - s_f\dot{z}_g}{z_g} \tag{8}$$

$$s_y = \frac{f\dot{y}_g - y_f\dot{z}_g}{z_g} \tag{9}$$

If the camera is pointed in a direction other than vertical, then an equivalent condition is obtained if the ground coordinate system is rotated about its axes (in the opposite sense from the camera rotation). This gives new coordinates (x_g', y_g', z_g') to the ground point, and we can write the relation

$$\begin{vmatrix} x_g \\ y_g \\ z_g \end{vmatrix} = \overbrace{\begin{vmatrix} A_xA_yA_z \\ B_xB_yB_z \\ C_xC_yC_z \end{vmatrix}}^{\text{M}} \begin{vmatrix} x_g' \\ y_g' \\ z_g' \end{vmatrix} \tag{10}$$

where the matrix M describes a succession of coordinate rotations about the X, Y, and/or Z axes through the angles ϕ, β, and/or θ respectively.

With the substitution of the identify $z_g' = -H$ in equation (10), it may be solved to give

$$\frac{1}{z_g} = -\frac{1}{fh}\Big[fm + Nx_f + Qy_f\Big] \tag{11}$$

where

$$M = A_xB_y - A_yB_x$$
$$N = B_xC_y - B_yC_x$$
$$Q = A_yC_x - A_xC_y$$

and substitution in equations (8) and (9) gives

$$s_x = -\frac{1}{H}\Big[fM\dot{x}_g + x_f(N\dot{x}_g - M\dot{z}_g) + y_fQ\dot{x}_g - \frac{x_f^2}{f}N\dot{z}_g - \frac{x_fy_f}{f}Q\dot{z}_g\Big] \tag{12}$$

$$s_y = -\frac{1}{H}\Big[fM\dot{y}_g + y_fN\dot{y}_g + y_f(Q\dot{y}_g - M\dot{z}_g) - \frac{y_f^2}{f}Q\dot{z}_g - \frac{x_fy_f}{f}N\dot{z}_g\Big] \tag{13}$$

Ground motion in Y-direction.—For ground motion components in the Y-direction, if the ground velocity is $-V$, then

$$\dot{x}_g' = 0$$
$$\dot{y}_g' = -V \tag{14}$$
$$\dot{z}_g' = 0$$

where V has been given a negative sign to indicate the typical case of a vehicle moving in the $+Y$-direction. Differentiation of equation (10) gives

$$\begin{vmatrix} \dot{x}_g \\ \dot{y}_g \\ \dot{z}_g \end{vmatrix} = \overbrace{\begin{vmatrix} A_xA_yA_z \\ B_xB_yB_z \\ C_xC_yC_z \end{vmatrix}} \begin{vmatrix} \dot{x}_g' \\ \dot{y}_g' \\ \dot{z}_g' \end{vmatrix} \tag{15}$$

TABLE III.—*Coefficients of Equations (1) and (2)*

Ground Motion	
Y-direction	*X*-direction
$a=A_y(A_xB_y-A_yB_x)$	$A_x(A_xB_y-A_yB_x)$
$b=A_y(B_xC_y-B_yC_x)-C_y(A_xB_y-A_yB_x)$	$A_x(B_xC_y-B_yC_x)-C_x(A_xB_y-A_yB_x)$
$c=A_y(A_yC_x-A_xC_y)$	$A_x(A_yC_x-A_xC_y)$
$d=-C_y(B_xC_y-B_yC_x)$	$-C_x(B_xC_y-B_yC_x)$
$e=-C_y(A_yC_x-A_xC_y)$	$-C_x(A_yC_x-A_xC_y)$
$g=B_y(A_xB_y-A_yB_x)$	$B_x(A_xB_y-A_yB_x)$
$j=B_y(B_xC_y-B_yC_x)$	$B_x(B_xC_y-B_yC_x)$
$k=B_y(A_yC_x-A_xC_y)-C_y(A_xB_y-A_yB_x)$	$B_x(A_yC_x-A_xC_y)-C_x(A_xB_y-A_yB_x)$

which, upon substitution from equation (14) yields

$$\begin{aligned}\dot{x}_g&=-A_yV\\ \dot{y}_g&=-B_yV\\ \dot{z}_g&=-C_yV\end{aligned}\tag{16}$$

and for this case, equations (12) and (13) become

$$s_x=\frac{V}{H}\left[fMA_y+x_f(NA_y-MC_y)+y_fQA_y-\frac{x_f^2}{f}NC_y-\frac{x_fy_f}{f}QC_y\right]\tag{17}$$

$$s_y=\frac{V}{H}\left[fMB_y+x_fNB_y+y_f(QB_y-MC_y)-\frac{y_f^2}{f}QC_y-\frac{x_fy_f}{f}NC_y\right]\tag{18}$$

Ground motion in X-direction.—For ground motion components in the *X*-direction at velocity $-V$, we have

$$\begin{aligned}\dot{x}_g'&=-V\\ \dot{y}_g'&=\ \ 0\\ \dot{z}_g'&=\ \ 0\end{aligned}\tag{19}$$

whence

$$\begin{aligned}\dot{x}_g&=-A_xV\\ \dot{y}_g&=-B_xV\\ \dot{z}_g&=-C_xV\end{aligned}\tag{20}$$

and therefore

$$s_x=\frac{V}{H}\left[fMA_x+x_f(NA_x-MC_x)+y_fQA_x-\frac{x_f^2}{f}NC_x-\frac{x_fy_f}{f}QC_x\right]\tag{21}$$

$$s_y=\frac{V}{H}\left[fMB_x+x_fNB_x+y_f(QB_x-MC_x)-\frac{y_f^2}{f}QC_x-\frac{x_fy_f}{f}NC_x\right]\tag{22}$$

Equations (17) and (21) and equations (18) and (22) may be written in the form

$$s_x=\frac{V}{H}\left[af+bx_f+cy_f+d\ \frac{x_f^2}{f}+e\ \frac{x_fy_f}{f}\right]\tag{23}$$

$$s_y=\frac{V}{H}\left[gf+jx_f+ky_f+e\ \frac{y_f^2}{f}+d\ \frac{x_fy_f}{f}\right]\tag{24}$$

which are equations (1) and (2). The coefficients have the values (using substitutions from equation (11)) as shown in table III.

Image Motions Due to Rotations

For image motions due to rotations, then differentiation of equation (10) gives

$$\begin{vmatrix}\dot{x}_g\\ \dot{y}_g\\ \dot{z}_g\end{vmatrix}\begin{matrix}\\ =\\ =\end{matrix}\begin{vmatrix}\dot{A}_x\dot{A}_y\dot{A}_z\\ \dot{B}_x\dot{B}_y\dot{B}_z\\ \dot{C}_x\dot{C}_y\dot{C}_z\end{vmatrix}\quad\begin{vmatrix}x_g'\\ y_g'\\ Z_g'\end{vmatrix} \tag{25}$$

Using the identity $z_g'=-H$, and the relations of equation (5), substitution of equation (25) into equations (8) and (9) gives

$$s_x=Af+Cy_f+D\frac{x_f^2}{f}+E\frac{x_fy_f}{f} \tag{26}$$

$$s_y=Gf+jx_f+E\frac{y_f^2}{f}+D\frac{x_fy_f}{f} \tag{27}$$

which are already given as equations (3) and (4). The coefficients have the values

$$\begin{aligned}
A&=C_x\dot{A}_x+C_y\dot{A}_y+(A_xB_y-A_yB_x)\dot{A}_z\\
C&=B_x\dot{A}_x+B_y\dot{A}_y+(A_yC_x-A_xC_y)\dot{A}_z\\
D&=-A_x\dot{C}_x-A_y\dot{C}_y-(B_xC_y-B_yC_x)\dot{C}_z\\
E&=-B_x\dot{C}_x-B_y\dot{C}_y-(A_yC_x-A_xC_y)\dot{C}_z\\
G&=C_x\dot{B}_x+C_y\dot{B}_y+(A_xB_y-A_yB_x)\dot{B}_z\\
J&=A_x\dot{B}_x+A_y\dot{B}_y+(B_xC_y-B_yC_x)\dot{B}_z
\end{aligned}$$

REFERENCE

1. Brown, E. B.: V/H Image Motion for Aerial Cameras. Photogrammetric Engineering, vol. 31, March 1965.

Page intentionally left blank

Page intentionally left blank

USE OF ELECTRO-OPTICAL IMAGE CORRELATION FOR MEASURING AND PROVIDING COMPENSATION FOR IMAGE MOTION

NORMAN G. ALTMAN
Bolsey Associates, Inc.
Glenbrook, Conn.

The V/H sensor the Bolsey Associates, Inc. developed for the NASA Lunar Orbiter photographic missions (fig. 1) weighed 10 pounds, required 8½ watts, and held image smear on the processed film itself to less than 2½ microns. This means that the residual image motion at the image plane of the sensor was less than 1½ microns. This V/H sensor used an electromechanical area scanner and an electronic correlator operating with an electromechanical closed-loop servosystem. A developmental model of a similar system, but operating in the IR domain with a cooled detector, is about to be delivered to Wright Air Development Center. These systems can not be considered "first generation" and have been superseded by much higher performance versions.

Second generation, all-electronic scanner-correlators have been developed by BAI that weigh 5 pounds, require 5 watts, and are capable of maintaining image stability to within ±1 micron over very large dynamic ranges. These systems operate with zero image motion as well as with V/H rates out to 10 radians per second. Concurrently, BAI has under development an all-electronic IR system that uses an uncooled detector.

This paper delineates some of the system considerations associated with reducing image smear and describes the operation of first and second generation BAI V/H sensors. Also described is an extension of the basic BAI system that can be used to measure the belt velocity of V/H sensor test sets to fractional micron (5 to 10 microinch) accuracy.

SYSTEM CONSIDERATIONS

The general problem of determining V/H for a photographic mission is that of determining the rate of image motion with an objective of generating a method of compensating for the image motion, the ideal result being a system in which the image is completely stabilized on the film during the entire time the system shutter is open. Thus the measure of V/H is an intermediate process; the desired output is the rate of image motion across the focal plane. Hence, a system that measures image motion (and ideally in the focal plane of the lens system used by the camera) is producing the information required for the optimum image motion compensation. To do this properly, the type of image motion measurement and technique to be used should be determined during the camera system design stage. Such an ideal situation arose in the Lunar Orbiter system, where the decision on image motion measurement and compensation was made early in the camera design. At this time, basic design decisions could be made to insure an optimum image motion compensation system. In particular, the following decisions were made that greatly improved the performance of the overall camera system and reduced the effect of image motion:

(1) The image motion sensing equipment shared the camera lens with the film itself

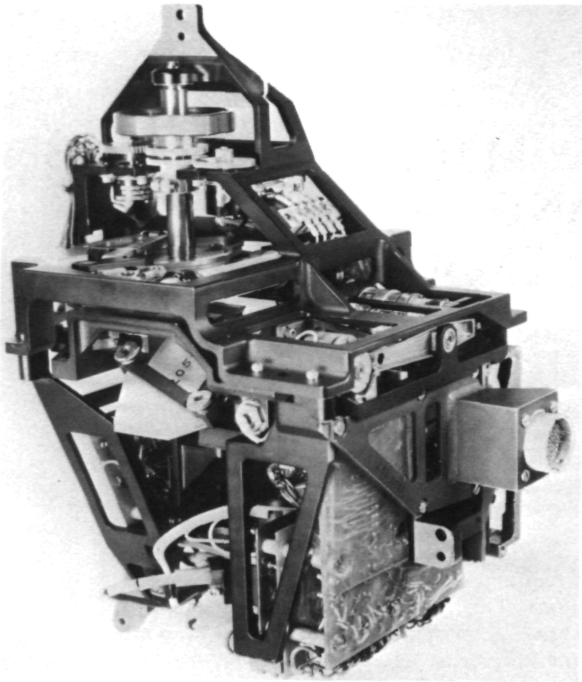

FIGURE 1.—Lunar orbiter V/H sensor (front view).

such that errors of measuring and calibrating lens focal lengths, etc., were completely eliminated. The image motion measured by the Lunar Orbiter image motion sensor was that which would be seen by the film were there no compensation.

(2) The measurement of image motion was done by means of a closed loop system (the BAI image motion sensor operated in a closed loop null-seeking mode, thus eliminating the effects of any nonlinearities in the sensing system itself).

(3) In order to close the loop, a mechanical link was used within the loop. This mechanical link, provided with a proper cam, directly furnished the motion required at the film platen of the Lunar Orbiter camera to provide the image motion compensation. This technique eliminated all of the errors that would arise from a follow-up servo and insured that the total error going from the BAI image motion sensor to the motion of the film platen consisted only of cam errors, which could be held to less than a micron, and cam follower error, which also could be held to less than a micron.

This is almost the ideal arrangement, where the camera design is made with full appreciation of the problems involved in measuring and compensating for image motion down to the micron level. Unfortunately, the designer of the image motion sensor does not normally run into as ideal a system situation as this. He is usually faced with a completed camera design in which a "provision" for image motion compensation has been made. Frequently, this "provision" is not one in which it is simple to tie a compensation system without a great loss in accuracy. While it is not the function of this paper to discuss the generation of an error budget for a camera system image motion compensation loop, it can be disheartening to learn that after having built an image motion sensor with one micron resolution and sensitivity that the link with the camera is so inaccurate that system performance is degraded by a factor of 10 or 20.

It is important to recognize that the closed-loop operation provides a powerful advantage, namely the ability to directly stabilize the image as seen at the film plane. The V/H sensor can view the image through the camera lens (as in the Lunar Orbiter) and provide compensation by moving elements of the optical train (i.e., the lens itself or an element in a relay in front of or behind the lens).

In an open-loop system, wherein image motion is measured, the measured V/H rate is a function of focal length. Hence it is essential to position the sensor at the focal plane of the lens to an accuracy comparable to the V/H requirement (typically, 0.1 percent) and maintain this position over significant temperature variation and other environmental factors. While this can be achieved with sufficient accuracy, it is only possible at a significant cost, time expenditure, and weight penalty. With a closed-loop system, image motion is reduced nominally to zero, washing out any errors in the measured V/H rate. The lack of positional accuracy results only in a blurred image as seen by the sensor, which blurring does not degrade performance of the BAI system. (It should be pointed out that the BAI system is the only system we know of whose performance is not degraded when operating out of the plane of optimum focus.)

Let us consider the errors which would result from an open loop V/H system operating at representative airborne or satellite mapping conditions, typically a focal length of 600mm and a V/H rate of 50×10^{-3} radians/second. Under these conditions, a 0.1 percent open loop system would have an error of 30 microns per second. Since the absolute value of uncorrected smear is proportional to exposure time, a 30 microns/second error is tolerable for short exposures, even in a high resolution system. For example, with a 1/100 second exposure, the residual smear would be reduced to 0.3 micron. However, for high resolution applications that require the shutter to be open for significant times (for example, long exposures for slow films or panoramic coverage), an error of 30 microns per second cannot be tolerated. In such cases, the type of closed-loop, ±1 micron image stability provided by an image correlation-tracking system is required.

GENERAL OPERATING PRINCIPLES OF THE BAI V/H SENSOR

The BAI image motion detector operates as a null-seeking, closed-loop system. The basic sensor consists of a lens system that creates an image on the surface of a scanner, which in turn examines the image and generates an electrical signal that uniquely defines the examined image. In normal operation the system will operate in cycles in the following manner. At the beginning of a cycle, the line of sight is swung as far forward as the system control parameters will allow. The image viewed with the line of sight at this position is scanned, and the electrical signal thus generated is memorized. As the vehicle flies over the terrain, a closed-loop servo maintains the system line of sight pointed at the memorized area of the terrain; thus the image on the face of the scanner stays constant and unchanged to the extent that the system gain and response time is able to provide perfect image stabilization. It is immediately obvious, or at least obvious after a small amount of consideration, that a system that can stabilize an image in one plane is generating the information to stabilize it in any other plane. The system as defined above provides information for directly determining V/H, since this is proportional to the angular rate of change of the system line of sight required to stabilize the image on the scanner face. However, what is much more important is that the image is indeed stabilized on the scanner face, and a simple mechanical linkage can provide the information generated by this stabilization to communicate the necessary stabilization motion to the camera IMC loop.

OPERATION OF THE ELECTROMECHANICAL V/H SENSOR

The electromechanical V/H sensor comprises an area scanner-correlator and servosystem in which an optical scanner and electronic correlator are combined to provide:

(1) Scanning of a scene in either the visible or infrared domain

(2) Processing of the information derived from scanning into a form suitable for memorizing and correlating

(3) Memorizing the processed information, which contains the indicia of the scanned scene

(4) Correlating the memorized information with information from the displaced scene scanned at a later time, yielding error signals that represent the displacement with respect to the memorized scene position

(5) Closing of a servoloop to minimize or "zero out" the error signals by proper motions of the image motion compensation mechanism, which motion is directly proportional to V/H rate

The basic elements of the area scanner-correlator are shown schematically in figure 2. A real image is formed by suitable optics and scanned by an image scanner. (This image scanner has been instrumented as a rotating opaque disc that has a radial slit aperture, as a fibre optic light pipe, or, in the Lunar Orbiter, as a rotating mirror segment.) The energy from the real image that passes through the image scanner aperture is collected and focused on a detecting element (photomultiplier in the case of the Lunar Orbiter system, or infrared detector). As the aperture rotates, it scans an annulus centered on the optical axis. As the image varies in brightness (energy

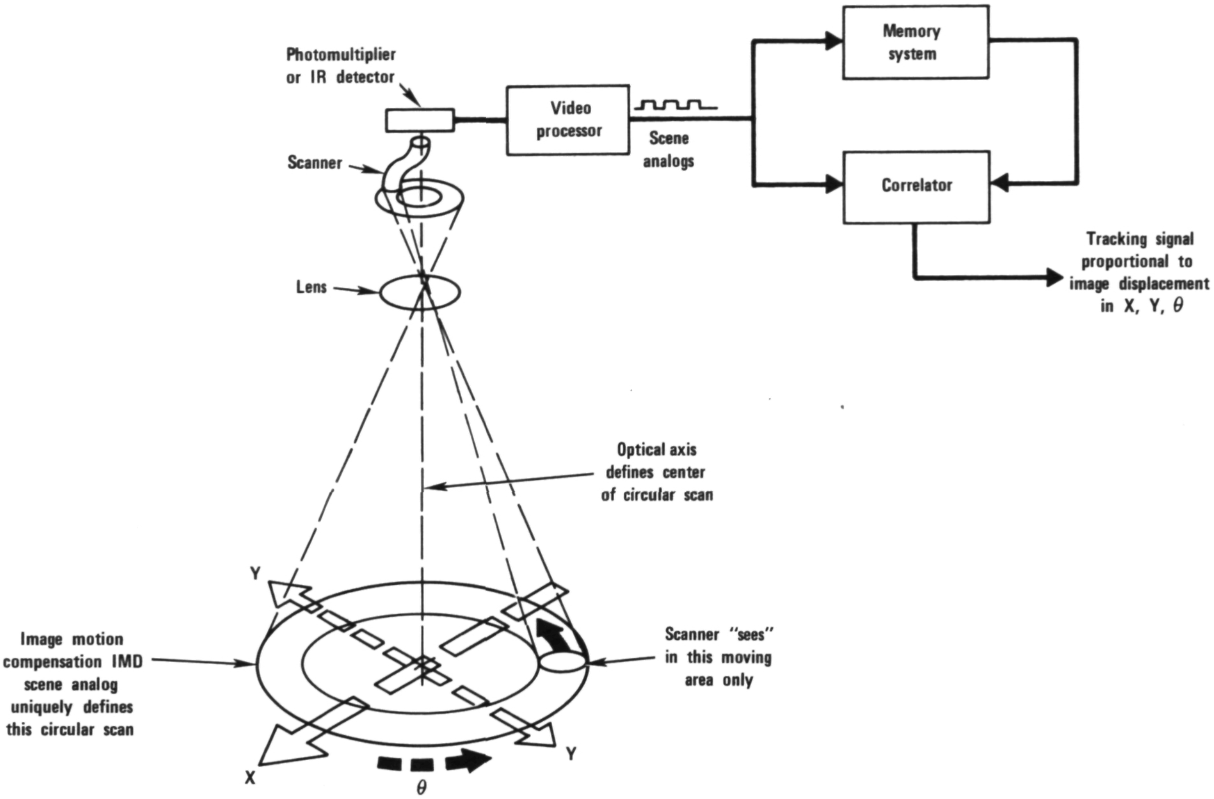

FIGURE 2.—Block diagram of electromechanical BAI area scanner-correlator.

content), the flux passing through the aperture varies in intensity; this variation is sensed by the detector, which produces a video rate electrical analog of the brightness variations around the scan. This video signal, when processed, is a quantized modulated pulse train and is called a scene analog. Generally, there are about 20 pulses in a given quantized scene analog. Leading and trailing edge time-position resolution is better than one part in 10 000.

The scene analog represents the image to be tracked. It is recorded on a magnetic storage drum that rotates in exact synchronism with the scanning aperture. (Generally, the two are mounted on the same shaft.) Only one recording track is required to store the complete unique scene analog of a reference scene.

When two scene analogs are compared by the correlator, the correlator output is normally presented in the form of voltages that are proportional to the displacements between the two scene positions. This displacement information is resolved into rotation, θ, plus two orthogonal displacements, X and Y. If there are no displacements between the two scene positions, that is, if they coincide perfectly, the output of the correlator will be zero. Displacements of as little as 1 or 2 microns (40 to 80 microinches) in the image plane will generate an error signal that can be used to control a closed-loop servo.

The closed-loop servo converts the error signals into motions of an image motion compensation (IMC) mechanism, a pair of moving mirrors in the LOP system. The motion of the IMC elements are so arranged as to null out the detected mismatch between the memorized scene position and the "live" scene position, stabilizing the image on the face of the scanner. In the LOP system, the loop was closed mechanically using a rotating shaft that directly furnished the film platen motion required to stabilize the film image.

The operating cycle of the V/H sensor is as

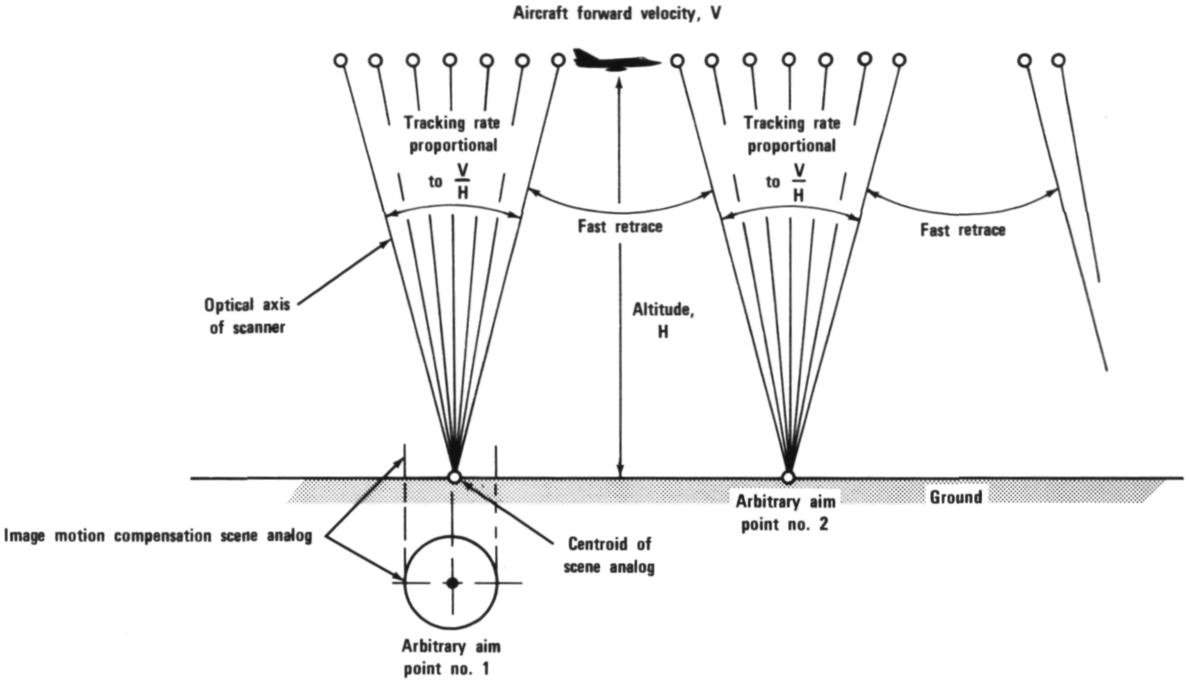

FIGURE 3.—V/H sensor tracking cycle.

enumerated below and as shown in figure 3 above.

(1) The sensor scans an area on the ground ahead of the vehicle, generates the appropriate scene analog, and stores it in the system memory.

(2) As the vehicle carries the system forward, the sensor continues to scan the ground and generates a scene analog for each scan. The scan rate is sufficiently high that there can be only a very small displacement of the image from one scan to the next. Any such motion is detected by the sensor and is used to servo the IMC mechanism to generate a compensating motion and completely stabilize the image on the scanner face.

(3) After the IMC mechanism has followed the image motion through its entire tracking range, the IMC recycles to a new starting point. During the retrace time, the system operates in memory so that an accurate V/H output is continuously available.

(4) The entire process then repeats.

LUNAR ORBITER SYSTEM PERFORMANCE

The BAI V/H sensor used in the Lunar Orbiter Program was allocated a total smear budget of only 2½ microns (100 microinches). This included not only the error of the sensor's area correlator and servomechanism but also errors in the mechanism that moved the film.

In the Lunar Orbiter Program, the BAI V/H system met this smear budget of 2½ microns, indicating a basic V/H accuracy of better than 1½ microns. (It is interesting to point out that with the 24-inch lens employed in this camera, the 2½ micron allowable smear corresponds to a total allowable error of ±1 second of arc.)

The area scanner-correlator is small, lightweight, and requires very little power. The entire V/H sensor used for the Lunar Orbiter Program, including three servosystems and a memory drum, weighs only 10 pounds and has an average power consumption of 8½ watts.

The unit is capable of scan times in the order of 5 to 10 milliseconds and correlation time between 20 and 100 milliseconds.

From the point of view of resolution and precise instrumentation, perhaps the most dramatic photograph obtained in the Lunar Orbiter Program is the Surveyor photograph taken by Lunar Orbiter III shown in figure 4.

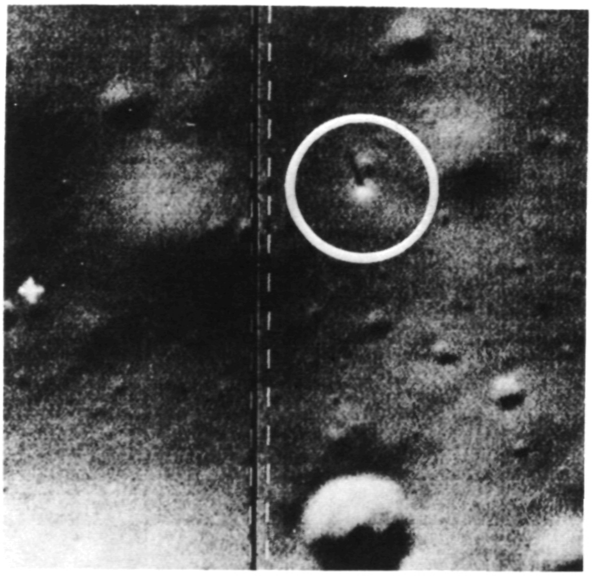

FIGURE 4.—Surveyor I photograph obtained by Lunar Orbiter III.

The orbit for Lunar Orbiter III was chosen to allow photography of the Surveyor I vehicle that had made a soft landing on June 2, 1966. On February 21, 1967, Lunar Orbiter III passed close enough to the area in which this landing was made to allow a wide angle photograph to be taken of it with the 80 mm lens. This photograph was developed and transmitted on a priority readout command. When received, details of the lunar surface that had appeared on Surveyor photographs were identified; from these, the position of the Surveyor was determined by triangulation.

On the next day, February 22, as Lunar Orbiter III made its closest approach to the calculated point, a high resolution photograph was made of the area. When this photograph was received and processed, the Surveyor was found where predicted. The shadow of the Surveyor, which is less than 1 meter wide, is clearly visible. Microdensitometer examination of this shadow shows several interesting features. First, there is no measurable smear, despite the fact that the camera was at a 12° oblique angle when the photograph was taken. Second, the shadow cast by the Surveyor should not be the same density through its length; it should consist of three darker sections with lighter portions in between. Although this is not apparent to the eye, the separate sections are readily seen on the microdensitometer output, not only establishing unquestionably that the shadow is that of the Surveyor, but also pointing out the superb resolution of the photography.

It is quite fascinating that the presence of Surveyor I made possible the only exacting test of the performance of the V/H system. It must be appreciated that it is not possible with today's state of the art to develop a test bed that is more stable than the BAI V/H sensor. The spacecraft, however, did represent a highly stable platform whose velocity and altitude were known with great precision. Unfortunately, no earth-based comparison could meaningfully be made between this information and the V/H output, since the telemetry system transmitted the V/H output from the sensor with an accuracy of only ±1 percent. Furthermore, image smear on the film could not be used as a criterion of V/H accuracy, since there was insufficient knowledge of the size and shape of features on the lunar terrain. Surveyor I, however, represented a target whose size and configuration were known. The shadow of the Surveyor body was known to be 80 cm wide and that of the connecting members 20 to 30 cm wide. At an altitude of 30 miles, 25 cm represents 1 second of arc. Examination of the photographs with a scanning microdensitometer showed that there was no measurable elongation of the image of the Surveyor shadow in the direction of vehicle motion. This unquestionably established that the residual smear represented less than a fraction of a meter projected to the lunar surface, determining, finally, an upper bound for the operational performance of the BAI image compensation system.

THE IR ELECTROMECHANICAL SYSTEM

BAI will shortly deliver to Wright Air Development Center a developmental system based on the Lunar Orbiter design, but intended for day and night operation. This system uses a mercury-doped germanium detector and a solid neon cooler to provide cooling to 28° K.

Other than the use of an IR detector in place of a photomultiplier, the major differences between the IR and Lunar Orbiter systems lies in the optics and servosystems.

The optical system (fig. 5) uses an on-axis mirror system of the Cassegrain type consisting of an aspherical primary and a spherical secondary element as the objective optics. An aperture in the primary mirror passes energy to the scanner cup via three folding elements (including the two mirrors of the translating mirror carriage). Inside the scanner cup, two mirrors (one flat, the other powered) scan an annular area of the image and transfer the energy so scanned to the detector through a germanium condenser lens (the only refractive element in the system).

The basic design of the scanner cup is the same as that in the Lunar Orbiter system, except that the scanning radius has been increased to reduce obscuration by the secondary mirror of the objective optics. To improve signal-to-noise ratio, a minimum number of attenuating reflective elements are used, and the image spot diameter is reduced.

THE ALL-ELECTRONIC VISIBLE-LIGHT SYSTEM

While the basic premises of operation of the electromechanical and the all-electronic area scanner-correlator are similar, the all-electronic system (fig. 6) recently developed by BAI represents a number of important differences both in terms of operation and performance.

The mechanical scan-photomultiplier combination has been replaced by a deflectable photomultiplier (DPM); scanning is achieved by electronically controlling the DPM deflection coils. The translating mirror carriage and associated servosystem that stabilizes the image on the scanner face have been replaced by an all-electronic servosystem that provides image stabilization by electronically controlling the position and shape of the DPM scan. The magnetic drum memory is replaced with an all-electronic memory.

The advantages achieved by the new all-electronic scanner-correlator are so great that it can be considered a brand-new instrumentation approach. Of particular interest are high speed slew rates that can provide control on low-altitude, high-Mach-number missions, with V/H rates upwards of 10 radians per second.

Scanner

A ruggedized, militarized deflectable photomultiplier (DPM) is used to accomplish the scanning function. To scan the image, the shaped aperture of the photomultiplier is electronically controlled to generate any desired locus that might be optimum for system requirements. (In many applications the shape of the aperture is also electronically controlled and is variable during the mission of interest.) Moreover, whatever basic scan pattern has been established is easily servoed to control its size and shape to compensate for changes in scale and other geometric variations. The entire scan pattern is moved to track a moving image in order to continue examination of a chosen area of that image and determine rate of image motion for IMC.

Signal Processing

For V/H applications, the video output of the servoed DPM is then a signal identically the same as that produced by the LOP system previously described. This signal is amplified and quantized by circuitry the same as that in the LOP system. Hence we end up with a quantized video signal that is now in standardized BAI form.

Similarly, the correlator is an integrated-circuit analog of previous BAI correlators, and the memory is an electronic analog of the rotating drum memory used in such systems as the LOP. (The all-electronic memory system is further described below.)

Error Signal Generation

A V/H sensor typically measures the resultant vector of cross-track and along-track motion. However, it is necessary to resolve the vector into its two components, since cross-track motion is usually corrected by rotating the camera and/or its mount or by trimming the vehicle, while compensation for along-track image mo-

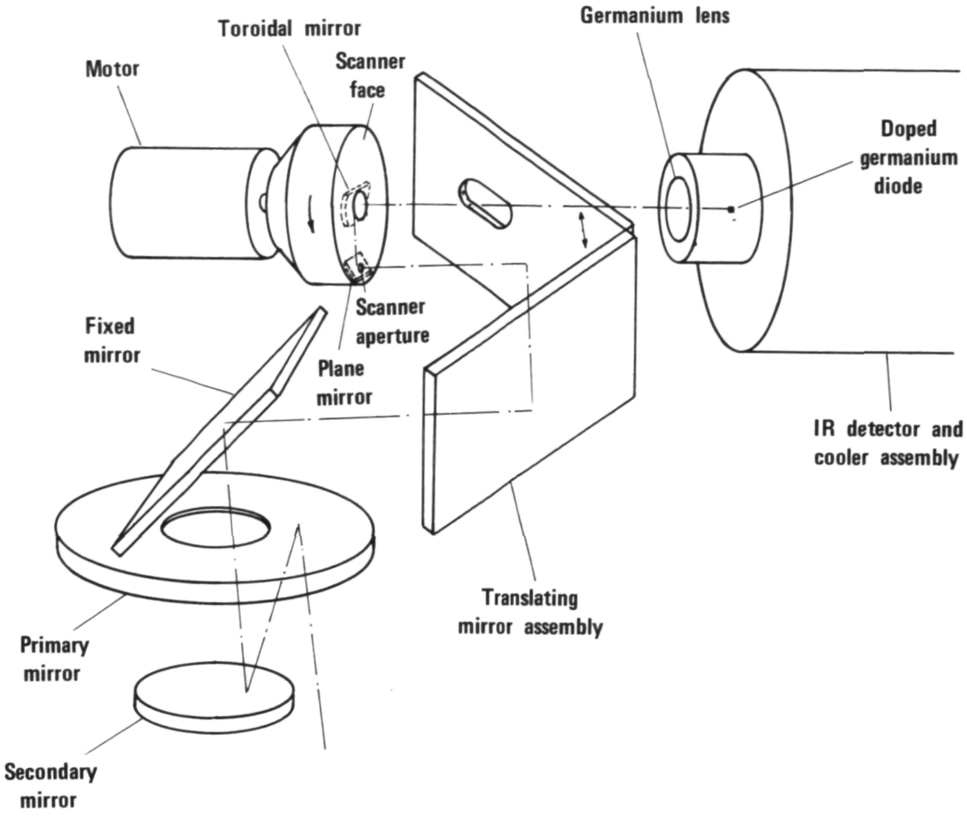

FIGURE 5.—Optical schematic of electromechanic IR V/H sensor.

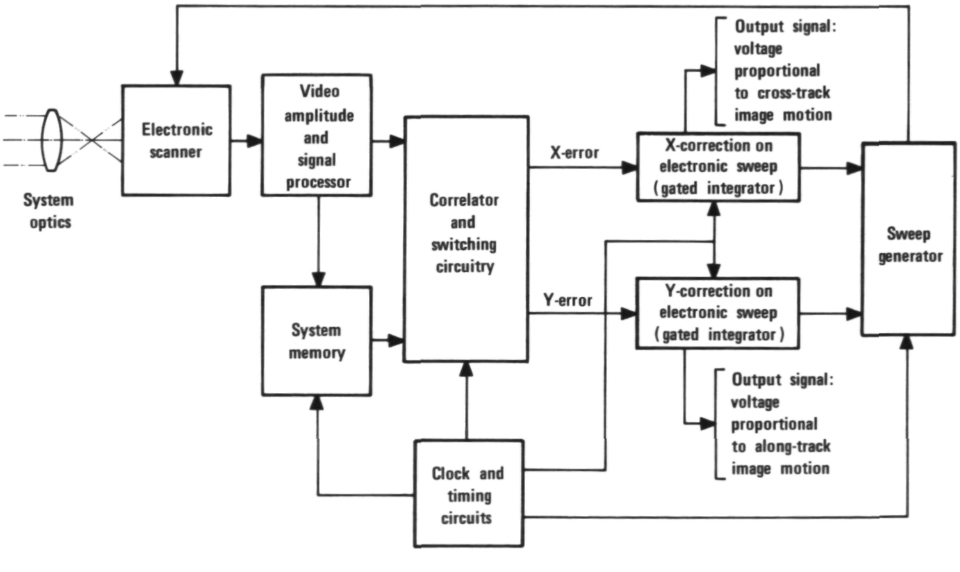

FIGURE 6.—All-electronic system.

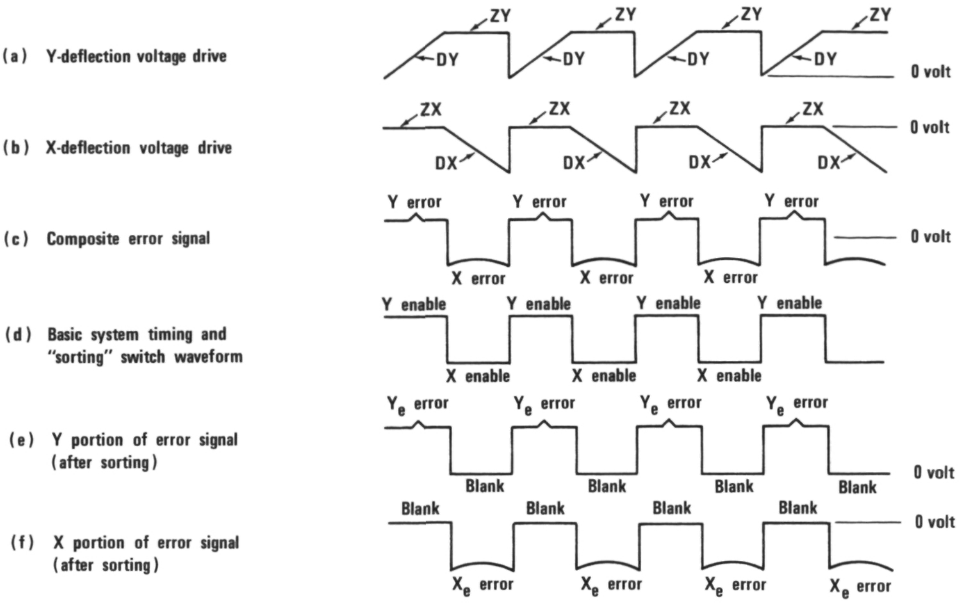

FIGURE 7.—System timing diagram.

tion is achieved within the camera by moving some element in the optical train or by moving the film platen. Any residual cross-modulation products between the along-track and cross-track outputs represent a residual error in the image motion compensation. The all-electronic system is capable of virtually eliminating these cross-product terms by time separating the along-track and cross-track portions of the scan, thereby time separating the error signals. The timing diagram shown in figure 7 illustrates how this is achieved.

The periodic voltage applied to the vertical deflection coils of the DPM produce the *Y* or vertical portion of the scanning pattern shown in figure 7(a). Each cycle consists of a sawtooth or deflection voltage portion, *DY*, and a square or nondeflection voltage portion, *ZY*. Similarly, periodic voltage applied to horizontal deflection coil (fig. 7(b)) consists of a square portion, *ZX*, and a sawtooth portion, *DX*.

Thus first the *Y*-drive voltage moves the scan up the face of the DPM, with *X* position fixed. Then with fixed *Y* position, *X*-drive voltage moves the scanning aperture across the face of the tube from left to right, and finally the *X*- and *Y*-drive voltages are returned to zero, bringing the aperture to its original starting point (fig. 8). Since the *X* and *Y* motions are sequentially applied to the scanner, the resultant *X*- and *Y*-error signal components produced in the composite output of the correlator are time separated, as shown in figure 7(c).

In order to sort the *X*- and *Y*-error signal components from each other, the correlator

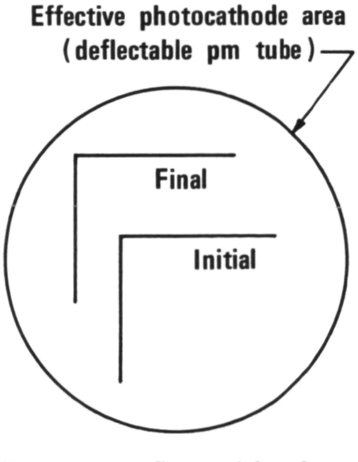

FIGURE 8.—Sequential along-track and cross-track scan.

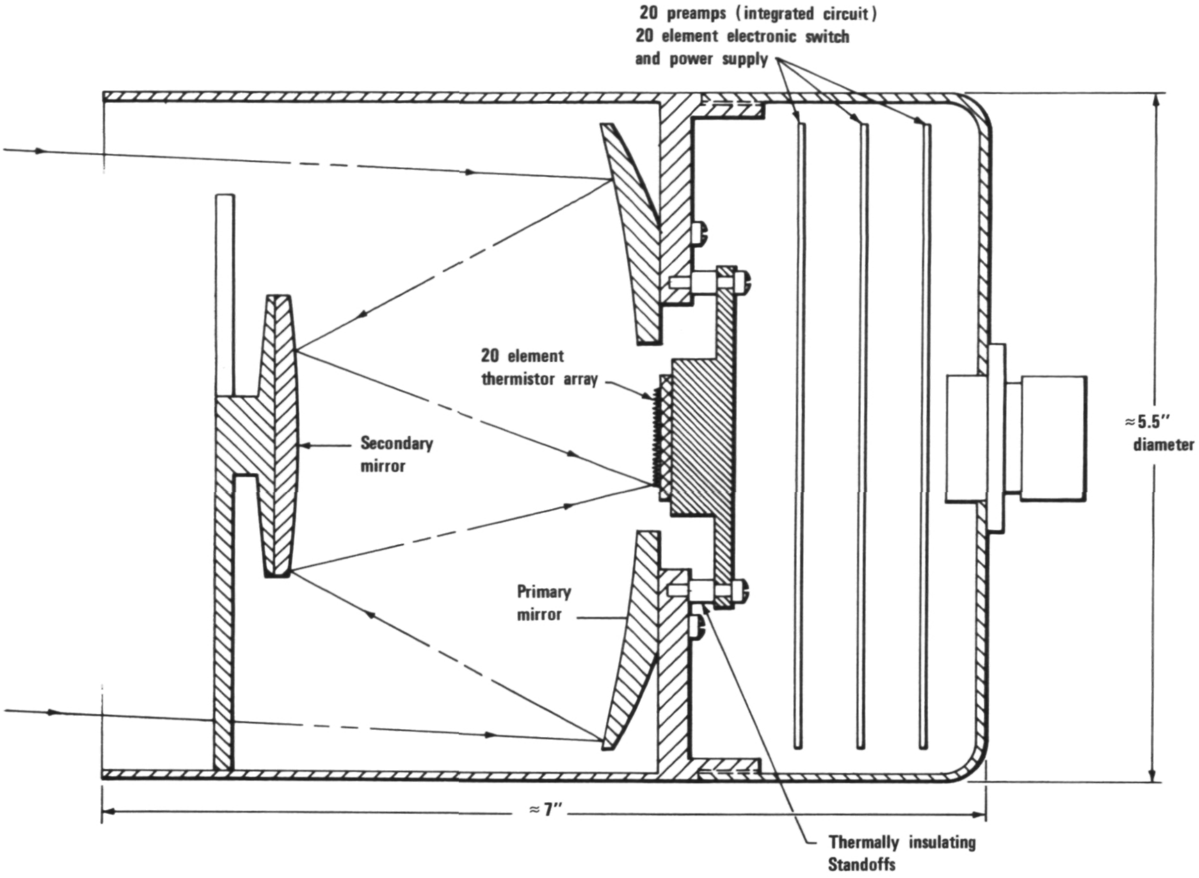

FIGURE 9.—Yaw sensor optical head.

is provided with electronic gates, one operative during the time of Y-scan motion and the other during the time of X-scan motion. Hence, after sorting, the Y_e-error signal (fig. 7(e)) has in each cycle an error component and a blank component, and similarly the X_e-error signal (fig. 7(f)) has a blank component and an error component in each cycle, the X_e and Y_e signals being 180 degrees out of phase.

X_e- and Y_e-error signals are applied to X-correction and Y-correction integrating circuits to produce dc outputs proportional to the error signals. These dc signals are applied directly to a sweep generator that produces the X- and Y-drive voltages for the DPM deflection coils, thereby closing the tracking servoloop, stabilizing the scanned image. The dc output signal of the X-correction circuit is proportional to cross-track image motion; the dc output signal of the Y-correction circuit is proportional to along-track image motion.

System Memory

The electronic system memory may be of any one of several standard memory circuits. An advantage in system configuration and simplicity arises when a first-in, first-out (FIFO) memory is used, since there is no necessity for random access to the memory. The incoming real-time video signal and the reference signal from the memory are always compared and correlated in phase. The FIFO memory stays in synchronization, and no additional micro-programming commands are required to maintain the desired order either in going into or in coming out of system memory. Typically, a shift register can be used to store the video information if it is properly time-quantized.

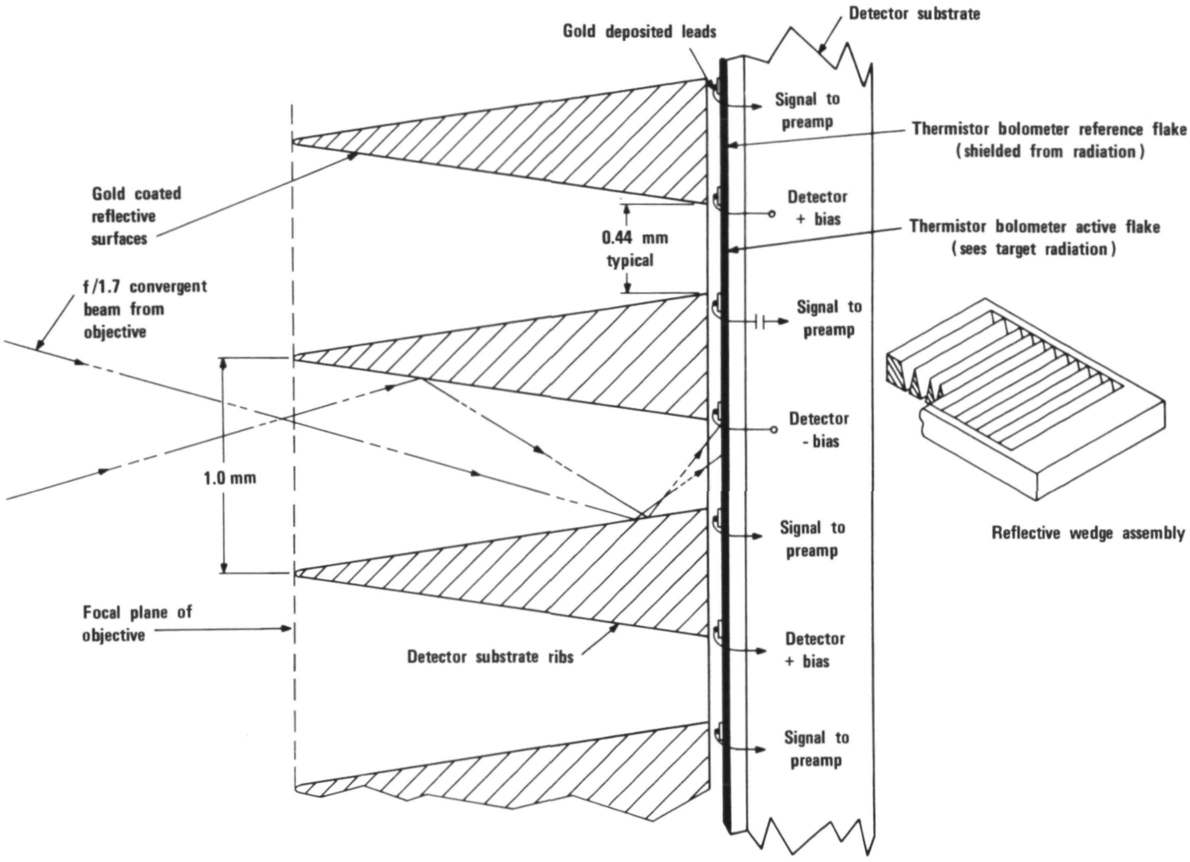

FIGURE 10.—Detector array detail.

THE ALL-ELECTRONIC IR SYSTEM

BAI is presently developing an all-electronic IR sensor (in a yaw detector configuration) under sponsorship of the NASA-Houston Manned Space Center. Basic operation of this system is the same as that of the all-electronic visible light system, except that the deflectable photomultiplier is replaced by an uncooled IR detector array to yield performance equivalent to a mechanically scanning aperture.

It can be shown that the information content of the annular scan can be considered as four quadrants, two containing cross-track information and two along-track motion, with each pair of quadrants being redundant. Further, since the information content varies as a cosine function, most of the information is contained in 45° sectors centered on the line of flight for cross-track motion and centered about the cross-track direction for the along-track motion. Thus we can use small segments of the annulus with little loss of information content. Further, since the mechanical scanned annulus uses a large aperture to examine only the low spatial frequency content of the image, we can operate with a detector array consisting of rather large elements to obtain performance analagous to the operation of a mechanically scanned large aperture. In the case of a yaw sensor, an array of 20 elements will provide performance with a quantizing degradation that is compatible with required system performance. The detector array and associated optics are shown in figures 9 and 10. An all-reflective Cassegrain optical system is used for the objective optics of the system. The detector array uses a 20-element unimmersed thermistor array combined with a wedge reflective optic to provide 20 elemental butting fields of view of 0.25×5°. The wedge optical element serves to increase the detector effective dimension in one direction, thereby providing increased optical gain, low optical cross-talk, and high optical quality because it allows a relatively slow speed front optical system. In addition, it allows space for the reference thermistor flake for each thermistor bolometer element, thus also inherently allowing the butting fields of view.

BELT VELOCITY MEASUREMENT SYSTEM

A conspicuous problem in bench testing of high accuracy V/H sensors is the fact that the test set's target belt motion is usually less stable than the V/H sensor, and the velocity of the target belt cannot conveniently be measured with accuracy comparable to that of the V/H sensor.

As an outgrowth of the basic sensor system, BAI has developed a noncontacting system that measures the velocity of moving belts, film strips, etc., to fractional micron (5 to 10 microinch) accuracy.

The new velocity sensor uses BAI very high resolution correlation equipment to determine the time required for the belt or film strip to traverse an accurately preestablished distance. This measurement is made continuously using a high precision clock to control the comparison function. Basic system resolution in measuring displacement is approximately 0. 1 micron (4 microinches). With displacement determinable to a fraction of a micron and time precision available to almost any desired accuracy (a part in 10^9 is easily and inexpensively obtained today), typical system accuracies are as follows:

High frequency response systems with sensitivities from ½ micron per millisecond: At velocities of 1 meter per second (1000 microns per millisecond) this corresponds to an accuracy of 0.05 percent with response time of a few milliseconds.

Low frequency response systems with displacement sensitivities of 1 or 2 microns over time bases varying from 1 second to minutes, if the application warrants the extra long time base: At velocities of 1 meter per second, a sensitivity of 1 micron/second corresponds to an accuracy of one part/million with a response time of the order of 1 second.

A simplified representation of the system is shown in figure 11. The velocity measuring system examines the moving belt at two points that are an accurately premeasured distance apart. (While it is necessary that there be information on the belt that can be correlated for tracking, low resolution (a few lines per mm) random information with a contrast as low as 1.1/1 is sufficient. Such information is normally inherent to the belt. Should it be necessary to add information to the belt—for example, in the case of unexposed film—system accuracy is in no way dependent on accurate positioning of this tracking information.)

The information seen by viewers No. 1 and 2 is then converted into digital form by the standard techniques developed by BAI for such typical applications as those listed above. In this convenient digital form, time delays can be effected by the simple procedure of using a controlled frequency clock and a shift register to provide a controllable variable delay. The precision and resolution of the available delay is a function of the clock rate and the propagation and rise time of the shift register elements used (which can be held to as little as 10 nanoseconds under worst case conditions).

Information from viewer No. 1 (which examines the information on the belt first), digitized and suitably delayed, is compared by means of the standard BAI correlator with the information from viewer No. 2. The time delay is servoed by the error signal from the correlator such that the delayed input to the correlator from viewer No. 1 is brought into time coincidence with the input obtained from viewer No. 2. As has been proven with previous BAI systems, this technique insures that viewer No. 2 is working with the same imagery as that represented by the delayed output from viewer No. 1 (with a displacement error controllable to a fraction of a micron).

Thus with the spacing between the two scanners established accurately and stably, velocity is measured directly by the required time delay to achieve maximum correlation. The numerical value of the time delay is continuously available and is continuously corrected and updated by the action of the servo.

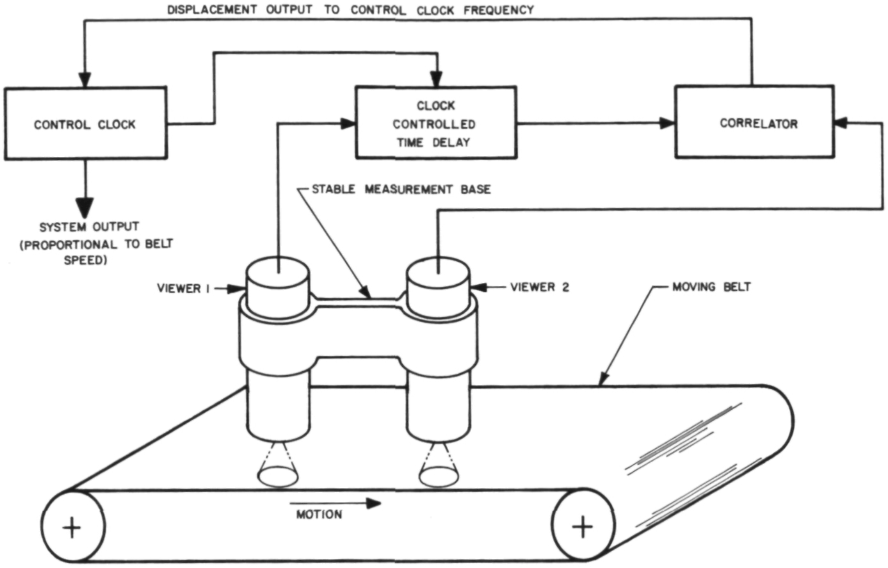

FIGURE 11.—Belt velocity measurement system, simplified representation.

System response times are a direct function of the spacing between the two viewers and the speed of the belt. As an example, with a belt traveling 1 meter per second, and the viewers spaced 1 millimeter apart (using simple folding optics to accomplish this), the information is relayed from viewer No. 1 to viewer No. 2 in 1 millisecond, and total system response time then is order of a few milliseconds. A system of this sort would provide accuracies of a fraction of a micron per millisecond. It would not measure very slow variations in velocity such as changes of 10 or 20 microns per second. For these slower variations the scanner heads would have to be spaced further apart. As the spacing between the heads is increased, the response time, of course, is increased proportionately, and also, the problems of mechanical stability become more severe. However, by judicious use of material such as Invar to provide stable reference beams, the scanner heads can be separated relatively widely without introducing incremental system errors of more than 1 micron.

For a system requiring high and low frequency control, three viewers would be used, two closely spaced to provide the high frequency information, and the third at a suitable distance to monitor the lower frequency velocity variations.

Page intentionally left blank

Page intentionally left blank

V/h SENSOR THEORY AND PERFORMANCE

RICHARD J. JONES
Itek Corporation
Lexington, Mass.

High resolution aerial photography requires the precise determination of aircraft angular motion over the earth (V/h). As aerial reconnaissance precision increases, greater precision is required of motion sensing and compensation equipment. Conventional V/h sensors employ photomultiplier-grid scanners, navigational devices, and other moderate performance techniques. More complex high performance devices employing image correlation techniques are under development. The scheme to be discussed here examines the power spectrum of an imaging system and shows substantial improvement over conventional methods.

The technique makes use of a vidicon camera. The detected output level of the integrated scene-related electrical spectrum from the vidicon is a measure of drift of the scene on the vidicon target. This output is a true autocorrelation function of the scene in the time domain with the integration time of the target of the vidicon as a parameter.

DESCRIPTION

General

Figure 1 is the general block diagram of the system. This unit has been designed to present a stationary image to a frame camera over a tracking angle of up to ±14° from nadir. This is accomplished by having the light from the scene reflect from a rotatable plane mirror prior to impinging on the frame camera. The rotation rate of the mirror is controlled to maintain the required stationary image on the film plane of the camera. This is a single axis system.

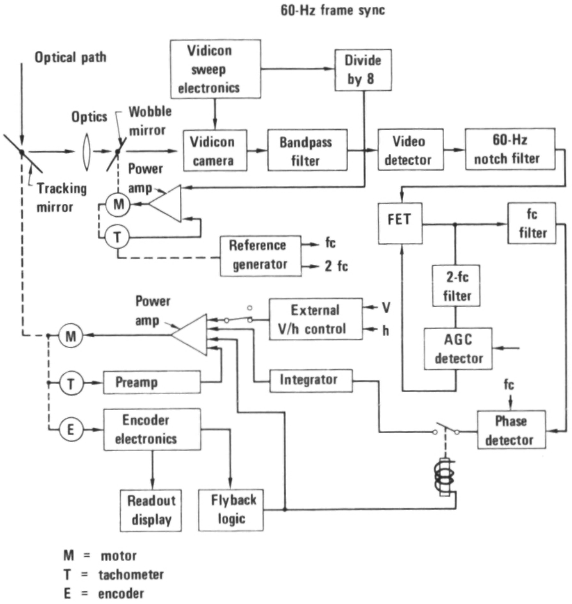

FIGURE 1.—V/h system functional block diagram.

Detailed

A portion of the light that reflects from the tracking mirror passes through on an *f*/4.5 lens and is imaged on the target of a vidicon. If the mirror is tracking perfectly, the scene is stationary on the vidicon target, resulting in the maximum possible spatial resolution.

As a consequence of this, the electron beam which reads the scene data from the target produces the highest possible electrical frequency spectrum. This then represents the tracking parameter: maximization of the integrated scene-related energy in the video output. If the tracking mirror is going either too fast or too slow, a drop in the electrical output will result, so that to develop an error signal of the proper polarity, a wobble plate is introduced into the optical path just in front of the vidicon. The wobble plate is a flat glass plate that is symmetrically tilted at a rate of 7.5 Hz about a plane parallel to the vidicon target. Neglecting higher-order effects, we observe that this produces a linear translation of the image on the target of the vidicon. The electrical energy from the vidicon is an inverse function of the wobble plate velocity. Thus, at the extremes of the plate's travel (fig. 2), the smear on the vidicon has its minimum value because the wobble velocity is zero. (This assumes that there is no scene motion.) Conversely, as the wobble plate traverses its central position, the smear (or loss in integrated high frequency electrical spectrum) is greatest. The result, with no scene motion, is a 15-Hz smearing of the vidicon target, and thus a 15-Hz output from the video detector. The phase relationships can be seen in figure 3. As previously mentioned, each time the wobble velocity goes to zero the smear has its minimum value. In figure 3, alternate crests are labeled A and B. This refers to the two directions of wobble indicated in figure 2. The video detector output (fig. 1) is out of phase with the smear because maximum smear produces minimum electrical energy out.

Thus, in the absence of scene motion, the video detector output is a 15-Hz signal. With further reference to figure 3, we can discuss scene motion in direction *A*. Assume that the amount of scene motion is not sufficient to prevent the wobble motion from cancelling it completely at some point during its cycle. Then the maximum video detector output, corresponding to a stationary scene, remains the same. But during wobble motion in direction *A*, the scene motion adds to the smear introduced by the wobble plate, reducing the minimum video detector output below that for a stationary scene. Conversely, during wobble motion in direction *B*, the scene motion subtracts from the wobble motion, raising the minimum detector output above that for a stationary scene. Thus scene motion in direction *A* introduces a 7.5-Hz signal that is out of phase with the wobble velocity. For scene motion in direction *B*, it can readily be seen that a 7.5-Hz signal in phase with the wobble velocity is generated. Therefore, we now have access to a 7.5-Hz error signal whose amplitude is a measure of the amount of scene motion and whose phase relative to the phase of the wobble velocity is a measure of its direction.

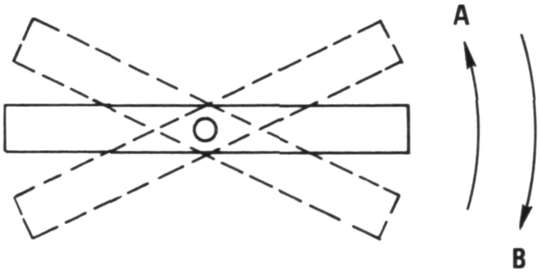

FIGURE 2.—Wobble plate.

Before leaving the subject of the wobble plate, it should be mentioned that it serves another important function. It provides an ac carrier which allows us to reject noise and avoid the buildup of dc offset through the chain of operational amplifiers in the loop.

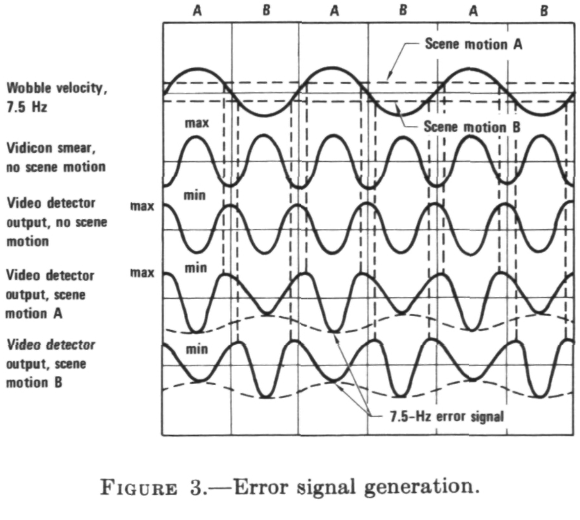

FIGURE 3.—Error signal generation.

VIDEO SIGNAL PROCESSING

A closer examination of the video processing can be made with reference to the system block diagram in figure 1. To prevent spurious detection later on in the loop, all the circuitry up to the output of the video detector is contained in shielded enclosures. The video signal from the vidicon control unit is first passed through a bandpass filter with 3-db response from 200 kHz to 3 MHz. The frame and line blanking pulses occur at 60 Hz and 31.5 kHz, respectively. This energy is not scene related, and thus we desire to discriminate against it. The 200-kHz lower cutoff represents a reasonable compromise to achieve this purpose. The upper limit of 3 MHz rejects noises of higher frequencies than are realizable as signals from the vidicon. The resulting electrical spectrum is amplified and presented to a video detector. The video detector then produces a modulation envelope, as discussed in connection with the wobble plate.

The 60-Hz frame blank signal still exhibits itself at this point, so that a 60-Hz notch filter has been inserted.

AGC Loop

As mentioned previously in connection with figure 3, in the absence of scene motion, a 15-Hz signal exists at the output of the video detector. Whereas the 7.5-Hz signal that appears in the case of scene motion is a function of both the spectral content of the scene and the amount of drift, this is not the case for the 15-Hz signal. The amplitude of the 15-Hz component is a measure of the spectral content of the scene. To provide uniform sensor response to a wide variety of scenes, we can use the 15-Hz signal for an AGC function to render the 7.5-Hz signal insensitive to the spectral content of the scene. This is accomplished with the aid of an FET, which acts as a variable resistor. The signal after the FET is passed through a filter to extract the 15-Hz component and then detected. The resulting dc voltage is filtered and amplified for use as a control signal to the gate of the FET. Thus the source to drain resistance is varied to maintain the amplitude of the 15-Hz component at its output at a constant level.

Error Detection

After the AGC function is performed, the signal is passed through an active filter to extract the 7.5-Hz component. This then represents the error signal discussed in connection with figure 3. The error detection process can be visualized with the aid of figure 4. The wobble velocity, as mentioned earlier, is either in phase or out of phase with the error signal. Since the wobble tachometer output is a measure of wobble velocity, its output is also either in phase or out of phase with the error signals. The wobble tachometer output is passed through a squaring amplifier having the form of a wide-open operational amplifier. The resulting square wave is passed through a phase splitter to develop switching signals of opposite phase. Full-wave synchronous detection is then

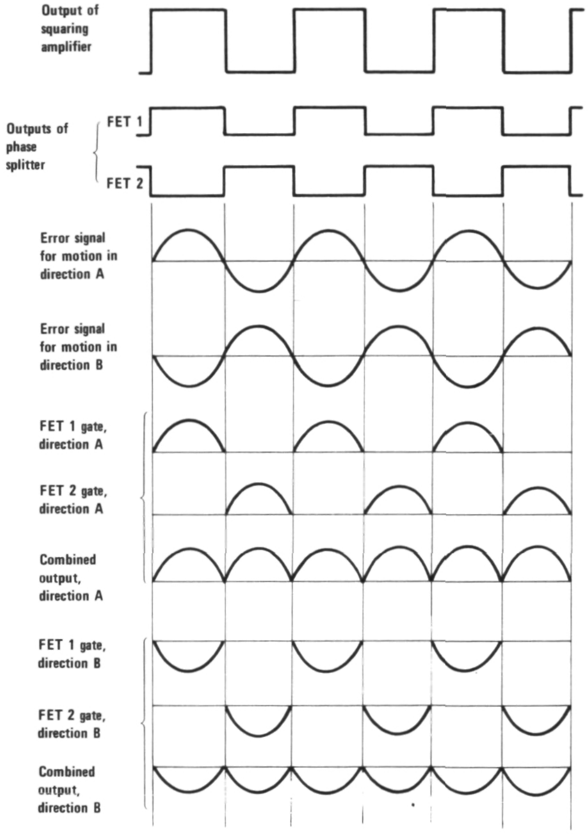

FIGURE 4.—Error detection process.

accomplished by applying these switching signals to two FET gates whose input is the error signal. Figure 4 illustrates how the half-wave rectified outputs from the two gates are combined by the differential amplifier to provide a full-wave detected output. Figure 4 also demonstrates that the polarity of the resulting detected output depends on the phase of the error signal.

The resulting error signal passes through the contacts of a relay to the input of an integrator. During normal operation, the mirror tracks a particular scene for a fixed number of degrees and then snaps back to track another scene. During the flyback interval, the error signal developed in the loop does not represent valid tracking data. Thus the relay contacts are opened during flyback to prevent the accumulation of erroneous data by the integrator. In the absence of an error signal, the integrator maintains a constant output and the tracking mirror is driven at a constant rate by this signal. Any error signal that develops due to scene drift results in a dc input to the integrator, and its output varies accordingly to compensate for the error.

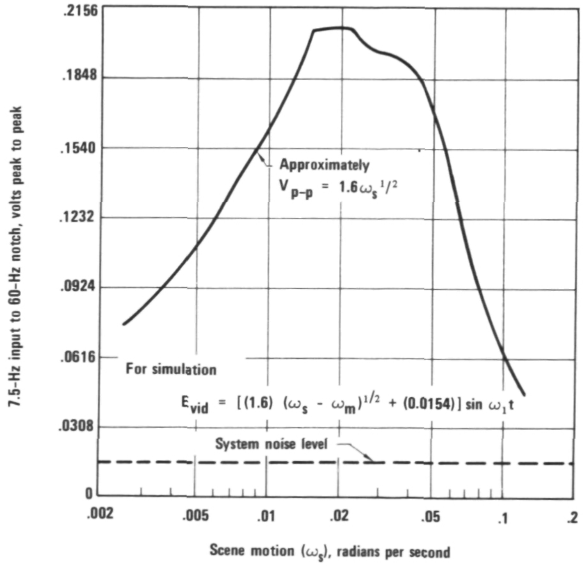

FIGURE 5.—Vidicon output at 7.5 Hz versus scene motion.

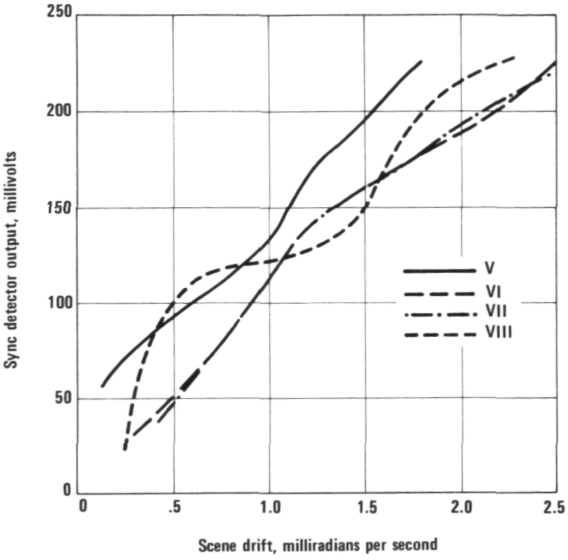

FIGURE 6.—Synchronous detector output versus scene motion for various loop gain settings.

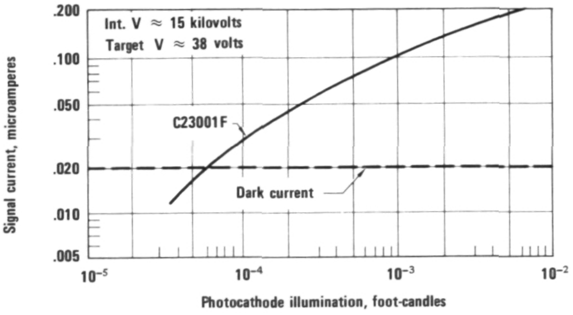

(a) C23001F

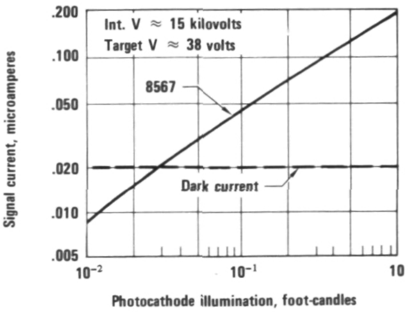

(b) 8567

FIGURE 7.—Vidicon illumination requirements.

Error Signal Characteristics

The 7.5-Hz component of the detected video output has the form indicated in figure 5. The measurements were made by locking the tracking mirror in a fixed position while allowing the scene simulator to move at known rates. The error voltage varies as the square root of the scene velocity up to about 0.015 radian per second. Beyond this point, the wobble plate cannot overcome the drift velocity at any time during its motion cycle. Thus the scene can never be brought to a stationary condition on the target of the vidicon. Further increases in scene velocity cause a rapid dropoff in developed error signal. As might be expected, the amplitude of the wobble has a significant effect on the shape of the error function.

Figure 6 indicates the dc error signal that exists at the output of the synchronous detector as a function of scene drift by the locked tracking mirror. The various forms indicated by the separate curves are caused by altering wobble amplitude, signal loop gain, and AGC loop gain.

PERFORMANCE

The system under discussion was designed to perform over the V/h range from 0.02 to 0.2 radian per second with an accuracy of 0.5 percent of the commanded rate. The unit meets these objectives for a wide variety of scenes. The operating illumination depends on the chosen vidicon, which in this case is an RCA 8567. Figure 7 indicates that a usable signal can be obtained down to about 0.1 foot-candle on the photocathode. Since the present unit utilizes an *f*/4.5 lens, this corresponds to a scene brightness of about 8 foot-lamberts. Considering a scene highlight reflectance of 25 percent, this corresponds to an illumination level of about 24 foot-candles. Reference to Figure 8 shows that this allows operation on a clear day down to about a 15° sun angle. Again with reference to figure 7, the addition of an intensifier stage before the 8567 tube, to make up the RCA model C12001F intensified vidicon, extends the luminous sensitivity by more than two orders of magnitude. The system can thus operate well into twilight, and possibly during

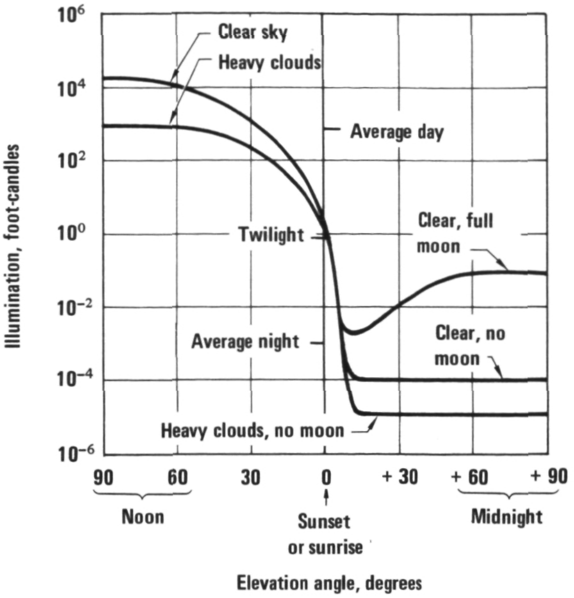

FIGURE 8.—Illumination levels versus elevation angles of sun and moon.

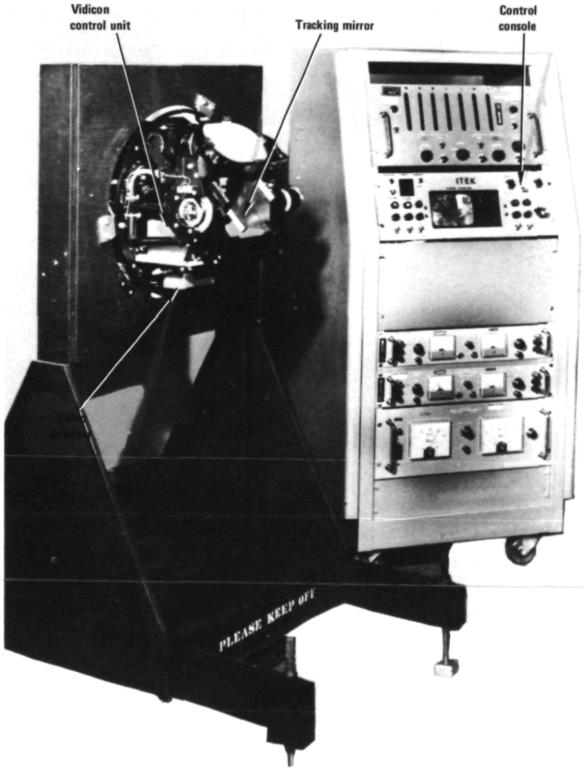

FIGURE 9.—V/h sensor and video display.

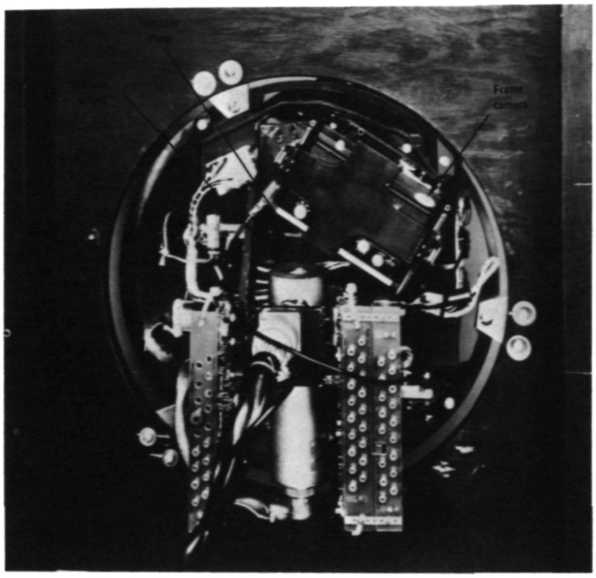

FIGURE 10.—V/h sensor, rear view.

clear full moonlight when the lunar elevation is greater than 60 degrees.

Scene contrast naturally places a boundary on system performance; the available contrast directly affects the amount of high frequency energy injected into the system. The goal for the present unit is 1.3:1.

Figures 9 and 10 illustrate the actual equipment. The complete V/h assembly weighs about 35 pounds and has been designed to interface with an Aeroflex AR–21 stabilized mount. The diameter of the mounting ring is 18 inches.

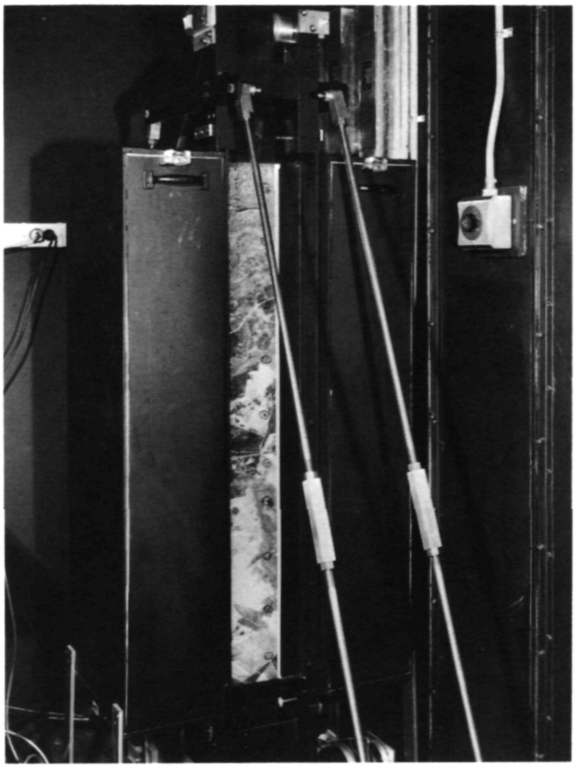

FIGURE 11.—Scene simulator.

The scene simulator, shown in figure 11, allows typical scene data to pass by the sensor at controlled light levels and velocity.

Page intentionally left blank

Page intentionally left blank

Session III

NEUTRALIZATION AND REMOVAL OF ATMOSPHERIC IMAGE DEGRADATIONS

JOSEPH W. GOODMAN, *Chairman*
Stanford University
Palo Alto, Calif.

SEEING AS CONSIDERED BY ASTRONOMERS*

ALFRED H. MIKESELL
U.S. Naval Observatory
Washington, D.C.

Despite average seeing motions or image dispersions on the order of at least 2 seconds of arc, the astronomer obtains astrometric precisions as great as 0.002 second of arc, at the cost of large bodies of data. Even such observing redundancy rarely if ever provides a view of image detail comparable to the diffraction limit of the equipment. Analog or digital procedures of deconvolution, based upon star images formed by the same telescope objective during the same viewing interval, might free data from seeing restrictions. A surprisingly large expenditure for new, easily-used equipment or procedures to provide such freedom is justified by the present cost of redundant data taking, digital deconvolution, and remote telescope sites (especially those outside the atmosphere). It is noted that some presently constructed telescopes not only are large enough to serve developmental routines, but also are fixed, using coelostats, as do laboratory devices.

The astronomer approaches the subject of seeing out of a need for many data which require large-aperture long-focus telescopes. He never has enough money for all he could undertake.

Think of his requirement for data; most of the 100 billion stars of the galaxy are fainter than the sun by more than five magnitudes, or 100 times. Only a few of these are close enough to appeal to observers of early programs who required significant or exciting results in a hurry. Yet sheer democracy indicates that astronomers should direct most of their attention to these faint objects. Large telescopes are required just to see them. For example, a 40-inch telescope is required to see comfortably a 15th magnitude star. About a 2-minute exposure is required for the star, with 100 millimicron bandwidth photography with a 50-inch effective aperture, and fair seeing; 30-minutes are required to expose adequately on an 18th magnitude star. Yet the solid background mess of the Palomar Sky Charts looks like 20th to 21st magnitude stars, some of which certainly are local, intrinsically faint, and important. Now, for these stars, as for all others, distances are basic data, and the most basic distance determination of a star is its trigonometric parallax, the annual shift in its look-direction when it is viewed from opposite sides of the earth's orbit. The first estimate of this shift must be relative, by comparison of the close star's position to that of a much more distant star. This looks like a simple problem—in only 6 months a moment or two looking at two stars yields a distance of a star. In a year, an observer should have the distances of the thousands of faint stars whose proper motions are so large they must either be close to the sun or they must be excitingly peculiar. Astronomers look, a bit plaintively, to modern practitioners of the communications sciences for ways to achieve this wonderful rate of data production.

These thousands of interesting, and mostly unexamined, stars appear fainter than 12.5

---

*This talk was presented as a tutorial study, in general terms, of the seeing problems facing observational ground-based astronomy. Any unreferenced numbers or quantities which it presents should be deemed exemplary only, representative of one astronomer's view of these problems.

magnitude. Let us pick a sample observing list of 15th-magnitude stars as representing unexplored stellar territory and obtain their parallactic shifts by photography. A developed photographic negative on glass is not a perfect registration of position; stochastic field distortions of the order of 1 micron are typical (refs. 1 and 2). Our interesting stars may have parallaxes of the order of 1/10th second of arc, and we should find these with a precision of 1 percent, or about ±0.001 second of arc. To make this angle equivalent to ±1 micron we must have a telescope scale of 1 second per millimeter, or telescope equivalent focus of about 8000 inches. This becomes impossible, because 15th-magnitude stars are distributed too far apart to provide very many which will serve as reference stars within a field of 5 minutes of arc, which would be as large a field as is currently afforded by manufacturers of plates and measuring machines. But seeing is not compatible with ±0.001 second of arc precision; in fact it is a worse problem than the plate.

At Mt. Wilson Observatory, 35 years ago, through a 4-inch telescope one could observe that with average seeing the image of a star was essentially perfect but moved about in an irregular manner in such a way that the center of the image remained inside a circle approximately 2 seconds of arc in diameter (ref. 3). Under these conditions of seeing the diameter of the smallest photographic star images provided by the 60-inch or 100-inch telescopes averaged 2 seconds of arc in diameter. This remains typical seeing distortion for the position astronomer who requires a precision about 1000 times smaller than the diameter of the images which will have to provide it. This is so whether they be the instantaneously formed images of a small telescope—and the central disk of the diffraction pattern of a star imaged by a 4-inch aperture is 2 seconds of arc in diameter—or the spatially or sequentially integrated image formed by a large telescope. Spatial integration implies the observed lack of coherence between the in-focus images formed by any two beams of

Hartmann test images in motion

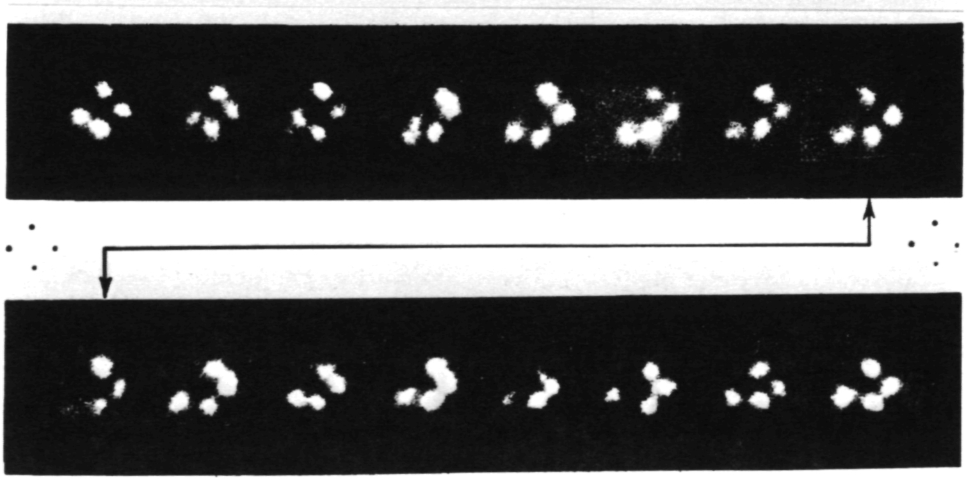

FIGURE 1.—The sequence of positive pictures is a 1-second of time strip from movies taken at the focus of a 40-inch f:7 telescope which was screened with a Hartmann diaphragm. The 4-inch holes were about 22 inches apart. Exposure time, about 1/40 second. The light-source: Sirius at about 10° altitude. Seeing at the zenith sometimes is this bad. Between the rows of Sirius pictures are two negative frames made with Arcturus as a source, near the zenith on a night of excellent seeing.

light from a single star, which are separated by more than a few inches. Incoherence can be shown by variations of instantaneous Hartmann test patterns (fig.1). These two forms of integration actually do provide the position astronomer with much of the precision he needs. Tests show that though star images may be as far apart as 20 minutes of arc in the telescope field, yet their images will appear identically formed by their simultaneous exposure through a single aperture of any practical size (ref. 4). This principle was recognized by H. H. Turner when he originated the first massive international project of astronomical photography, the astrographic catalog, but it was specifically examined and stated by Schlesinger in 1916 as he helped inaugurate the heyday of trigonometric parallaxes (ref. 5). It does not function when astrometric photography is attempted without sequential integration, as with photographic zenith tube observations for time and variation of latitude (ref. 6). And it does not provide precision as great as ±0.001 second of arc.

Hence the astronomer is forced to utilize redundancy in order to achieve precision, given his classical tools of large telescopes in the best site he is willing to travel to and seemingly unlimited patience. Thus, on account of seeing, his star images are so distorted that the 1-micron film distortion no longer seems so limiting and instead of an 8000-inch focus, a 600-inch focus becomes acceptable, and plate distortion alone contributes an error of about ±0.013 second of arc. Actually we observe that our measurements of two images on photographs made with a 61-inch (integrative aperture) f:10 telescope provide a mean error of ±0.024 second of arc, or ±1¾ microns. To achieve our required precision we now go redundant: 50 plates spread over five or more seasons, instead of two plates over one season. We undertake to use five reference stars instead of one. We make three exposures on each plate. (The whole subject of long-focus telescope astrometry has been recently reviewed (ref. 7).) Now for each star for which parallax is sought there must be 150 exposures and measurements of position of 900 star images. Quite a few plates must be repeated because the observer overestimated the quality of the seeing; maybe 200 exposures will be attempted. A pilot program of these 15th magnitude stars will show little about stars or equipment unless it includes at least 400 stars. About 360 000 star images must be located on about 20 000 plates. Not including the cost of the special telescope (fig. 2) and plate measuring comparator (2½ million dollars) we can estimate conservatively that these 400 parallaxes cost us about $100.00 a plate, or 2 million dollars. We reasonably argue that the program is scientifically worth this price, but we can speculate on the merit of spending half the cost to develop observing methods requiring only half the redundancy. At the very least, we toy with the merit of using the 60-inch McMath Solar Telescope of Kitt Peak, presumably free at night, which does provide an 8000-inch focal length and all our required precision, except where decreased by seeing effects.

Another similar use of redundancy was the determination by Markowitz of the presence of lunar tides in the solid crust of the earth. He used 35 000 star observations for latitude made on 2414 nights over 24 years, with the photographic zenith tube (ref. 8). Four exposures were required for each observation, and since Schlesinger's principle did not apply to these, at least half of the average mean error of ±0.190 second of arc for each observation may be charged to seeing. The remainder is large because of the relatively small scale, so that plate shifts of 1 micron represent at least ±0.045 second of arc, and probably much more considering the small plate size. Because the aperture is only 8 inches, and exposure 20 seconds instead of 2 minutes, both spatial and sequential integration of seeing effects would be less than for the parallax example. But the vast quantity of data fitted more accurately than usual a Gauss error curve and Markowitz could determine an effect of the moon on latitude, $\Delta\phi=[(0.0103\pm0.0017)\cos 2t]$ second of arc, where t is the hour angle of the moon, compared with a theoretically expected value of $(0.0090 \cos 2t)$ second of arc.

The foregoing examples of astronomical problems, wherein the effects of seeing can

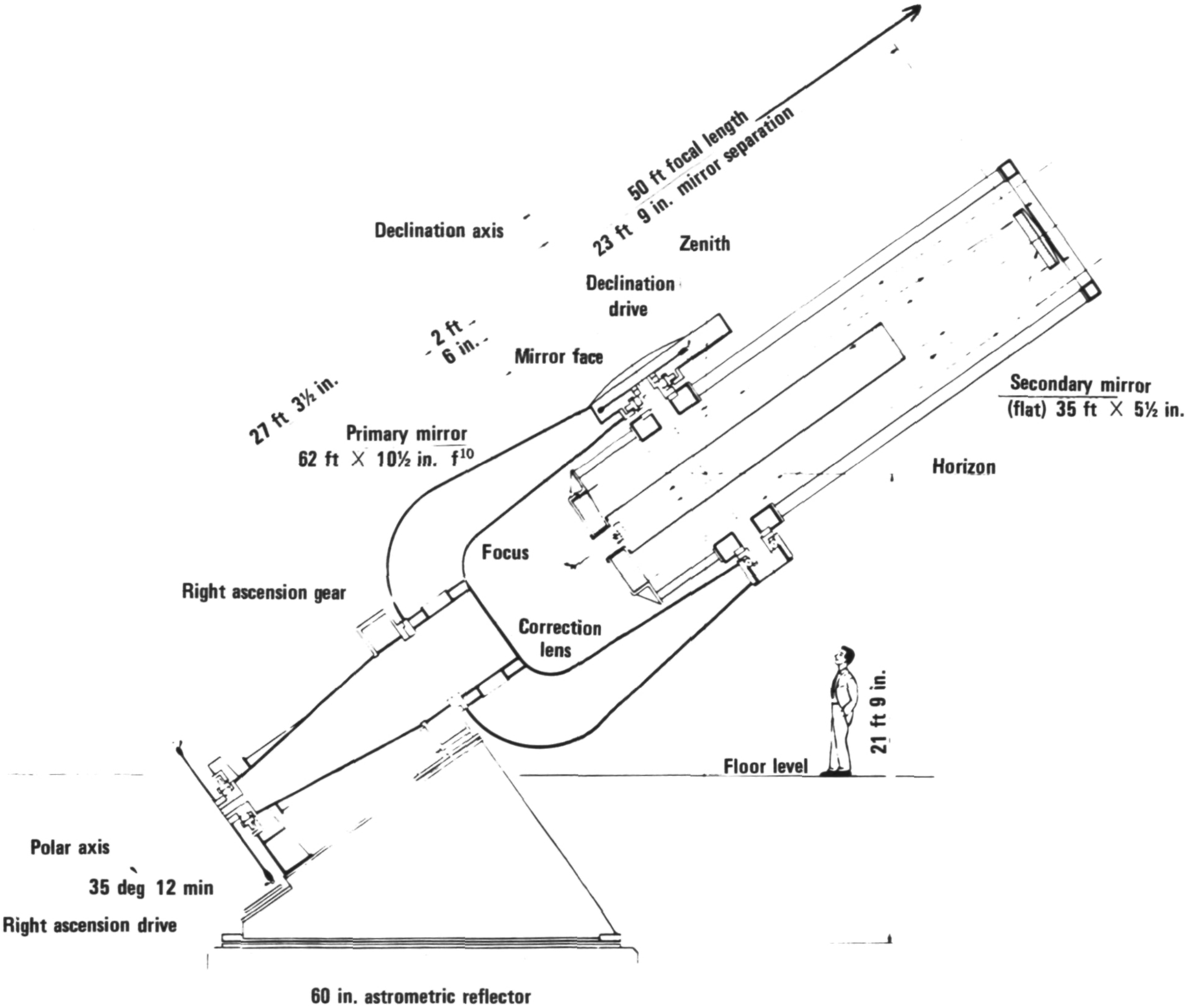

FIGURE 2.—A 61-inch reflector designed especially to meet pressing needs of astrometry of faint stars (24). This is a folded prime focus *f*:10 camera which yields good images over a 10-minute uncorrected field. The flat secondary mirror serves as a large central stop which reduces light-gathering power of the system to that of a 50-inch system, but which does not seriously enlarge images, relative to seeing effects.

be surmounted by means of redundancy and patience, contrast with the large collection of problems where the effect of seeing is to limit definition so as to make impossible any attempt of obtaining the required information. The problem exceeds the recovery of information from noise; it is the recovery of an unknown modulation pattern from the midst of the result of subsequent modulation supplied by the stochastic pattern of seeing and the rarely known or constant pattern of performance of telescope and receiver. (Operation of long-focus telescopes is discussed in many places, e.g., references 9 and 10.) Simple redundancy has been attempted, to little advantage. The limit of 2 seconds of arc definition cited above, represents 2½ miles on the face of the moon, or over ⅒th the diameter of Mars at a close opposition. In an attempt to achieve some reasonable approximation of the diffraction limited view of such objects, hundreds of thousands of observations of each have been made in hopes that sometime there will be an instant when all the column of air before the telescope will be perfectly steady. Eye-observers report interesting experiences, such as the morning when Kuiper saw Venus through the 84-inch to be covered with well-defined sharp cloudy patches or cells. Janssen obtained a photograph in 1885 which may be one of the best photographs of solar granulation in existence, not neglecting consideration of the pictures provided by balloon flights (refs. 11 and 12). These and the many reports of visual observers still must be deemed exceptional, if only out of consideration of the time spent looking for the perfect observing moments. Because of seeing, few of the photographs taken in the routinely long series of exposures on planetary objects provide sharp definition for even small portions of the planet, let alone the whole disc. (My standards require a good approximation of the diffraction limit). We are not concerned with gross image motion which readily can be offset, even when it is represented by frequencies as high as 10 or 20 hertz (for examples, see refs. 13 and 14). We are concerned instead by the distortions of the wavefront of light from a point source, incident on a large objective (as represented by focograms of schlieren patterns in starlight (refs. 15 and 16) as shown in fig. 3).

In place of redundancy, astronomers must look to more imaginative techniques, such as autocorrelation. One demonstration of this is the reversal of the customary practice in photographing the moon. Instead of shorter and shorter exposures on faster and faster negative material, use very long exposures on very slow, high resolution, material. Fast material processes with large grains, short scale—intrinsically low information content in the presence of low *S/N*. The slow emulsion, while on development it may appear almost clear, can prove to have a very long scale, 10^5 or more, with intrinsically high information content in the presence of high *S/N*. What may be the best lunar photograph ever taken from the ground, was produced on an Eastman 649–F plate by the 61-inch reflector on a night when it was in particularly good adjustment. This pragmatic method of separating information

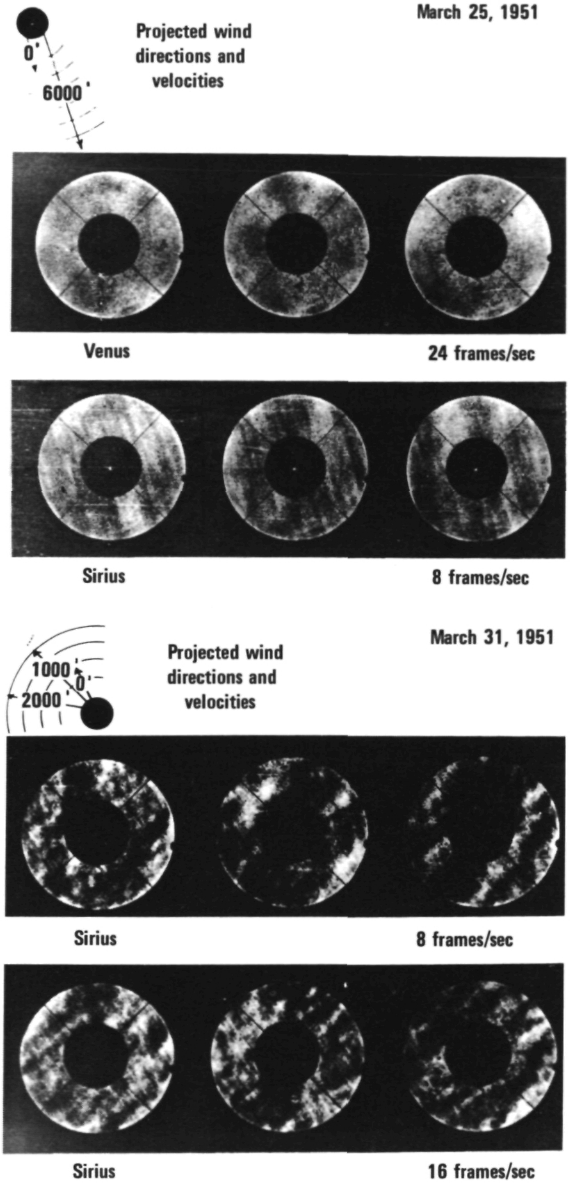

FIGURE 3.—Shadows in light focussed by the 40-inch reflector on the movie camera. Exposure at 8 frames per second was about 1/20 second; others, proportional. The higher velocity winds aloft on March 25 caused shadows in light of Sirius to appear as streaks. The Venus shadows represent the integrative effect of light from an extended surface. Even so, note how transient the patterns appear on these consecutive frames.

from background smear with the linear transfer characteristic of a long-scale negative has not been well exercised because good automatic tracking of the telescope throughout the long exposure is essential. Otherwise the astronomer need change his technique only slightly, to utilize the very thin negatives.

Many applications of electronics have gone onto telescopes, effectively to use autocorrelation to improve image definition or information yield, despite seeing. One of these is an extension of the foregoing but was, actually, the means of discovering the value of the long-scale emulsion (ref. 17). This is the electronographic camera which uses the photographic emulsion in the same evacuated container as a photocathode. It records on the emulsion, in the time storing manner of any photograph, the images produced by the accelerated and focussed photoelectrons from the cathode. Slowness of high resolution emulsions is offset by high quantum efficiency of the photocathode, so that a linear density range (no observed threshold) of 10^6 to 1 still is associated with comfortable speed (ref. 18). In another system, a small area of the image plane is swept optically by a slit or small aperture, usually by swinging a mirror (ref. 19). Light passing the aperture is imaged on a phototube whose signal may be recorded on an oscilloscope. The oscilloscope sweep is synchronized with the scanning system, and the signal may be developed by electronic auto-correlation methods. This scheme has been applied to observing eclipses of Mars satellites by Mars, for the purpose of detecting the Martian atmosphere. Of course, at much greater expense the same data might be recorded and analyzed digitally.

One other recent application of both electronics and correlation, which also uses the statistics of large numbers like the redundant attacks on seeing, is Høg's photoelectric meridian-transit telescope (ref. 20). For this the image of a star or other objects moves at what is, except for seeing, uniform speed across a precisely formed grid. Instead of forming an analog equivalence to the time-spread light pattern, Høg accumulates a digital record of the total light passed in a time sequence by the grid and compares the steps of buildup with the steps which should occur were no seeing distortion present. The reductions of these observations can be construed as a deconvolution process (ref. 21).

Deconvolution is so far applied by astronomers only to a correction of object profile for effects of the instrumental blurring function. We have examples where this has been done at great effort, by dividing a field into 1/10-micron square zones and correcting the observed density of the image in each zone. A simpler project has been reported by Kron, of the profile of a distant globular cluster, Baade 282, in the Andromeda Nebula (ref. 18). The cluster profile differs markedly from that of a nearby field star, whose measured profile provided the instrumental profile or blurring function.

A much more complicated blurring function than a symmetrical diffraction pattern can be derived by detailed analysis of an adjacent field star (e.g., the wavefront pattern represented by fig. 3), and correction undertaken of each point in the image of the object of interest—for example, Mars—for seeing, relying on Schlesinger's principle (ref. 5). To the astronomer, the cost of this is so prohibitive that no one, as far as I know, has undertaken it. Furthermore, the psychology of the astronomer leads him to search for corrections to the image before it finally is recorded. Poor image definition, he argues, is due to deformation of the wavefront incident upon the telescope objective. Therefore it should instantaneously be made good by counter deformation of the objective (ref. 22). This might, of course, be made by a correcting plate appropriately located in the light path, or by deformation of a plastic speculum. The Eidophor system operates by deforming an oil surface with electrostatic charges, controlled by television receiver electronics, so that light of almost any useful intensity can be gated to project full color scenes upon a large screen. The various researches in scintillation, such as those cited earlier (ref. 17) or those made with two telescopes (ref. 23), all suggest that average seeing occurs with little change of wavefront of incident light during periods of about 1/100 second of arc to, at best, 1/10 second of arc. Present television technology might be able to maintain a constantly deformed surface of useful size (such as 10-inch aperture) with time lag no greater than those, provided a sufficiently bright stellar source could be located in the field of interest. This requirement for large control signal almost certainly means that the first attempt to apply one of these correction schemes will be to a large telescope, with correction of only a very small portion, perhaps an inch, of the image plane. At such small size a television correction scheme such as suggested for counteracting image motion (ref. 13), combined with signal detail sensing, may prove adequate to introduce the new era of astronomy.

REFERENCES

1. STRAND, K. AA.: Accomplishments and Reliability of Trigonometric Parallaxes. Astron. J., vol. 63, 1958, p. 153.
2. GOLLNOW, H.; AND HAGEMANN, G.: Displacements of Photographic Emulsions and a Method of Processing to Minimize this Effect. Astron. J., vol. 61, 1956, pp. 399–404.
3. ANDERSON, J. A.: Astronomical Seeing. J. Opt. Soc. Am., vol. 25, 1935, p. 152.
4. HOSFELD, R.: Comparisons of Stellar Scintillation with Image Motion. J. Opt. Soc. Am., vol. 44, 1954, 284–288.
5. SCHLESINGER, F.: Irregularities in Atmospheric Refraction. Publ. Allegheny Obs., vol. 3, 1916, pp. 1–10.
6. MARKOWITZ, W.: The Photographic Zenith Tube and the Dual-Rate Moon Position Camera. Telescopes, Kuiper and Middlehurst, eds., University of Chicago Press, 1960, pp. 88–114.
7. VAN DE KAMP, P.: Astrometry with Long-focus Telescopes. Astronomical Techniques, Hiltner, ed., University of Chicago Press, 1962, pp. 487–536.
8. MARKOWITZ, W.; AND BESTUL, S. M.: Effect of the Moon in the Determination of Latitude at Washington. Astron. J., vol. 49, 1941, pp. 81–86.
9. BAKER, J. G.: Planetary Telescopes. Appl. Opt., vol. 2, 1963, pp. 111–129.
10. IANNA, P. A.: On Aberrations and Field Errors. Vistas in Astronomy 6, Beer, ed., Pergamon Press, 1965, pp. 93–123.
11. JANSSEN, J.: Ann. Obs. Paris, Meudon 1, Plate 10, 1896. Reproduced in The Sun, Kuiper, ed., University of Chicago Press, 1953, p. 340.
12. SCHWARZSCHILD, M.; AND SCHWARZSCHILD, B.: Balloon Astronomy. Sci. Am., vol. 200, no. 5, May 1959, pp. 52–59.
13. DEWITT, J. H.; HARDIE, R. H.; AND SEYFERT, C. K.: A Seeing Compensator Employing Television Techniques. Sky and Telescope, vol. 17, no. 1, Nov. 1957.
14. LEIGHTON, R. B.: Sharper Planetary Photography with the 60-inch. Sci. Am., vol. 194, no. 6, June 1956, pp. 157–166.
15. GAVIOLA, E.: On Seeing, Fine Structure of Stellar Images, and Inversion Layer Spectra. Astron. J., vol. 54, 1949, pp. 155–161.
16. HOSFELD, R.: Scintillation, Stellar Shadow Bands and Winds Aloft. (abstract), Astron. J., vol. 60, 1955, p. 164.
17. ABLES, H. D.; AND KRON, G. E.: The Linearity and Information Gain of an Electronic Camera. Publ. Astr. Soc. Pacific, vol. 79, pp. 423–424.
18. KRON, G. E.: A Technical Description of the Construction, Function and Application of the U.S. Navy Electronic Camera. To be published in the Proceedings of the Fourth Symposium on Photoelectric Image Devices, Advances in Electronics and Electron Physics, vol. 30, Academic Press, 1969.
19. RAKOSCH, K. D.: Photoelectric Area Scanner. Appl. Opt., vol. 4, 1965, pp. 1453–1455.
20. HØG, E.: A Photoelectric Meridian Circle. Astron. Abhand. Hamburger Sternwarte, vol. 5, 1962, pp. 263–272.
21. BRACEWELL, R. N.: The Fourier Transform and its Application. McGraw-Hill Book Company, 1965, p. 30.
22. BABCOCK, H. W.: The Possibility of Compensating Astronomical Seeing. Publ. Astr. Soc. Pacific, vol. 65, 1953, pp. 229–236.
23. BARNHART, P. E.; PROTHEROE, W. M.; AND GALLI, J.: Direct Observation of Element Motion in Stellar Shadow Patterns. J. Opt. Soc. Am., vol. 46, 1956, p. 904.
24. STRAND, K. AA.: The 60-Inch (152 cm.) Astrometric Reflector of the U. S. Naval Observatory. Appl. Opt., vol. 2, 1963, pp. 1–7.

Page intentionally left blank

DIGITAL COMPUTER ANALYSIS OF LINEAR SHIFT-VARIANT SYSTEMS

THOMAS S. HUANG
Massachusetts Institute of Technology
Cambridge, Mass.

We discuss here the problem of how often we should sample in analyzing linear shift-variant systems on a digital computer, and also the problem of whether it would be faster to perform the analysis via the frequency domain rather than directly in the spatial domain. Fourier analysis provides partial answers to the first problem. In particular, it can be used to find sufficient sampling rates. The analysis can be done faster, however, directly in the spatial domain rather than via the frequency domain.

Let $f(x, y)$ be the intensity of the ideal image at point (x, y), and let this image be degraded by a linear shift-variant system with an impluse response $h(x, y; \alpha, \beta)$. The degraded image is

$$g(x, y)=\iint_{-\infty}^{\infty} d\alpha d\beta f(\alpha, \beta) h(\alpha, \beta; x-\alpha, y-\beta) \quad (1)$$

This would be the case, for example, when the image is blurred by rotational motion, or when the image is obtained through certain aberrating media. If we ignore the noise problem, a direct way of getting the ideal image, f, back from the degraded image, g, and the degrading impulse response, h, is to digitalize equation (1) into a set of linear algebraic equations, and then to solve this set of equations for the samples of f. The solution, of course, is not always unique.

When analyzing equation (1) on a digital computer (either when we want to simulate the degrading system to see its effect on the image or when we want to recover the ideal image from the degraded image), the first question is, how often should we sample f, g, and h so that we shall get meaningful results? We shall try to provide partial answers to this question via Fourier analysis.

The use of Fourier analysis in analyzing linear shift-invariant systems is well known. As we shall see, its use can also provide much insight into linear shift-variant systems. Other approaches to analyzing linear shift-variant systems have been discussed by Lohmann and Paris (ref. 1) and by Cutrona (ref. 2).

MATHEMATICAL FORMULATION

For the sake of simplicity, we consider the one-dimensional case of equation (1):

$$g(t)=\int_{-\infty}^{\infty} d\beta f(\beta) h(\beta, t-\beta) \quad (2)$$

where $h(\beta, t-\beta)$ = output at t caused by an input impulse at β.

Let the Fourier transforms of $f(t)$, $g(t)$, and $h(t, \tau)$ be $F(u)$, $G(u)$, and $H(u, v)$, respectively. Let

$$f_1(x, y)=\delta(x+y) f(y)$$

where δ is the Dirac delta function. The Fourier transform of $f_1(x, y)$ is

$$F_1(u, v)=F(-u+v) \quad (3)$$

Let

$$G_1(u, v) = F_1(u, v)\ H(u, v) \tag{4}$$

and

$$G(v) = \int_{-\infty}^{\infty} G_1(u, v)\ du \tag{5}$$

Then the inverse Fourier transform of $G(v)$ is $g(t)$.

GRAPHICAL INTERPRETATION

Assume that $f(t)$ is bandlimited and has a bandwidth $2A$, that is, $F(u)=0$ for $|u|>A$, as shown in figure 1(a). Then $F_1(u, v)=F(-u+v)$ is zero outside an infinite strip bounded by the straight lines $-u+v=\pm A$, as shown in figure 1(b). Now, if $H(u, v)$ is zero outside the shaded region of figure 2(a), then $G_1(u, v)=F_1(u, v)$ $H(u, v)$ is zero outside the intersection of this region and the infinite strip, as shown in figure 2(b). Integrating $G_1(u, v)$ along the straight line $v=v_0$ gives $G(v_0)$ whose inverse Fourier transform is $g(t)$. Therefore the bandwidth of $g(t)$ is equal to the vertical extent of the shaded region of figure 2(b), namely $2D$.

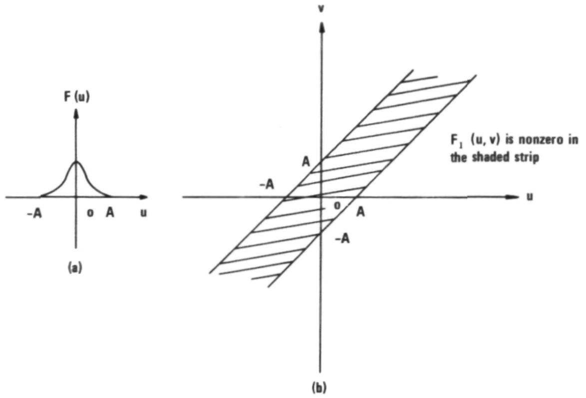

FIGURE 1.—(a) $F\ (u)$ and (b) $F_1\ (u, v)$.

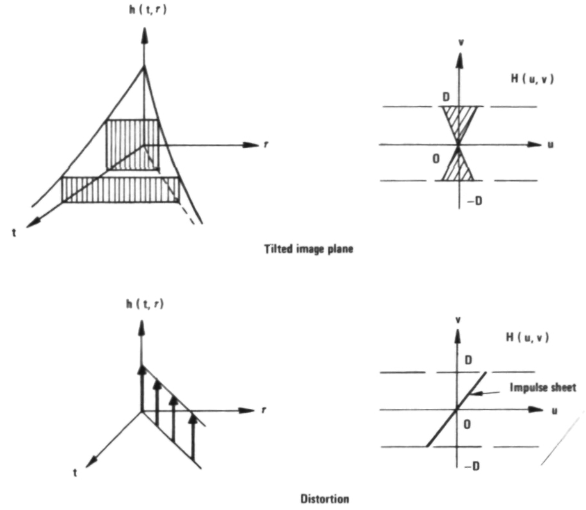

FIGURE 3.—$H\ (u,\ v)$ for aberrating cylindrical lenses.

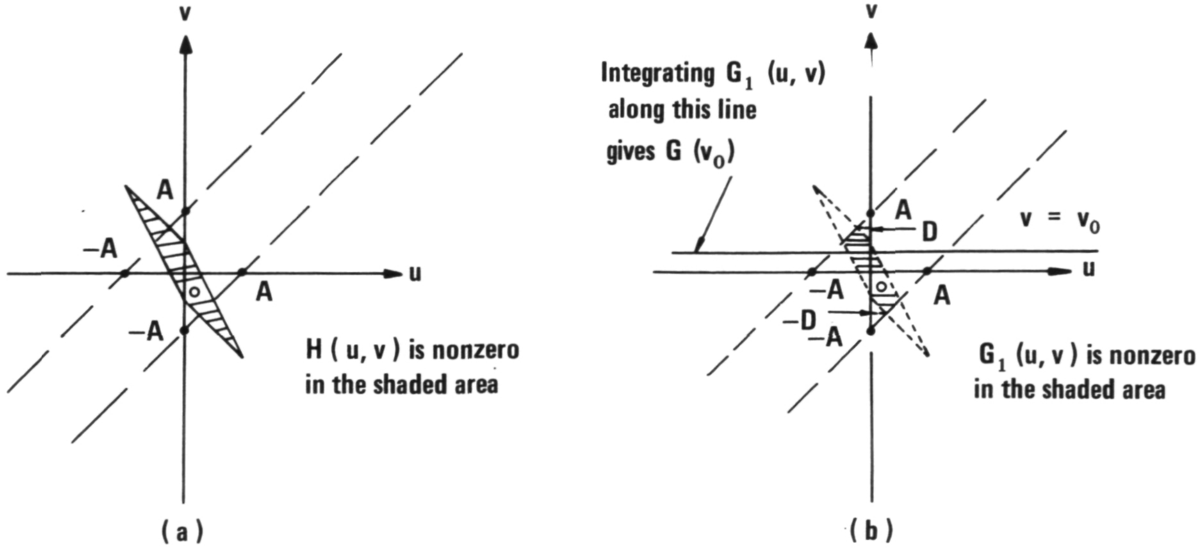

FIGURE 2.—(a) $H\ (u,\ v)$ and (b) $G_1\ (u,\ v)$.

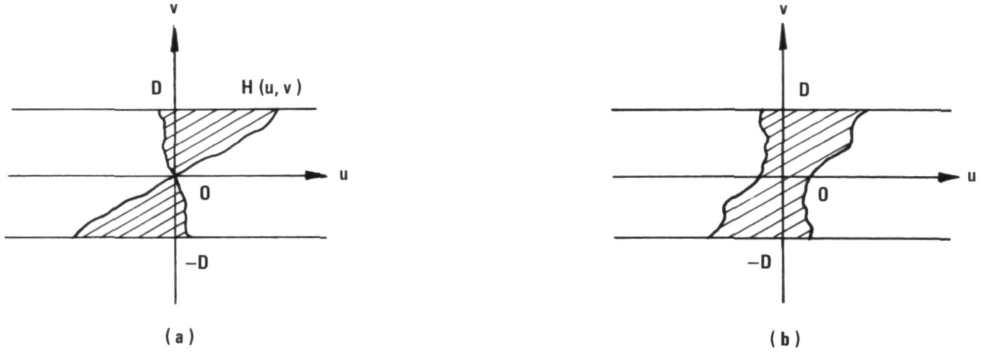

FIGURE 4.—H (u, v) for a general aberrating cylindrical lens. (a) Area of impulse response independent of position of input impulse. (b) Area of impulse response not constant.

Some examples of $H(u, v)$ for aberrating cylindrical lenses are shown in figures 3 and 4. The vertical extent $(2D)$ is limited by the finite aperture size. Notice that for a linear shift-invariant system, $H(u, v)$ will be an impulse sheet on the v axis. For a linear shift-variant system, roughly speaking, the vertical spread of $H(u, v)$ indicates the frequency response of the system, while the horizontal spread indicates the degree to which the system is shift-variant.

DETERMINATION OF SAMPLING RATE

Now let us sample $f(t)$ and $h(t, \tau)$ with sampling periods T, and $T \times T$, respectively, to get $f^*(t)$ and $h^*(t, \tau)$. The Fourier transforms of these latter functions, $F^*(u)$, and $H^*(u, v)$, consist of periodically repeated versions of $F(u)$ and $H(u, v)$, respectively. Let

$$F_1^*(u, v) = F^*(-u+v) \tag{6}$$

$$G_1^*(u, v) = F_1^*(u, v) H^*(u, v) \tag{7}$$

and

$$G^*(v) = \int_{-\infty}^{\infty} G_1^*(u, v)\, du \tag{8}$$

Equation (7) is illustrated graphically in figure 5.

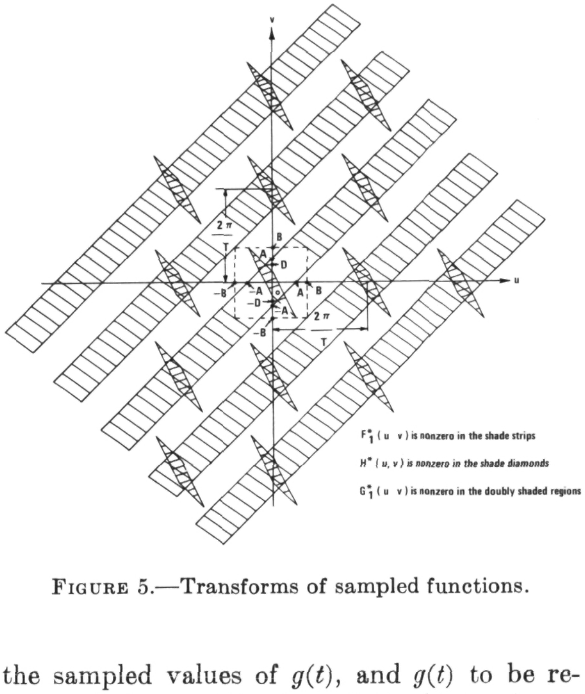

FIGURE 5.—Transforms of sampled functions.

A sketch such as figure 5 is a convenient way of determining the sampling rate when we perform equation (2) on a digital computer. If we want the calculated values $g^*(t)$ to be equal to the sampled values of $g(t)$, and $g(t)$ to be recoverable from $g^*(t)$, then T should be chosen small enough so that $G_1^*(u, v)$ consists of nonoverlapping periodically repeated versions of $G_1(u, v)$. Let the bandwidth of $f(t)$ be $2T$, and let the size of the smallest square which encloses the nonzero region of $H(u, v)$ in the u–v plane be $2B \times 2B$. Then one might think that it is sufficient to choose $T = \pi/C$ where $C = \text{Max}(A, B)$. Not so. For example, if we let $2\pi/T = 2B$ in figure 5, then $G_1^*(u, v)$ will contain extraneous components in addition to periodically repeated versions of $G_1(u, v)$ (fig. 6).

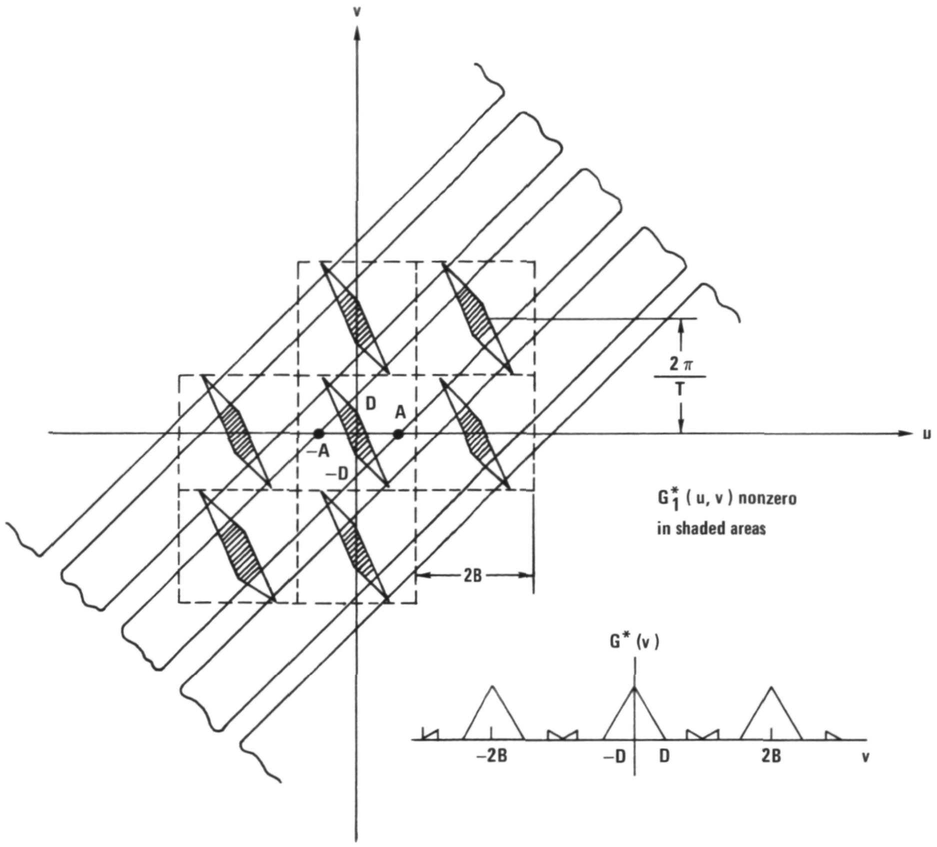

FIGURE 6.—Insufficient sampling rate for getting exact samples.

If we do not require that $g^*(t)$ be equal to the sampled values of $g(t)$, but only require that $g(t)$ be recoverable from $g^*(t)$, then T should be chosen small enough so that $G^*(v)=G(v)$, wherever $G(v)$ is nonzero. This can be achieved by requiring that in the strip bounded by $v=\pm D$ in the u–v plane, $G^*{}_1(u,v)$ consists of only nonoverlapping periodically repeated versions of $G_1(u,v)$. For the example in figure 5, it is sufficient to chose $2\pi/T=A+B$. Since in this example $A<B$, it is also sufficient to choose $2\pi/T=2B$. For some other $H(u,v)$, however, this sampling rate is not sufficient for recovering $g(t)$ (fig. 7).

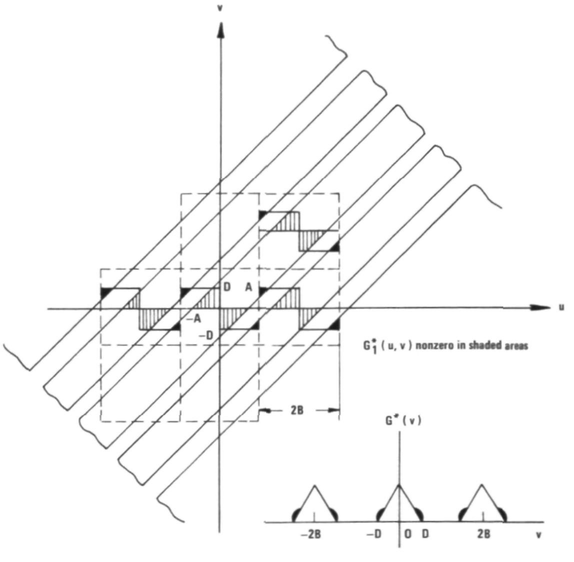

FIGURE 7.—Insufficient sampling rate for recovering $g(t)$.

To require that $g^*(t)$ be equal to the sampled values of $g(t)$ obviously demands a higher sampling rate than to require only that $g(t)$ be recoverable from $g^*(t)$. The former is probably more convenient, however, since in the latter case, complicated interpolation (lowpass filtering) may be needed to obtain sampled values of $g(t)$ from $g^*(t)$. (In the former approach, the sampling rate can be reduced, if we modify $h(t,\tau)$ by setting the value of $H(u,v)$ to zero for all (u,v) not lying in the infinite strip determined by the bandwidth of $f(t)$.)

It is easy to find sufficient (but not necessary) sampling rates. Let f be bandlimited to A cycles per unit length, and h to B cycles per unit length in either dimension. Assume that we want $g^*(t)$ to be equal to the sampled values of $g(t)$. Then if $2B<A$, it is sufficient to sample the functions at a sampling period $\frac{1}{2}A$, while if $2B>A$, it is sufficient to sample at a period $1/(A+2B)$ (fig. 8).

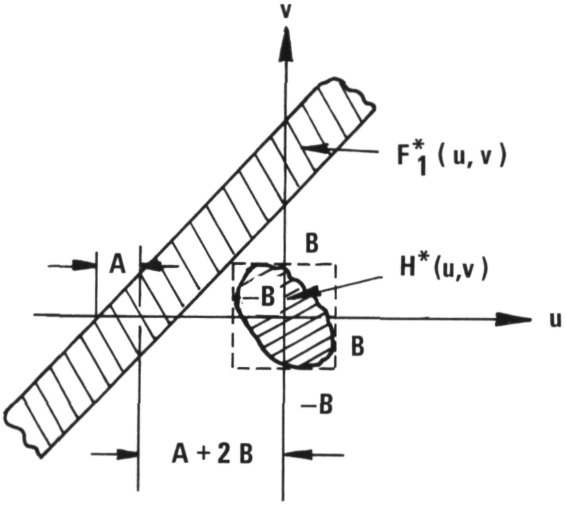

FIGURE 8.—Sufficient sampling rate for getting exact samples.

SPATIAL VERSUS FREQUENCY DOMAIN CALCULATION

Let the number of samples in $f(t)$ be N, and that in $h(t,\tau)$ be Nm, where $m<<N$. To obtain the N samples of $g(t)$ by convolution in the spatial domain, as indicated in equation (2), requires approximately Nm multiplications and additions. We can also get $g(t)$ by frequency-domain calculation, using equations (2) through (5). In this approach, however, to take the Fourier transform of $h(t,\tau)$ alone requires $2Nm \log_2 Nm$ multiplications and additions, under the assumption that we employ the Cooley-Tukey algorithm (ref. 3). Therefore it is more time-consuming than the spatial-domain approach.

ACKNOWLEDGMENT

This work was supported principally by the National Institutes of Health (Grants 1 PO1 GM–14940–02 and 5 PO1 GM–15006–02), and in part by the Joint Services Electronics Program (Contract DA28–043–AMC–02536 (E)).

REFERENCES

1. LOHMANN, A. W.; and PARIS, D. P.: Space-Variant Image Formation. J. Opt. Soc. Am., vol. 55, no. 8, Aug. 1965, pp. 1007–1013.
2. CUTRONA, L. J.: Recent Developments in Coherent Optical Technology. Optical and Electro-optical Information Processing, J. T. Tippett et al., eds., The M.I.T. Press, Cambridge, Mass., 1965, pp. 120–122.
3. COOLEY, J. W.; and TUKEY, J. W.: An Algorithm for the Machine Calculation of Complex Fourier Series. Math. Comput., vol. 19, Apr. 1965, pp. 297–301.

Page intentionally left blank

Page intentionally left blank

USE OF A LARGE-APERTURE OPTICAL SYSTEM AS A TRIPLE INTERFEROMETER FOR REMOVAL OF ATMOSPHERIC IMAGE DEGRADATIONS

JOSEPH W. GOODMAN
Stanford University
Palo Alto, Calif.

A new method for image restoration is discussed, based on an interferometric technique first proposed by Jennison. This method is accomplished by inserting a movable mask in the optical system to remove the redundancy normally present, and by inserting a beam-splitting arrangement which allows the formation of three separate images. By properly combining the phases of various spatial frequency components of the three images, a composite image with the correct phases may be constructed. No information concerning the point-spread function of the atmosphere is required.

The chief difficulties associated with this technique are (1) its extremely low detection sensitivity, due to the fact that redundancy has been eliminated, (2) the requirement that the object be motionless while the images are recorded, and (3) the requirement that the object lie within a single isoplanatic region of the atmospheric inhomogeneities.

Turbulence and the associated atmospheric inhomogeneities provide the prime limitation to the resolution achieved by any large imaging system operating within the earth's atmosphere. A diffraction limited system with a sizable collecting aperture will seldom achieve a resolution better than that associated with the diffraction limit of a 10-cm aperture, the larger aperture area serving only to collect more light. Resolutions better than 1 second of arc are rare for both horizontal and vertical paths through the atmosphere.

Recently, considerable interest has arisen in the use of processing techniques (refs. 1 and 2) to remove atmospheric degradations and thereby to allow considerable improvement of resolution achieved by systems operating within the earth's atmosphere. Unfortunately, the majority of these processing techniques require some knowledge of the point-spread function associated with the atmospheric aberrations if successful image restoration is to be achieved. Only in rare cases is such knowledge available.

We discuss here a new image processing technique which offers the potential of restoring atmospherically degraded images without any knowledge required of the detailed point-spread function of the atmosphere. The technique, which applies to self-luminous or incoherently illuminated objects, rests on interferometric principles first elucidated by the radio astronomer R. C. Jennison (ref. 3) and later brought to the attention of the optics community by D. H. Rogstad (ref. 4).

EFFECTS OF ATMOSPHERIC INHOMOGENEITIES

To understand the basic principles of this technique, it is first necessary to appreciate the particular effects of the atmosphere on a wavefront originating from a distant point source of light. What would normally be a perfect spherical wavefront diverging from the point-source becomes an aberrated and distorted wavefront due to passage through the atmospheric inhomogeneities. For vertical viewing of astronomical objects, the phase distortions of the wavefront are typically correlated over a linear dimension of 10 cm, and approximately uncorrelated for larger separations.

For a moment we consider the effects of the atmosphere on the portion of the wavefront striking an aperture of size 10 cm or less. Four different effects of the atmosphere can be specified:

(1) There is a distortion of the wavefront, which for such a small aperture would often amount to a quadratic phase error, or equivalently a focusing error. For apertures of 10 cm or less, this effect is second-order by comparison with the other effects to follow.

(2) A random tilt of the entire wavefront results in a shift of the position of the image of the point source. Under typical conditions this random shift would have an rms value of 1 second of arc. Since the diffraction limit of a 10-cm aperture (at 5000Å wavelength) is about 1 second of arc, we see that for apertures somewhat smaller than 10 cm the amount of image jitter is negligible by comparison with the diffraction spreading of the image.

(3) A uniform but random advance or retardation of the segment of the wavefront as a whole, corresponds to a differential delay caused by variations of the optical path-length through the atmosphere. Thus the entire wavefront striking an aperture of size 10 cm or less may be delayed or advanced by the atmosphere, with a typical rms phase delay being several times 2π radians.

(4) Atmospherically induced scintillations of the intensity of the light striking the aperture are experienced.

For an aperture of size somewhat less than 10 cm, effects (1) and (2) are negligible, and the primary effects of the atmosphere are the random phase delays (3) and the random intensity scintillations (4). If that aperture alone were to be used to form the image, the random phase delays would not be of concern. However, in the technique we propose here it will be desired to use a single large-aperture system as a collection of several small-aperture systems, and differential delays will consequently be important.

USE OF A LARGE-APERTURE SYSTEM AS AN INTERFEROMETER

As further background material pertinent to the technique to be proposed here, consider the optical imaging system of figure 1(a). In this case a limiting mask is placed in the converging cone of rays produced by a large-aperture optical system. Under the conditions of interest here, the presence of this mask is entirely equivalent to the presence of a larger mask directly against the face of the large collecting aperture. Placement of the real mask behind the aperture is solely for the reason of physical convenience, since the mask can then be smaller than the full aperture. The mask of interest here initially is shown in figure 1(b)—it consists of two small, separated, circular apertures, each of diameter less than 10 cm. In the absence of atmospheric effects, the modulation transfer function of the imaging system (with the mask in place) is as shown in figure 1(c). Thus, aside from the very low frequency passband corresponding to frequencies resolvable by the individual apertures, only spatial frequencies in the vicinity of

$$f_0=\frac{\ell'}{\lambda z}$$

where ℓ' is the separation of projected pupils, λ is the wavelength, and z is the focal length, appear in the final image. Note that the full range of spatial frequencies covered by the unobstructed aperture can be built up by time-exposing the film with the two smaller apertures sequentially rotated, and their separation sequentially decreased and increased, such that the entire range of spatial frequencies covered by the unobstructed aperture is detected by the modified optical system. (The reason for placing such a mask in the system is discussed subsequently.)

Now consider the effects of the atmosphere on this system when the limiting mask is in place. Since the diameters of the small projected

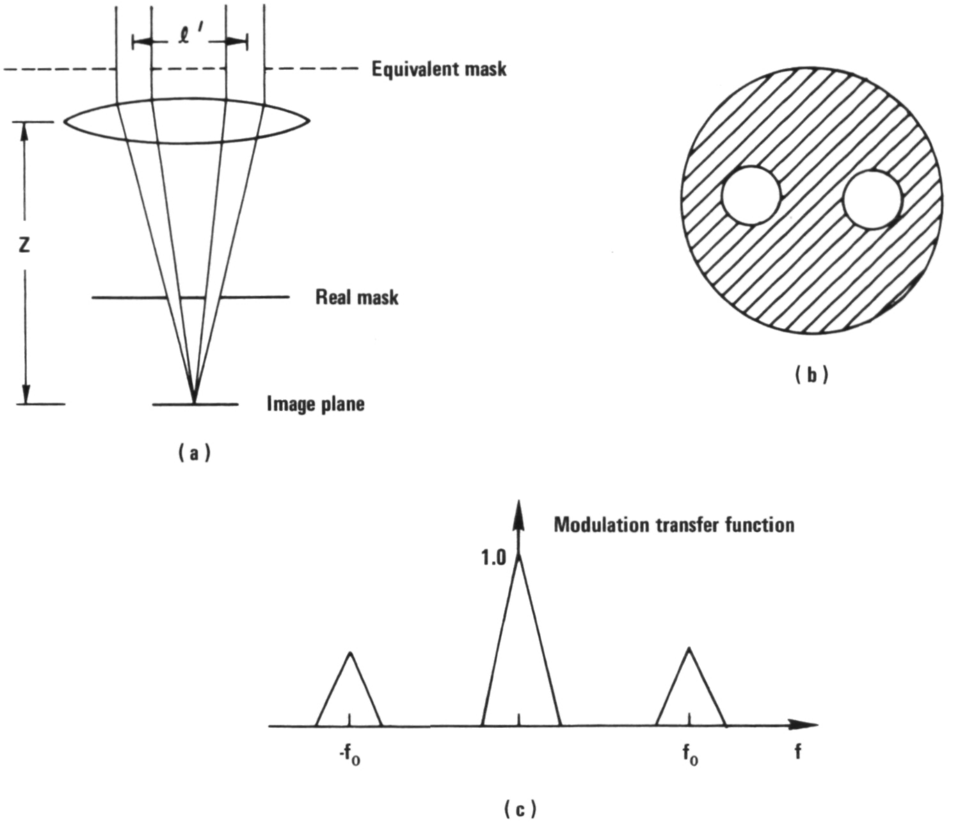

FIGURE 1.—(a) Imaging system operates as a two-element interferometer. (b) The mask inserted in the converging cone of rays. (c) Modulation transfer function of the imaging system.

apertures are less than 10 cm, the primary effect of the atmosphere is a shift of the phase of the frequency component at f_0 to

$$\psi' = \psi + \Phi$$

where ψ' is the measured phase, ψ is the true phase that would be measured in the absence of the atmosphere, and Φ is the differential phase delay introduced by the atmosphere. In addition, for an exposure time less than 1/100 second, during which time the atmosphere is reasonably stationary, the atmospheric scintillation phenomenon causes an error in the amplitude of the frequency component. However, it is well known (ref. 2) that for short exposure times the primary cause of image degradation is the error in phase of the various frequency components of the image, while errors in amplitude are far less important. Thus, if the phase error Φ can be removed, the quality of the images will be vastly improved.

A TRIPLE INTERFEROMETER

While there is no obvious way to remove the phase errors in the images produced by the above simple two-aperture system, improvements can be made if a three-aperture mask is inserted in the system. The optical system proposed here is that shown in figure 2(a). The mask to be inserted is shown in figure 2(b). Again the individual apertures have diameters on the order of 10 cm or less, so the primary atmospheric effects of concern are differential phase delays. The negative lens in this system collimates the converging bundle of rays so that an appropriate beam splitting device

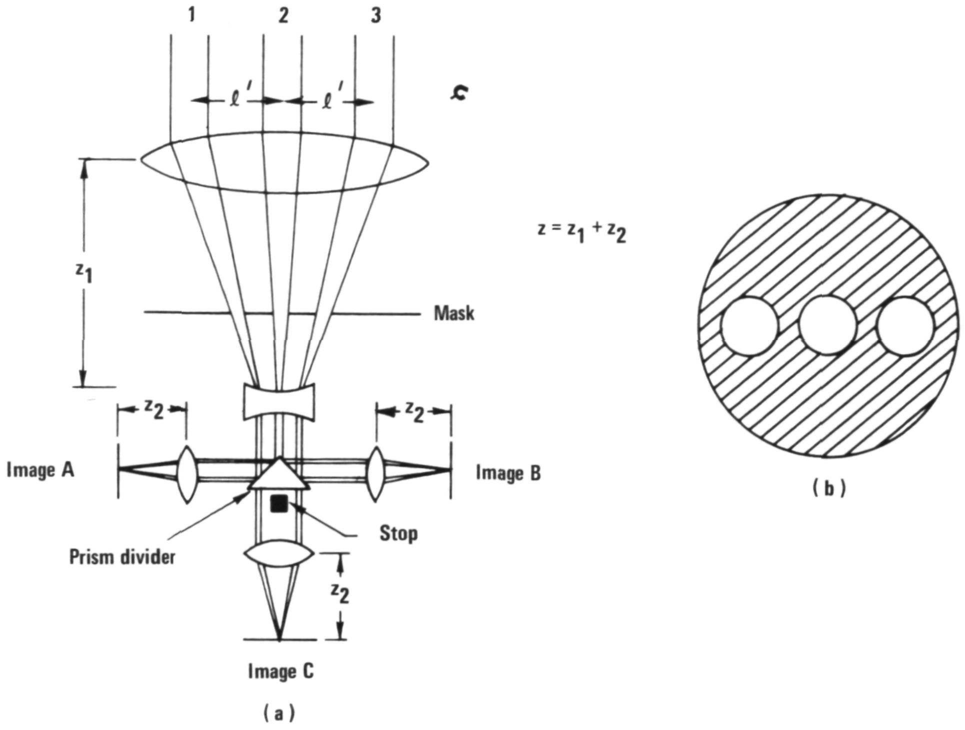

FIGURE 2.—(a) Imaging system operated as a three-element interferometer. (b) The mask inserted in the converging cone of rays.

(shown here as a prism) can be inserted with a minimum of resulting aberrations. The bundle of rays is split and three positive lenses cause three separate images to fall on photographic film where they are recorded.

In the absence of the atmosphere, the images recorded at positions A and B would be identical, for each is formed by two apertures with the same spacing ℓ_1'. Thus the spatial frequencies contained in the image would be centered at zero frequency and at frequency

$$f_1 = \frac{\ell_1'}{\lambda z}$$

(The high-frequency components are the ones of primary interest in our present discussion.) For detector C, however, the two apertures are spaced by $2\ell_1'$, so the high spatial frequency band in the image is centered at $2f_1$.

Now consider the effects of the atmosphere on this system. In image A, the phase of the frequency component at f_1 is

$$\psi_1' = \psi_1 + \Phi_1$$

where ψ_1 is the true phase that would be measured in the absence of the atmosphere, and Φ_1 is the atmospheric phase delay of path 2 relative to that of path 1. Similarly, in image B, the phase of the frequency component f_1 is

$$\psi_2' = \psi_1 + \Phi_2$$

where ψ_1 is the same as previously defined, and Φ_2 is the atmospheric phase delay in path 3 relative to that in path 2. Finally, the phase of the frequency component at frequency $2f_1$ in image C is

$$\psi_3' = \psi_2 + (\Phi_2 + \Phi_1)$$

where ψ_2 is the true phase, and $\Phi_2 + \Phi_1$ is the phase delay of path 3 relative to that of path 1.

Having recorded the images, it is now possible to process them such as to produce a single final image that is completely free from the atmospheric phase shifts Φ_1 and Φ_2. To do this we use Fourier analysis of the three images, measuring the phases of the frequency components at f_1 in images A and B, and at $2f_1$ in image C. Thus we know the phases ψ_1', ψ_2', and ψ_3'. We now add the phases ψ_2' and ψ_1' and subtract the sum from the phase ψ_3'. The result is

$$\psi=[\psi_2+(\Phi_2+\Phi_1)]-[2\psi_1+\Phi_1+\Phi_2]=\psi_2-2\psi_1$$

We have thus removed the atmospheric phase shifts. Note ψ is simply a number that results from our manipulations. We may now express ψ_2 as

$$\psi_2=\psi+2\psi_1$$

This equation expresses ψ_2 up to an unknown additive constant $2\psi_1$.

To gather a whole range of space-frequency information, we rotate the mask and also vary the separation of the two outer apertures from the inner aperture. Assuming that the object is stationary during this time, it can be shown that the phases of the various spatial frequency components can be expressed up to an additive multiple of the phase ψ_1 corresponding to the smallest spacing. The atmospherically induced phase errors are completely removed; spatial frequency phases are all expressed in terms of a single unknown (but constant) phase ψ_1. The effect of a lack of knowledge of ψ_1 can be shown (ref. 4) to be a lack of knowledge as to the exact position of the object in the sky. Thus the brightness distribution of the object can be measured with a resolution corresponding to the diffraction limit of the large-aperture system used, but the position of the source in the sky can only be specified to an accuracy of about 1 second of arc (i.e., that allowed by the small apertures in the mask).

The processing of the three images can be accomplished digitally, using fast Fourier transform algorithms, without any undue requirements for processing time. Coherent optical processing schemes to achieve the same operations can also be envisioned.

LIMITATIONS

The chief limitation of the above technique lies in its extremely poor sensitivity. Poor sensitivity is a consequence of two constraints: (1) the small size (a few centimeters) of the individual apertures, as dictated by the characteristic dimension of the wavefront perturbations, and (2) the short exposure times (about 1/100 second) for each orientation of the three apertures, as dictated by the characteristic fluctuation time of the turbulence. We emphasize, however, that the total time allowable for synthesis of the entire large aperture can be far greater than 1/100 second, the only constraint being imposed by the requirement that the object be stationary during the time the complete image is formed.

As a second limitation, it has been implicitly assumed that the atmospherically induced phase shifts Φ_1 and Φ_2 are identical for light from all points on the object. This assumption is equivalent to the usual isoplanatic condition required in other methods of image restoration.

As a final limitation we note that, while the phases of the various spatial frequency components are measured by this technique free from the usual atmospherically induced errors, their amplitudes remain subject to atmospheric fluctuations. Some degradation of the images will therefore remain, but image quality should be vastly better than would be obtained with additional phase errors.

ACKNOWLEDGMENT

This work was sponsored by the Office of Naval Research.

REFERENCES

1. McGlamery, B. J.: J. Opt. Soc. Am., vol. 57, 1967, p. 293.
2. Restoration of Atmospherically Degraded Images. Vols. I–IV, National Academy of Sciences, National Research Council, Washington, D.C., 1967.
3. Jennison, R. C.: Introduction to Radio Astronomy. Philosophical Library, Inc., New York, 1967, pp. 125–129.
4. Rogstad, D. H.: A Technique for Measuring Visibility Phase with an Optical Interferometer in the Presence of Atmospheric Seeing. Appl. Opt., vol. 7, 1968, p. 585.

Page intentionally left blank

Page intentionally left blank

ON PROCESSING OPTICAL IMAGES PROPAGATED THROUGH THE ATMOSPHERE FROM OBJECTS WITH UNKNOWN MOTION PARAMETERS

ROBERT O. HARGER
University of Maryland
College Park, Md.

The problem of how to process the optical wavefronts received in a spatial and temporal aperture after scattering from an object of interest and after propagation through the turbulent atmosphere is considered here. It is assumed that: (1) the turbulence and geometry are such that the received signal wavefront is multiplied by a complex phase error that is a time-independent, homogeneous, and isotropic Gaussian field over the receiving aperture (conditions for which this approximation is valid being discussed); (2) thermal noise is received additively along with the distorted signal wavefront; (3) certain parameters of the object are to be measured and the maximum likelihood criterion is used; (4) the object has unknown motion parameters; (5) a relatively short-time-duration coherent illumination of the object is made; and (6) the complex phase error has a correlation distance short relative to the aperture size.

A model for the scattered wavefront from the moving object is given and the likelihood functional is derived. Optical systems useful in physically realizing the likelihood functional are briefly described.

General expressions for the minimum error that can be achieved in estimating the object's desired unknown parameters—the Cramer-Rao lower bound—are derived and the effect of the object's unknown motion parameters discussed. A comparison is made with the turbulence-free and the unknown-motion free cases.

Specific combinations of parameters and motions, among them object scale and uniform translational motion, are investigated.

The relatively recent advent of the laser, especially the high energy, pulsed laser, has led to the study of the problem of imaging objects by transmitting and receiving locally generated coherent light. Since often the transmission path will be at least partially in the turbulent atmosphere, the ultimate limitations of such systems will be in part determined by the effects of such turbulence. We investigate here one specific approach to the problem, but because of the considerable difficulties of these problems we shall have to be rather specific, and somewhat restrictive, concerning assumptions in order to proceed at all.

The first major difficulty is that a satisfactory analytic description of an optical wavefront after it has passed through turbulence does not exist for many geometries of practical interest, including the one we wish to consider here. The information required about such a wavefront depends upon the theoretical approach adopted: the determination of optimum processing structures and their performance can require a complete statistical description. Further, the nature of the statistics, it seems quite clear, will depend upon the geometry even when the nature of the turbulence is fixed. We will assume statistics that seem to be at least partially implied by the majority of experimental studies.

The second major difficulty is a long familiar one—that of describing in a tractable way the wavefront scattered by an object of interest. We shall assume a "reflectivity density" for the object as we discuss below.

The third major difficulty is describing what is known, and what we wish to find out, about the object. Such a description interacts strongly with selected statistical performance criteria. We shall here assume that the object is of known form up to unknown parameters which may be arbitrarily divided into two classes: (1) motion parameters that are not of actual interest (e.g., position, velocity); and (2) other object parameters that are of interest (e.g., scattering cross section, size). We will use the method of maximum likelihood.

The final major difficulty is finding the likelihood functional and calculating performance for the models assumed above. We shall assume that the correlation distance of the received wavefront is small relative to the receiving aperture size in order to find the likelihood functional. In calculating performance we shall consider the case of small phase errors here: this restriction is not necessary but simplifies the form of the answers and hence their interpretation.

Our discussion given here is a continuation of that in references 1 and 2.

THE MODEL

We consider the imaging system and geometry shown in figure 1 which models satellite imaging from a terrestrial site. The object is assumed to be illuminated by a transmitted pulse of duration T during which the turbulent atmosphere is assumed unchanging: this restricts T to be less than about 1 millisecond.

In references 1 and 2 the following model was introduced to describe the received field in the aperture. Suppose $E_s(\mathbf{r}, t)$ is the scattered field in the immediate vicinity of the object. Then, in the absence of turbulence, the received field, $F(\mathbf{r}, t)$, is calculable by the Kirchhoff-Huygens diffraction integral. In the presence of turbulence we assume that the received field is multiplied by a complex phase error $\exp\psi(\mathbf{r})$, $\psi(\mathbf{r}) \equiv B(\mathbf{r}) + i, S(\mathbf{r})$, where $\{B(\mathbf{r}), \mathbf{r}\epsilon A_R\}$ and $\{S(\mathbf{r}), \mathbf{r}\epsilon A_R\}$ are homogeneous, isotropic Gaussian fields. We also assume that a noise field $\{N(\mathbf{r}, t), \mathbf{r}\epsilon A_R, t\epsilon T\}$ is received additively with the scattered field: such noise represents the ever-present background radiation and mathematically prevents unwanted "singular" situations. Thus the received data is assumed to be

$$Z(\mathbf{r}, t) \equiv F(\mathbf{r}, t)e^{\psi(\mathbf{r})} + N(\mathbf{r}, t), \ \mathbf{r}\epsilon A_R, \ t\epsilon T \quad (1)$$

We adopt this model for several reasons. First, it appears that most optical propagation experiments seem to imply that the received signal field has log-normal statistics in so far as they are measured. Second—and we are aware of the controversy surrounding it—the Rytov model (refs. 3 and 4) for propagation through turbulence suggests such a model. Third, analytically the model yields results which, as a minimum, are suggestive in the general situation. There is one deficiency the model, equation (1), possesses: $\{\psi(\mathbf{r}), \mathbf{r}\epsilon A_R\}$ depends upon the scattered field itself. (Such a dependence is predicted by the Rytov model.) We shall assume this dependence can be neglected.

We denote the covariance functions of $\{B(\mathbf{r}), \mathbf{r}\epsilon A_R\}$ and $\{S(\mathbf{r}), \mathbf{r}\epsilon A_R\}$ by $\sigma_B^2 R_B$ and $\sigma_s^2 R_s$ ($R_B(0) = 1$, $R_s(0) = 1$), respectively, and their covariance by $\sigma_B \sigma_s^2 \, R_{Bs}$. Assuming the means of these normal fields are zero, they are of course completely determined by these covariances. We also assume that the additive noise is a (complex) zero-mean white Gaussian field with spectral density N_0 over the spatial and temporal spectrum of the scattered signal.

If the illumination in the region of the object is $E_i(\mathbf{r})$, we assume that the reradiated wave is given by $E_i(\mathbf{r})\phi(\mathbf{r},t)$ at the (illuminated) surface of the object. We call $\phi(\mathbf{r},t)$ the "reflectivity density" and it characterizes the object for our purposes. Although this assumption concerning the nature of the scattering mechanism is rather restrictive—e.g., multiple reflections are ignored—we note that unless the object can be so characterized at least approximately, the "image" of the object will bear a

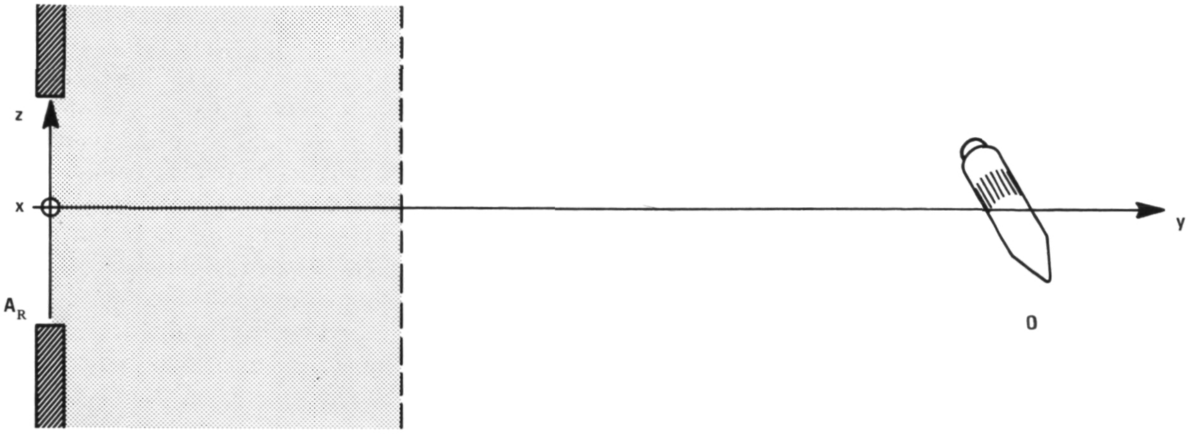

FIGURE 1.—A model for a space object imaging system. The receiving aperture is A_R and the object to be identified is O.

rather confused relation to the physical structure of the object and, very likely, to its ordinary ambient-light photographic image. Further, if the object is smooth (with respect to the wavelength) and a good conductor, then this model is quite good and the reflectivity density is essentially given by $2(\mathbf{n}_0 \cdot \mathbf{n})$ where $\mathbf{n}_0$ is the unit vector of the incident field and $\mathbf{n}$ is the unit normal vector to the surface of the object (ref. 5).

Thus for a rigid object in translational motion we have the scattered field given by $E_i(\mathbf{r}-\boldsymbol{\rho}_t)\ \phi(\mathbf{r})$, where $\mathbf{r}\epsilon W$ and W is the illuminated surface of the object and $\boldsymbol{\rho}_t$ is the (relative) position vector of the object. Using the Kirchhoff-Huygens diffraction integral, the wavefront at the receiving aperture A_R is given by

$$F(\mathbf{r},\ t)=\int_W \frac{e^{ik}|\mathbf{r}-\mathbf{r}'-\boldsymbol{\rho}_t|}{4\pi|\mathbf{r}-\mathbf{r}'-\boldsymbol{\rho}_t|}\,\phi(\mathbf{r}')E_i(\mathbf{r}-\boldsymbol{\rho}_t)d\mathbf{r}' \qquad (2)$$

LIKELIHOOD FUNCTIONAL

If the complex phase error $\exp\ \psi \equiv \exp\ (B+iS)$ were fixed, we would have a three-dimensional generalization of the well-known "sure-signal in white Gaussian noise" problem of communication theory. The likelihood functional is—trivially generalizing the well-known one-dimensional form—

$$f(Z|\psi)=\exp\left\{\frac{2}{N_0}\,Re\left(\int \overline{Z}G\right)-\frac{1}{N_0}\int |G|^2\right\} \qquad (3)$$

where $G\equiv Fe^{\psi}$ is the "sure signal" (ψ fixed) and the integrals are over the spatial aperture A_R and the time interval T.

To find the desired likelihood functional we must average $f(Z|\psi)$ as given by equation (3) with respect to the distribution of $\{\psi_{\ \mathbf{r}},\ \mathbf{r}\epsilon A_R\}$. In order to get a tractable result we make the assumption—which is frequently true in practice—that the correlation distance of ψ is small with respect to the aperture dimension $\sqrt{A_R}$. Then we can formally appeal to the Central Limit theorem and conclude that the exponent, call it α, appearing in equation (3) is approximately a Gaussian random variable. Now the calculation greatly simplifies for if α is a Gaussian random with mean m_α and variance σ_α, $E\{\exp\ \alpha\}=\exp\ \{m_\alpha+\sigma_\alpha{}^2/2\}$. Note further that we need only be concerned with

$$L(Z)\equiv\log E_\psi\{\,f(Z|\psi)\,\}=m_\alpha+\sigma_\alpha{}^2/2 \qquad (4)$$

The calculations are straightforward now because all the required expectations are simply joint characteristic functions of jointly Gaussian random variables evaluated at various points. We find

$$m_\alpha=\frac{2}{N_0}Re\left\{E(e^{\psi})\int \overline{Z}F\right\}-\frac{E(e^{2B})}{N_0}\int |F|^2$$

and

$$\sigma_\alpha{}^2=\frac{4}{N_0{}^2}T_1-\frac{4}{N_0{}^2}T_2+\frac{1}{N_0{}^2}T_3$$

where

$$T_1\equiv\frac{1}{2}Re\left\{\int\overline{Z}_1F_1\int\overline{Z}_2F_2 \text{ Cov } (e^{\psi 1},e^{\psi 2})\right\}$$

$$+\frac{1}{2}\int\overline{Z}_1F_1\int Z_2\overline{F}_2 \text{ Cov } (e^{\psi 1},e^{\psi 2})\Big\}$$

$$T_2\equiv Re\left\{\int\overline{Z}_1F_1\int|F_2|^2 \text{ Cov } (e^{\psi 1},e^{2B_2})\right\}$$

$$T_3\equiv\int|F_1|^2\int|F_2|^2 \text{ Cov } (e^{2B_1},{}^{2B_2})$$

and

$$\text{Cov}(\xi_1,\xi_2)\equiv E\left\{\Big[\xi_1-E(\xi_1)\Big]\Big[\xi_2-E(\xi_2)\Big]\right\}$$

We shall omit exhibiting the various covariances explicitly.

These expressions are rather complicated. We point out that linear and quadratic functionals of the data ($Z_{\mathbf{r}}$, $_t$, $\mathbf{r}\epsilon A_R$, $t\epsilon T$) appear: the optimum processor is nonlinear. It is possible, in principle at least, to perform all these calculations with, basically, coherent optical systems (ref. 2). Further the role of the quadratic functionals can be interpreted in a very satisfying way: they are "mixed-processors" in the sense that they coherently process (sum) as large-as-desirable pieces of the data and incoherently process (sum) all such contributions (ref. 2).

In the detailed calculations of accuracy limits below, we shall consider just one special case: $\sigma_B{}^2\equiv 0$, $\sigma_s{}^2<<1$. Then $L(Z)$ simplifies to

$$L(Z)=\frac{2(1-\sigma_s{}^2/2)}{N_0}Re\left\{\int\overline{Z}F\right\}-\frac{1}{N_0}\int|F|^2$$
$$-\frac{\sigma_s{}^2}{N_0{}^2}Re\left\{\int\overline{Z}_1F_1\int\overline{Z}_2F_2R_s(1-2)\right\}$$
$$+\frac{\sigma_s{}^2}{N_0{}^2}\int\overline{Z}_1F_1\int Z_2\overline{F}_2R_s(1-2) \qquad (5)$$

Sometimes the a priori knowledge about a subset $\boldsymbol{\beta}=(\beta_1, \ldots, \beta_k)$ of the unknown parameters may reasonably lead to an assumption of a known probability distribution function. It can be shown (ref. 6) that, if this distribution is given by a probability density function $\rho_\beta(\beta_1, \ldots, \beta_k)$, then the likelihood functional is now $f(Z)\cdot\rho_\beta(\beta_1, \ldots, \beta_k)$. (Note that we are suppressing the dependence of $f(Z)$ on $\boldsymbol{\beta}$ in our notation.) We shall assume such a priori knowledge about the vehicle velocity in examples below.

Before we proceed to the problem of calculating performance bounds we point out briefly how coherent optical systems can perform some of the required operations of this optimum receiver.

ON OPTIMUM COHERENT OPTICAL PROCESSORS

As has been discussed in references 1 and 2, coherent optical systems can be employed to perform some of the essential calculations involved in finding the likelihood functional. That is to say, coherent optical systems can form the essential parts of the receiver/processor.

We consider the special case of large bandwidth phase errors (ref. 2). Then we find, e.g., if b is the complex amplitude of F,

$$\frac{\max}{b}L(Z)=\frac{e^{-\sigma_s{}^2}|\int\overline{Z}F|^2}{N_0\int|F|^2-\int\overline{Z}_1F_1\int Z_2\overline{F}_2\psi(1-2)} \qquad (6)$$

here the integrals are over T and A_R and the covariance function

$$\psi\equiv e^{-\sigma_s{}^2}(e^{\sigma_s{}^2R_{s}}{}_{-1})$$

We note that the integral over T is approximately realized by passing the wavefront through a filter—e.g., a Fabray-Perrot filter—with bandwidth T^{-1} Hz. (It has recently become possible to use such filters in this type of application.) Let

$$Y\equiv\int\overline{Z}dt\cdot F$$

To form Y we of course multiply $\overline{Z}$—or $\int\overline{Z}dt$—by a transmission function F. (F can be complex (refs. 2 and 7).) Now we wish to form

$$Q \equiv \int_{A_R} Y_1 \int_{A_R} \overline{Y}_2 \psi(1-2) = \frac{1}{2\pi} \int |\tilde{Y}|^2 \tilde{\psi} \qquad (7)$$

and

$$P \equiv \left| \int_{A_R} \overline{Y} \right|^2 = |\tilde{Y}(0)|^2$$

where $\tilde{Y}$ devotes the Fourier transform of Y over A_R, $\tilde{\psi}$ is the Fourier transform of ψ—a spectral density and therefore a real, positive function, and we have used Parseval's identity.

But the forms, equations (7), are easily computed by the coherent optical system shown in figure 2 which basically computes the Fourier transform. Note that the distance from the aperture to the lens is not critical and within the sagittal approximation this distance determines a quadratic phase on $\tilde{Y}$ and only $|\tilde{Y}|$ enters into equations (7).

Basically this is a remarkably simple circuit. Whether or not it is practical depends on the specific application. In quite another application, communication, F is a constant and the receiver is highly attractive (ref. 8).

THEORETICAL ACCURACY LIMITS

Having the likelihood functional $f(Z)$ we can now find lower bounds on the error variances of any estimate of the object's unknown parameters. Such bounds are commonly referred to as "Cramer-Rao" lower bounds (refs. 9 and 10).

If $\hat{\alpha}$ is an estimate of α with bias $b(\alpha) = E\{\hat{\alpha}\}$ then one has the inequality (refs. 9 and 10)

$$E\{(\hat{\alpha}-\alpha)^2\} \geq \frac{(1+db/d\alpha)^2}{E\left\{\left[\frac{d}{d\alpha}\ln f(Z)\right]^2\right\}} \qquad (8)$$

If the estimator $\hat{\alpha}$ is unbiased, then the right side of equation (8) is a lower bound on the (error) variance of the estimator $\hat{\alpha}$. Estimators that achieve this lower bound are termed "efficient." It will be convenient to note that the denominator of the right side of equation (8) may be alternately written

$$-E\left\{\frac{d^2}{d\alpha^2}\ln f(Z)\right\}$$

In the case of multiple parameters $\boldsymbol{\alpha} \equiv (\alpha_1, \ldots \alpha_k)$, we define the elements C_{ij} of a matrix G by

$$C_{ij} \equiv E\left\{\left[\frac{\partial}{\partial\alpha_i}\ln f(Z)\right]\left[\frac{\partial}{\partial\alpha_j}\ln f(Z)\right]\right\}$$

which can also be written

$$C_{ij} = -E\left\{\frac{\partial^2}{\partial\alpha_i\partial\alpha_j}\ln f(Z)\right\}$$

Then the inverse matrix Λ (assuming it exists), with elements λ_{ij}, is the covariance

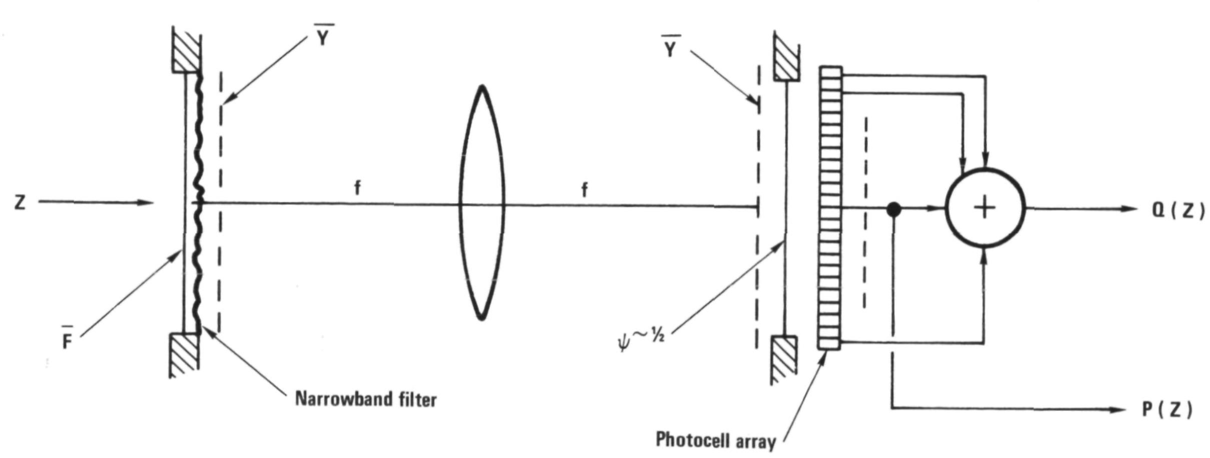

FIGURE 2.—An optical receiver/processor optimum for large, large-bandwidth phase errors. $\overline{F}$ and $\psi^{\sim 1/2}$ are spatial filters—i.e., transmission functions.

matrix of the efficient estimators $\hat{\alpha} \equiv (\alpha_1, \ldots, \alpha_l)$. The elements λ_{ij} are given by $(-1)^{i+j}$ det $C(j|i)$ det C, where "det" denotes determinant and the submatrix $C(j|i)$ is obtained from the matrix C by deleting the j^{th} row and i^{th} column. Since C is symmetric $(c_{ji}=c_{ij})$, det $C(j|j)=\det C(i/j)$. Thus two efficient estimates, $\hat{\alpha}_i$ and $\hat{\alpha}_j$, are uncorrelated if and only if det $C(j|i)=0$. For this it is sufficient that $c_{ij}=0$, $j=l, \ldots, k (j \neq i)$.

In order to keep the results simple and still be of practical interest we consider the special case $\sigma_B{}^2 \equiv 0$, $\sigma_s{}^2 \ll 1$: this would model a thin layer of turbulence close to the receiving aperture. The log-likelihood functional is given above in equation (5).

By straightforward calculation one finds

$$-E\left\{\frac{\partial^2 L}{\partial a^2}\right\} \equiv \frac{2(1-\sigma_s{}^2)}{N_0}\int |F_\alpha|^2 - \frac{4\sigma_s{}^2}{N_0{}^2}\int Im\{\overline{F}_1 F_{\alpha 1}\}\int Im\{\overline{F}_2 F_{\alpha 2}\} R_s(1-2) \qquad (9)$$

and.

$$-E\frac{\partial^2 L}{\partial\beta\partial\alpha} = \frac{2(1-\sigma_s{}^2)}{N_0} Re\left\{\int F_\alpha \overline{F}_\beta\right\} + \frac{2\sigma_s{}^2}{N_0{}^2}\int Im\left\{\overline{F}_1 F_{\alpha 1}\right\}\int Im\left\{\overline{F}_2 F_{\beta 2}\right\} R_s(1-2). \qquad (10)$$

Suppose that there is a single unknown parameter α. Then by eqs. (8) and (9) we have, for any unbiased estimator $\hat{\alpha}$,

$$\operatorname{Var}\left\{\hat{\alpha}\right\} \geq \left[\frac{2(1-\sigma_s{}^2)}{N_0}\int |F_\alpha|^2 - \frac{4\sigma_s{}^2}{N_0{}^2}\int Im\left\{\overline{F}_1 F_{\alpha 1}\right\}\int Im\left\{\overline{F}_2 F_{\alpha 2}\right\} R_s(1-2)\right]^{-1} \qquad (11)$$

We note that since the quadratic term appearing in equation (9) is positive definite, as is easily seen by Parseval's theorem and the fact that $\sigma_s{}^2 R_s$ is a covariance function, the presence of phase errors, $\sigma_s{}^2 > 0$, strictly increases the variance of an efficient estimator (assuming it was finite when $\sigma_s{}^2=0$). This of course is to be expected, but we emphasize the linear dependence of $-E\{\partial^2 L/\partial\alpha^2\}$ on $\sigma_s{}^2$. That is, for sufficiently small $\sigma_s{}^2$ the variance of an efficient estimator will increase linearly with $\sigma_s{}^2$, so that

$$\operatorname{Var}\left\{\alpha\right\} \approx \operatorname{Var}\left\{\hat{\alpha}\right\}\Big|_{\sigma_s{}^2 \equiv 0} \cdot \left\{1+\sigma_s{}^2 \left[1+\frac{2}{N_0}\frac{\int Im(\overline{F}_1 F_{\alpha 1})\int Im(\overline{F}_2 F_{\alpha 2}) R_s(1-2)}{\int |F_\alpha|^2}\right]\right\} \qquad (11a)$$

APPLICATIONS: SINGLE PARAMETER

Example 1.—As a first simple example we consider estimating the amplitude, say $|b|$, of the signal scattered by a "point" scatterer—that is, an object small with respect to the system's (turbulence-free) resolution. For such an object $|b|$ can give an estimate of object size. If the object is stationary at $(x, y, z) = (O, R_0, O)$, then $\boldsymbol{\rho}_t = R_0 \boldsymbol{j}$, $\phi(\boldsymbol{r}) = \phi_0 \delta(x, y-R_0, O)$ and $F(\boldsymbol{r}, t) = |b|\, e^{i\theta(\mathbf{r})}$, $\boldsymbol{r} \epsilon A_R$.*

We can easily calculate that if $|\tilde{b}|$ is an estimator of $|b|$,

$$\operatorname{Var}\left\{|b|\right\} \geq \left[\frac{2(1-\sigma_s{}^2)}{N_0} A_R T - \frac{\sigma_s{}^2}{N_0{}^2}|b|^2 T \int_{A_R} dr_1 \int_{A_R} dr_2 R_s(1-2)\right]^{-1} \qquad (12)$$

When $\sigma^2{}_s=0$ we find, as we expect, that the variance of the efficient estimator of amplitude is proportional to N_0, the noise level, and inversely proportional to A_R and T, the interval over which we collect data, and is independent of the actual value of the amplitude.

When $\sigma^2{}_s \neq 0$ we note that the variance of the efficient estimator does depend on the amplitude. Since we are in the large-bandwidth phase-error case, we have

$$\int dr_1 \int dr_2 R_s(1-2) \approx 2 A_R A_s$$

where A_s is the approximate support of R_s—that is, $R_s(\mathbf{r}) \approx 0$, $\mathbf{r} \notin A_s$—and

$$\operatorname{Var}\left\{|b|\right\} \geq \left\{\frac{2A_R T}{N_0}\left[1-\sigma_s{}^2\left(1+\frac{|b|^2 A_s}{N_0}\right)\right]\right\} \qquad (12a)$$

---

*The unit vectors in the x, y, and z directions are **i**, **j**, **k**, respectively.

Therefore, the variance of the efficient estimator increases as A_s increases ($A_s << A_R, \sigma_s^2 > 0$). Put another way, the greater the bandwidth of phase errors ($\sigma_s^2 << 1$), the less their effect on an efficient estimator of amplitude.

Example 2.—Suppose now we estimate the x position of a stationary point object. Now

$$\phi(\mathbf{r}) = \phi_0 \delta(x, y, z),\ \boldsymbol{\rho}_t = x_0\mathbf{x} + R_0\mathbf{y}$$

and

$$F(\mathbf{r}, t) = b \exp\left\{ i\frac{k}{2R_0}\left[(x-x_0)^2 + z^2 \right]\right\}$$

(We used equation (2) and the quadratic expansion of the phase—the so-called sagittal approximation—which should be very good for the problem we are discussing.)

Straightforward calculation gives, for any estimate $\hat{x}$ of X_0,

$$\mathrm{Var}\left\{\hat{x}\right\} \geq \left[\frac{2(1-\sigma_s)^2}{N_0} T|b|^2\left(\frac{k}{R_0}\right)^2 \int_{A_R} (x-x_0)^2 \right. \tag{13}$$

$$\left. -\frac{4\sigma_s^2 T^2 |b|^4}{N_0^2}\left(\frac{k}{R_0}\right)^2 \int_{A_R} (x_1 - x_0) \int_{A_R} (x_2 - x_0) R_s(1-2)\right]^{-1}$$

When $\sigma_s^2 = 0$ we may write

$$\mathrm{Var}\left\{\hat{x}\right\} \geq \left[\frac{2}{N_0}|b|^2 A_R T\cdot\left(\frac{k}{R_0}\right)^2 \cdot \int_{A_R} \frac{(x-x_0)^2}{A_R}\right]^{-1} \tag{13a}$$

a reasonable-appearing form, only the last factor possibly being unexpected. Note

$$\int_{A_R} (x-x_0)^2 \approx \begin{cases} x_0^2 A_R, & x_0 >> x \\ A_R \dfrac{A_x^2}{48}, & x_0 << x \end{cases}$$

A_X is the aperture x-extent.

Generalization of example 2.—Suppose that we wish to measure a position parameter of a point scattering object. Such a parameter enters equation (2) via $\boldsymbol{\rho}_t$ which will depend functionally upon it. As $\phi(\mathbf{r}) = \Phi_0\ \delta(x,y,z)$, equation (2) gives

$$F(\mathbf{r}, t) = b e^{ik\theta(\mathbf{r},\alpha)}$$

where $\theta(\mathbf{r},\alpha) \equiv |\ \mathbf{r} - \boldsymbol{\rho}_t|$. Calculating equation (11) directly we obtain, for any unbiased estimate $\hat{\alpha}$,

$$\mathrm{Var}\left\{\hat{\alpha} \geq \left[\frac{2(1-\sigma_s)^2}{N_0} k^2 |b|^2 T \int_{A_R} (\theta_\alpha)^2 \right.\right. \tag{14}$$

$$\left. \frac{-4\sigma_s^2 k^2 |b|^4 T^2}{N_0^2} \int_{A_R} \theta_\alpha(\mathbf{r}_1) \int_{A_R} \theta_\alpha(\mathbf{r}_2) R_s(\mathbf{r}_1 - \mathbf{r}_2)\right]^{-1}$$

Example 3.—Suppose the x velocity, v, of a point scattering object is unknown. The geometry of figure 1 would provide directly a rather poor estimate of velocity; rather the more appropriate point of view is that the unknown velocity may interfere with the estimate of other parameters. Further it is likely that the x velocity will be known quite well a priori. Therefore let us assume a distribution on v given by the normal density

$$\frac{1}{\sqrt{2\pi\nu}} \exp\left[\frac{-(v-v_0)^2}{2\nu^2}\right]$$

where the mean (v_0) and variance (ν_2) are assumed known:

The expression

$$-E\{\partial^2 \ln[f(z)p(v)]/\partial v^2\}$$

will become

$$-E\{\partial^2 L(z)/\partial v^2\} + \nu^{-2}$$

From equation (2) with $\boldsymbol{\rho}_t = vt\mathbf{x} + R_0\mathbf{y}$ we have

$$\theta(\boldsymbol{r}; v) = [(x-vt)^2 + z^2]/2R_0$$

so that

$$\theta_v(\boldsymbol{r}, v) = -\frac{t}{R_0}(x - vt)$$

(We have again used the sagittal approximation.) Thus for any unbiased estimate $\hat{v}$ of v, equation 14 gives

$$\mathrm{Var}\{v\} \geq \left[\frac{1}{v^2} + \frac{2(1-\sigma_s^2)|b|^2}{N_0}\left(\frac{k}{R_0}\right)^2 \int [t\,(x-vt)]^2\right.$$

$$-\frac{4\sigma_s^2 |b|^4}{N_0^2}\left(\frac{k}{R_0}\right)^2 \int t_1(x_1 - vt_1) \int t_2(x_2$$

$$\left. -vt_2) R_s(\mathbf{r}_1 - \mathbf{r}_2)\right]^{-1} \tag{15}$$

We note that if the quadratic term in t can be neglected—for this it is sufficient that

$$\frac{k}{R_0}(vt)^2 << 1 \text{ rad}$$

—then the quadratic term will be zero and

$$\text{Var}\{v\} \geq \left[\frac{1}{\nu^2} + \frac{2(1-\sigma^2{}_s)|b|^2}{N_0}\left(\frac{k}{R_0}\right)^2 \cdot \frac{T}{24} \cdot \frac{A_R A_x{}^2}{24}\right]^{-1} \tag{15a}$$

Example 4.—Suppose we wish to measure the scale of a stationary object of known shape. This is a fairly practical problem, e.g., one might want to estimate the size of a booster whose shape might reasonably be approximated. In order to exhibit an example with reasonably simple calculations we assume that the object is in the farfield; to be sure this usually will not be true.

With the far-field assumption—and assuming $E_1(\mathbf{r}-\boldsymbol{\rho}_t)$ is constant over the object—we have a Fourier transform relation between ϕ and F. Thus, if $\phi(\mathbf{r})=\Phi(a/x, z)$ and $\boldsymbol{\rho}_t=R_0\mathbf{y}$, equation (2) gives

$$F(\mathbf{r}, t) = b\tilde{\Phi}\left(\frac{k}{R_0}ax, \frac{k}{R_0}z\right)$$

$$\equiv bf(ax, z)$$

where the tilde denotes Fourier transform.

Equation (11) results in

$$\text{Var}\{\hat{a}\} \geq \left[\frac{2(1-\sigma_s{}^2)|b|^2T}{N_0}\int_{A_R} x^2|f_x|^2 - \frac{4\sigma_s{}^2|b|^4T^2}{N_0{}^2}\int_{A_R} x_1 Im\{\bar{f}_1 f_{x1}\} \int_{A_R} x_2 Im\{\bar{f}_2 fx_2\} R_s(r_1-r_2)\right]^{-1} \tag{16}$$

When $\sigma_s{}^2\equiv 0$ we note that an integral of $(xf_x)_2$ is involved. Its presence is intuitively reasonable since the fluctuation over the aperture A_R of the received field depends directly on object scale.

We note also that if f is real, as would be true if the object $\Phi(x, z)$ is symmetric in x and z separately, then the quadratic term is zero.

APPLICATIONS: MULTIPLE PARAMETERS

We shall consider an interesting example with two unknown parameters. One can show that, if α_1 and α_2 are efficient estimators, then

$$\text{Var}\{\hat{\alpha}_1\} = \frac{1}{C_{11}}\frac{1}{1-\rho^2}$$

and

$$\text{Var}\{\hat{\alpha}_2\} = \frac{1}{C_{22}}\frac{1}{1-\rho^2}$$

where

$$\rho^2 \equiv \frac{C_{12}{}^2}{C_{11}C_{22}}$$

Thus it is clear that if $C_{12}=C_{21}\neq 0$, the variances of the efficient estimators are increased. The calculation of C_{12} is therefore of some interest.

(It might be thought that if α_2 is a parameter we are not finally interested in, then it might be possible to devise an estimator α_1 that could have smaller variance than the efficient estimator α_1. It is not possible (ref. 9).)

Example 5—Suppose we wish to estimate the unknown scale of an object whose velocity is known only up to a known normal distribution. Assuming that the object is in the far field and that we may also ignore the quadratic in t, we find

$$F(\mathbf{r}, t) = be^{i\frac{k}{R_0}vt}f(ax, z), \mathbf{r}\epsilon A_R, \; t\epsilon T$$

It is clear that the derivative F_v is directly proportional to t as are $F_v\overline{F}$ and $F_v\overline{F}_a$: therefore each term in equation 10 is zero and hence $C_{12}\equiv C_{21}\equiv 0$ and hence $\rho\equiv 0$. That is, under the linear phase and far-field approximations, the efficient estimate of object scale is uncorrelated with that of velocity.

It might be guessed that if it is necessary to include the quadratic term in t then the efficient estimates might be correlated, since then F_v, $F_v\overline{F}$, and $F_v\overline{F}_a$ have parts proportional to t^2. However, this is not sufficient, for if f is real—as would be true if the object is symmetric in x and z separately—then $F_v\overline{F}_a$ will be imaginary (so that the first term of $C_{12}=C_{21}$, equation 10, is zero) and $\overline{F}F_a$ will be real (so that the second term of equation 10 is zero).

This implies that $C_{12}=C_{21}=0$ and hence the efficient estimate of scale and velocity are uncorrelated.

REFERENCES

1. HARGER, R. O.: On Processing a Signal with Multiplicative and Additive Errors. Restoration of Atmospherically Degraded Images, report of Woods Hole Summer Study, National Academy of Sciences, National Research Council, July 1966.
2. HARGER, R. O.: On Processing Optical Images Propagated Through the Atmosphere. IEEE Trans. on Aerospace and Electronic Systems, vol. AES–3, no. 5, September 1967, pp. 819–828.
3. CERNOV, L. A.: Wave Propagation in a Random Medium. McGraw-Hill, 1960.
4. TATARSKI, V. I.: Wave Propagation in a Turbulent Medium. McGraw-Hill, 1961.
5. KERR, D. E.: Propagation of Short Radio Waves. McGraw-Hill, 1951.
6. PARZEN, E.: Extraction and Detection Problems and Reproducing Kernel Hilbert Spaces. J. SIAM Control, sec. A, vol. 1, 1962, pp. 35–62.
7. VANDERLUGT, A.: Signal Detection by Complex Spatial Filtering. IEEE Trans. on Information Theory.
8. HARGER, R. O.: Optimum Receiving Structures for Coherent Optical Communication through Turbulent Media. Symposium on Applications of Coherent Light, Florence, Italy, September, 1968.
9. CRAMER, H.: Mathematical Methods of Statistics. Princeton University Press, 1954.
10. GRENANDER, U.: Stochastic Processes and Statistical Inference. Ark. Mat., bond 1, no. 17, 1950, pp. 195–277.

Page Intentionally Left Blank

OPTICAL RESTORATION USING OPTIMUM FILTER THEORY OF IMAGES BLURRED BY ATMOSPHERIC TURBULENCE

JOSEPH L. HORNER
Conductron Corporation
Ann Arbor, Mich.

By manipulation of the Fourier spectrum of a degraded optical image recorded on photographic film, it is possible to reduce the effects of out-of-focus lenses, lens aberrations, linear motion, and atmospheric turbulence. In addition to the simple inverse filter, which is proportional to the reciprocal Fourier transform of the system point spread function (PSF), the use of an optimum least means square (LMS) filter has been successfully demonstrated, experimentally, for images degraded by long-term atmospheric turbulence. The PSF due to the turbulence was measured, and used in designing the optimum filter, as was the signal-to-noise ratio of the recording film. Smear lengths of twice the minimum resolution length in the object scene were successfully restored. The superiority of the optimum LMS filter over the inverse filter is shown conclusively.

The restoration is performed on a coherent optical analog computer, using the Fourier transform property of a lens.

The enhancement may be accessed quantitatively from the modulation transfer function (MTF) of the restored image. Experimental curves of the MTF are presented. An enhancement of four times is obtained in the mid-frequency range of spatial frequencies.

The theory of image enhancement starts with a convolution description of the image forming process

$$i(x',y')=\iint_{-\infty}^{\infty} s(x,x',y,y')\cdot o(x,y)dx\,dy \qquad (1)$$

where

$i(x', y')$ = illuminance of image in x', y' coordinates

$s(x, x'; y, y')$ = point spread function (PSF)

$o(x, y)$ = illuminance of object in x, y coordinates.

This describes the image of a self-luminous or incoherently illuminated object. When the PSF is spatially invariant—or isoplantic—equation (1) simplifies to

$$i(x', y')=s(x, y)\circledast o(x, y) \qquad (2)$$

where $\circledast$ is the convolution operator. The PSF is characteristic of the optical system (and its degradation) and particular degradations (out-of-focus, linear smear, random medium, etc.) produce unique PSF. For a near perfect system, $s(x, y)$ approaches a two-dimensional delta function.

In photo-optical systems $i(x', y')$ is allowed to expose a photographic emulsion. The developed film transparency, if it is linear, contains a signal proportional to the convolution of s with o. The restoration problem then is to deconvolve s from o, and obtain a restored, and hopefully near perfect image. The problem of film linearity is discussed later.

This deconvolution problem can be solved by taking the Fourier transform, F, of each side of equation (2).

$$F[i(x', y')]=I(\nu_x, \nu_y)$$

$$=\iint_{-\infty}^{\infty} dx'dy'\, i(x', y')e^{i2\pi(\nu_x x'+\nu_y y')} \quad (3)$$

This can either be done on a digital computer, after the image intensity values have been digitized, or on an auxiliary optical system using the Fraunhofer diffraction pattern occurring in the focal plane of a lens. The latter approach has been used here.

Applying the convolution theorem to equation (2) gives

$$I(\nu_x, \nu_y)=S(\nu_x, \nu_y)\cdot O(\nu_x, \nu_y) \quad (4)$$

Recovery of the original signal then consists of filtering $I(\nu_x, \nu_x)$ with $1/S(\nu_x, \nu_y)$ and inverse Fourier transforming (F^{-1}) the result

$$F^{-1}[I(\nu_x, \nu_y)]=i(x, y)$$

$$=F^{-1}\left[S(\nu_x, \nu_y)\cdot O(\nu_x, \nu_y)\cdot\frac{1}{S(\nu_x, \nu_y)}\right]=o(x, y) \quad (5)$$

The filter whose characteristic is $1/S(\nu_x, \nu_y)$ is referred to as the simple inverse filter. Whether or not it is physically realizable, due to zeros in $S(\nu_x, \nu_y)$, remains to be seen. All the above operations can be done by digital or optical computation.

EFFECT OF NOISE ON INVERSE FILTERING

The above derivation has assumed nothing about uncertainties in the determination of the point-by-point image illuminance. Where photographic emulsion is used to record the image, the image is unavoidably corrupted by the granularity of the film. Then, in addition to doing simple inverse filtering to remove the effects of an undesirable PSF, it is reasonable to ask if the effects of recording noise can be simultaneously reduced. Using the criterion of minimum least mean square error between original and restored illuminances, it has been shown (refs. 1, 2, and 3) that the "best" inverse filter is ($\nu=\nu_x, \nu_y$)

$$H(\nu)=\frac{1}{S(\nu)}\cdot\frac{O(\nu)/N(\nu)}{O(\nu)/N(\nu)+|S(\nu)|^{-2}} \quad (6)$$

where N is the noise power spectrum, and O the undistorted image spectrum. As before, S is the transform of the point spread function. This is simply the product of the simple inverse filter and an infinite lag Wiener filter. Note that when the signal-to-noise ratio $O(\nu)/N(\nu)$ goes to infinity, $H(\nu)$ approaches the simple inverse filter, $1/S(\nu)$.

It will be noted that equation (6) contains a logical contradiction that we call a Wiener demon—a close kin of Maxwell's celebrated demon. Namely, in order to specify the filter, one must know what the undistorted image spectrum, $O(\nu)$, is a priori. If one had this much information about the undistorted object, there would be no need to attempt restoration. In practice, then, $O(\nu)$ for continuous tone scenes, e.g., aerial photographs or planetary images through a telescope, is a complicated function, and the best one can do is to approximate $O(\nu)$ for a certain class of scenes. For restoring very simple geometric objects, an exact filter could probably be made from the computed object spectrum. But for complicated scenes one is essentially operating somewhere between simple high-pass filtering and exact least mean square optimum filtering.

EXPERIMENTAL

To produce an image distorted by a turbulent medium, the simple setup in figure 1 was used.

The amount of turbulence could be controlled by varying the power to the hot plate.

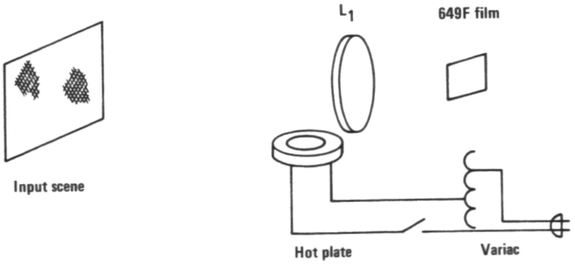

FIGURE 1.—Laboratory system used to produce atmospheric turbulence degraded transparencies.

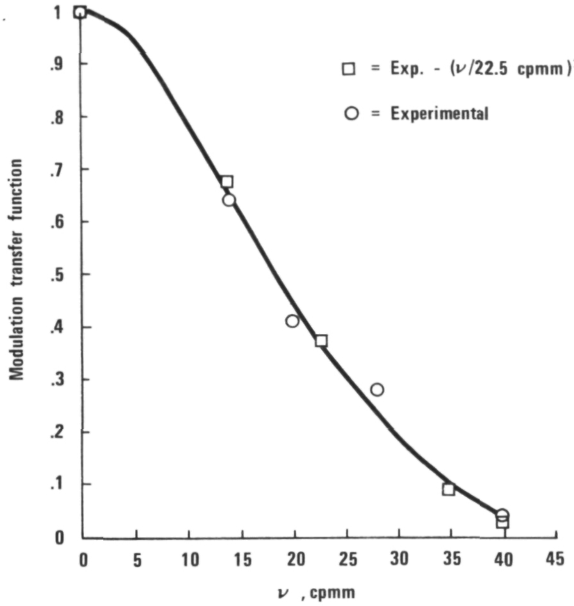

FIGURE 2.—Experimentally determined transfer function due to moderate turbulence. The Gaussian width is 22.5 cpmm.

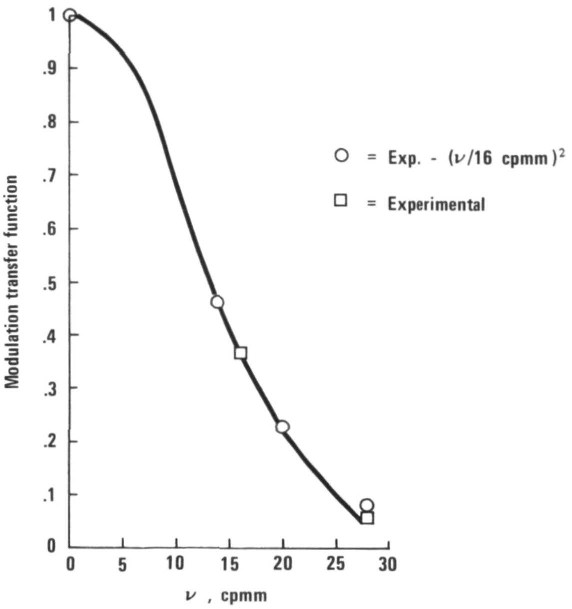

FIGURE 3.—Experimentally determined transfer function due to severe turbulence. The Gaussian width, ν_0, is 16.8 cpmm.

In order to avoid problems with a nonstationary (or nonisoplanatic) PSF, a time exposure of approximately 1 minute was made on the film at plane P_1. This way the instantaneous PSF tends to average out, and produce a symmetric but smeared PSF which is isoplanatic.

Using the Air Force three-bar resolution target, the modulation transfer function (MTF)—the Fourier transform of the PSF—was determined for several different heater power levels. Three runs were taken at each of two power settings. The average results are shown in figures 2 and 3, corresponding to moderate and heavy degradation of the image. Points of a Gaussian curve are shown for comparison, as there is some theoretical justification for this (ref. 4). The experimental curves have been corrected for the MTF of the optical system in the absence of the turbulence. Hence, the filter will only be correcting for the loss of information produced by the turbulence. The measured PSF transform is approximately

$$S(\nu)=e^{-(\nu/\nu_0)^2} \tag{7}$$

where ν_0 is determined by the heater power. The simple inverse filter equation is

$$H(\nu)=\frac{1}{S(\nu)}=Ke^{(\nu/\nu_0)^2} \tag{8}$$

where K is a normalization constant to make the maximum value of this passive filter unity at the highest spatial frequency in the image. This, then, is the simple inverse filter.

Using this PSF, the optimum filter is calculated using equation (6). The results are shown in figure 4 for various constant values of signal-to-noise ratios.

The curves are all normalized to a maximum value of 1.0. Since this will be an optical filter in a coherent system, the ordinate corresponds to the amplitude transmission, T_a, of the filter. As the signal-to-noise ratio decreases, the cut-off frequency of the filter decreases. The existence of a cut-off frequency in the optimum filter is reasonable, since accentuating frequencies much higher than the reciprocal resolution length could only contribute to the noise.

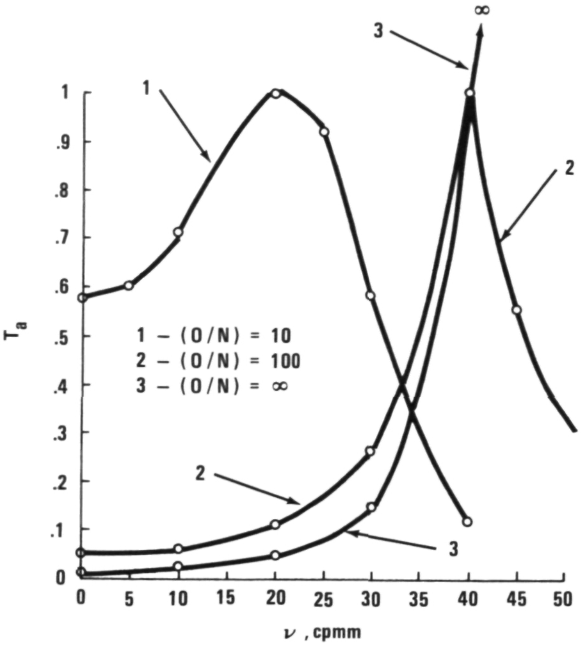

FIGURE 4.—Theoretically required inverse filter for various signal-to-noise ratios.

In addition to the constant signal-to-noise ratio assumed for the filter equation, a monotonically decreasing function was also tried. It was reasoned that while the film noise spectrum of high resolution photographic film is constant over the frequencies used here, the spectrum of a continuous tone aerial scene has a maximum at zero frequency, decreasing to the noise level at a spatial frequency between zero and the passband of the optical system used to image the original scene. Therefore, equation (6) was plotted for a signal-to-noise ratio of

$$O(\nu)/N(\nu)=\exp(-\nu/30 \text{ cpmm})$$

Figure 5 shows the optimum filter under these conditions. The difference between the constant and exponential signal-to-noise filter is not very great.

The filters were made according to the plots of figure 4 and on 649F glass plates. Since the filters have rotational symmetry, a properly shaped light source was imaged onto the filter plate, and the plate rotated. An accuracy of approximately 7 percent between 1 and 100 percent amplitude transmission was obtained.

The optical system used for restoration is shown in figure 6. A collimated coherent source illuminates the input film plane P_1. Lens L_2 extracts the two-dimensional Fourier transform one focal length behind L_2 at plane P_2. This is also where the spatial filter is placed. Lens L_3 extracts the inverse Fourier transform and forms an inverted filtered image in plane P_3. An important accessory to the system is the part labeled CONS (coherent optical noise suppressor) which effectively averages out the diffraction noise produced by the optical components (ref. 5).

RESULTS

Restoration on two different types of scenes were performed, a frequency modulated bar target (Sayce Target), and a transparency made from an aerial photograph (continuous-tone scene). The hot plate power corresponding to a ν_0 of 22.5 cpmm was used in making the smeared transparencies on 649F emulsion.

The usual method for linearizing the photographic process—contact printing to a γ product of two—was not used here. This process is cumbersome, degrades the resolution, and significantly increases the macroscopic noise of the signal carrying film. Instead, the linear portion of the amplitude transmittance (T_a)

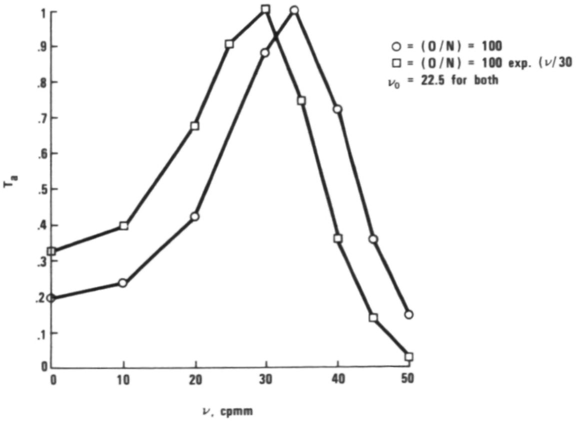

FIGURE 5.—Theoretical filter for monitonically decreasing signal-to-noise ratio.

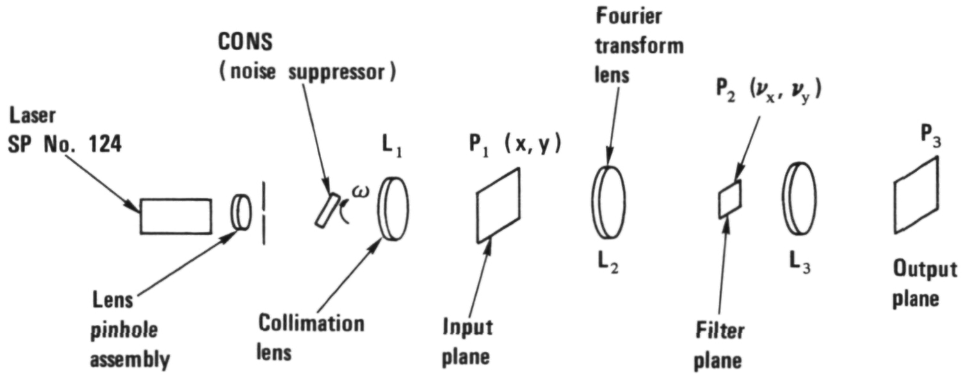

FIGURE 6.—Optical system used for enhancement by optical spatial filtering.

versus exposure (E) curve was utilized. Figure 7 shows a typical curve for 649F film. The film is linear to a transmission of about 25 percent, corresponding to an optical density of 1.0.

The spatial frequency corresponding to the highest resolution element of the aerial scene was approximately 45 cpmm. Filters were fabricated with assumed noise ratios of 10, 100, 1000, and ∞ (the simple inverse filter). Figure 8 shows the result of filtering with a simple inverse filter ($O/N=\infty$). The high noise level hides any restoration that might be present.

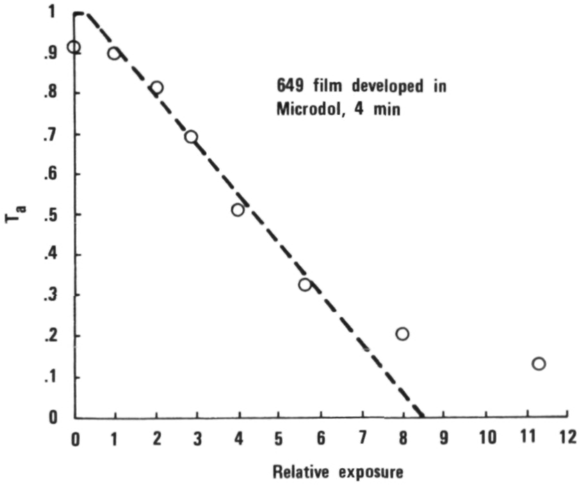

FIGURE 7.—Linearity of 649F emulsion in the Ta vs E representation. Development: Microdol-X, 4 minutes.

Figure 9 shows the Sayce target filtered with the $O/N=1000$ filter, a considerable improvement. Figure 10 shows the result of the $O/N=1000$ filter, which provided slightly better restoration than the $O/N=100$ filter, although the difference between these two was not great.

Hence, we can conclude that the use of optimum filter theory in the design of the spatial filters definitely gives a superior restored image.

RESTORATION MTF

In order to access the restoration quantitatively, the Sayce target contrast was computed from the microdensitometer trace. The result is shown in figure 11. It is normalized to a maximum value of 1.0 at the lowest spatial frequency. The result shows an enhancement factor of approximately four in the mid-frequency range, 30 to 40 cpmm.

CONCLUSIONS

Making spatial filters according to the dictates of optimum least mean square error analysis does definitely give better restored imagery. When this theory is applied to the case of image recording on a photographic emulsion, the question of the nature of the noise arises. Namely, the theory presented here assumes that the random noise process adds to

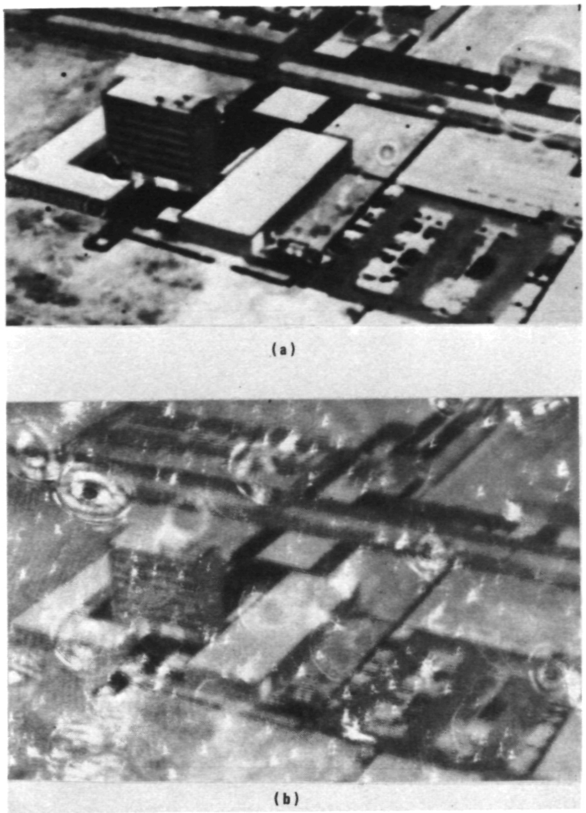

FIGURE 8.—(a) Unrestored aerial scene, distorted by atmospheric turbulence. (b) Same scene filtered by simple inverse filter ($O/N=\infty$).

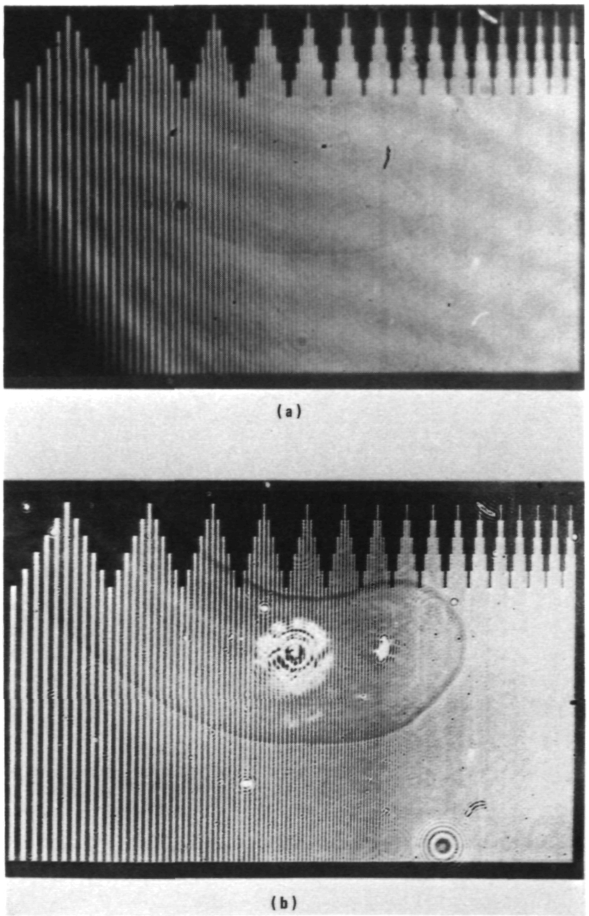

FIGURE 9.—(a) Unrestored Sayce target distorted by atmospheric turbulence. (b) Same scene restored with LMS filter ($O/N=1000$ assumed).

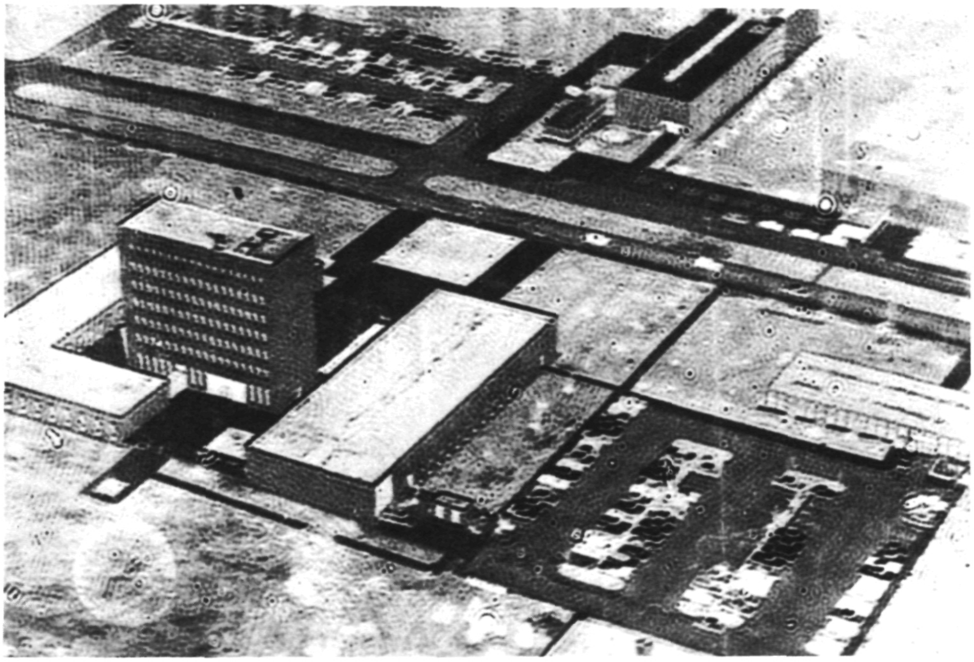

FIGURE 10.—Aerial scene restored with LMS filter ($O/N=1000$ assumed).

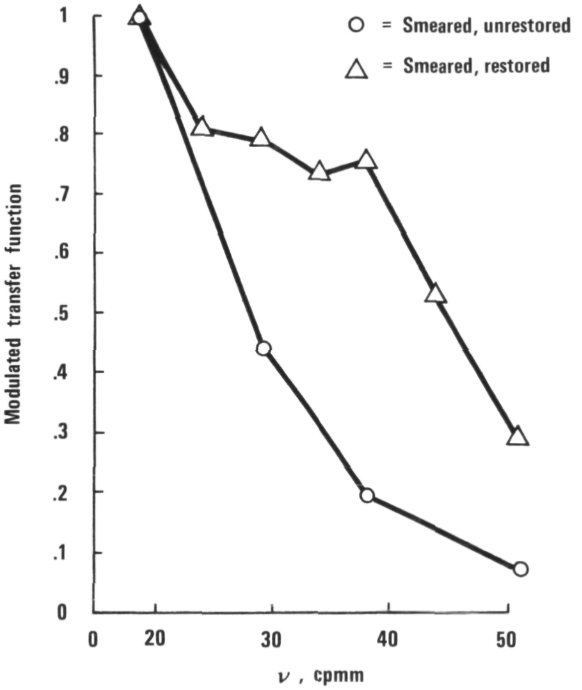

FIGURE 11.—Unrestored and restored MTF, from Sayce target.

the signal, which is the usual situation in electronics. Recent measurements here indicate that the relationship for photographic emulsion between signal and noise is a multiplicative one, or to put it another way, additive and signal dependent. Exactly what implications this type of noise has for optimum filtering will have to await the results of further analysis. However, judging by the success of the results presented here, the optimum filter cannot be too radically different from its present form.

REFERENCES

1. DAVENPORT, W. B.; and ROOT, W. L.: Introduction to Theory of Random Signals and Noise. McGraw-Hill Co., 1958, Chapter 11.
2. Final Report Air Force Contract AF 33 (657)–13558, SRL Subcontract No. 755–7–42707, Conductron Corporation, Ann Arbor, Michigan, November 1965.
3. HELSTROM, C. W., JOSA, vol. 57, 1967, p. 297.
4. HUFNAGEL, R. E.; and STANLEY, N. R.: JOSA vol. 54, 1964, p. 52.
5. THOMAS, C. E.: Applied Optics, vol. 7, 1968, p. 517.

Page intentionally left blank

Page intentionally left blank

PHOTOELECTRONIC RESTORING SYSTEM FOR IMAGES DEGRADED BY ATMOSPHERIC TURBULENCE

WERNER H. BLOSS, GÜNTER H. LOHNERT, AND RICHARD T. SCHNEIDER
University of Florida
Gainesville, Fla.

An electronic image restoration process is described based on an image orthicon detection system and an analog processing system. Conventional components of TV equipment and of analog computers have been used in the procedure. A laboratory experiment has been set up using flame gases to degrade the image. The image restoration technique was found to give a significant improvement in the quality of the image.

Theoretical considerations demonstrate the effectiveness as well as the limitations in applying this procedure to restore degraded images.

The image of an incoherently illuminated object is degraded in several ways when the light is transmitted through the atmosphere. Light propagation undergoes scattering and absorption processes and diffraction and refraction by random imhomogeneities in the air density. Time-varying random fluctuations of the refractive index in turbulent air is usually the major degrading process on image quality.

The interaction of turbulent air with the image-transmission and image-detection system results in a decrease of the information content. Although this reduction of information content cannot be compensated for by any device, it is possible to increase the information which is extractable from direct visual observations.

Processing of degraded images has gained considerable interest during the last few years. A number of papers have been published on theoretical aspects of image restoration (refs. 1 to 4) as well as on various experimental approaches (refs. 5 to 10) to this subject. Part of the efforts on image processing is based on the principles of holography (ref. 5), designated as active image processing. Passive image restoration represents a broad field of research which is matched to the problems of astronomical observations. This procedure is realized by means of optical analog filtering (refs. 7 and 10), by automatically selecting instants of best seeing in a series of short time exposures (refs. 8 and 9) or by data processing with digital computers (refs. 6 and 11).

The experimental approach to image restoration described in this paper is characterized by two features: (1) a photoelectronic recording system with an image orthicon and readily available components from TV equipment; and (2) conversion of spatial frequencies into frequencies in the ordinary sense, which allows the use of electronic filters and components of analog computers. The restoration procedure has been applied to signals degraded by Gaussian randomization processes although it is not restricted in its application to this special case.

THEORETICAL CONSIDERATIONS

When the point-spread function, S, is invariant over the region of the image plane to be examined, the degraded image can be described by the convolution integral

$$D(x,y)=\int_{-\infty}^{+\infty}\int_{-\infty}^{+\infty} I(x,y)S(x-\xi,\, y-\eta)d\xi d\eta \qquad (1)$$

where I is the ideal image (i.e., the image without degradation), and D is the degraded image. Picture processing can be said to be an attempt to solve this equation for I with the condition that D and S are known. If we assume that, for a turbulent atmosphere, the point-spread function is Gaussian, we can write

$$D(x,y) \qquad (2)$$

$$=\frac{1}{2\pi\sigma^2}\int_{-\infty}^{+\infty}\int_{-\infty}^{+\infty} I(x,\,y)\ \mathrm{e}\,[-\frac{(x-\xi)^2+(y-\eta)^2}{2\sigma^2}]d\xi d\eta$$

where σ is a measure of the degree of turbulence.

Both the operational characteristics as well as the limitations of the procedure will be demonstrated using an intensity distribution that is one dimensional, periodic and symmetric with respect to its space coordinate, and not band limited.

The intensity distribution of the ideal image is then represented by a Fourier series

$$I(x)=a_0+\sum_{k=1}^{\infty} a_k \cos\,(kux),$$

$$a_k=\frac{1}{L}\int_0^L I(x)\cos\,(kux) \qquad (3)$$

This expression can now be used to give

$$D(x)=a_0+\sum_1^{\infty} a_k e^{-\frac{k^2u^2\sigma^2}{2}}\cos\,(kux) \qquad (4)$$

Equation (4) shows the importance of the factor σ which is a measure of the degree of randomization, i.e., turbulence. High-order terms of the Fourier series are reduced exponentially with k^2, demonstrating the fact that the degrading system acts like a low pass for the spatial frequencies.

The ideal inverse transformation of equation (1) is given by

$$F^{-1}=\frac{F\{D(x)\}}{F\{S(x)\}}=I(x)$$

where F indicates the Fourier transform. It can be shown that for small arguments of the exponent in equation (4), the above transformation reduces to

$$I(x)=D(x)-C_1D^{\mathrm{II}}(x) \qquad (5)$$

where $D^{\mathrm{II}}(x)$ is the second spatial derivative of $D(x)$. With equation (4) we find

$$D^{\mathrm{II}}(x)=-\sum_{k=1}^{W_{\lim}} a_k k^2u^2 e^{-\frac{k^2u^2\sigma^2}{2}}\cos\,(kux) \qquad (6)$$

which gives the constant

$$C_1=\frac{\sigma^2}{2} \qquad (7)$$

Equation (7), which holds for small values of k and σ only, gives the desired factor C_1 for the restoration process. The original intensity distribution is obtained from a linear combination of the degraded intensity distribution and its second derivative. Figure 1 demonstrates this process for a one-dimensional intensity distribution. Figure 1(a) shows the degradation process of the signal with varying turbulence parameter, $p=(\pi/\sqrt{2})\sigma/L$. The restored signal according to equation (6) is shown in figure 1(b). It is obvious from these curves that the restoration process gives a good approach to the original signal if p is small. However, even at higher p values, the increase gained in contrast should result in an improved recognition of the original pattern.

In treating real two-dimensional images two variables with different spatial frequencies have to be considered. Two square objects which differ in area as well as in intensity by a factor of two have been smeared by an isotropic randomization process as illustrated in figure 2(a). The highly degraded image has been restored by the addition of two directional derivatives to the intensity profile. Figure 2(b)

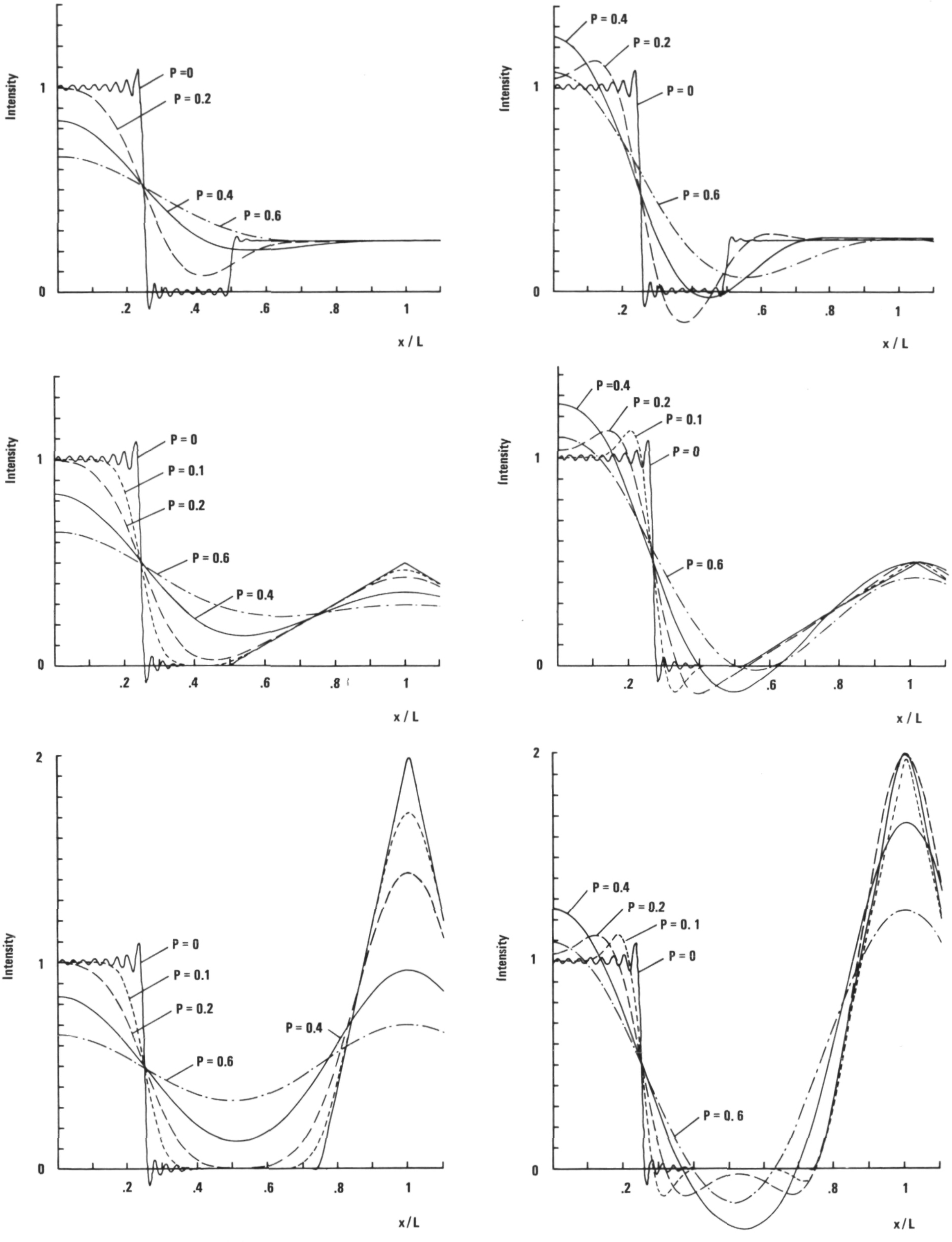

(a)

(b)

FIGURE 1.—(a) Bloss degraded and (b) restored intensity distribution of a one-dimensional image.

shows the restored pattern which allows recognition of the original image. If the perturbation process is not isotropic, for example the case of a random motion in one direction, this can be accounted for in the restoration process by using different constants for the partial derivatives.

OPERATIONAL CHARACTERISTICS

A modified image orthicon camera RCA-5820-A has been used as a detection system to the image restoring procedures. Besides the fact that no chemical processing is involved, the image orthicon provides a linear response and the availability of electric signals, from linear scanning, for further processing. The storage plate integrates the input signals for a period defined by its temperature. Using a cooled storage plate the sensitivity of the image orthicon camera may be higher than the most sensitive photographic emulsion (ref. 12).

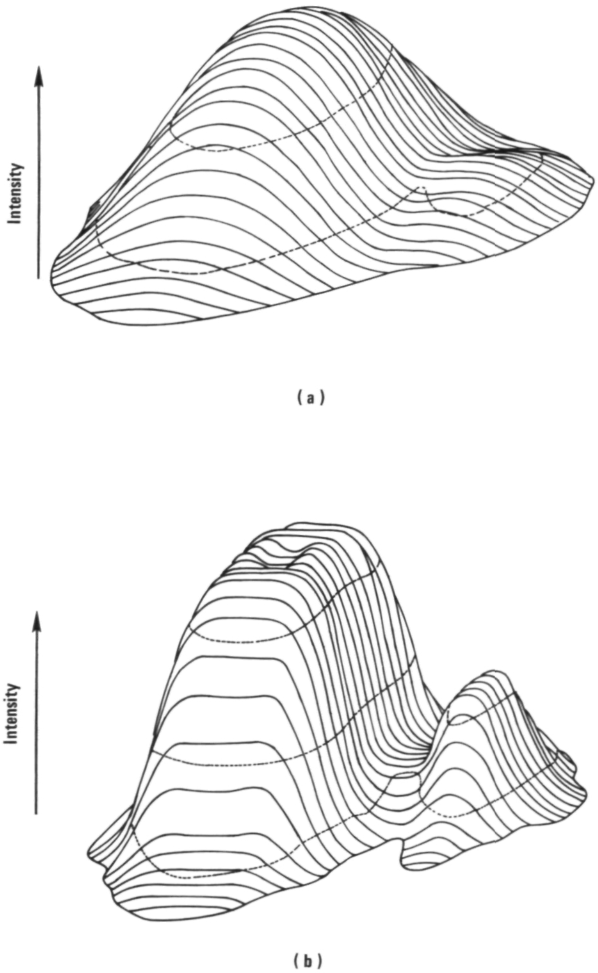

FIGURE 2.—Computed intensity profiles of two squares with different intensities. (a) Degraded image and (b) restored image.

The time averaged signal obtained from a large number of scans (32 or 64) is formed in a digital signal averager (Fabritek) in which 1024 different addresses are selected automatically in an adjustable sequence which is correlated to the scanning speed in the image orthicon (20 Hz).

For further processing it is required that the time averaged signal represent the real intensity distribution with a minimum of noise interference. Repetitive scanning not only provides the desired time-averaged intensity distribution but also results in a considerable increase of signal-to-noise ratio (ref. 13)

$$S/N=\sqrt{n}S_i/2\pi RP_i\left(\frac{1}{\epsilon}-\frac{1}{T}\right) \tag{8}$$

Here n represents the number of scans, S_i the peak signal value of a single scan, and P_i the noise power density per rad/sec and ϵ the sampling time.

The averaged signals which are stored in the magnetic core memory are fed to a low-pass filter which transforms the step function of the digital data at the output of the digital signal averager into a smooth curve which is used for further evaluation.

Besides using the second derivative, which proved to be insufficient at higher parameters p, a ring modulator can be used to give the first derivative with the appropriate sign defined by the second derivative. This represents an electronic component generating the function

$$-|D^{\mathrm{I}}(x)|\cdot \operatorname{sign}(D^{\mathrm{II}}(x))$$

The block diagram in figure 3 shows the complete process of image restoration and the shape of the signals after each step of processing.

After electronical processing the signals were used to modulate the electron beam intensity

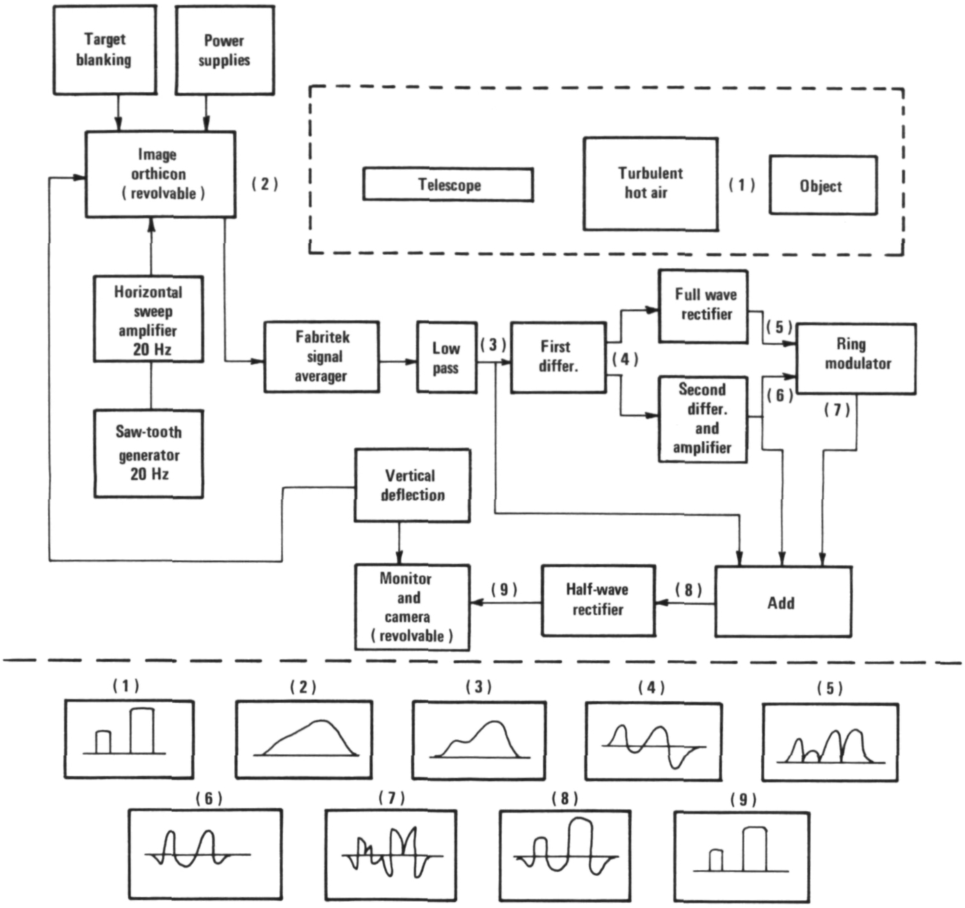

FIGURE 3.—Block diagram of electronic restoring system.

in a conventional oscilloscope, then each individual trace of a horizontal scan was stored on a photographic plate. After storing one line of the image a new vertical position in both the image orthicon and the oscilloscope was automatically adjusted thereby integrating the output image, line by line. The time required for processing one line is about 4 seconds and the total image restoring time for scanning in one direction varies from about 20 to 40 minutes (depending on the number of lines, 300 to 600). The total time required for scanning in horizontal and vertical direction requires a processing time of 40 to 80 minutes.

There is a different procedure, however, that is based on cooled storage plates in the image orthicon. The time averaging process is then performed on the storage plate. After a long time exposure of the image orthicon, the restoration process itself requires much less time (on the order of one minute) depending on the number of scans for each of the 2×600 lines.

EXPERIMENTAL RESULTS

To prove the effectiveness of the procedure a laboratory experiment has been carried out. An image of two similar symbols "8" and "*B*" of approximately 1 cm^2 size has been projected by a telescope to the photocathode of the image orthicon. The degradation due to turbulent air from flames in front of the telescopes can be seen in a photographic picture of 1 second exposure time (fig. 4(a)). The image restoration process according to the block diagram (fig. 3) has been carried out for one-directional scanning (horizontal) only and this yielded a fairly good reproduction of the original image (fig. 4(b)).

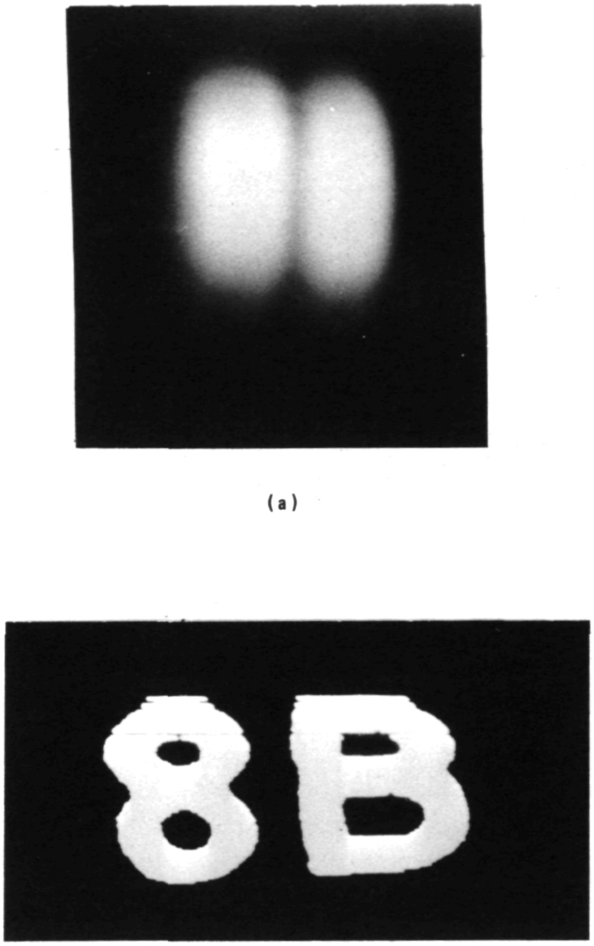

Figure 4.—(a) Degradation due to turbulent air from flames in front of telescopes, and (b) horizontal scanning of image restoration process.

References

1. Helstrom, C. W.: Image Restoration by the Method of Least Squares. J. Opt. Soc. Amer., vol. 57, 1967, pp. 297–303.
2. Hufnagel, R. E.; and Stanley, N. R.: Modulation Transfer Function Associated with Image Transmission through Turbulent Media. J. Opt. Soc. Amer., vol. 54, 1964, pp. 52–61.
3. Duntley, S. Q.; Culver, W. H.; Richey, F.; and Preisendorfer, R. W.: Reduction of Contrast by Atmospheric Boil. J. Opt. Soc. Amer., vol. 53, 1963, pp. 351–358.
4. Slepian, D.: Linear Least-Squares Filtering of Distorted Images. J. Opt. Soc. Amer., vol. 57, 1967, pp. 918–922.
5. Goodman, J. W.; Huntley, W. H.; Jackson, D. W.; and Lehmann, M.: Wavefront-Reconstruction Imaging through Random Media. Appl. Phys. Letters, vol. 8, 1966, pp. 311–312.
6. Harriss, J. L.: Image Evaluation and Restoration. J. Opt. Soc. Amer., vol. 56, 1966, pp. 569–574.
7. Cutrona, L. J.: Optical Computing Techniques. IEEE Spectrum, vol. 1, 1964, pp. 101–108.
8. Gregory, R. L.: A Technique for Minimizing the Effects of Atmospheric Disturbance on Photo, graphic Telescopes. Nature, vol. 203, 1964- pp. 274–275.
9. Dewitt, J. H.; Hardie, R. H.; and Seyfert, C. K.: A Seeing Compensator Employing Television Techniques. Sky and Telescope, vol. 17, 1957, p. 8.
10. Mueller, P. F.; and Reynolds, G. O.; Image Restoration by Removal of Random-Media Degradations. J. Opt. Soc. Amer., vol. 57, 1967, p. 1338.
11. McGlamery, B. J.: Restoration of Turbulence-Degraded Images. J. Opt. Soc. Amer., vol. 57, 1967, p. 293.
12. Luedicke, E.; Cope, A. D.; and Flory, L. E.: Astronomical Image-Integration System Using a Television Camera Tube. Appl. Optics, vol. 3, 1964, p. 677.
13. Ernst, R. R.: Sensitivity Enhancement Magnetic Resonance. Rev. Sci. Inst., vol. 36, 1965, pp. 1689, 1696.

FOURIER TRANSFORM HOLOGRAM CAMERA WITH AUTOMATIC VELOCITY SYNCHRONIZATION

EARL C. KLAUBERT
Electronics Research Center, NASA
Cambridge, Mass.

AND

JOHN H. WARD
Technical Operations, Inc.
Burlington, Mass.

A concept has been devised which provides a method for recording nonsmeared holograms of particles of 50 to 100 microns diameter at velocities from 0 to 40 km/sec with automatic velocity synchronization using no moving parts. This concept uses some of the properties of Fourier transform holograms; however, in this case the coherent reference wavefront will be derived from back reflected light from the moving particle. The feasibility of the proposed method is currently being investigated. This paper describes the basic concept and the anticipated properties of the hologram system. The major points of the feasibility investigation are also described.

In studies of hypervelocity impact associated with micrometeoroid impact phenomena and protection, one class of particles of considerable interest lies in the size range from 100 microns down to perhaps 10 microns. In present experiments, these particles travel at velocities up to 20 km/sec, or slightly higher; future efforts are aimed at speeds of 40 km/sec or more. In achieving such velocities, particles of these sizes are subjected to extremely high accelerations and often very rigorous ambient conditions of temperature and radiation. Consequently, particles may be shattered, and often some mass is ablated or otherwise lost. Since impact mass is a vital parameter, it is highly desirable to have a means of performing in-flight diagnostics to assess particle integrity and residual mass. A sharply resolved photograph which would permit determination of size, shape and integrity would be very helpful.

Unfortunately, it is virtually impossible to use conventional photographic techniques for this purpose. The very small size of the objects requires lenses of very short focal length and low *f*-number at high magnifications. The useful field diameter is on the order of 1 mm and depth of field is only a very few microns. If rotating mirror cameras could be used to provide image motion compensation, holography would offer adequate increases in both depth of field and field of view. However, velocities are so great and necessary system *f*-numbers so low that even the most advanced rotating mirror camera falls about two orders of magnitude short of the requirement.

Recently a novel solution to this problem was proposed.* This is to use the fundamental

---

*Basic concept of camera is due to Brian J. Thompson, The University of Rochester, College of Engineering and Applied Sciences, Institute of Optics, Rochester, N.Y.

characteristics of a Fourier transform hologram (refs. 1 and 2) to assign the individual optical tasks to those elements best capable of performing each. The result would be a system for recording Fourier transform holograms which is automatically synchronized to any, a priori unknown, particle velocity. A feasibility study was initiated a few months ago to verify the critical principles involved and to find solutions to certain problems involved in optical and mechanical implementation of the idea. The purpose of this paper is to describe the conceptual features of such a camera, and to discuss the experimental program presently being conducted. The physical realizability of the device will be determined by this study.

BASIC CONCEPTS

For the present, it is assumed that only a single particle, of arbitrary shape, is to be observed. The flight path of the particle can be arranged to lie in, or very nearly in, the front focal plane of a high quality, low *f*-number lens. The particle is backlighted by a collimated, quasimonochromatic beam from a laser. Under these conditions, the lens produces in its back focal plane the Fourier transform of the amplitude distribution of light diffracted by the particle. This situation is shown schematically in figure 1. Provided the particle does not rotate significantly while in the field of view of the lens, the intensity pattern will not move or change as the particle moves about in the field of view; i.e., the transform is stationary (ref. 2). Thus no image motion compensation is required to stabilize the intensity pattern (ref. 3).

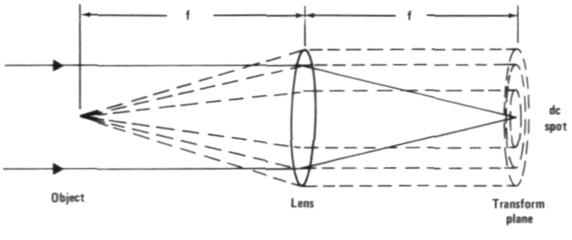

FIGURE 1.—Optical geometry for Fourier transform.

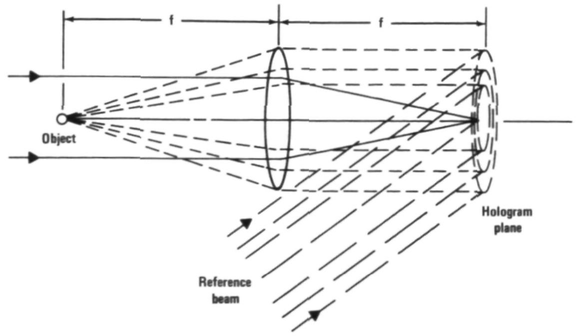

FIGURE 2.—Optical geometry for Fourier transform hologram.

A Fourier transform hologram may be formed by interfering with this pattern a plane wave tilted at an angle to the plane normal to the transformed diffracted light from the particle. This configuration is shown in figure 2. Although the intensity pattern of the transformed beam is stationary as the object is translated, the phase angle of the amplitude pattern is not. The plane wave front of the diffracted light rotates about an axis in the transform plane that is perpendicular to the direction of the object translation. Since the hologram is formed by interference of the object diffracted beam and the reference beam, the reference beam phase must rotate in precisely the same manner as that of the transform beam and remain synchronized throughout the exposure in order to hologram a moving object. If the rotations of the two beams are not synchronized, the interference fringes will be blurred out during a finite time exposure. Conceivably, the reference beam could be synchronized by reflecting it from a high speed rotating mirror ($\sim 10^6$ rpm). However, actual particle velocities can be anticipated to within only ±20 percent, while good quality holograms can tolerate a lack of phase synchronization of only a fraction of a wavelength during the exposure. Therefore, the probability of recording an adequately synchronized hologram by such a technique is extremely low.

It is here that the Fourier transform hologram concept offers a breakthrough. The particle itself will be used as a "synchronized mirror" to provide the coherent reference beam. A second collimated beam of light derived from the same laser source will be directed at the moving particle from the opposite direction (i.e., from the lens side). The basic arrangement is depicted in figure 3. Light reflected from the particle will be collected by the transform lens and rendered nearly collimated, since the particle lies approximately in the front focal plane of the lens. Further, the beam sweeps across the back focal plane of the transform lens producing a phase rotation precisely the same as that of the forward diffracted light. In this manner, the two beams derived from the same moving object will exhibit phase rotations which are synchronized.

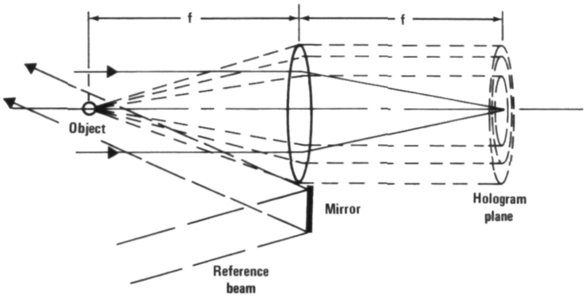

FIGURE 3.—Optical geometry for automatic synchronization of reference beam.

However, to produce a Fourier transform hologram, an angle of inclination between the transform and reference beams is required, as noted above. Introduction of this angle in the proposed configuration is somewhat more difficult than in conventional arrangements. Fortunately, a small angle is not only sufficient but quite desirable. Figure 4 is a schematic of a possible configuration. Two symmetric *f*/4 transform systems are proposed. The particle would travel in the direction perpendicular to the plane of the two optical axes. The lower arm of the optical system would produce the Fourier transform of the object. The upper arm of the system would collect back-reflected light and produce the synchronized reference beam.

BASIC PROPERTIES

Holograms recorded by this technique will have several distinctive properties. First, if the hologram is transilluminated by collimated light, it will reconstruct in the back focal plane of a lens, as would a conventional Fourier transform hologram. The off-axis angle of the first-order reconstructed images will be determined by the acute angle between the reference and forward diffracted beams at the hologram plane as shown in figure 4. Secondly, the reconstructed image will have the appearance of a Schlieren-blocked image; only the edges of the particle cross-sectional geometry will be observable. This effect is due to the focussed energy from the undiffracted portion of the backlighting collimated beam. When the hologram is properly exposed, this focussed spot will overexpose the center of the hologram and obliterate the low frequency information. Thus, only the high frequency, or edge, information will be recorded in the hologram. Thirdly, if more than one particle is in view during an exposure and if there is relative motion between the particles, all the particles will reconstruct concentrically about the same point and superimpose. This is true since the reference beam for each particle is derived from that particle at a fixed angle determined by the angle between the two optical axes of the system. Thus the "field of view" is limited to one particle. Lastly, the resolution of the hologram is dependent upon the quality of the back-reflected reference beam.

FEASIBILITY STUDY

Several specific points must be studied both theoretically and experimentally in order to

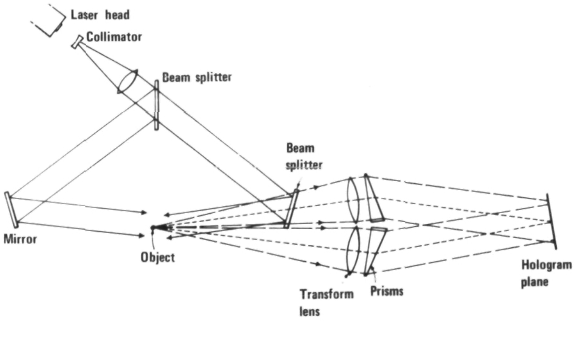

FIGURE 4.—Schematic of possible configuration of microparticle camera.

demonstrate the feasibility of constructing a hologram camera based on these concepts. The more important points of the study program are outlined here.

In figure 4, a triangular arrangement of two beam splitters and a mirror is used to produce the two beams which illuminate the object. The optical path lengths should be equal to the coincident front focal points of the two Fourier transform systems. The object must pass through the plane of the optical axes to within the coherence interval of the laser light. Since the two front focal planes are not coincident everywhere, the object translation must be parallel to their line of intersection. The hologram film must be placed in the back focal plane of the lower transform system so that the intensity pattern of the forward diffracted light from the object will be stationary. Since the back focal planes are not coincident, the reference beam will sweep across the hologram film. However, the phase of the reference beam will be synchronized with the phase of the forward diffracted light.

A field of view of about 4 cm diameter is desirable to minimize the problems of synchronizing the laser pulse with the particle arrival. Within this field of view, a particle will move no more than 4 mm during a laser pulse of 50×10^{-9} seconds or less. Therefore, stationarity is required only over any 4mm interval within the field of view. Lenses will be tested in order to select one which will produce a stationary intensity pattern as the object is translated through 4 mm. Lens selection will be carried out by translating two pinholes through a collimated He–Ne laser beam. As a further test, holograms must be recorded in the presence of the focussed backlighting beam. This is necessary to determine the "noise" level of any given lens.

Experiments to estimate the amount of back-reflected energy will be carried out with a He–Ne gas laser. Metal spheres of various sizes will be used and the relative intensity of reflected radiation will be measured. Using currently available data on film response to pulsed laser light, an estimate of the laser power and energy requirements then can be made (ref. 4).

An additional problem has been encountered in initial reflection experiments. The light returned from polished steel ball bearings is speckled. This is due to the fact that the surfaces of the bearings are not optically smooth. The resolution of the proposed system will be limited by the scale of resultant speckle spots; i.e., the average spot size will be the limiting aperture of the hologram. It is expected that as the metal objects become smaller, the speckle spots will grow larger inversely proportional to the object diameter (ref. 5). It is hoped that for objects in the 50- to 100-μ size range the characteristic spot size will be large enough to permit sufficient resolution.

CONCLUSIONS

To date the basic concept of the automatic velocity synchronized Fourier transform hologram camera has been proven to be theoretically sound. It is anticipated that data on lens stationarity and resolution along with data on back-reflected light intensity and speckle size will suffice to determine the feasibility of the basic concept. If technically feasible, this concept will make practicable a microparticle camera with automatic synchronization for any particle velocity, with no moving parts.

REFERENCES

1. LEITH, E. N.; AND UPATNIEKS, J.: Wavefront Reconstruction with Diffused Illumination and Three-dimensional Objects. J. Opt. Soc. Am., vol. 54, 1964, p. 1295.
2. DEVELIS, J. B.; AND REYNOLDS, G. O.: Theory and Applications of Holography, Addison-Wesley Publishing Company, Reading, Mass., 1967, p. 64.
3. NEWMANN, D. B.: Moving Object Holography with Unblurred Images of Normal Brightness. SPIE Holography Seminar Proceedings, vol. 15, 1968, p. 123.
4. THOMPSON, B. J.; WARD, J. H.; AND ZINKY, W. R.: Application of Hologram Techniques for Particle Size Analysis. App. Opt., vol. 6, no. 3, 1967, p. 519.
5. WARD, J. H.: Scattering of Laser Radiation by a Time-Varying Random Scatter. J. Opt. Soc. Am., vol. 58, no. 5, 1968, p. 715.

HOLOGRAPHIC IMAGERY THROUGH ATMOSPHERIC INHOMOGENEITIES

Joseph W. Goodman, D. W. Jackson, M. Lehmann, and J. W. Knotts
Stanford University
Palo Alto, Calif.

Certain holographic techniques show considerable promise for high resolution imaging through atmospheric inhomogeneities. If a reference wave is supplied from a point very close to the object, then under certain conditions the aberrations imparted to both the reference and object waves will be nearly identical. Interference of the two similarly aberrated waves yields a hologram which is free from distortion.

Experiments have been conducted in the laboratory and over outdoor paths to determine the applicability of this technique in the real atmosphere. For horizontal paths, experiments have shown that the so-called "isoplanatic region" within which improved resolution can be obtained is often very small. No corresponding information is yet available for vertical paths.

Experiments have been conducted over a 12 km horizontal path using a Q-switched ruby laser as the source and a 48-inch diameter telescope as the light collector. Resolutions obtained varied from 3 seconds of arc to 0.5 seconds of arc, depending on atmospheric seeing conditions. The primary practical problem encountered was the limited dynamic range of the photographic detector, which led to a loss of both resolution and sensitivity on nights of bad seeing.

BASIC HOLOGRAPHIC TECHNIQUES

A number of methods are known for using holography to form high resolution images in the presence of inhomogeneous media. For example, both Leith and Upatnieks (ref. 1) and Kogelnik (ref. 2) have demonstrated that if the inhomogeneities present during the recording process can be reintroduced during the reconstruction process, the aberrations can be largely canceled. Alternatively, if a hologram of a point-source object is recorded in the presence of the inhomogeneities, then that hologram may be used as a compensating plate to allow a more conventional system to form aberration-free images through the inhomogeneities (ref. 3). Such an approach is a generalization of the holographic technique used by Upatnieks et al. (ref. 4) to compensate for lens aberrations. Unfortunately neither of these techniques can be directly applied to the problem of atmospheric inhomogeneities, due primarily to the fact that the atmosphere is dynamic when examined over a time duration greater than about 1/100 of a second.

A holographic technique (ref. 5) which will allow cancellation of dynamic wavefront distortions is illustrated in figure 1. This technique differs from the others mentioned in that both the object and the reference waves pass through the same inhomogeneous medium, whereas in the previous cases an unaberrated reference wave was used. In this case, if the object and the reference point lie within a common "isoplanatic region" of the inhomogeneous medium, the two respective wavefronts will undergo nearly identical aberrations. When the two aberrated wavefronts interfere, the aberrations will largely cancel, leaving an undistorted pattern of interference. Images are obtained from this "lensless Fourier transform" hologram in the usual fashion shown in figure 2.

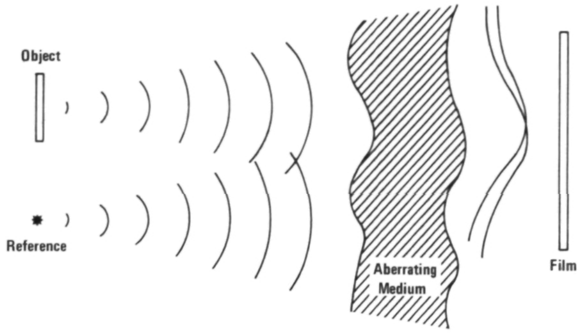

FIGURE 1.—Recording an undistorted hologram in the presence of an aberrating medium.

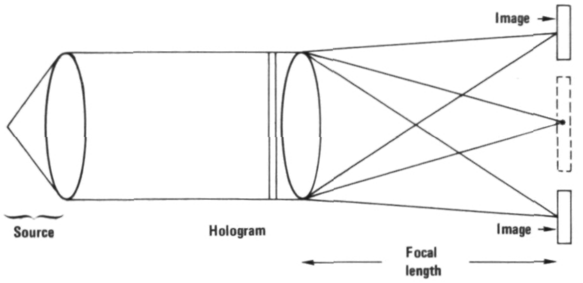

FIGURE 2.—Obtaining the images.

The atmosphere poses two fundamental limitations to the utility of this latter technique in real applications. First, the reader will recall that the reference and object wavefronts must undergo identical aberrations if an undistorted pattern of interference is to be obtained. This condition will occur only for object points situated within a certain "isoplanatic region" about the reference point. The size of the isoplanatic region thus determines the field-of-view (about the reference point) over which diffraction-limited images can be obtained.

For horizontal paths through the earth's atmosphere, this field-of-view is indeed small. Figure 3 illustrates an experiment performed by J. D. Gaskill (ref. 6) to determine the size of the isoplanatic region for a 90-meter horizontal path. The output of a CW (He–Ne) laser is divided to form two mutually coherent point sources separated by a variable distance r_1. The interference pattern generated by the two sources is recorded some 90 meters away. The visibility $m(r_1)$ of the fringe is thus measured as a function of separation r_1 of the two sources. The measurement is in all cases averaged over 1 minute, which far exceeds the characteristic time associated with the atmospheric fluctuations. The result is a plot of visibility squared as a function of separation r_1, as shown in figure 4. The two solid curves bound 90 percent of the experimental points and thus indicate the general trend of the data. The linear dimension of the isoplanatic region, as estimated from this data, is less than 5 cm. For longer paths the size of the region is smaller.

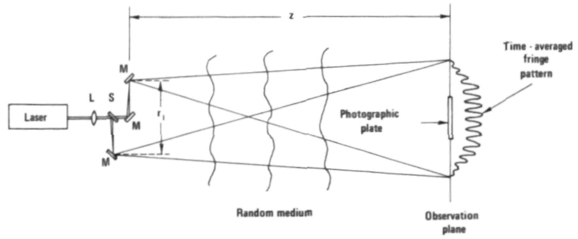

FIGURE 3.—Measuring the size of an isoplanatic region.

The holographic technique is, in fact, least affected by turbulence introduced close to the collecting aperture. This fact suggests that holography may be of most interest for looking upwards through the atmosphere at coherently illuminated space objects. Measurements of the atmospheric distortions of images of twin stars indicate that the size of the isoplanatic region looking up exceeds a few seconds of arc, and there is speculation that it may be as large as 20 seconds of arc (ref. 7). There is not yet any experimental evidence to confirm the latter number, however.

Turning now to the second fundamental limitation introduced by the atmosphere, we consider the effects of the atmospherically-induced intensity perturbations of the collected waves. If the exposure time is long compared to the characteristic fluctuation time of the atmosphere, the random intensity patterns are sufficiently averaged to be of little concern. However, for short exposures, such as obtained with a pulsed laser, the intensity perturbations have important effects. First, the hologram has a mottled structure, which is equivalent to a random apodization of the collecting aperture. As a consequence, the images obtained have a background glow, which can be troublesome if the image is weak.

More important, the large dynamic range of the intensity pattern of the reference wave prevents efficient use of the transmittance-exposure characteristic of the recording medium. Over a considerable region of the collecting aperture the reference wave may be so weak or so strong as to place the operating point (on the transmittance-exposure curve) in a region of low slope, where fringes of intensity are not efficiently transferred to variations of transmittance. As a consequence the sensitivity of the holographic process may be seriously degraded. Comparison of laboratory bench experiments carried out in the absence of turbulence and field experiments carried out over a 12 km horizontal path indicate that a loss of sensitivity of at least two orders of magnitude was attributable to this phenomenon. It is possible that the use of electronic detectors (e.g., image orthicons) may provide sufficient dynamic range to overcome this limitation.

EXPERIMENTAL RESULTS

A number of holographic imaging experiments have been carried out over horizontal paths through the atmosphere. The illumination source for these experiments was a commercially

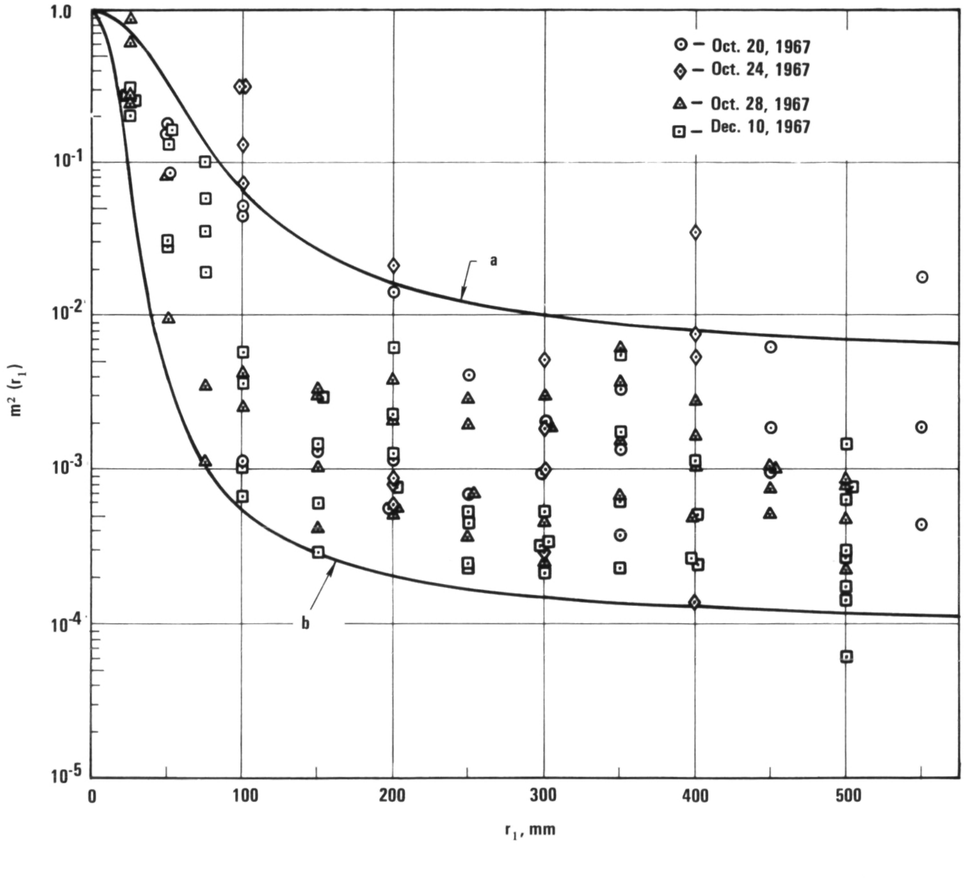

FIGURE 4.—Visibility squared as a function of source separation for a 90-meter path (courtesy of J. D. Gaskill).

available Q-switched ruby laser which had been modified to obtain a highly coherent output. The transmitted pulse contained approximately ½ joule of energy per pulse and had a duration of about 20 nanoseconds.

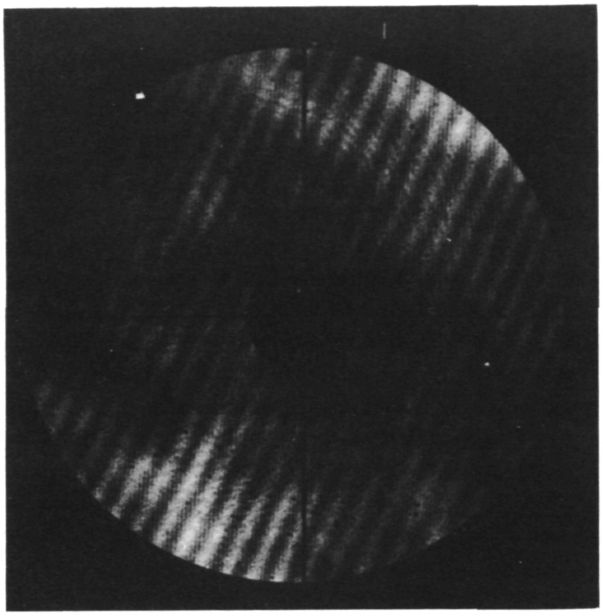

FIGURE 5.—Hologram of retroreflector objects.

The first set of experiments was carried out at the Air Force Electro-Optical Facility near Cloudcroft, New Mexico, in late fall of 1967. A 4-foot-square target panel was placed at the target site some 12 kilometers from the transmitting and receiving site. Cube corner retroreflectors and aluminized resolution charts were available for use as references and targets. The receiving system utilized a 48-inch aperture reflecting telescope. A 35mm camera with a 50mm, $f/1.4$ lens was mounted near the Newtonian focus of the primary mirror. To record fringes the camera was focused on the surface of the primary mirror. The resulting image of the mirror was 7.5 mm in diameter. Linograph Shellburst film was used to record these images.

The reference was in all cases supplied by a retroreflector on the target board. Figure 5 shows a typical hologram recorded for retroreflector objects. Figure 6 shows holographic images of retroreflector objects obtained under conditions of good atmospheric "seeing." The resolution achieved is estimated to be about 0.5 second of arc. Figure 7 shows corresponding results obtained under conditions of poor seeing. In this case the resolution is 3 or 4 seconds of arc. Figure 8 shows holographic images of a man's head silhouetted against a skotchlite panel (adequate precautions were taken to prevent eye damage). The drawing of figure 9 will help to define the outlines of the subject.

In summer and early autumn of 1968,

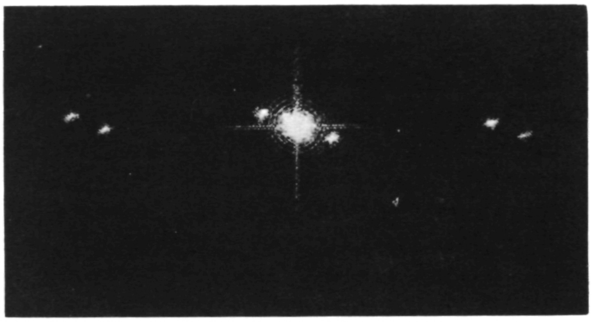

FIGURE 6.—Holographic images of retroreflector objects under conditions of good "seeing."

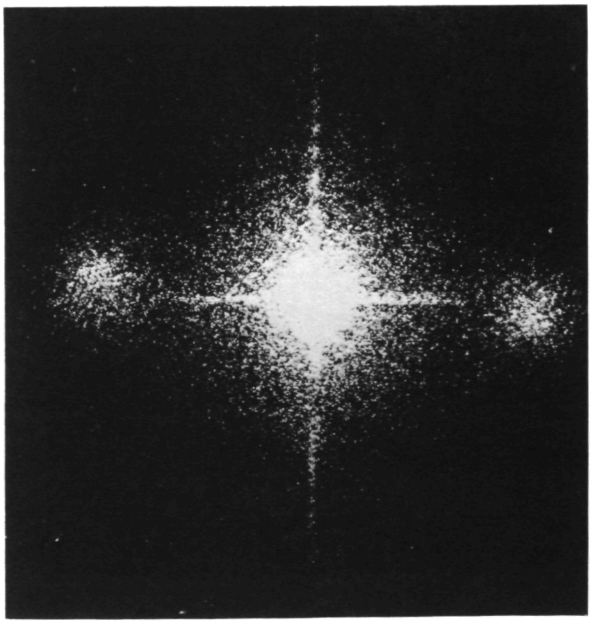

FIGURE 7.—Holographic images of retroreflector objects under conditions of poor "seeing."

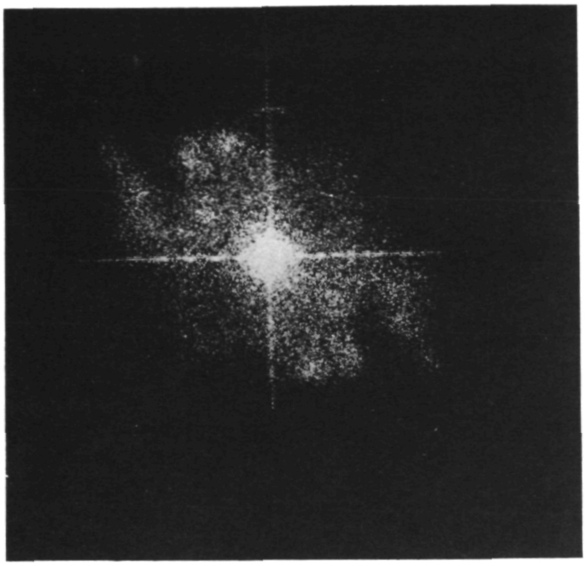

FIGURE 8.—Holographic image of the silhouette of a man's head.

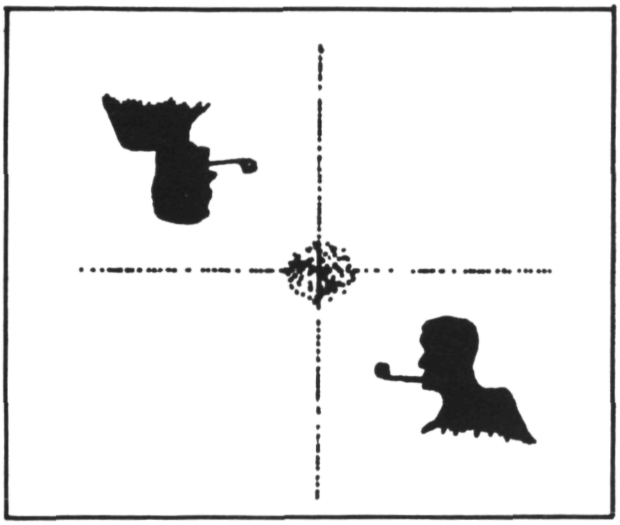

FIGURE 9.—Outline of the image shown in figure 8.

additional experiments were conducted over a 1.9 km path at Stanford. In this case a very low contrast developer (POTA) was used to process the Linograph Shellburst film. The resulting holograms showed far less saturation effects (due to the random intensity variations of the reference wave) than were observed using HRP developer. The resolution obtained in the reconstructed images was greatly improved by the use of the low contrast developer, but the image signal-to-noise ratios remained poor, a consequence of the very low slope of the transmittance-exposure curves under low contrast development. Thus the very large dynamic range of the reference-wave intensity after propagation through atmospheric inhomogeneities causes the most severe practical limitations to the quality of holographically obtained images.

ACKNOWLEDGMENT

The work reported here was supported by the U.S. Air Force Avionics Laboratory.

REFERENCES

1. LEITH, E. N.; AND UPATNIEKS, J.: J. Opt. Soc. Am., vol. 56, 1966, p. 523.
2. KOGELNIK, H.: B. S. T. J., vol. 44, 1965, p. 2451.
3. GOODMAN, J. W.: Introduction to Fourier Optics. McGraw-Hill Book Co., 1968.
4. UPATNIEKS, J.; VANDER LUGT, A.; AND LEITH, E.: Appl. Opt., vol. 5, 1966, p. 589.
5. GOODMAN, J. W.; HUNTLEY, W. H.; JACKSON, D. W.; AND LEHMANN, M.: Appl. Phys. Let., vol. 8, 1966, p. 311.
6. GASKILL, J. D.: Holographic Imaging Through a Randomly Inhomogeneous Medium. Ph.D. Thesis, Dept. of Electrical Engineering, Stanford University, Stanford, California, 1968.
7. Restoration of Atmospherically Degraded Images. National Academy of Sciences, National Research Council, 1966.

Page intentionally left blank

Page intentionally left blank

Session IV

POST-FACTO REMOVAL OF MOTION DEGRADATIONS

BRIAN J. THOMPSON, *Chairman*
University of Rochester
Rochester, N.Y.

Page intentionally left blank

Page intentionally left blank

POTENTIAL AND LIMITATIONS OF TECHNIQUES FOR PROCESSING LINEAR MOTION-DEGRADED IMAGERY

JAMES L. HARRIS, SR.
Scripps Institution of Oceanography
University of California, San Diego

This paper deals with computer processing of images degraded by linear image motion. An attempt is made to emphasize the fundamental aspects of the processing problem including questions of information content of the degraded images, the implication of errors in the processing. Such errors are induced by misestimation of the amount of image motion, inadequate correction for sensor nonlinearities, and the presence of noise. Various approaches to optimum filtering are discussed and several simple but sometimes effective nonoptimum filtering operations are described. Examples of computer processing are given to illustrate these topics.

INFORMATION LOSS IN THE DEGRADED IMAGE

It is important to recognize that a degraded image has suffered a fundamental loss of information as compared to the recording which would have been produced in the absence of degradation. This fundamental loss is not recoverable by post-detection processing.

One approach to a quantitative discussion of the penalty imposed by an image degradation is to determine the extent to which the degradation alters the ability to distinguish between members of a set of possible objects. For the case of a binary decision, i.e., two object alternatives, it has been shown that in the presence of Gaussian, white noise, the probability of correct decision, utilizing optimum processing, is uniquely determined by the noise variance and the quadratic content of the difference image (ref. 1) defined as,

$$Q=\int\int[H_1(x, y)-H_2(x, y)]^2\,dx\,dy \qquad (1)$$

where H_1 and H_2 are the irradiance maps of the images of the two object alternatives positioned and oriented such as to produce maximum cross-correlation.

The effect of any image degradation is to reduce the quadratic content of the difference image and therefore the probability of correctly distinguishing between the two alternatives.

Figure 1 shows a set of three images, U, C, and O degraded by linear image motion of various amounts corresponding to 2, 4, 6, . . . , 24 picture elements. Also shown are the difference images U–C, U–O, and C–O. It is important to recognize that the difference image U–C has both positive and negative components, shown squared in the pictures. It is clear that in the absence of degradation, U–C has a greater Q than U–O or C–O.

Because of the linearity of the operations, the degraded difference image can be found either by degrading the original difference image or by differencing the two degraded image alternatives. When a difference image has positive and negative components in close proximity, the difference image will be rapidly diminished by a degradation which smears the two components together. Therefore while *U–C* is the most easily distinguished pair in the absence of degradation, it becomes the most difficult pair in the presence of a large amount of degradation. This can be seen by careful examination of the most severe degradation shown in figure 1. This fact is made quantitative by the quadratic content calculated curves shown in figure 2. The difference images *U–O* and *C–O* are numerically identical and therefore fall on the same curve.

This example illustrates the fact that the extent to which a specific degradation reduces information can be quantitatively defined only if the specific image alternatives are also defined. It is important to recognize that the ability to distinguish between object alternatives involves not only the extent of the degradation but also the inherent contrast of the objects, the contrast transmittance of the atmosphere, the size of the recorded image, and the noise level of the sensor. Improvements with respect to any of these factors increase the information contained in the image and makes possible more extensive processing operations.

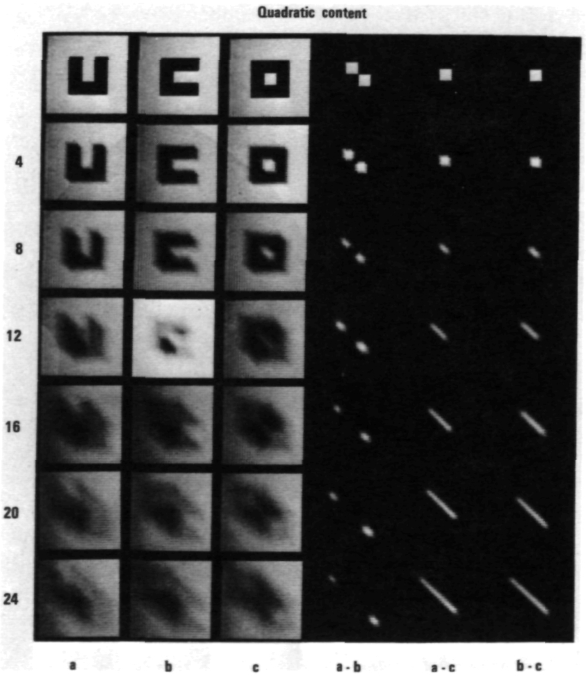

FIGURE 1.—Computer generated degradations of three objects to illustrate the quadratic content concept. The degradation is image motion at an angle of 45 degrees with respect to the horizontal. The numbers on the left are the amount of image motion in terms of number of picture elements. The three difference images are shown at the right. The difference images have been squared so that all values are positive.

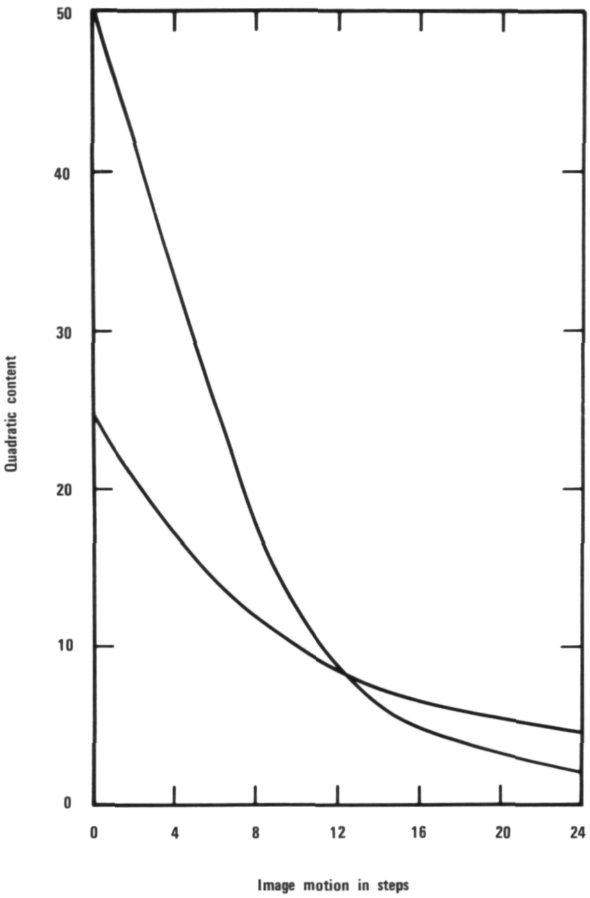

FIGURE 2.—The quadratic content values calculated for the case shown in figure 1. The topmost curve on the left is for *U–C*. The bottom curve is for both *U–O* and *C–O*. The quadratic content scale is arbitrary.

THE IMAGE AND ITS TRANSFORM

Image restoration procedures used at the Visibility Laboratory generally employ Fourier transformations. The calculations are made on a digital computer with the results displayed a cathode-ray tube (CRT). The CRT is then

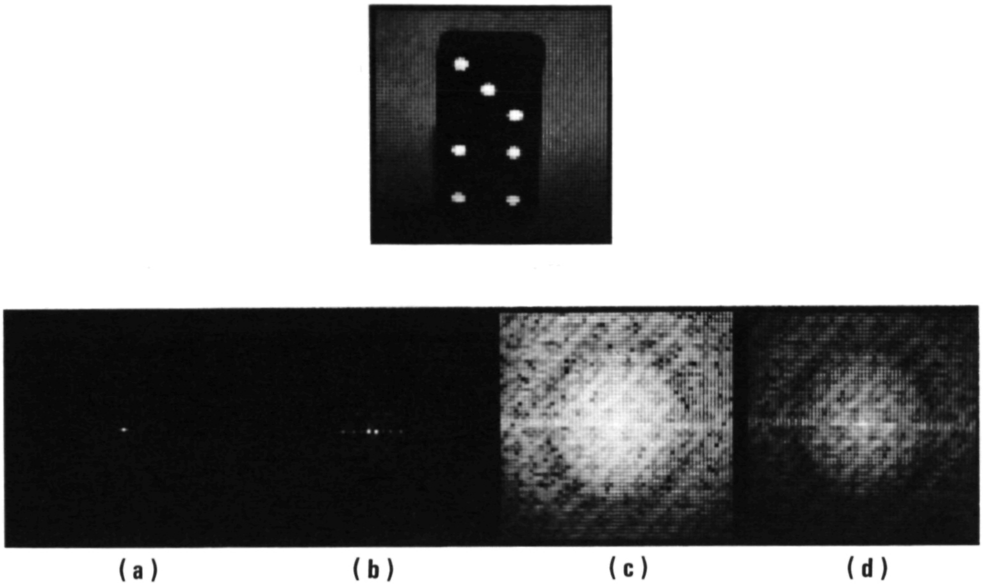

FIGURE 3.—Illustration of the various ways of displaying the modulus of the image spectrum; (a) is a linear presentation, (b) is linear after removal of the zero-frequency term, (c) is the logarithm of the modulus map, (d) is the modulus map raised to the 0.25 power.

photographed. Figure 3 shows a CRT photograph of a digitized domino image. The bottom of that figure shows a number of ways of displaying the modulus of the Fourier transform of the image. In figure 3(a) the transform is displayed linearly and little is visible other than the zero-frequency component in the center of the picture. This is because the zero-frequency component is large compared with all other modulus values. In figure 3(b) the zero-frequency component is removed so that more of the spectrum is visible, but it is apparent that the spectrum falls off rapidly with increasing spatial frequency and that much of the spectrum is still not visible. In figure 3(c) the logarithm of the modulus was taken prior to display. In figure 3(d) a gamma was applied to the modulus image prior to display, i.e., the array of numbers was raised to a power, in this case 0.25. This technique, which is most frequently used, seems to give good results, is well adapted to the display used in the research, and is an integral part of the software of our picture generation.

For the case of linear image motion, each point on the object becomes a line in the image, the length of which is equal to the extent of the image motion. The direction and extent of image motion is readily seen in the computer generated domino image degradation shown in figure 4. The modulus of the degraded image is shown to the right. (All remaining modulus pictures shown in this paper are at a gamma of 0.25.)

The dark bars in the modulus picture perpendicular to the direction of the motion result from the fact that the optical transfer function (OTF) for the degradation is of the form,

$$\tilde{s}_I = +\frac{\sin 2\pi k(f_y \sin\theta - f_x \cos\theta)}{2\pi k(f_y \sin\theta - f_x \cos\theta)} \qquad (2)$$

where K is a constant determined by the amount of image motion with respect to the f_x axis and f_x and f_y are the x and y components of spatial frequency.

The modulus picture is therefore an interesting diagnostic tool for the case of linear image motion since the picture shows both the direction and extent of the motion. It should be noted that since the OTF is multiplicative, the bar structure will be present no matter what the nature of the object although it will be more visible with some object spectra than others.

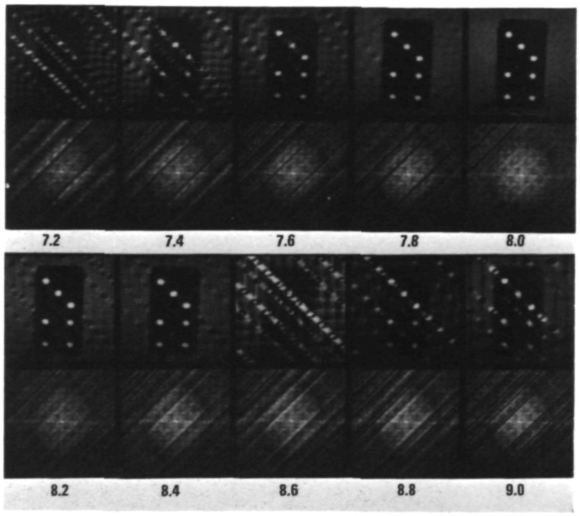

FIGURE 5.—A restoration experiment in which the assumption of the amount of image motion is varied. The correct value is eight picture elements. The assumed value is shown below each picture. The spectra shown are those after the processing OTF has been applied.

As a diagnostic tool it is important to determine the extent to which the bars are visible in the presence of noise. The second row of pictures in the figure shows the spectrum with Gaussian, white noise added such that the peak signal-to-noise ratio in the degraded domino is 100, 10, and 1 respectively. The bottom row of pictures show a technique which has been found useful in determining the presence of image motion in noisy images. The bottom half of each picture is identical to the modulus picture above. In the top half of the picture the actual modulus values have been replaced at each point in the spectrum by an average value computed along a line through the spectrum. This technique of signal integration in the presence of noise makes visible bars not easily seen in the original modulus picture. If the direction of image motion is unknown it is necessary to search in angle.

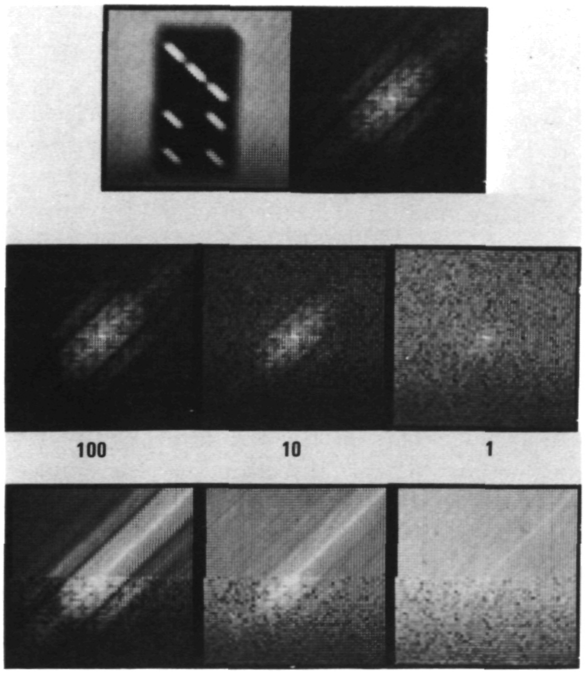

FIGURE 4.—An image motion degraded image and its spectrum. The middle row shows the spectrum when additive noise is present. The numbers are signal-to-noise ratios in terms of the average signal to root-mean-square noise. The bottom row shows a technique for locating the null structure by replacing the true modulus with its average along a line.

THE RESTORATION OPERATION

The restoration operation in the frequency domain is accomplished by applying an OTF which is the reciprocal of $\tilde{s}_I$. In many practical cases, the extent of the image motion may be unknown and it is therefore a matter of interest to determine the impact on the restoration attempt associated with incorrect assumptions as to the extent of the smear.

Figure 5 shows the results of such a computer study. In this case the computer generated image motion was eight resolution elements in length at an angle of −45° with respect to the horizontal. The pictures show the processing results obtained assuming a smear of extent given by the numerical value below the picture. It is interesting to observe the onset of spurious image detail as the assumed value departs from the correct value. In the numerical print out from this processing, the spurious detail is accompanied by negative values in the restored image. Their magnitude appears to be roughly proportional to the error in assumption of the extent of the image motion.

It is somewhat comforting to see that the errors are of this spurious type. It would be discomforting if incorrect processing turned this domino into another domino of different denomination.

Below each processing is the restored spectrum. It is clear that only at the correct value does the processing OTF correctly compensate the spectrum. The spurious detail clearly arises when some large correction is applied to a frequency which has suffered a much smaller attenuation. Since the OTF also involves 180° phase shifts, incorrect processing shifts phase at frequencies where no phase shift was created in the degradation and fails to shift phsae at frequencies where phase shifts were created in the degradation. It may be noted that even with the correct processing, the pictures show dark bars at the higher spatial frequencies in the corrected spectrum. This is because the computer was instructed that if the required restoration factor exceeded a value of 100, the restoration factor should be set equal to zero. This procedure has significance when noise is considered.

UNCORRECTED SENSOR NONLINEARITY

Photographic films, and, to varying degrees, other sensors, have nonlinear properties. In the case of photographic film, the transmission of the processed film is not directly proportional to the irradiance on the film which caused the exposure. The characteristic curve of the film defines this input-output relationship. This type of nonlinearity is correctable, i.e., if the characteristic curve is stable and known, then transmission readings can be converted to image irradiance values prior to initiating the processing. This is an important step because the Fourier processing described in this paper is based on the representation of the degraded image as a linear convolution of the ideal geometric image and the point spread function of the degraded image. For this reason it is important to utilize established photometric calibration procedures of imprinting gray scales on the film.

To establish some feeling for the tolerance of the processing to uncorrected or residual nonlinearities in the sensor a computer study was made in which nonlinearity was intentionally introduced.

The results of this study are shown in figure 6. The processing employed correct values for the extent and direction of the motion. The nonlinearity introduced was of the gamma type, i.e., the degraded image was raised to a power. The corresponding gamma values are shown below each picture. It is interesting that

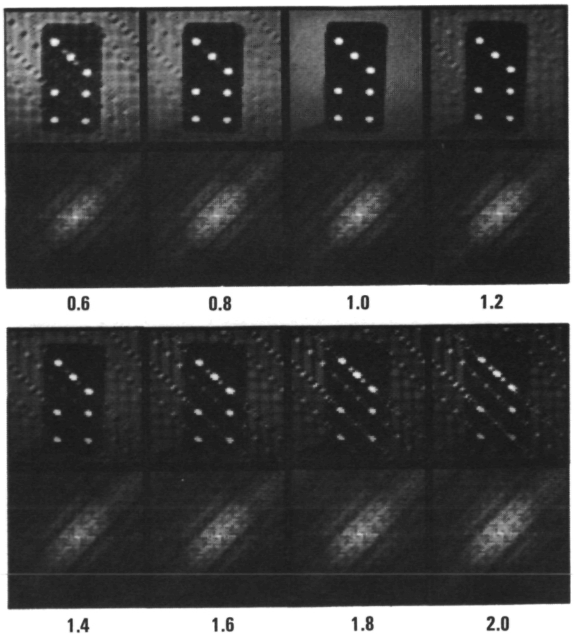

FIGURE 6.—A computer study of the effect of film nonlinearity on the processing results. Nonlinearity in the degraded image was introduced by raising the image array of numbers to the power shown below each picture. The spectra shown are obtained from the transform of the nonlinear image prior to doing the processing. The processing used the correct values of the amount and direction of the image motion.

the result of nonlinearity is spurious detail very similar to that introduced by errors in the assumption of extent.

Below each processing is the uncorrected spectrum. The spectrum changes caused by the nonlinearity are subtle and not readily recognized.

PROCESSING IN THE PRESENCE OF NOISE

The computer studies described in the preceding sections were made in the absence of noise. Noise is the critical factor in any image processing work. Given sufficient signal-to-noise ratio an image can be manipulated at will. It is a matter of the utmost importance to determine the extent to which processing can be performed in the presence of noise.

Noise was introduced into the degraded domino image. Since additive noise does not properly characterize the noise properties of many sensors, the noise used was multiplicative in the sense that the noise variance at each point in the image was made directly proportional to the irradiance at that point. Figure 7(a) shows the degraded image at three different noise levels, labeled 1, 10, and 100. These numbers refer to the maximum, i.e., highlight, signal-to-noise ratio in the picture. Figure 7(b) shows the corresponding spectrum modulus pictures.

Figure 7(c) shows the poor results obtained by applying the direct inverse filter of the degradation process. Large enhancements are applied to spectral regions containing mostly noise with the result that the processed image is noise dominated.

If a mathematical criterion is adopted then an optimum filtering can be derived. One such criterion is that the processed image is to be made a best-least-squares fit to the correct image. For Gaussian, white, additive noise the processing OTF is then,

$$\tilde{S}_P=\frac{1}{\tilde{S}_I}\,\frac{1}{1+\dfrac{2\sigma^2}{\tilde{H}_I^2}}. \qquad (3)$$

where $\tilde{S}$ is the OTF with subscripts I and P indicating input (degraded image) and processing, σ^2 is the noise variance in the frequency

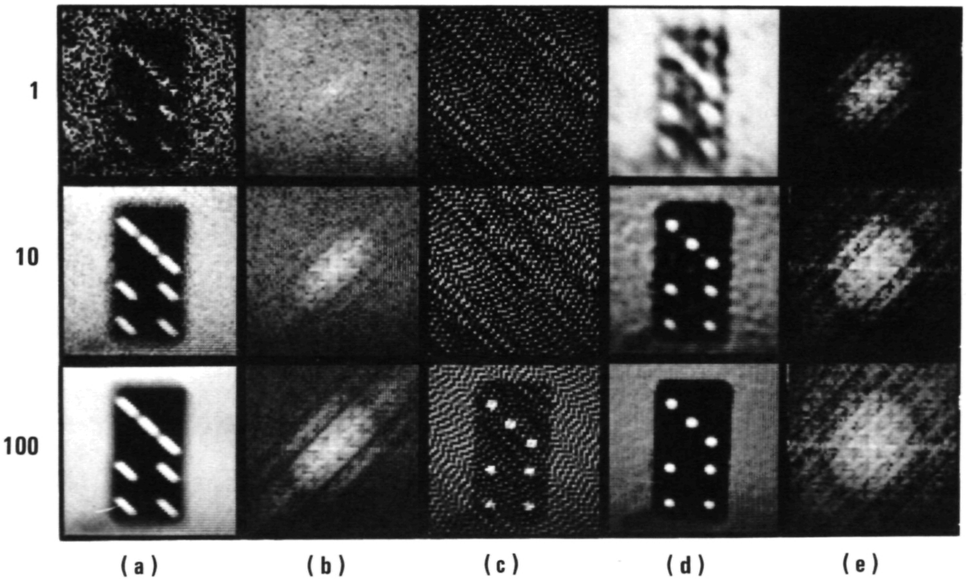

FIGURE 7.—(a) Comparison of processing results for direct inverse filtering, (b) and best-least-squares filtering, (d). The noise is multiplicative with the maximum signal-to-noise ratio in the degraded image shown in the numbers to the left. (b) The spectra of the unprocessed, noisy, degraded image. (e) The corrected spectra after the best-least-squares filtering.

domain, and $\tilde{H}_I$ is the degraded image spectrum. The equation indicates that when the noise level is very low, inverse filtering is to be used, but that in regions of the spectrum where the signal is small relative to the noise, an attenuation is introduced.

Figure 7(d) shows processing of the noisy images based on equation (3). The results are a dramatic improvement over the direct inverse filter results shown in figure 7(c). The restored spectra from the best-least-square filtering is shown in figure 7(e).

The results of column D cannot be realized practically in most cases of interest. The direct application of equation (3) implies a knowledge of the degraded spectrum whereas all that is known by measurement is the value of the degraded spectrum plus noise.

A large portion of the research in image processing is directed toward attempting to optimize the filtering operations. The comparison of (c) and (d) in figure 7 shows that this is a matter of prime importance.

One final comment must be made with respect to the question of optimum processing. The final customer for an image restoration is the human visual system. The state of the art does not permit a set of equations to describe the human. Lacking these equations it is not possible to define precisely the meaning of optimum filtering and there is no solid basis for the assumption of best-least-square or any other criterion.

OTHER COMPUTER PROCESSING TECHNIQUES

It was stated earlier in this paper that the OTF for linear image motion has periodic 180° phase shifts. This phase shift is very important to the problem.

In figure 8(a), the same degraded domino and spectrum are shown. In figure 8(b) the result of applying a filter as shown by the lower picture is demonstrated. This filter passes only those spatial frequencies which have undergone 180° phase shifts. The resulting image is shown above. In figure 8(c) the filter passes only those spatial frequencies which were not shifted in phase in the degrading process. The image generated by application of this mask is shown above.

It is the sum of these two images that generates the degraded image. If however the image of figure 8(b) is *subtracted* from the image of figure 8(c), then the phase shift has been corrected although the amplitudes of the spatial frequencies have not been corrected. An image obtained in this way is shown in figure 8(d). The domino spots are noticeably improved. A somewhat better result is obtained in figure 8(e) by multiplying the image of (b) by a factor of two prior to subtracting it from (c). Partial correction of imagery by phase shift only is of considerable interest because it can be accomplished at high noise levels. In the presence of white additive noise where the noise at each spatial frequency is independent, a phase shift applied to any frequency does not alter the signal-to-noise ratio since the noise phase was random initially.

Correction of image motion degraded images by spatial differentiation has been discussed elsewhere (ref. 2). Since the point spread function for linear image motion is a line, differentiation in the direction of the line results in a pair of Dirac functions opposite in sign and separated by a distance equal to the extent of the image motion. To an image, the two Dirac functions imply a restored image on which is superimposed a ghost image displaced by the extent of the image motion. A processing of the domino degraded image by spatial differentiation is shown in figure 8. Since a spatial differentiation will produce both positive and negative values, there are a number of options for displaying the result. In figure 8(f) the largest negative value was made the black level for the picture. In figure 8(g) all negative values were made equal to zero, and in figure 8(h) all negative values were made positive, i.e., rectified.

NONDIGITAL PROCESSING TECHNIQUES

There are many nondigital image-restoration techniques which can be applied to the linear image motion case. These would certainly include coherent optical processing, incoherent convolution techniques, and, in the case of electronic sensors, real-time video processing.

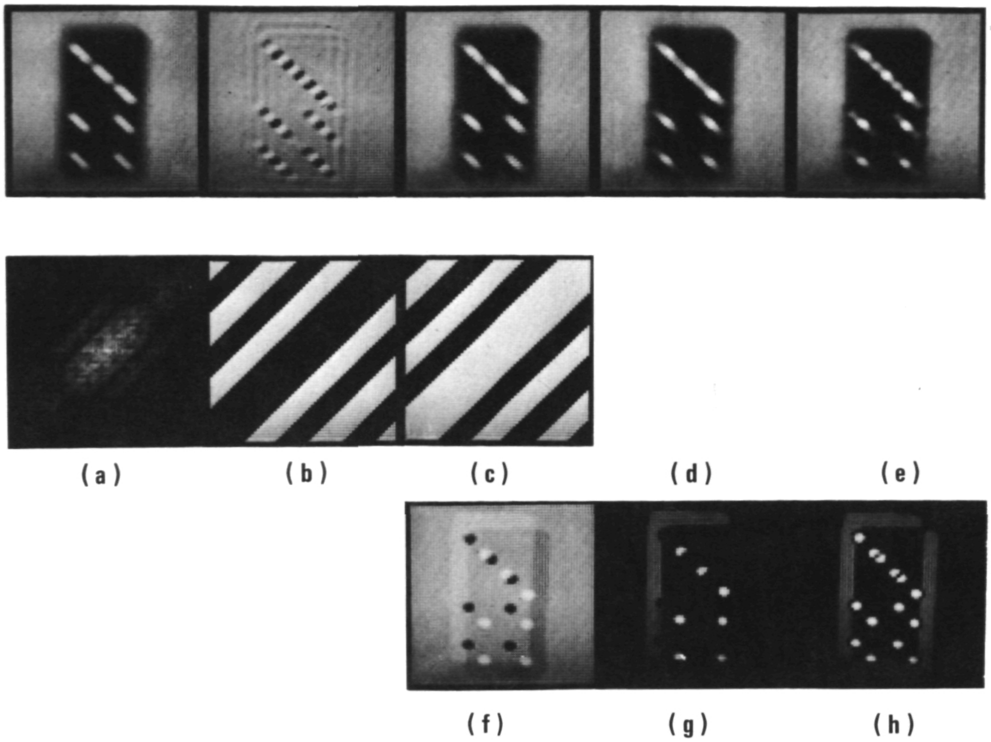

FIGURE 8.—A computer study showing results of phase shifting and spatial differentiation operations. (a) The degraded image and its spectra, and (b) the image which results from passing only those frequency components which have been shifted 180 degrees by the degradation process. (c) The image produced by passing only those frequencies which have not been shifted in phase. (d) The difference between the images of (b) and (c). (e) The results of multiplying images (b) by 2 before subtracting it from (c). The images shown in (f), (g), and (h) are the results of spatial differentiation of the degraded image. They differ only in the manner in which the negative values are displayed. In (f), the most negative value was made the black level. In (g), all negative values were made equal to zero. In (h) all negative values were made positive.

Each of these techniques has advantages and disadvantages in terms of cost, size, weight, volume of data handling, real-time capabilities, precision, extent to which affected by sensor nonlinearity, etc. Each specific application must be studied on an individual basis to determine the most suitable approach.

The one-dimensional nature of this degradation would appear to make it particularly well suited to direct electrical filtering of the output of a scanning type sensor with the direction of scan oriented with the image motion. Each line can be processed independently so that there is no requirement for line to line storage.

The fundamentals of the restoration operations are common to all mechanizations and it is hoped that the fundamental studies conducted on the digital computer can help to advance technology not only for digital processing but analog as well.

REFERENCES

1. HARRIS, J. L.: J. Opt. Soc. Am., vol. 54, 1964, p. 606.
2. HARRIS, J. L., Sr.: J. Opt. Soc. Am., vol. 56, 1966, p. 569.

SOME CONSIDERATIONS IN POST-FACTO BLUR REMOVAL

LOUIS J. CUTRONA AND WILLIAM D. HALL
KMS Industries
Ann Arbor, Mich.

There are a number of considerations of importance in the problem of post-facto blur removal. In this paper some of these aspects will be considered.

In the recording of images, degradation occurs when there is relative motion between the image and the recording material. This relative motion can be due either to object motion or to movement of the camera. In each case the image of a spot is recorded as a streak. It is the purpose of this paper to consider operations which can be performed upon the recorded image to remove or reduce the blur due to the motion.

In attempting to use filtering techniques one must first ascertain that such techniques are applicable. It can be shown that filtering techniques apply when blurring operation can be written as a convolution. In such cases the motion blur is equivalent to passing the image through a filter; it is useful to attempt to recover the scene by passing the image through a second filter intending to remove or reduce the blur.

A naive approach is one in which the restoring filter is constructed as the reciprocal of the smearing filter. In general, this technique fails because wherever the distorting filter had zeros the correcting filter has poles and one cannot mechanize the transfer function with such poles.

This problem is eased if, instead of requiring the correcting filter to be the reciprocal of the distorting filter, one requires the product of these filters to be an appropriate function.

A further complication arises when the distorted or smeared photograph is imbedded in noise. In this case the filter design must take into account the statistics of the signal as well as the statistics of the noise. These statistics plus the operation desired, for example, can be used to specify a Wiener least-mean-square error filter. The selection of this filter is an exercise in information theory.

In attempting to mechanize the filter, a number of problems may arise. The problem of poles in the filter has already been mentioned. Additionally, there is often a requirement for a very wide dynamic range in the filter. Inasmuch as photographic film has a limited dynamic range, this often is a problem.

Vander Lugt has described several configurations whereby a complex filter function can be recorded. Unfortunately, his technique requires that the impluse response be real. Often this may not be a problem.

The recording of the filter usually requires that the film transmissivity be proportional to the magnitude squared of the incident amplitude. Film characteristics have to be carefully selected and the operating point carefully chosen to achieve this result as an approximation.

In using the Vander Lugt type filter, the filter must be carefully and accurately positioned. This also may be a source of difficulty.

In some cases, some of the difficulties of the Vander Lugt configurations may be avoided by the use of a configuration suggested by C. S. Weaver, D. Ramsen, and A. Silvestri of Stanford University. This configuration avoids the necessity for careful adjustment of the filter position. It may also have some advantage with respect to dynamic range problems. This configuration will be described in the talk.

351-160 O—69——10

The Stanford configuration can be modified to make real time spatial filtering possible. For example, it is possible to record the signal and filter onto photochromic material, free radical material, or dry silver material by exposure to blue light from an argon laser. The output can then be observed using a He–Ne laser which does not expose these materials. Additional details for achieving real time spatial filtering will be discussed.

The problem will be illustrated by considering primarily the problem of smear along a straight line such as might occur in a camera with inadequate motion compensation. If the smearing pattern is not a straight line segment, in principle the same types of techniques with different filters would be applicable. However, there is not much loss in generalities by considering primarily the linear case.

In this paper a number of considerations pertinent to post-facto blur removal using coherent optical techniques are discussed. The blur is generated by image motion during its recording. While more general motion can be handled, this paper will concern itself with a smear along one direction only.

The smearing operation can be represented as a filtering operation in the spatial frequency domain. An insistence on perfect reconstruction in the noiseless case leads to a correction filter which is the reciprocal of the smearing filter. The smearing filter unfortunately has zeros. The correction filter, being the reciprocal function, has poles. Such poles cannot be fabricated in optical filters. Thus, the correcting filter cannot be constructed.

Fortunately, relaxed requirements on the reconstruction can lead to realizable optical filter functions.

One of the relaxations comes about by recognizing that a photograph is of finite extent. The reciprocal filter discussed above, if realizable, would give perfect reconstruction of the image with zero output elsewhere. If one merely requires perfect reconstruction over the interval covered by the photograph without requiring the reconstruction to be zero elsewhere one can get rid of the poles in the reconstruction filter.

A further decrease in the difficulty of making the optical filter occurs if one relaxes the required resolution to a finite value.

The detailed nature of the optical filter functions resulting in each of the cases above is described in this paper.

There are also some problems associated with making and using the filters. Some remarks regarding these problems are made below.

TECHNICAL DISCUSSION

It is useful to consider the problem of blur removal by writing an expression describing the blurred image, $g(x)$, due to a linear smear of length x_0 of the function $f(x)$

$$f_2(x)=\int_0^{x_0} f_1(x-q)dq=\int_{x-x_0}^{x} f_1(q)dq \qquad (1)$$

To obtain the filter function description of the operation above one takes the Laplace transform of equation (1). If $F_2(s)$ and $F_1(s)$ represent respectively the transforms of $f_2(x)$ and $f_1(x)$ one obtains

$$F_2(s)=[1-exp(-sx_0)]F_1(s)/s=H_1(s)F_1(s) \qquad (2)$$

Here

$$H_1(s)=[1-exp(-sx_0)]/s \qquad (3)$$

is the filter function corresponding to the linear smearing operation.

An approach to correcting the smear is that of operating on the smeared photograph with a filter $H(s)$ such that

$$H(s)=1/H_1(s)=s/[1-exp(-sx_0)] \qquad (4)$$

If the filter described by equation (4) could be built it would give a perfect reconstruction of $f_1(x)$ from its smeared image $f_2(x)$. However, it is evident from equation (4) that $H(s)$ has poles at

$$s=j2\pi m/x_0 \qquad m=\pm 1, \pm 2 \ . \ . \ . \qquad (5)$$

Some attempts have been made to construct $H(s)$ for combatting smear images. However, the inability to realize the filter poles has limited the smear reduction capability using this approach.

Let the requirement for reconstruction now be relaxed so that a filter $H_2(s)$ operating upon $F_2(s)$ as given by equation (2) has $f_1(x)$ as its output over the interval spanned by the smeared image and an arbitrary output elsewhere. This possibility was discussed by D. Slepian (ref. 1) as a means to get a filter function without poles. The following analysis exploits the same degree of freedom in a different manner and arrives at a slight generalization of Slepian's results.

Let $f_1(x)$ as above represent the original unsmeared object with $f_2(x)$ its smeared image. It is assumed that $f_1(x)$ is of finite extent—namely

$$f_1(x)=0 \text{ for } x<0 \text{ and for } x>L \tag{6}$$

Equations (1), (2), and (3) give relations among these quantities.

Let it now be required to specify a correcting filter $H_2(s)$ to operate on $f_2(x)$ so that its output is $f_3(x)$ with the properties that

$$\begin{aligned} &f_3(x)=0 \text{ for } x<0\\ &f_3(x)=f_1(x) \text{ for } 0\leq x\leq L\\ &f_3(x)=g(x-L) \text{ for } x>L \end{aligned} \tag{7}$$

with $g(x)=0$ for $x<0$

Thus the reconstruction is required to give $f_1(x)$ in the interval containing the image of interest, with to this point, an arbitrary output for $x>L$.

It will be the purpose of the continuing analysis to choose $g(x)$ and $H_2(s)$ to give $f_3(x)$ with the properties given by (7).

If $F_3(s)$ represents the Laplace transform of $f_3(x)$ then (8)

$$F_3(s)=F_1(s)+\exp(-sL)G(s) \tag{9}$$

Equation (8) simply states that the function $f_2(x)$ is operated on by the filter $H_2(s)$ to produce $f_3(x)$ at its output. Equation (9) is an immediate consequence of relations (7) and the Laplace transform theorem on translation.

If equations (8), (9), and (2) are combined and the resultant expression is solved for $H_2(s)$, one obtains

$$H_2(s)=\frac{1}{H_1(s)}+\Big[\exp(-sL)G(s)\Big]/F_2(s) \tag{10}$$

Let $G(s)$ be written as the product of two functions, one of them being $F_2(s)$

$$G(s)=H_3(s)F_2(s) \tag{11}$$

Equation (11) states that $g(x)$ is obtained by passing $f_2(x)$ through a filter $H_3(s)$.

With $G(s)$ selected according to equation (11), equation (10) becomes

$$H_2(s)=\frac{1}{H_1(s)}+\exp(-sL)H_3(s) \tag{12}$$

With $H_1(s)$ as given by equation (3) the poles of $1/H_1(s)$ are given by equation (5). At this point one attempts to remove the poles of $H_2(s)$ by requiring that the residues of $H_3(s)$ cancel the residues of $\exp(sL)/H_1(s)$ at the poles of the latter function.

It can be shown that the residues of the function $\exp(sL)/H_1(s)$ are given by

Residue $[\exp\ (sL)/H_1(s)]$

$$=(j2\pi m/x_0^2)\quad \exp(j2\pi mL)/x_0 \tag{13}$$

at the pole $s=j(2\pi m/x_0)$, $m=\pm 1, \pm 2\ .\ .\ .\ .$

The function $H_3(s)$ is given by

$$H_3(s)= \tag{14}$$

$$\sum_{m=-\infty}^{\infty}(j2\pi m/x_0 2)\ \mathrm{e}\ [(-j2\pi mL)/x_0][1/(s-j2m/x_0)]$$

In equation (14) L has been an arbitrary interval length spanning the desired image. Use of the filter $H_2(s)$ given by equation (12) with $H_3(s)$ given by equation (14) will reconstruct the scene correctly for $0\leq x\leq L$. It can be verified, however, that if one chooses

$$L=Nx_0 \tag{15}$$

where N is an integer that the exponential factor in equation (14) has unity value and that in this case the expansion for $H_3(s)$ becomes identical to that for $1/H_1(s)$; i.e.,

$$H_3(s)=1/H_1(s)=s/[1-\exp(-sx_0)] \tag{16}$$

Use of this result and equation (15) in equation (12) gives

$$H_2(s)=s[1-\exp(-sNx_0)]/[1-\exp(-sx_0)] \quad (17)$$

This result is identical with that derived by Slepian. In his paper, Slepian speculates that the price of requiring the reconstruction of the smeared function to be zero outside the interval containing the image is a set of poles for the reconstructing filters. The analysis above has verified the speculation made by Slepian.

The analysis made in this paper is a slight generalization of Slepian's result. Slepian's analysis gives the filter function written as equation (17) by selecting the value of L according to equation (15). However, equation (14) shows that L can be chosen arbitrarily and each value of L gives another filter giving exact reconstruction over the interval $0\leq x\leq L$.

It will be noted that the filter given by equation (17) is proportional to s. This may be difficult to instrument in an optical filter for high spatial frequencies. Apart from this factor, the terms involving experimental factors have peak values whose magnitude is N. This indicates that there is also a greater problem with respect to filter dynamic range required for longer intervals (in terms of smear length multiples).

The second relaxation can now be introduced. In a given situation there is often a required resolution, d. In such cases one might be satisfied to have a reconstruction with a smear length reduced to length d instead of the original length x_0. Conceptually one can consider the reconstruction to consist of two steps. In the first step the filter function of equation (17) is used and gives perfect reconstruction over the interval $0\leq x\leq L$. This is followed by a filter which smears each point to a length d. By analogy to equation (3) this latter filter, designated by $H_4(s)$ has the form

$$H_4(s)=[1-\exp(-sd)]/s \quad (18)$$

Thus if one requires that reconstruction over the interval $0\leq x\leq L$ have a resolution length d and that one allows the reconstruction to have nonzero values outside the interval, one gets for the equivalent filter function $H_5(s)$ such that

$$H_5(s)=H_2(s)H_4(s) \quad (19)$$

$$=[1-\exp(-sNx_0)][1-e(-sd)]/[1-e(-sx_0)]$$

It will be noted that the filter $H_5(s)$ no longer has the factor s in the numerator. This filter also has no poles and it is more readily constructed than the filter $H_2(s)$.

It is worthwhile to compare the filters given respectively by equations (4), (17), and (19). The first of these equations has an infinite set of poles at locations given by equation (5). The second of these equations has no poles but has a factor proportional to s. The third of these functions has no poles and the term proportional to s has been removed. The reconstructions for the first two cases give a perfect reconstruction in the interval $0\leq x\leq L$. The first filter, however, gives zero output for $x>L$, while the second filter produces a nonzero output for $x>L$. The third filter gives a smeared version of the output of the second filter with smearing length set by the resolution required.

Another interesting comparison is that of the spatial impulse response functions which can be found by taking inverse Laplace transforms of equations (4), (17), and (19). If $h(x)$, $h_2(x)$ and $h_5(x)$ represent these inverse transforms (spatial impulse response), one has

$$h(x)=\sum_{m=0}^{\infty}u_{+1}(x-mx_0) \quad (20)$$

$$h_2(x)=\sum_{m=0}^{n-1}u_{+1}(x-mx_0) \quad (21)$$

$$h_5(x)=\sum_{m=0}^{n-1}[u_0(x-mx_0)-u_0(x-mx_0-d)] \quad (22)$$

where $u_{+1}(x)$ is the unit doublet function and $u_0(x)$ is the unit impulse function.

Thus the spatial impulse response functions of the filters are an infinite sequence of unit doublet functions for the filter of equation (4), a sequence of N unit doublets for the filter of equation (17) and a sequence of N positive and N negative impulse functions for the filter of equation (19).

In the discussion above the noiseless case has been discussed. In practical situations, noise, particularly grain noise, is always present. In such cases it is desirable to reformulate the filter problem to take into account the effects of the noise. The Wiener minimum-mean-square error approach is an example. Given the statistics of signal and noise on the assumption of additive noise (which may not be a good approximation for photographic signals) one can formulate a Wiener Filter. Such cases will not be discussed further in this paper other than to note that such filters often do not have troublesome poles.

OPTICAL FILTERING CONSIDERATIONS

The analysis of the last section has concerned itself primarily with the theoretical information aspects of finding a desirable filtering operation to recover a smeared image. In this section the nature of the optical filter and the optical configuration using the filter are the items of concern.

The optical configurations in use for optical filtering are those described or derived from the work of Vander Lugt (ref. 2). In his configurations a hologram of the Fourier transform of a function is constructed. This hologram becomes the optical filter.

After photographic development to a gamma of two, the filter is inserted into a configuration such that the Fourier transform (refs. 3 and 4) of the function to be filtered is incident upon the filter. The Vander Lugt filters represent a major step in optical filtering technology because they make possible complex filter functions despite the fact that only real functions are recorded.

In using the Vander Lugt filters it is necessary to position the filter with great accuracy particularly for cases having high spatial frequency content. This extreme positioning problem is avoided in a modified optical configuration described by Weaver and Goodman (ref. 5).

In the Weaver and Goodman configuration, the signal to be filtered and spatial impulse function are placed in the input plane of an optical spectrum analyzer. The light in the Fourier transform plane is recorded to have a gamma of two. After photographic processing this signal is placed into the input plane, and the Fourier transform plane contains the filtered function.

In some cases Weaver and Goodman modify their process by causing a coherent reference to be incident upon the Fourier transform plane as well as the signals described above. In this case a hologram of the filters is made. Reconstruction gives the desired filtered output.

The Weaver and Goodman technique avoids the extreme accuracy requirements in placement of the filter because in a sense the filter positions are built into the filter.

The optical configurations of Weaver and Goodman are shown in figure 1. The input plane P contains both $f(x)$, the signal to be operated on, and $h(x)$, the impulse response function corresponding to the filtering operation.

An intermediate output is obtained in plane P–2. The film exposed in plane P–2 is developed photographically and then inserted into plane P–1. The filtered output then appears in plane P–2.

The filter functions considered in this paper are shown in figure 2.

It will be noted that the filter specified by equation (19) requires less dynamic range than do the filters specified by equations (4) and (17).

In some cases real-time operation is desired. This can be done if the recording is done on photochromics, free radical material, or dry silver material. These materials can all be exposed with blue light such as from an Argon laser but are not exposed by the red light of a He–Ne laser. Thus exposure can be made with an Argon laser to record the signals needed and the red He–Ne laser light can be used to perform the filtering operations desired.

RELATED EXPERIMENTAL RESULTS

The experimental results described in this section were obtained using medical X-rays [index finger of human hand] in which the contrast was improved by means of dc filtering and the signal to noise improved by low-pass filtering. The degradation introduced in X-ray images can be described as an attenuation of the high spatial frequencies due to the finite

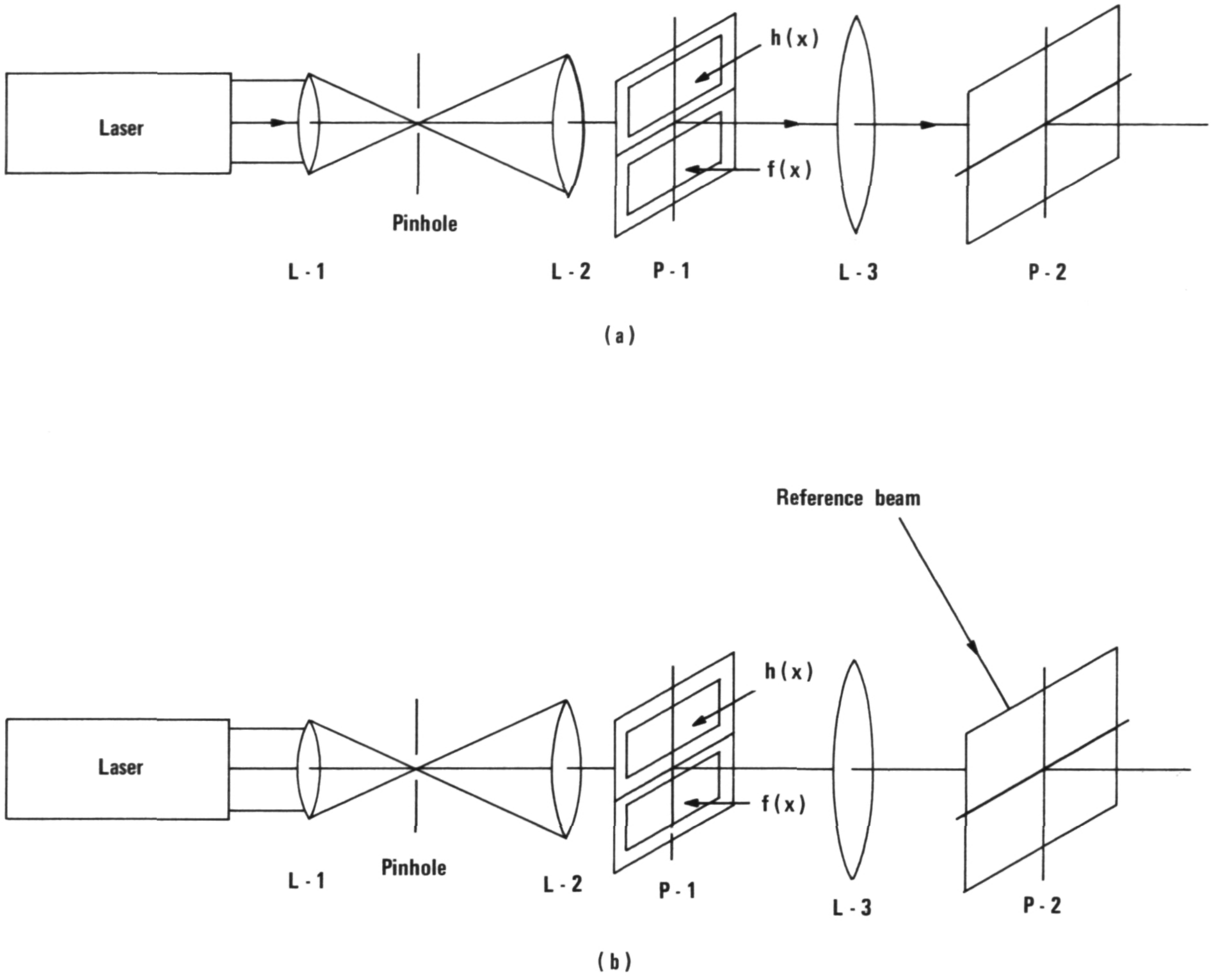

FIGURE 1.—(a) Configuration for optical convolution, and (b) Alternate configuration for optical convolution.

size of the X-ray source. Optically this is equivalent to the blurring of a photograph taken with an ideal camera in which the medium between the image and the object broadens the impulse response function of the system, resulting in an attenuation of the higher spatial frequencies. Ideally, the optical spatial filtering techniques are intended to generate a second image whose appearance would be similar to the original object produced by an X-ray source of smaller dimensions, i.e., a point source.

In order to specify the form of the desired filter in the optical processor let us consider a simplified mathematical model. The light amplitude distribution in Fourier transform plane of figure 3 is given by

$$A(u, v) = C \iint_{\text{aperture}} I_\lambda(x, y) \exp\left[-j2\pi\ (ux+vy)\right] dx\, dy \tag{23}$$

where $I_\lambda(x, y)$ is the incident intensity distribution of the X-ray image. The constant C includes a quadratic phase variation in the u direction inherent in the converging optical processor which can for our purposes be

$$H(s) = s/\left[1-\exp(-sx_0)\right]$$

$$h(x) = \sum_{m=0}^{\infty} \mu_{+1}(x-mx_0)$$

$$\mu_{+1}(x) = \text{Unit doublet}$$

$$H(s) = s\left[1-\exp(-sNx_0)\right]/\left[1-\exp(-sx_0)\right]$$

$$h(x) = \sum_{m=0}^{N-1} \mu_{+1}(x-mx_0)$$

$$\mu_{+1}(x) = \text{Unit doublet}$$

$$H(s) = \left[1-\exp(-sNx_0)\right]\left[1-\exp(-sd)\right]/\left[1-\exp(-sx_0)\right]$$

$$h(x) = \sum_{m=0}^{N-1} \left[\mu_0(x-mx_0-d)\right]$$

$$\mu_0(x) = \text{Unit impulse}$$

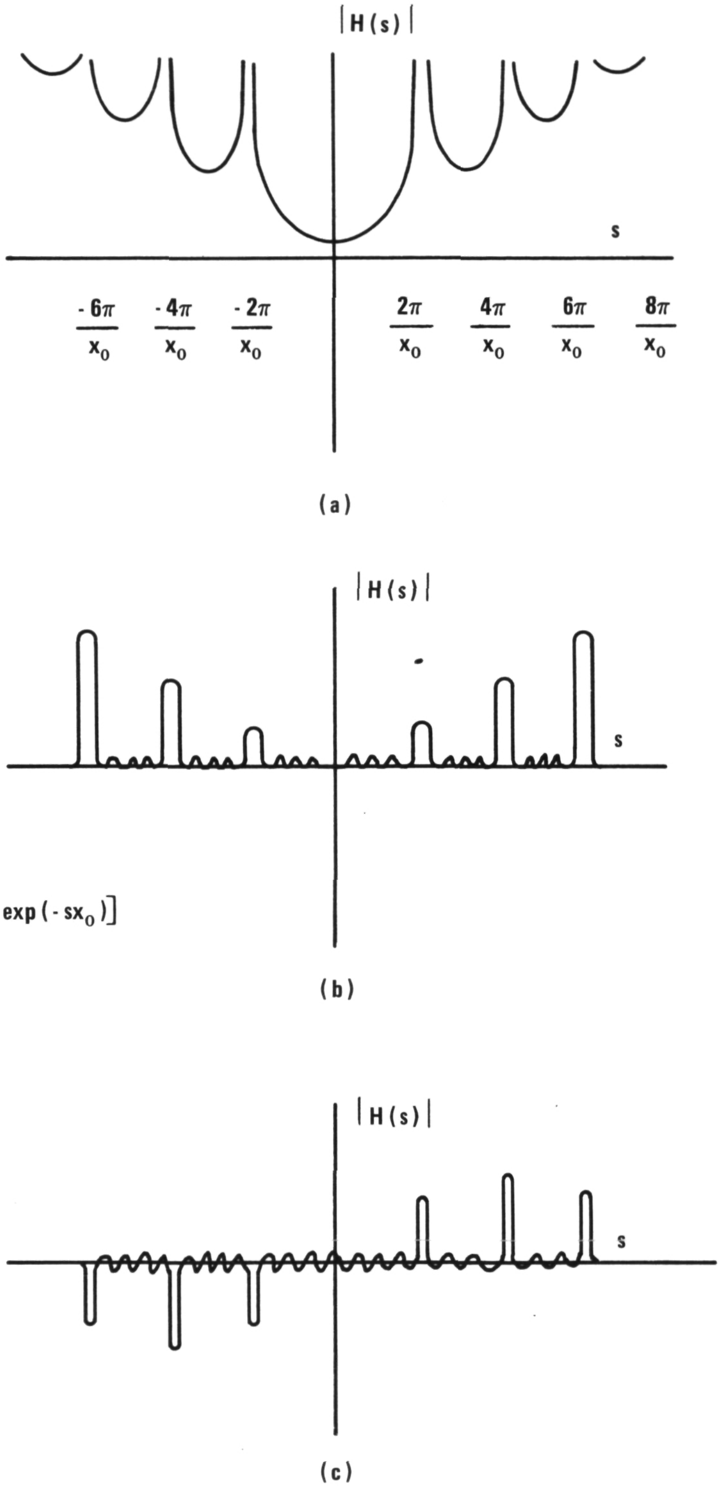

FIGURE 2.—(a) The filter defined by Equation 4, (b) the filter defined by Equation 17, and (c) the filter defined by Equation 19.

ignored. The incoherent intensity distribution of the X-ray image is given by convolution integral

$$I_\lambda(x, y)=C'\iint_{\text{area}}\sigma(\alpha, \beta)I(x-\alpha, y-\beta)d\alpha\, d\beta \quad (24)$$

of the spatial intensity of the X-ray source $\sigma(\alpha, \beta)$ and the intensity distribution $I(x, y)$ which is proportional to transmission function of the object. Applying the Fourier transform convolution theorem to equation (24) we obtain

$$A(u, v)=\Gamma(u, v)\ H(u, v) \quad (25)$$

where

$$\Gamma(u, v)=K\iint_{\text{aperture}} Ix, y)\ \exp[-2\pi j(ux+vy)]dx\, dy \quad (26)$$

$$H(u, v)=K'\iint_{\text{area}}\sigma(x, y)\ \exp[2\pi j(ux+vy)]dx\, dy \quad (27)$$

Thus it is obvious that in order to obtain the amplitude distribution in the transform plane equal to the ideal image distribution we must multiply $A(u, v)$ by the inverse of $H(u, v)$. If we assume that $\sigma(x, y)$ is finite, positive and real, we can neglect phase shifting but $H(u, v)$ can have zeros resulting in the loss of certain spatial frequencies in the filtered image. In general the desired filter, $[H(u, v)]^{-1}$, will have high pass characteristics while attenuating the lower spatial frequencies. Further, if we assume that $\sigma(x, y)$ is uniform the implied filter consists of a dc block selectively removing the lower spatial frequencies. The net result of such a filter is contrast enhancement plus edge sharpening.

Experimentally, the above described filter was constructed using the optical processor shown in figure 3 with the signal removed from the liquid gate. The procedure consisted of placing an unexposed 1 inch by 3 inch 649F glass photographic plate in a precision position mount located in the Fourier transform plane and recording the central airy diffraction lobe of the circular lens aperture. The size was controlled by the magnification of the 25μ pinhole object and the aperture of the lens. The transmission characteristics were controlled by selecting the exposure time and using neutral density filters in the laser beam before the pinhole. Complete removal of the dc term was avoided since this would introduce frequency doubling distortion in the final image. The attenuation of the dc term was determined by the amount of dc reduction necessary to reduce the minimum signal level in the unfiltered image to zero. This was experimentally determined by measuring the Wiener spectrum in the transform plane of the processor for the processor alone, processor plus film noise, and processor plus signal with appropriate normalization and comparison techniques of the three spectrums.

The recorded spot size used in the processor was 34μ in diameter with an average attenuation of 15 db. One of the advantages of using

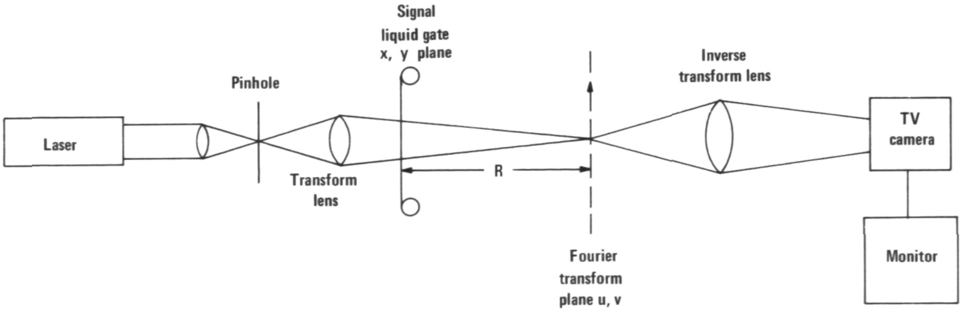

FIGURE 3.—Converging optical processor.

the converging processor as shown in figure 3 is the fact that the spatial frequency distribution in the transform plane can be varied by changing the signal position R with respect to the transform plane. In figure 3, r refers to the radial distance from the optical axis in the transform plane. The relationship between the spatial frequency distribution k (line pairs/mm) and r is given by

$$r = k\lambda R \tag{28}$$

where λ is the wavelength of the laser radiation (6328Å). Thus one can, in a continuous fashion, vary the spatial frequency attenuation cutoff point by changing R.

The experimental results of the spatial filtering are shown in figures 4 through 6. The pictures were obtained by photographing the television monitor using Polaroid 3000 ASA film at $f/22$ with a shutter speed of 1/50 of a second. The three pictures were all obtained at equivalent light levels so that no artifical photographic enhancement was introduced. Figure 4 is the unfiltered coherently illuminated image of an X-ray of the bone joint of the index finger. Figure 5 is the contrast enhanced edge-sharpened dc filtered image. The spatial frequency cutoff as determined by subjective "best" image quality was 1/8 line pair/mm. This corresponds to $R \approx 500$ mm. Figure 6 is the bandpass filtered image. The high pass filter and cutoff condition is identical to figure 5. The difference is the addition of a circular low-pass filter; the combination is called a bandpass filter. The far field Wiener spectrum measurements indicated that film noise and processor noise exceeded the signal at a spatial frequency of three line pairs/mm thus indicating that the rest of the spatial frequency spectrum consisted of film grain and processor noise. Thus the limiting aperture selected for the low pass filter was 0.100 inch in diameter. Thus, as shown by comparison of figure 6 to figure 5, the signal to noise has increased resulting in better contrast and definition in the filtered image. Smaller apertures were tried resulting in resolution reduction as one would expect.

Future work in this area should concentrate in methods for coherent noise reduction (i.e., noise introduced by dust particles and cosmetic

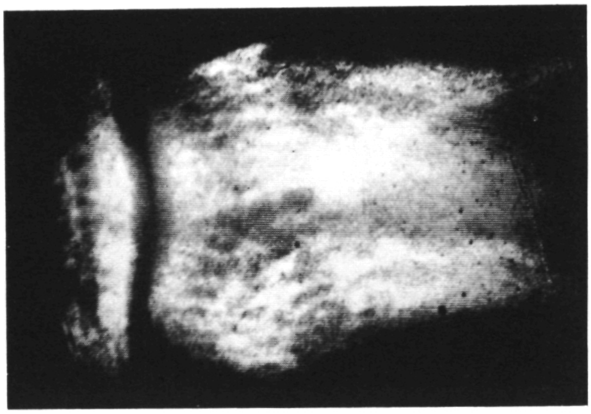
FIGURE 4.—Unfiltered image.

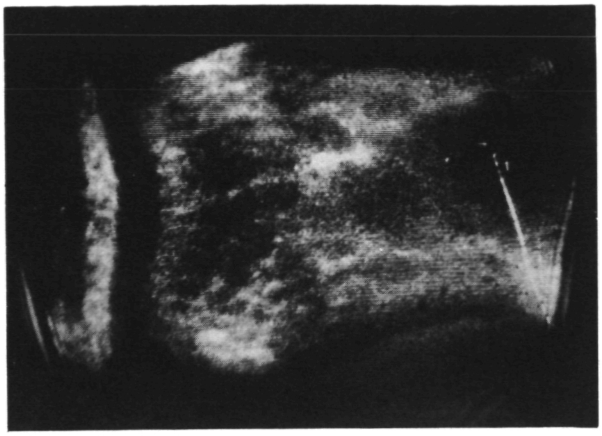
FIGURE 5.—High-pass filtered image.

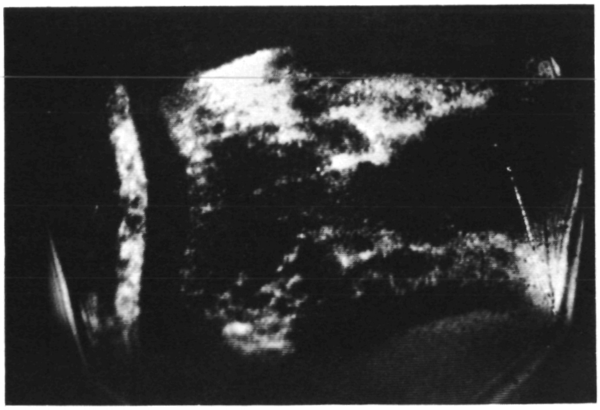
FIGURE 6.—Bandpass filtered image.

imperfections of the lens) and additional signal processing of the electrical nature by taking advantage of the presence of the video signal and current video signal processing techniques. Another area for investigation is filter synthesis techniques.

CONCLUDING REMARKS

In this paper some theoretical and experimental results have been obtained. The theoretical results have not yet been subjected to experimental verification.

The experimental results pertain to image blurring due not to image motion but to finite source size (X-ray sources). However, this corresponds quite closely to an out-of-focus image. The contrast and high spatial frequency content are increased due to the processing.

REFERENCES

1. SLEPIAN, D.: On the Restoration of Photographs Blurred By Image Motion. Miscellaneous Paper No. 3, Woods Hole Summer Study Report on Restoration of Atmospherically Degraded Images, July 1966.
2. VANDER LUGT, A.: Signal Detection by Complex Spatial Filtering. IEEE Trans. on Info. Theory, April 1964.
3. CUTRONA, L. J.; LEITH, E. N.; PALERMO, C. J.: AND PORCELLI, L. J.: Optical Data Processing and Filtering Systems. IRE Trans. Info. Theory, June 1960.
4. CUTRONA, L. J.: Recent Developments in Coherent Optical Technology. Optical and Electro-Optical Information Process, MIT Press, Cambridge, Mass.
5. WEAVER, C. S.; AND GOODMAN, J. W.: A Technique for Optically Convolving Two Functions. Applied Optics, vol. 5, no. 7, July 1966.

COMPUTING TECHNIQUES FOR CORRECTION OF BLURRED OBJECTS IN PHOTOGRAPHS*

CLARON W. SWONGER AND FAITH Y. CHAO
Cornell Aeronautical Laboratory, Inc.
Buffalo, N.Y.

In the deconvolution by digital techniques of sampled blurred gray-level images of moving objects, noise disturbances prove to be a major obstacle. Since the linear deconvolution filter which would ideally be used is unstable or marginally stable and thus intensifies the effect of the noise, various techniques for noise compensation have been studied.

In this paper, a set of such computing techniques, which employ adaptive filtering concepts, are considered and presented along with experimental results. These techniques involve a preliminary process which includes a determination of maximal edge area around the blurred object in the photograph, major reduction of noise samples of "large" magnitude, and some reduction of those of a low magnitude. Given the noise level, a set of weights can be automatically obtained for a noise compensation filter that minimizes, in the sense of least squares, the difference between the resulting processed image and the ideal noise-free still object image for one or more training sample images. This set of weights is then used to calculate the processed image with the same statistical noise level.

The purpose of this paper is to present a description of algorithms and some initial experimental results from these algorithms for removal of motion degradations in imagery. The approach employed is that of sampled data filtering theory and emphasizes the desirability of:

(1) Minimizing the amplification of noise during the corrections for motion degradation through the use of a priori knowledge and nonlinear filtering

(2) Maximum automatic compensation for noise and signal characteristics in order to avoid the need for manual noise measurement

There are, of course, a host of other problems and goals which may further complicate the problem of post-facto image motion removal, but these are not addressed here.

Because the techniques presented here will be formulated as sampled data processes, it is most convenient to characterize the image to be processed as spatially sampled. In practice, two-dimensional arrays are used, varying from about 20 to over 1,000 elements in each dimension, depending upon the nature of the application. Also, because digital computing methods will be considered, the sampled image elements will be assumed to be quantized into a finite number of gray-levels, for example 64 levels encoded in 6 bits.

THEORETICAL BACKGROUND

As is well known, the degradation of imagery due to relative motion of the scene and the camera (film) is a process of convolution of the scene with a space-time function which represents the image motion and which is modulated by the exposure (camera shutter) time function. In the case of general motion, especially if it is not specifically known, very difficult problems of process identification must be faced. Further, to the extent that the film exposure, film

---

*The research reported herein was supported by internal funds of Cornell Aeronautical Laboratory, Inc.

processing, or image sensing for motion degradation correction are not linear processes (in some dimension corresponding to gray level), convolution is only an approximation to the actual degradation process.

In what follows here, these complicating considerations will be set aside to focus on the use of nonlinear sampled data filtering (ref. 1) to process noisy imagery for correction of image motion degradation. For linear object motion in the X-coordinate only, the degradation may be expressed by

$$G(x, y)=\sum_{\delta} W(x+\delta, y)M(\delta) \qquad (1)$$

where $G(x,y)$ is the blurred image, a function of the spatial coordinates x,y, $W(x,y)$ is the stationary object scene, and $M(\delta)$ is the modulation function expressing the exposure when the (sampled) scene was displaced from its reference position by an amount δ in the X-direction. The convolution is performed over all values of δ, but in practice, of course, needs only to be performed over values for which $M(\delta)$ is nonzero.

Equation (1) can also be written in the form of a difference equation

$$G_J=W_J M_O+W_J+{}_1M_1+\ldots W_{J+n}M_n \qquad (2)$$

where J is the X-coordinate index of any point in $G(x, y)$ or $W(x, y)$ and n indicates the extent of blurring (the number of spatial samples convolved with nonzero $M(\delta)$).

Given $M(\delta)$, which generally acts as a low pass filter, it is a straightforward matter to derive the inverse filters which would theoretically recover the signal $W(x, y)$ from $G(x, y)$. Figure 1 illustrates inverse filtering for a noise free blurred image and two different simulated shutter characteristics. However, just as motion degradation is a low pass filtering process, its inverse is a high pass filtering process. In imagery as in most other signals, random and deterministic high frequency disturbances or "noise" inevitably exist due to (1) film grain (2) imperfections in the original scene, such as haze, and (3) image gray level quantization and other effects. The action of "ideal" inverse filter for motion degradation correction is thus, at best, to amplify or enhance such disturbances. In fact, for many reasonable examples, the inverse filter is unstable and will therefore ring and/or saturate under the slightest random disturbance.

A number of investigators (refs. 2 and 3) have investigated the use of optical and other spatial frequency filtering methods for addressing this problem area. This paper considers how certain a priori knowledge not usable in the frequency plane may be used to limit noise effects.

ALGORITHM FORMULATION

The algorithm to be described herein includes four major steps:

(1) The bounds of the blurred object (assumed to be immersed in a stationary field) are estimated and variations outside those boundaries are removed.

(2) The blurred object is examined to detect gray-level variations which are not likely to occur given the degree of blurring which was originally experienced. These variations are removed by an averaging process.

(3) The resulting image is processed by an "ideal" inverse filter augmented with a "clipping" or limiting filter which prevents generation of impossible gray levels.

(4) Finally, the inverse-filtered image is processed by a filter designed to minimize the mean-squared difference between its output and the ideal noise-free stationary object image.

Figure 2 summarizes the process in the form of a flow-chart. Each of these steps will now be discussed in some detail.

The initial step of object boundary estimation is performed in order to minimize the effects of amplifying background high frequency detail during the inverse-filtering step. Implicit in this process is the assumption that recovery of a "moving" object in a nonmoving scene is of interest. If this is not the case, alternative procedures should be considered. In the experiments described here, an average background level B is computed by observing the samples at the edge of the input image, and each row of the sampled image is searched from the left end to determine where the actual picture of

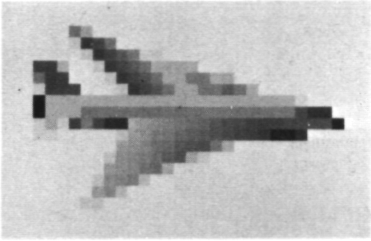

Stationary object

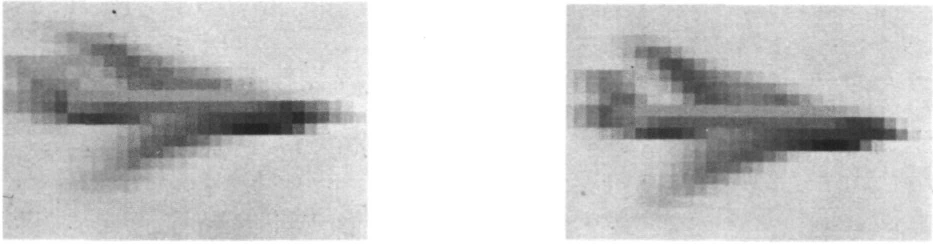

Object blurred by rectangular exposure function aperture

Object blurred by triangular exposure function aperture

Object restored by filtering

Object restored by filtering

FIGURE 1.—Spatial frequency filtering to remove the effects of blurring of moving objects.

the blurred object begins. This is accomplished by reasoning that a single nonblurred picture sample will affect the blurred matrix $N+1$ entries starting from that corresponding to the picture entry, to N entries following it. In the case of a rectangular exposure function where all the coefficients of the filter function are equal, the affect is the same throughout the $N+1$ entries. The probability of the background level B appearing among these $N+1$ entries is small. If the blurred object affects more than one entry, clearly, the blurred matrix will be effected at least $N+1$ entries. Further, the probability of the appearance of noise of intensity B among the effected entries of the blurred matrix must also be small. As the picture is scanned inward from the end of each row, all signals that appear with the property that their duration is under $N+1$ adjacent entries can therefore be erased and replaced by B. The first N entries of each row are automatically set equal to B. The scan of each row ceases when a signal of greater than $N+1$ samples occurs.

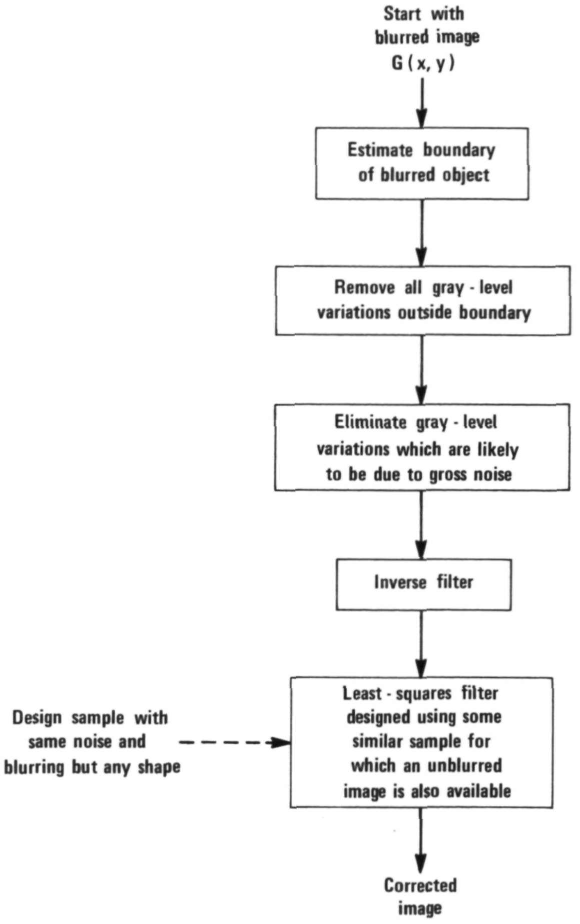

FIGURE 2.—Image motion degradation correction algorithm.

Having determined the beginning of the object, obviously, the next step is to affix its termination. Starting from the reverse (i.e., right) end of the line, the program searches for the first appearance of at least $N+1$ consecutive non-B entries. Assuming this to signify the object signal, the j^{th} entry, $N-2$ places prior to the first appearance of a non-B entry, determines the end of the image of the object. Hence, every entry following the j^{th} entry can be set equal to B. This position $(j+1)$ is then remembered for future reference.

The input matrix G is now scanned for noise samples of "large" magnitude. Given the degree of the filter N, and knowing that the range of unblurred object gray-levels is 0 through 63, it must be that

$$|G(j+i)-G(j)|\leq\frac{63i}{N+1}$$

where $G(k)$ is the k^{th} entry of the given line of G, and

$$\leq\frac{63i}{N+1}$$

The program now searches for those $G(j)$ such that

$$|G(j)-G(j-1)|>\frac{63}{N+1}$$

The $G(j)$ are then considered as beginnings of occurrences of gross noise. The next step is to determine how many continuous sequences of length up to $N+1$ are also likely to be gross noise samples. Each of these sequences is then replaced, usually along with some correct information, by setting all its entries to the value of the entry just prior to the sequence. The positions of the altered entries are then "remembered."

The inverse filtering is performed next. Letting G and P denote the input and output line respectively, we have

$$G(j)=[1/(N+1)]\sum_{i=j-N}^{j}W(i)$$

Thus, the output line can be obtained by the formula

$$F(j)=(N+1)[G(j)-G(j-1)]+F(j-N-1)$$

As each $F(j)$ is obtained, it is checked to ascertain whether it is within the limits of 0 and 63. If so, we proceed to calculate $F(j+1)$, if not we check to see if $G(j-1)$ is one of the "remembered" entries from above where gross noise was estimated to exist. If so, $G(j-1)$ is altered so that $F(j)$ lies just within the limits of 0 and 63. If not, $G(j)$ is altered, and we proceed to calculate $F(j+1)$.

In order to economically investigate the algorithm, figures 3 through 6 will illustrate the process to this point. Figure 3 shows a numerically precise description of the same stationary noise-free object previously pictorially shown at the top of figure 1. A noisy

```
5 5 5 5 5 5 5 5 5 5 5 5 5 5 5 5 5 5 5 5 5 5 5 5 5 5 5 5 5 5 5 5 5 5 5 5
5 5 5 5 5 5 5 5 5 5 5 5 5 5 5 5 5 5 5 5 5 5 5 5 5 5 5 5 5 5 5 5 5 5 5 5
5 5 5 5 5 5 5 5 5 5 5 5 5 5 5 5 5 5 5 5 5 5 5 5 5 5 5 5 5 5 5 5 5 5 5 5
5 5 5 5 5 5 5 5 5 5 5 5 5 5 5 5 5 5 5 5 5 5 5 5 5 5 5 5 5 5 5 5 5 5 5 5
5 5 5 5 5 5 5 5 5 5 5 5 5 5 5 5 5 5 5 5 5 5 5 5 5 5 5 5 5 5 5 5 5 5 5 5
5 5 5 5 5 5 5 5 5 5 5 5 5 5 5 5 5 5 5 5 5 5 5 5 5 5 5 5 5 5 5 5 5 5 5 5
5 5 5 5 5 5 5 5 5 5 5 5 5 5 5 5 5 5 5 5 5 5 5 5 5 5 5 5 5 5 5 5 5 5 5 5
5 5 5 5 5 5 5 5 5 5 5 5 5 5 5 5 5 5 5 5 5 5 5 5 5 5 5 5 5 5 5 5 5 5 5 5
5 5 5 5 5 5 5 5 5 5 5 5 5 5 5 5 5 5 5 5 5 5 5 5 5 5 5 5 5 5 5 5 5 5 5 5
5 5 5 5 5 5 5 5 5 5 5 5 5 5 5 5 5 5 5 5 5 5 5 5 5 5 5 5 5 5 5 5 5 5 5 5
5 5 5 5 5 5 5 5 5 5 5 5 5 5 5 5 5 5 5 5 5 5 5 5 5 51520 5 5 5 5 5 5 5 5
5 5 5 5 5 5 5 5 5 5 5 5 5 5 5 5 5 5 5 5 5 5 5 520242610 5 5 5 5 5 5 5 5
5 5 5 5 5 5 5 5 5 5 5 5 5 5 5 5 5 5 5 510102022242610 5 5 5 5 5 5 5 5 5
5 5 5 5 5 5 5 5 5 5 5 5 5 5 5 5 515151515202224261O 5 5152525 5 5 5 5 5
5 5 5 5 5 5 5 5 5 5 5 5 5 515152020151520222426 10 5 5 5252520 5 5 5 5 5
5 5 5 5 5 5 5 5 5 5 5 5152022202015152022242610 5 5 525252510 5 5 5 5 5
5 5 5 5 5 5 5 510151515151515151515151515151515151515151540 5 5 5 5 5
5 5 5 5 5 531312520202020202020202020202020202020202015151540 5 5 5 5 5
5 5 5 5 540252525252626252423222120191817161531312520251015 10 5 5 5 5 5
5 5 5 5 5 5 5 531404028262524232221201918161510 5 5 5 5 51010 5 5 5 5 5
5 5 5 5 5 5 5 5 5 5 5 5 5 515202322212019171615 5 5 5 5 5 5 5 5 5 5 5 5
5 5 5 5 5 5 5 5 5 5 5 5 5 5 5 5101522211918171610 5 5 5 5 5 5 5 5 5 5 5
5 5 5 5 5 5 5 5 5 5 5 5 5 5 5 5 5 5 5152019171615 5 5 5 5 5 5 5 5 5 5 5
5 5 5 5 5 5 5 5 5 5 5 5 5 5 5 5 5 5 5 5 51219171610 5 5 5 5 5 5 5 5 5 5
5 5 5 5 5 5 5 5 5 5 5 5 5 5 5 5 5 5 5 5 5 5 5121715 5 5 5 5 5 5 5 5 5 5
5 5 5 5 5 5 5 5 5 5 5 5 5 5 5 5 5 5 5 5 5 5 5 5 51010 5 5 5 5 5 5 5 5 5
5 5 5 5 5 5 5 5 5 5 5 5 5 5 5 5 5 5 5 5 5 5 5 5 5 5 5 5 5 5 5 5 5 5 5 5
5 5 5 5 5 5 5 5 5 5 5 5 5 5 5 5 5 5 5 5 5 5 5 5 5 5 5 5 5 5 5 5 5 5 5 5
5 5 5 5 5 5 5 5 5 5 5 5 5 5 5 5 5 5 5 5 5 5 5 5 5 5 5 5 5 5 5 5 5 5 5 5
5 5 5 5 5 5 5 5 5 5 5 5 5 5 5 5 5 5 5 5 5 5 5 5 5 5 5 5 5 5 5 5 5 5 5 5
5 5 5 5 5 5 5 5 5 5 5 5 5 5 5 5 5 5 5 5 5 5 5 5 5 5 5 5 5 5 5 5 5 5 5 5
5 5 5 5 5 5 5 5 5 5 5 5 5 5 5 5 5 5 5 5 5 5 5 5 5 5 5 5 5 5 5 5 5 5 5 5
5 5 5 5 5 5 5 5 5 5 5 5 5 5 5 5 5 5 5 5 5 5 5 5 5 5 5 5 5 5 5 5 5 5 5 5
5 5 5 5 5 5 5 5 5 5 5 5 5 5 5 5 5 5 5 5 5 5 5 5 5 5 5 5 5 5 5 5 5 5 5 5
5 5 5 5 5 5 5 5 5 5 5 5 5 5 5 5 5 5 5 5 5 5 5 5 5 5 5 5 5 5 5 5 5 5 5 5
5 5 5 5 5 5 5 5 5 5 5 5 5 5 5 5 5 5 5 5 5 5 5 5 5 5 5 5 5 5 5 5 5 5 5 5
```

FIGURE 3.—Matrix representation of the stationary, noise-free object (airplane) used in the following experiments.

motion-degraded image of the object is similarly shown in figure 4. In this case, object smear occurred uniformly over six image samples in the horizontal direction, so that a fifth-order filter is required ($N=5$). For ease of interpretation, the pictorial equivalent blurred image is shown in the upper left of figure 5. By examination of figure 4, the algorithm first selects level 5 as the background level. It then examines each image row for six or more consecutive cells whose value is not equal to level 5 and thus estimates the boundaries of the object as shown in figure 4. Gross noise variations exceeding 63/6 = 10.5 levels change between adjacent cells are deleted. Next, the image of figure 4 is inverse filtered. In the example, the motion degradation was

$$G_J=\tfrac{1}{6}[W_J+W_{J-1}+W_{J-2}+W_{J-3}+W_{J-4}+W_{J-5}]$$
$$\text{with } 1\leq J\leq NC$$

so that the inverse filter can be derived as

$$F_J=6[G_J-G_{J-1}]+F_{J-6} \text{ with } 1\leq J\leq NC$$

Figure 6 provides the numerical output of the inverse filter where, for example, the circled entry was calculated as

$$G_6=6(11-5)+5=41$$

recalling that the edge values G_1 through G_5 are all set to the background value of 5 to initiate the filter for the row. Again, when the inverse filter produces a negative or excessively large (>63) output, the output is limited, to zero or 63 respectively, by recalling whether G_J or G_{J-1} was modified by an estimate of gross noise and restoring the corresponding one of these inputs to the filter accordingly.

Now using a stationary noise-free object as a reference, a filter of the form

$$X_I=\frac{1}{N+1}\sum_{J=1}^{N+1}C_JF_{J+I-1}$$

is designed to optimally suppress noise in the least-squares sense. Pursuing the example used above, the coefficients of the filter were computed using *another* noisy and motion-degraded image of the same object. The resulting filter had the equation

$$X_J=\frac{1}{6}[3.31F_J+1.66F_{J+1}+0.85F_{J+2}-0.02F_{J+3}$$
$$-0.15F_{J+4}+0.30F_{J+5}] \text{ with } 1\leq J\leq NC-5$$

Figure 7 shows the output image from the least-squares filter in numerical form where, for example, the circled point is calculated as

$$X_6=\frac{1}{6}[135.9+38.2+24.6-0.4-2.55+12.2]$$
$$=\frac{208.0}{6}=34.7$$

which is rounded to level 35. Finally the previously detected object boundaries are again used to remove any variations which entered the background during the last filtering step. The upper right image of figure 5 shows the pictorial form of the final output image. The lower portion of figure 5 shows corresponding images for a higher noise level in the blurred image. It is difficult to define a "signal-to-noise" ratio for these two examples. However, some useful indication can be obtained by observing

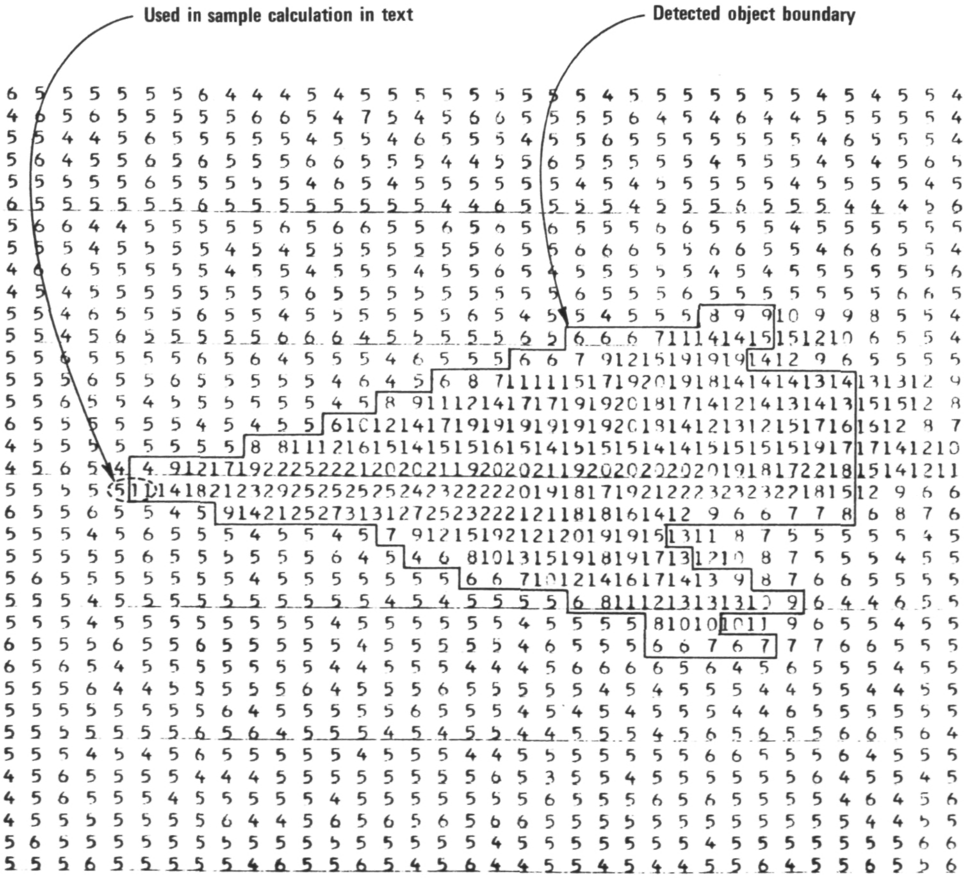

```
6 5 5 5 5 5 5 6 4 4 4 5 4 5 5 5 5 5 5 5 5 5 4 5 5 5 5 5 5 5 4 5 4 5 5 4
4 6 5 6 5 5 5 5 5 6 6 5 4 7 5 4 5 6 6 5 5 5 5 6 4 5 4 6 4 4 5 5 5 5 5 4
5 5 4 4 5 6 5 5 5 5 5 4 5 5 4 6 5 5 5 4 5 5 6 5 5 5 5 5 5 5 4 6 5 5 5 4
5 6 4 5 5 6 5 6 5 5 5 6 6 5 5 5 4 4 5 5 6 5 5 5 5 5 4 5 5 5 4 5 4 5 6 5
5 5 5 5 5 6 5 5 5 5 5 4 6 5 4 5 5 5 5 5 5 4 5 4 5 5 5 5 5 4 5 5 5 5 4 5
6 5 5 5 5 5 5 6 5 5 5 5 5 5 5 5 4 4 6 5 5 5 5 4 5 5 5 6 5 5 5 4 4 4 5 6
5 6 6 4 4 5 5 5 5 5 6 5 6 6 5 5 6 5 6 5 6 5 5 5 6 6 5 5 5 4 5 5 5 5 5 5
5 5 5 4 5 5 5 5 4 5 4 5 5 5 5 5 5 5 6 5 5 6 6 6 5 5 6 6 5 5 4 6 6 5 5 4
4 6 6 5 5 5 5 5 4 5 5 4 5 5 5 4 5 5 6 5 4 5 5 5 5 5 4 5 4 5 5 5 5 5 5 6
4 5 4 5 5 5 5 5 5 5 5 6 5 5 5 5 5 5 5 5 5 6 5 5 5 6 5 5 5 5 5 5 5 6 6 5
5 5 4 6 5 5 5 6 5 5 4 5 5 5 5 5 5 6 5 4 5 5 4 5 5 5 8 9 910 9 9 8 5 5 4
5 5 4 5 6 5 5 5 5 5 6 6 6 4 5 5 5 5 5 6 5 6 6 6 711141415151210 6 5 5 4
5 5 6 5 5 5 5 6 5 6 4 5 5 5 4 6 5 5 5 6 6 7 912151919191412 9 6 5 5 5 5
5 5 5 6 5 5 6 5 5 5 5 5 4 6 4 5 6 8 711111517192019181414141314131312 9
5 5 6 5 5 4 5 5 5 5 5 5 4 5 8 911121417171919201817141214131413151512 8
6 5 5 5 5 5 5 4 5 4 5 5 61012141719191919191920181412131215171616 12 8 7
4 5 5 5 5 5 5 5 5 8 811121615141515161514151515141415151515191717141210
4 5 6 5 4 4 912171922252221202021192020211920202020201918172218 15141211
5 5 5 5 5 11141821232925252525242322222019181719212223232322181512 9 6 6
6 5 5 6 5 5 4 5 914212527313127252322212118181614 12 9 6 6 7 7 8 6 8 7 6
5 5 5 4 5 6 5 5 5 4 5 5 4 5 7 91215192121201919151311 8 7 5 5 5 5 5 4 5
5 5 5 5 5 6 5 5 5 5 5 5 6 4 5 4 6 810131519181917131210 8 7 5 5 5 4 5 5
5 6 5 5 5 5 5 5 5 4 5 5 5 5 5 5 5 6 6 71012141617141 3 9 8 7 6 6 5 5 5 5
5 5 5 4 5 5 5 5 5 5 5 5 5 5 4 5 4 5 5 5 5 6 8111213131310 9 6 4 4 6 5 5
5 5 5 4 5 5 5 5 5 5 5 5 4 5 5 5 5 5 5 4 5 5 5 5 81010101011 9 6 5 5 4 5 5
6 5 5 5 6 5 5 6 5 5 5 5 5 4 5 5 5 5 5 4 6 5 5 5 6 6 7 6 7 7 7 6 6 5 5 5
6 5 6 5 4 5 5 5 5 5 5 5 4 4 5 5 5 4 4 4 5 6 6 6 6 5 6 4 5 6 5 5 5 4 5 5
5 5 5 6 4 4 5 5 5 5 5 6 4 5 5 5 6 5 5 5 5 5 4 5 4 5 5 5 4 4 5 5 4 4 5 5
5 5 5 5 5 5 5 5 6 4 5 5 5 5 5 6 5 5 5 4 5 4 5 4 5 5 5 4 4 6 5 5 5 5 5 5
5 5 5 5 5 5 5 6 5 6 4 5 5 5 4 5 4 5 5 4 4 5 5 5 4 5 6 5 6 5 5 6 6 5 6 4
5 5 5 4 5 4 5 6 5 5 5 5 5 4 5 5 5 4 4 5 5 5 5 5 5 5 6 6 5 5 5 6 4 5 5 5
4 5 6 5 5 5 5 4 4 4 5 5 5 5 5 5 5 5 6 5 3 5 5 4 5 5 5 5 5 5 6 4 5 5 4 5
4 5 6 5 5 5 4 5 5 5 5 5 4 5 5 5 5 5 5 5 6 5 5 5 6 5 6 5 5 5 5 4 6 4 5 6
4 5 5 5 5 5 5 5 6 4 4 5 6 5 6 5 6 5 6 6 5 5 5 5 5 5 5 5 5 5 5 5 4 4 5 5
5 6 5 5 5 5 5 5 5 5 5 5 5 5 5 5 5 5 4 5 5 5 5 5 5 5 4 5 5 5 5 5 5 5 6 6
5 5 5 6 5 5 5 5 5 4 6 5 5 6 5 4 5 6 4 4 5 5 4 5 4 4 5 5 6 4 5 5 6 5 5 6
```

FIGURE 4.—Airplane 0.5 blurred for testing.

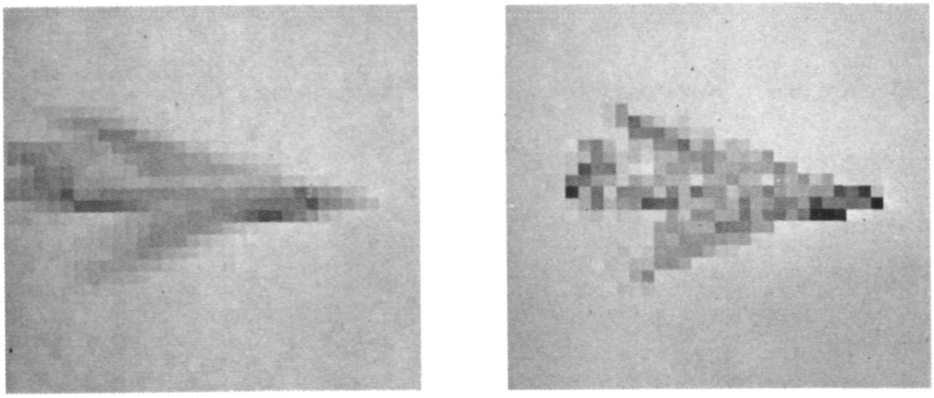

Noisy blurred image

Deblurred image

Noise standard deviation = 0.5 levels

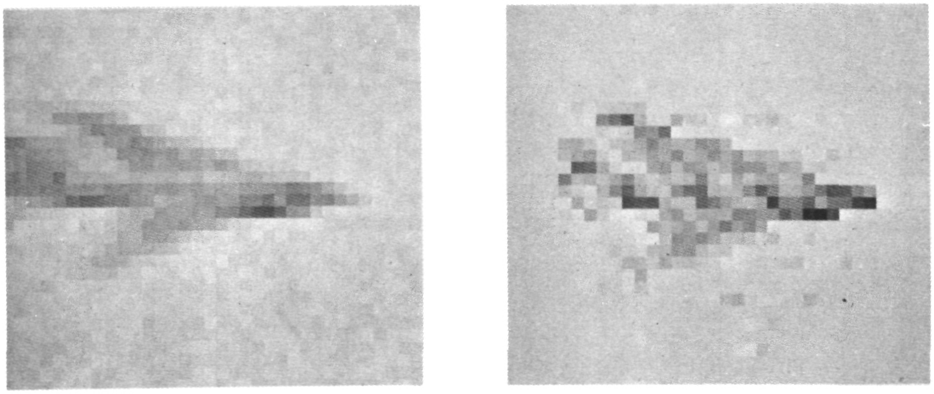

Noisy blurred image

Deblurred image

Noise standard deviation = 1.0 levels

FIGURE 5.—Deblurring of a noisy image using a computer-implemented adaptive spatial filter which was trained on this object shape.

that the variance of high frequency (sample-to-sample) steps in the signal *plus*-noise *within* the detected boundary of the blurred image of figure 4 is 6.50 levels. The variance of the difference between adjacent noise samples is approximately 0.5 and 2.0 levels for the two examples shown. Since the signal and noise are not dependent, the signal variance is 6.0 units, or its standard deviation is 2.45 levels. On this basis the high frequency "signal-to-noise ratios" for the two examples can be computed as 10.8 db and 4.8 db respectively.

FILTER GENERALITY

In order to investigate the use of the least squares filter for motion-degradation correction of objects not previously seen, two abstract shapes, a cube and a sphere, were applied to the over-all algorithm. The same filter coefficients, derived from the "airplane" shape were employed. Figure 8 shows the resulting images. Because low resolution and low contrast objects were used, the object boundary detection algorithm did not locate one surface of the

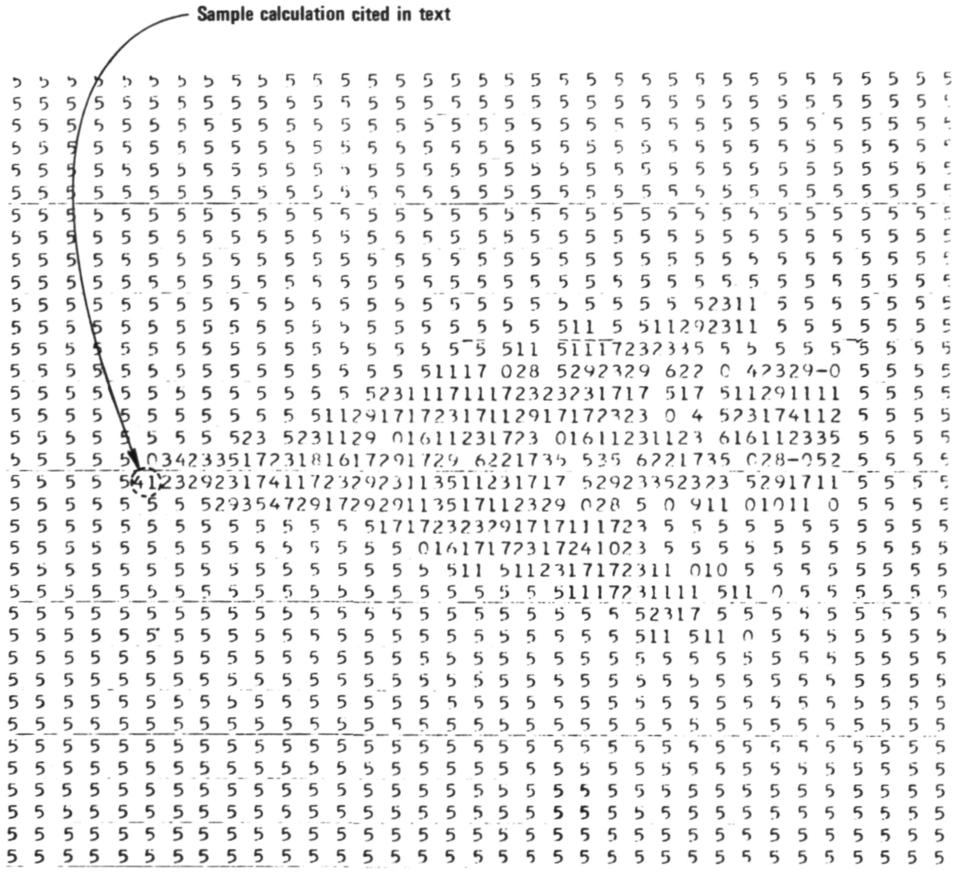

```
5 5 5 5 5 5 5 5 5 5 5 5 5 5 5 5 5 5 5 5 5 5 5 5 5 5 5 5 5 5 5 5 5 5 5
5 5 5 5 5 5 5 5 5 5 5 5 5 5 5 5 5 5 5 5 5 5 5 5 5 5 5 5 5 5 5 5 5 5 5
5 5 5 5 5 5 5 5 5 5 5 5 5 5 5 5 5 5 5 5 5 5 5 5 5 5 5 5 5 5 5 5 5 5 5
5 5 5 5 5 5 5 5 5 5 5 5 5 5 5 5 5 5 5 5 5 5 5 5 5 5 5 5 5 5 5 5 5 5 5
5 5 5 5 5 5 5 5 5 5 5 5 5 5 5 5 5 5 5 5 5 5 5 5 5 5 5 5 5 5 5 5 5 5 5
5 5 5 5 5 5 5 5 5 5 5 5 5 5 5 5 5 5 5 5 5 5 5 5 5 5 5 5 5 5 5 5 5 5 5
5 5 5 5 5 5 5 5 5 5 5 5 5 5 5 5 5 5 5 5 5 5 5 5 5 5 5 5 5 5 5 5 5 5 5
5 5 5 5 5 5 5 5 5 5 5 5 5 5 5 5 5 5 5 5 5 5 5 5 5 5 5 5 5 5 5 5 5 5 5
5 5 5 5 5 5 5 5 5 5 5 5 5 5 5 5 5 5 5 5 5 5 5 5 5 5 5 5 5 5 5 5 5 5 5
5 5 5 5 5 5 5 5 5 5 5 5 5 5 5 5 5 5 5 5 5 5 5 5 5 5 5 5 5 5 5 5 5 5 5
5 5 5 5 5 5 5 5 5 5 5 5 5 5 5 5 5 5 5 5 5 5 5 5 5 52311 5 5 5 5 5 5 5
5 5 5 5 5 5 5 5 5 5 5 5 5 5 5 5 5 5 5 5 511 5 511292311 5 5 5 5 5 5 5
5 5 5 5 5 5 5 5 5 5 5 5 5 5 5 5 5 5 511 51117232335 5 5 5 5 5 5 5 5 5
5 5 5 5 5 5 5 5 5 5 5 5 5 5 5 51117 028 5292329 622 0 42329-0 5 5 5 5
5 5 5 5 5 5 5 5 5 5 5 5 5 523111711172323231717 517 511291111 5 5 5 5
5 5 5 5 5 5 5 5 5 5 5 5112917172317112917172323 0 4 523174112 5 5 5 5
5 5 5 5 5 5 5 5 523 5231129 01611231723 01611231123 616112335 5 5 5 5
5 5 5 5 5 03423351723181617291729 6221735 535 6221735 028-052 5 5 5 5
5 5 5 5 541232923174117232923113511231717 52923352323 5291711 5 5 5 5
5 5 5 5 5 5 5 529354729172929113517112329 028 5 0 911 01011 0 5 5 5 5
5 5 5 5 5 5 5 5 5 5 5 5 5 517172323291717111723 5 5 5 5 5 5 5 5 5 5 5
5 5 5 5 5 5 5 5 5 5 5 5 5 5 5 01617172317241023 5 5 5 5 5 5 5 5 5 5 5
5 5 5 5 5 5 5 5 5 5 5 5 5 5 5 5 511 5112317172311 010 5 5 5 5 5 5 5 5
5 5 5 5 5 5 5 5 5 5 5 5 5 5 5 5 5 5 5 5 51117231111 511 0 5 5 5 5 5 5
5 5 5 5 5 5 5 5 5 5 5 5 5 5 5 5 5 5 5 5 5 5 5 52317 5 5 5 5 5 5 5 5 5
5 5 5 5 5 5 5 5 5 5 5 5 5 5 5 5 5 5 5 5 5 5 5 511 511 0 5 5 5 5 5 5 5
5 5 5 5 5 5 5 5 5 5 5 5 5 5 5 5 5 5 5 5 5 5 5 5 5 5 5 5 5 5 5 5 5 5 5
5 5 5 5 5 5 5 5 5 5 5 5 5 5 5 5 5 5 5 5 5 5 5 5 5 5 5 5 5 5 5 5 5 5 5
5 5 5 5 5 5 5 5 5 5 5 5 5 5 5 5 5 5 5 5 5 5 5 5 5 5 5 5 5 5 5 5 5 5 5
5 5 5 5 5 5 5 5 5 5 5 5 5 5 5 5 5 5 5 5 5 5 5 5 5 5 5 5 5 5 5 5 5 5 5
5 5 5 5 5 5 5 5 5 5 5 5 5 5 5 5 5 5 5 5 5 5 5 5 5 5 5 5 5 5 5 5 5 5 5
5 5 5 5 5 5 5 5 5 5 5 5 5 5 5 5 5 5 5 5 5 5 5 5 5 5 5 5 5 5 5 5 5 5 5
5 5 5 5 5 5 5 5 5 5 5 5 5 5 5 5 5 5 5 5 5 5 5 5 5 5 5 5 5 5 5 5 5 5 5
5 5 5 5 5 5 5 5 5 5 5 5 5 5 5 5 5 5 5 5 5 5 5 5 5 5 5 5 5 5 5 5 5 5 5
5 5 5 5 5 5 5 5 5 5 5 5 5 5 5 5 5 5 5 5 5 5 5 5 5 5 5 5 5 5 5 5 5 5 5
5 5 5 5 5 5 5 5 5 5 5 5 5 5 5 5 5 5 5 5 5 5 5 5 5 5 5 5 5 5 5 5 5 5 5
```

FIGURE 6.—Preliminary filtered testing picture 0.5 stdv airplane.

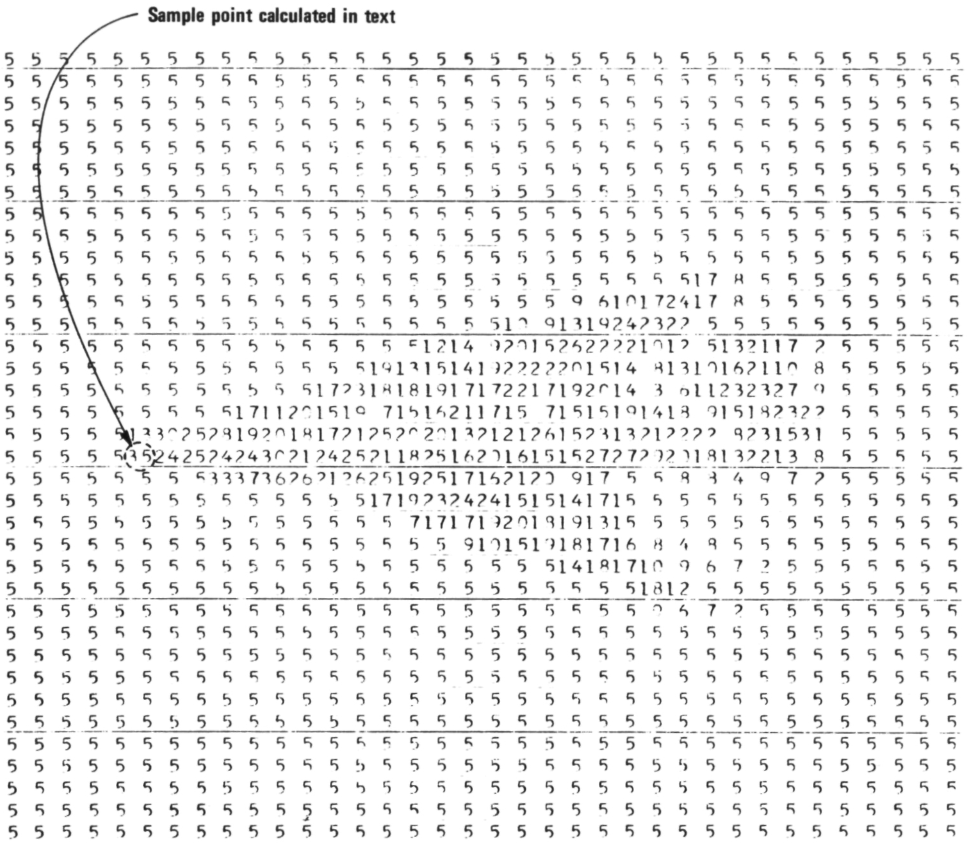

FIGURE 7.—Weighted stdv 0.5 testing airplane picture.

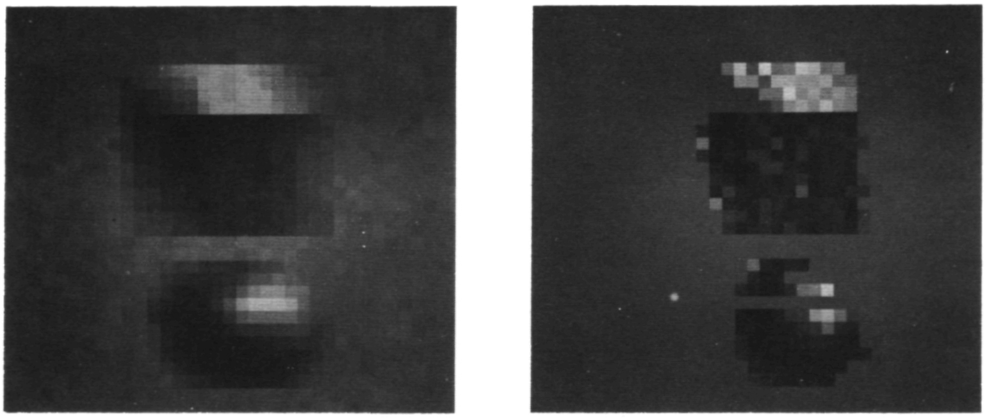

Noisy blurred image

Deblurred image

Noise standard deviation = .5 level

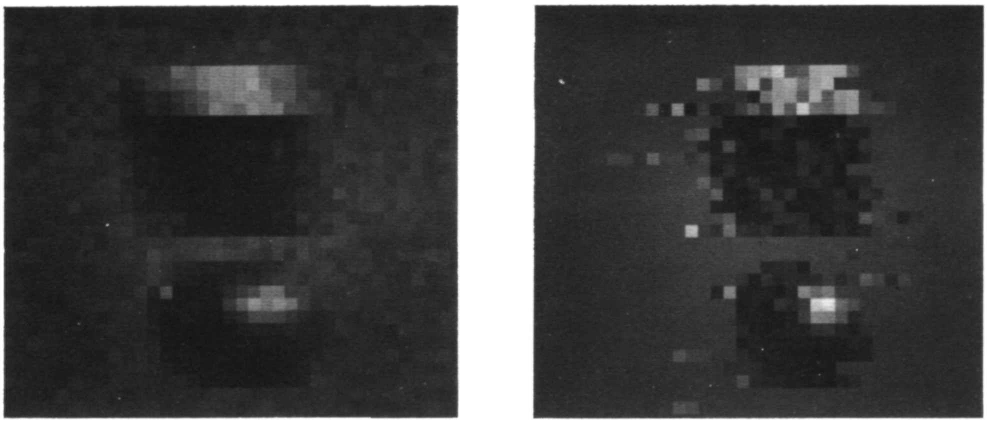

Noisy blurred image

Deblurred image

Noise standard deviation = 1 level

FIGURE 8.—Deblurring of a noisy image using a computer-implemented adaptive spatial filter which was trained on another object shape.

upper cube and passed through one row of the sphere. The probability of this occurring on higher resolution imagery is vanishingly small. In the higher noise case, considerable breakup of the objects occurs.

CONCLUSIONS

A multistage filtering process for correction of motion-degraded imagery suitable for digital computer use has been described. In this preliminary development, emphasis has been placed on the maximum use of a priori knowledge of the characteristics of possible signal and noise contributions to the noisy motion-degraded images. Such information includes the limited dynamic range of both signal and noise, the expectation of distinct object edges, or boundaries, and the limited possible gradient of signals given a specific degree of image smear. Since such information can most specifically be incorporated in the spatial domain, techniques of spatially-sampled data filtering have been employed rather than spatial frequency domain methods.

Considerable opportunity exists for further improvements in this approach to image motion correction. Particularly, the use of process identification and more sophisticated hypothesis testing methods should provide substantially greater capabilities for such correction without undue noise amplification.

REFERENCES

1. Regazzini, J. R.; and Franklin, G. F.: Sampled Data Control System. McGraw-Hill, 1958.
2. Frieden, B. R.: Optimum Nonlinear Processing of Noisy Images. J. Op. So. Am., Sept 1968.
3. Kinzley, R. E.; Haas, R. C.; and Roetling, P. G.: S.P.I.E. Seminar-in-Depth, Image Information Recovery, Philadelphia, Pa., October 24–25, 1968.

Page intentionally left blank

Page intentionally left blank

RESTORATION OF IMAGES DEGRADED BY SPATIALLY VARYING SMEAR

EDMUND M. GRANGER
Eastman Kodak Company
Rochester, N.Y.

Image motion is not uniform across the image plane of a camera on a moving vehicle. Image motion compensation can cancel an average value of image motion but cannot compensate higher order motions produced by topographical changes or rotation motions of the camera. The image recorded in the presence of spatially variant image motion is shown to be the result of a convolution of the image with a four-dimensional image motion function. The degraded image is restored on a four-dimensional correction space. Two dimensions on this space represent sample points taken on the image. The second set of dimensions is spatial frequency. The number of samples required in the correction process is shown to be a function of the magnitude and rate of change of the image motion and of the signal-to-noise ratio in the degraded image.

The restoration is performed by suitably weighting the degraded image at each sample point. The weighted image is Fourier-transformed and multiplied by a correction filter function. The result is back-transformed to form the restored image at the sample points. The total restoration is achieved by summing the restoration for each sample.

The variant image motion problem can be simulated on the computer. Restorations are displayed for signal-to-noise ratios of 10, 100, and 1000.

The image of an incoherently illuminated object is spatial frequency band limited by the lens. This band limiting process can be written

$$I(x,y)=B[O(x_0,y_0)]$$

where the object is represented by the function $O(x_0,y_0)$ and $I(x,y)$ represents the image. $B\ [\cdot]$ is the spatial frequency band limiting process associated with a lens.

If the image motion function is invariant, the degraded image is found by convolving the image motion spread function with the image $I(x,y)$. This convolution is written

$$D(x,y)=\iint_{-\infty}^{\infty} I(\alpha,\beta)\cdot S(x-\alpha,\,y-\beta)\,d\alpha\,d\beta$$

where $S(x,y)$ is the motion spread function, and $D(x,y)$ is the degraded image.

Figure 1 illustrates an example of variant image motion. The object plane is at an angle with respect to the camera and the image

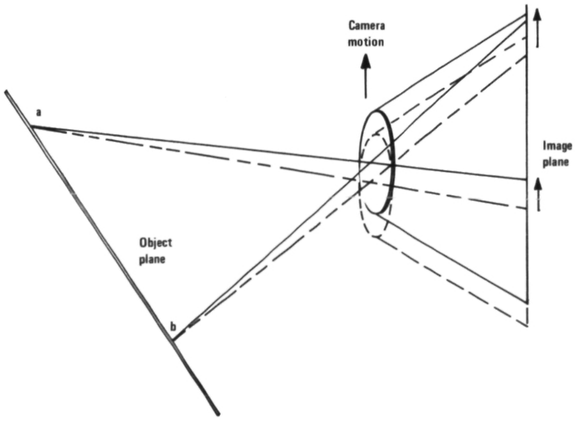

FIGURE 1.—Generation of variant image motion.

plane. As the camera is translated during an exposure, the images of the points *a* and *b* on the object move as shown on the figure. It can be seen from this construction that the image motion is varying as a function of object position. Therefore, the degraded image can be computed by considering what happens to each point on the object as it is transferred to the image plane and then integrating the contribution of all object points to obtain the degraded image.

The contribution of an individual object point to the illumination in the image plane is

$$P(x_0,y_0;x,y)= B\Bigg[\iint_{-\infty}^{\infty} O(\alpha,\beta)\cdot S(x_0-\alpha,y_0-\beta)d\alpha\, d\beta$$

where P is the point spread function in the image plane produced by imaging the point (x_0,y_0) on the object. The point spread response of the camera as defined is a four-dimensional function.

The image motion spread function associated with each object point is also four-dimensional and is denoted $S(x_0, y_0; x, y)$. The degraded image is computed by

$$D(x, y) = \iiiint_{-\infty}^{\infty} P(x_0, y_0; \alpha, \beta) \cdot S(x_0, y_0; x-\alpha, y-\beta)\, d\alpha\, d\beta\, dx_0\, dy_0$$

The above equation can be approximated by

$$D(x, y)= \sum_{i=1}^{n}\sum_{j=1}^{m}\iint P_{ij}(\alpha,\beta)\cdot S_{ij}(x-\alpha, y-\beta)\, d\alpha\, d\beta\, \Delta x_0\, \Delta y_0$$

where P_{ij} is the spread function produced by a small object area with index (i, j). The image motion function S_{ij} is considered to be invariant over the small object area.

One element in this approximation gives the illumination in the image plane produced by a conjugate object area. With increasing image motion, greater amounts of the illumination extend into adjacent image areas. If the degrading function were invariant, the image could be recovered by linear filtering. In the case of a varying smear function, the energy contributed to adjacent areas will confound reconstruction of the image in those areas. An exact restoration of the image could be accomplished by writing out a system of equations developed from sampling the degraded image and knowing the degrading spread function, $S(x_0, y_0, x, y)$.

In practice this process is limited by noise and a lack of knowledge of the function $S(x_0, y_0, x, y)$. Under these conditions, the reconstruction can be approximated by a number of linear filters. Each filter would have maximum effect over that portion of the degraded image that most nearly approximates the proper correction. The number of areas, and therefore the number of approximating filters required, are a function of the signal-to-noise ratio in the degraded image, the rate of change of the degrading function, and the extent of the degrading function.

Looking at the problem in one dimension will give an idea of the sampling rate. If the degrading function is invariant, the optimum correction filter in the frequency domain is

$$T_c(\omega)=\frac{T(\omega)^*}{|T(\omega)|^2+\Delta(\omega)}$$

where $T(\omega)$ is the Fourier transform of the degrading function, and $\Delta(\omega)$ is the noise-to-signal ratio. The mean-square error in the reconstructed image is

$$\epsilon=\int_{-\infty}^{\infty}\gamma(\omega)|1-T(\omega)\cdot T_c(\omega)|^2 d$$

where $\gamma(\omega)$ is the power spectrum of the image. Since the image is band-limited by the lens, the above integration can be rewritten as

$$\epsilon=\int_{-A}^{A}\gamma(\omega)|1-T(\omega)\cdot T_c\omega|^2 d\omega$$

where A is the bandpass limit of the lens.

The mean-square error as written is a function of the image spectrum, the signal-to-noise ratio, and the magnitude of the image motion implied by $T(\omega)$. The mean-square error would increase if our estimate of the degrading function were in error. The mean-square error for this condition can be written

$$\epsilon=\int_{-A}^{A}\gamma(\omega)\left|1-\frac{T(\omega)T_c^*(\omega)}{|T\epsilon(\omega)|^2+\Delta(\omega)}\right|^2 d\omega$$

where $T\epsilon(\omega)$ is the Fourier transform of the estimated degrading function.

The variant image-motion problem is similar to the problem of misestimating the amount of smear. An approximate correction scheme is to apply a simple linear correction to the frequency spectrum of the degraded image. Such a correction would be proper only over a small portion of the image space. The size of this area is related to the sampling rate and can be found in the following manner. Let the degrading function in the frequency domain be denoted $T(x_0, \omega)$. The optimum correction filter for image structure about the point x_0 is

$$T_c(\omega)=\frac{T^*(x_0, \omega)}{|T(x_0, \omega)|^2+\Delta(\omega)}$$

where $\Delta(\omega)$ represents the spectral noise-to-signal ratio. The mean-square error in the reconstructed image in the image area about an arbitrary point x is

$$\epsilon(x)=\int_{-A}^{A}\gamma(\omega)|1-T(x, \omega)T_c(\omega)|^2 d\omega$$

Since the correction filter has been centered at the point x_0, the error function can be expanded in a series,

$$\epsilon(x)=\epsilon(x_0)+\frac{\partial\epsilon(x_0)}{\partial x}(x-x_0)$$

One criterion for limiting the range of this filter is to let the mean-square error grow by 10 percent. Therefore,

$$\frac{\epsilon(x)-\epsilon(x_0)}{\epsilon(x_0)}\leq 0.1$$

which implies a sampling rate, $\frac{1}{\Delta x}=\frac{10}{\epsilon(x_0)}\frac{\partial\epsilon(x_0)}{\partial x}$

It can be shown that the derivative of the error function is,

$$\frac{\partial\epsilon(x_0)}{\partial(x)}\leq 2\int_{-A}^{A}\gamma(\omega)\left[1+|T_c(\omega)|\cdot|T(x_0, \omega)|\right]|T_c(\omega)|\cdot\left|\frac{\partial T(x_0, \omega)}{\partial x}\right|d\omega$$

Therefore, the sampling rate about the point x_0 is,

$$\text{Sample rate}\leq\frac{20}{\epsilon(x_0)}\int_{-A}^{A}\gamma(\omega)[1+|T_c(\omega)|\cdot|T(x_0, \omega)|]|T_c(\omega)|\cdot\left|\frac{\partial T(x_0, \omega)}{\partial x}\right|d\omega$$

The sampling rate is a measure of the number of corrective filters required per unit area of image.

The degraded image is approximated by,

$$D(x)=\sum\int_{-\infty}^{\infty}P_i(x)\cdot S_i(x-\alpha)d\alpha$$

and in the spatial frequency domain by,

$$d(\omega)=\sum P_i(\omega)\cdot T_i(\omega)$$

where $d(\omega)$, $P_i(\omega)$, and $T_i(\omega)$ are transforms of $D(x)$, $P_i(x)$, and $S_i(x)$, respectively. In the space domain, the degraded image can be rewritten in the form

$$D(x)=\sum_{i=1}^{n}D_1(x)$$

where

$$D_i(x)=\int_{-\infty}^{\infty}P_i(\alpha)\cdot S_i(x-\alpha)d\alpha$$

Since the image is given by

$$I(x)=\sum_{i=1}^{n}P_i(x)$$

the image can be restored by obtaining the best estimate for $P_i(x,y)$. This can be done in the spatial frequency domain by noting that

$$P_i(\omega)\simeq\frac{d_i(\omega)\cdot T_i(\omega)^*}{|T_i(\omega)|^2+\Delta(\omega)}=d_i(\omega)\cdot T_{ic}(\omega)$$

The function $d_i(\omega)$ can be developed from the degraded image in the following fashion,

$$d_i(\omega)=\mathcal{F}[W_i(x)\cdot D(x)]$$

where $\mathcal{F}[\cdot]$ is the Fourier transform operation, and $W_i(x)$ is a weighting function. The restored image can be developed,

$$I(x,y)\approx \mathcal{F}^{-1}\left[\sum_{i=1}^{n} d_i(\omega)\cdot T_{ic}(\omega)\right]$$

The proper weight function can be found by looking at the makeup of the degraded image. The irradiance in the image plane at the point (x) is

$$D(x)=\sum_{i=1}^{n} D_i(x)$$

where the $D_i(x)$ are the contributions of each object area sample to the irradiance of the image plane.

The best weight function would be,

$$W_i(x)=\frac{D_i(x)}{D(x)}$$

since it would select only that portion of $D(x)$ which was contributed by the i^{th} object area. In practice, one would have to estimate the contribution of each object area. The best estimate with no a priori knowledge would be to take the degraded image and assume that the object was of similar nature. This estimate is band limited and degraded in the same fashion as the original object area. The process produces an estimate of the i^{th} contribution to the sum total irradiance which can be called $\hat{D}_i(x)$. The estimated weight function can be written,

$$\hat{W}_i(x)=\hat{D}_i(x)\Big/\sum_{i=1}^{n}\hat{D}_i(x)$$

The restored image is calculated by,

$$I(x)\approx\sum_{i=1}^{n}\mathcal{F}^{-1}[\mathcal{F}[\hat{W}_i(x)\cdot D(x)]\cdot T_{ic}(\omega)]\cdot Q_i(x)$$

where $Q_i(x)$ is a partitioning function which has value 1 over the i^{th} image area and value *0* outside this region. $T_{ic}(\omega)$ is the correction filter applied to the i^{th} weighted sample.

FIGURE 2.—The object

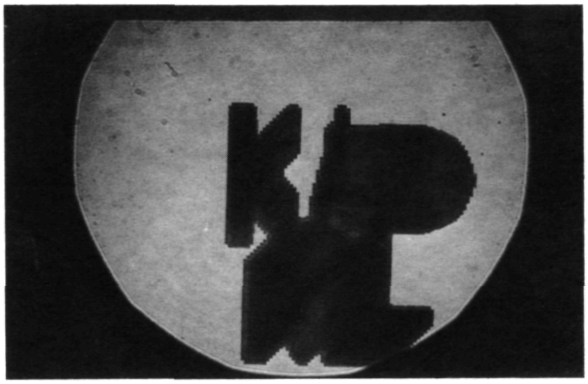

FIGURE 3.—Blurred image.

A computer simulation of this problem has been developed to demonstrate the principles and to show the restoration ability at various signal to noise levels. The object was constructed as shown in figure 2. The *K* and left half of the *A* were blurred in a vertical direction. The right half of the A and the *D* were blurred horizontally. The letters *R* and *L* were blurred at 45° to the horizontal. The sum result of the process is shown on figure 3. The correction procedure was applied with knowledge of the proper weight functions. Reconstructions were made for values of $\Delta(\omega)=0.1$, 0.01 and 0.001. This was done to simulate signal-to-noise power ratios of 10, 100, and 1000. The results of the reconstruction process are shown on figures 4, 5 and 6, respectively.

A reconstruction was also made without knowledge of the weight functions. The weighting functions were estimated by using the procedure outlined above. The reconstruction was made using a value of $\Delta(\omega)=0.1$. The reconstructed image is displayed on figure 7.

FIGURE 4.—Reconstruction S/N ratio$=10$.

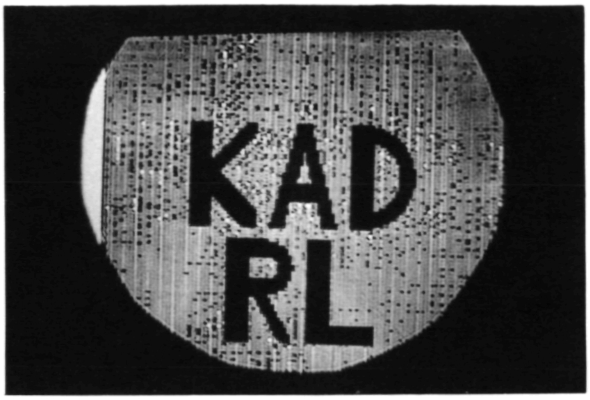

FIGURE 6.—Reconstruction S/N ratio$=1000$.

FIGURE 5.—Reconstruction S/N ratio$=100$.

FIGURE 7.—Reconstruction with estimated weighting function.

Page intentionally left blank

Page intentionally left blank

SOME PRACTICAL ASPECTS OF MEASUREMENT AND RESTORATION OF MOTION-DEGRADED IMAGES

Paul G. Roetling,* Roger C. Haas, and Robert E. Kinzly
Cornell Aeronautical Laboratory, Inc.
Buffalo, N.Y.

This paper discusses several of the practical aspects of measurement of image quality and image enhancement for the case of images degraded by uncompensated image motion. Some theoretical limitations on the restoration process are considered and examples of attempts to restore detail blurred by image motion are shown.

In practice one seldom has test charts available on the image of interest in order to perform a quality evaluation prior to image restoration. For this reason the method of edge gradient analysis is now more or less commonly applied to evaluate image quality. Examples of the application of edge gradient analysis to images blurred by uniform image motion and by vibration are shown and the importance of zero crossings of the modulation transfer function in the identification of the type of degradation is stressed. Turning specifically to the case of uniform image motion, such as that obtained by failure of the image motion-compensation system, we show that the location of the zeros of the modulation transfer function makes it theoretically impossible to restore a motion-blurred image by any linear filtering technique without introducing some spurious structure near edges or producing ghost images in addition to the restored image.

Some of the practical aspects of restoration attempts with motion-blurred pictures are demonstrated by examples utilizing the Lunar Orbiter I high resolution photographs which were badly blurred by image motion. Two techniques, namely, coherent optical spatial filtering and an incoherent optical differentiation technique, are compared and results are shown illustrating both true and spurious enhancement and illustrating interpretation techniques which allow enhanced noise to be distinguished from true enhanced images. These results also illustrate the relative advantage or disadvantage of each enhancement technique for restoring various types of detail degraded by image motion.

In the course of this paper we will attempt to illustrate some of the practical aspects of the problems of starting with a motion-blurred image and enhancing it by partial deblurring. To accomplish this, it is necessary to first measure the image degradation. From these measurements and a knowledge of the future potential use of the image, both a filter and an implementation of a filtering technique must be selected. During each step of the process one is attempting to separate signal from noise, and the characteristics of both must be considered during each step. Moreover, when the enhanced image is to be interpreted, an understanding of the enhancement process is essential to avoid interpreting the false signal characteristics as true signals.

MEASUREMENT OF DEGRADATIONS

It is highly unlikely that we will find test charts in a blurred image to evaluate the degradations. We therefore turn to targets of opportunity. Of the various possible choices of targets for transfer function evaluation, most authors (refs. 1, 2, and 3) now tend to agree that edges are most common, and readily interpretable as initially sharp. Noise characteristics, when required in filter design, are best determined

---

*Now with the Xerox Corporation, Rochester, New York.

from a scan of a uniform area, attributing fluctuations to noise. One is seldom sure that the area is truly uniform and in practice the scan usually includes some detail. The total noise power can be estimated by high pass filtering to eliminate the residual signal power. Thus we see, in figure 1, that two scans are used to estimate the image quality for purposes of enhancement. The noise scan can also be used to measure contrast, but exact knowledge of this factor is of little interest in most cases. The edge scan of course gives the transfer function (MTF) in only one direction, so several may be needed to estimate a nonisotropic degradation.

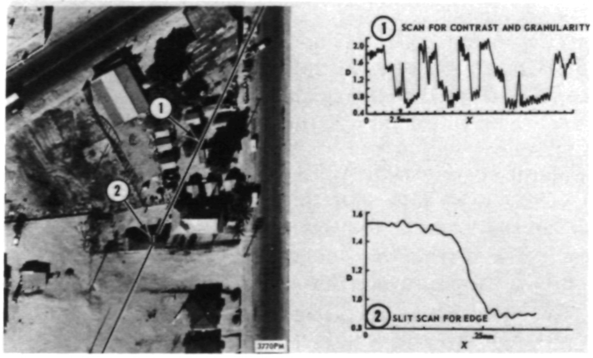

FIGURE 1.—Image quality measurement techniques.

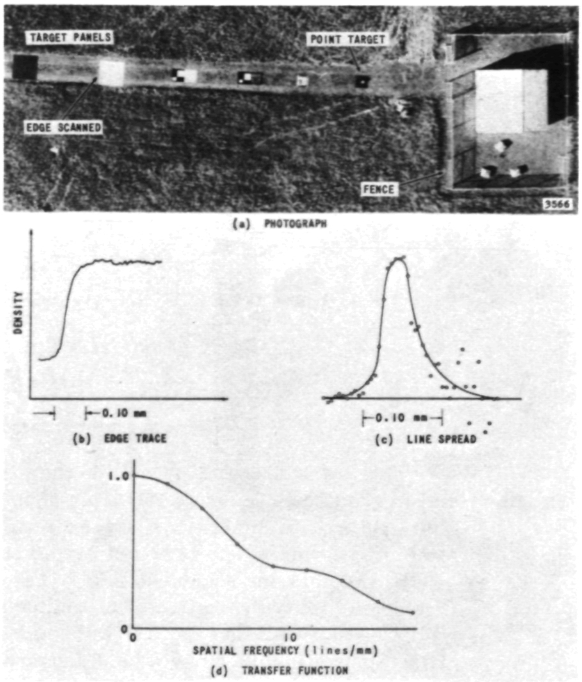

FIGURE 2.—Edge gradient analysis applied to high quality photograph. (a) Photograph, (b) edge trace, (c) line spread, and (d) transfer function.

Let us now turn our attention to the edge scan. Figure 2 shows an aerial image including a fenced garage, a dirt road, and some test target panels. The trace shown was made of the edge between one of the panels and the dirt road. (Use of the edge between the panel and the road may be considered inappropriate, although the road is a natural object. This yields a less noisy trace than one might otherwise obtain.) Differentiating the edge trace yields the line spread function shown and, in spite of the noise, a reasonable MTF results from taking the Fourier transform. This MTF represents a normal operation of the camera system. Figure 3 shows the same area, imaged on another pass of the aircraft, with the motion compensation purposely set wrong. The blur is obvious in the point source. In this case we can see a distinct flattening of the peak of the line spread. The MTF is shown compared to the analytical form of uniform image motion with the first zero location matched to the data. Because of the low noise, agreement is excellent except that the measured values of MTF are smaller in magnitude because of other degrading factors of the system. Using noisy data, one measurement would not be sufficient (ref. 2) and bias errors could be introduced (ref. 1) in addition to random errors. Another paper (ref. 4) presented at this meeting discussed these factors in more detail.

Figure 4 illustrates the main point to be made here with regard to measurement. This image was initially picked as another case of uniform motion. The double peak apparent in the line spread makes one suspicious. When the MTF is examined, the peak beyond the first zero seems too large to be uniform motion. The most obvious distinguishing factor, however, is the relative location of the zeros. The analytical form of the MTF for sinusoidal vibration is shown in figure 4 and when compared to the measured MTF fits quite well.

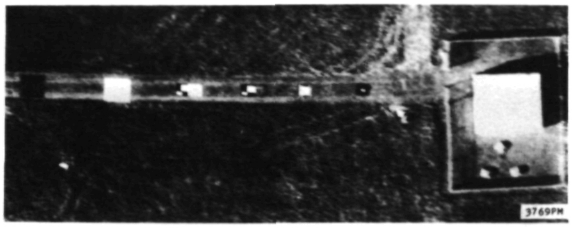

(a) AERIAL PHOTO WITH UNCOMPENSATED MOTION

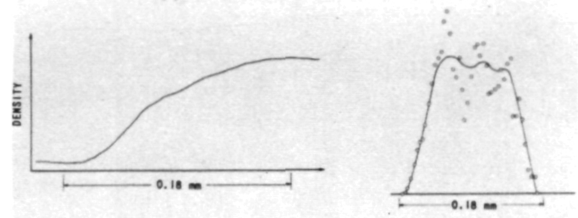

(b) EDGE TRACE (c) LINE SPREAD

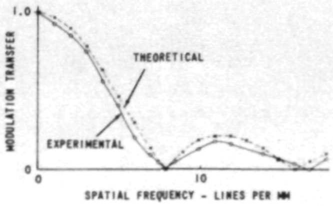

(d) TRANSFER FUNCTION

FIGURE 3.—Evaluation of image motion. (a) Aerial-photograph with uncompensated motion, (b) edge trace, (c) line spread, and (d) transfer-function.

Table I shows a tabulation of MTF for several types of degradation. It is clear that the relative locations of the zeros are a distinguishing factor and that only sinusoidal vibration would fit the data shown in figure 4. Upon discovering this result we checked the flight log and found that a hold-down bolt was found to be loose on this camera immediately after this pass.

Let us now return to the case of uniform image motion, where the zeros in the MTF occur at equal frequency intervals, and examine the effect of this characteristic on enchancement filtering.

(a) AERIAL PHOTO WITH VIBRATION

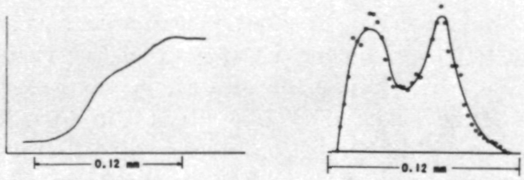

(b) EDGE TRACE (c) LINE SPREAD

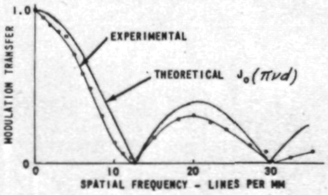

(d) VIBRATION TRANSFER FUNCTION

FIGURE 4.—Evaluation of image vibration. (a) Aerial photograph with vibration, (b) edge trace, (c) line spread, and (d) vibration transfer function.

FILTER DESIGN

The concept of image quality is inextricably linked to the filter design problem. If we agree that "enhancement" means to increase the image "quality," the first step of filter design for enhancement is to select a measure for image quality, then design a filter to maximize it. Unfortunately, image quality, in this sense, is not well understood. Most work on image quality (refs. 5, 6, and 7), which relates quality to physical characteristics such as MTF, tends to utilize linear theories in such a way that signal and noise spectra enter as a ratio. For example, one method, which we have used ourselves (refs. 2 and 6), utilizes statistical decision theory, and leads to a performance (quality) expression of the form:

$$P=\int\frac{|\tau(\vec{\nu})|^2W(\vec{\nu})}{P_N(\vec{\nu})}d\vec{\nu} \tag{1}$$

where the quality measure, P, depends on the square modulus of the MTF, $|\tau(\vec{\nu})|^2$, the noise power spectrum, $P_N(\vec{\nu})$, and weighting factors, $W(\vec{\nu})$, which depend on the use of the image. If we accept any equation of this form as functionally correct, we see that any linear filtering multiplies both $P_N(\vec{\nu})$ and $W(\vec{\nu})$ by the same factor, so that no linear filters can achieve enhancement.

Before we give up on linear filters, however, let us consider that the current state of image

TABLE I.—*Characteristics of Several Types of Degradations*

DEGRATION	POINT OR LINE SPREAD FUNCTION	THEORETICAL TRANSFER FUNCTION	SPATIAL FREQUENCY OF FIRST ZERO OF THE TRANSFER FUNCTION	AMPLITUDE OF FIRST NEGATIVE PEAK OF TRANSFER FUNCTION	RATIO OF SPATIAL FREQUENCY AT THE SECOND TO THE FIRST ZERO
DEFOCUS	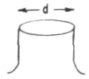	$\frac{2J_1(\pi\nu d)}{\pi\nu d}$	$\frac{1.22}{d}$	0.12	1.83
UNIFORM IMAGE MOTION	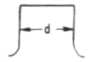	$\frac{\sin(\pi\nu d)}{\pi\nu d}$	$\frac{1}{d}$	0.22	2.00
VIBRATION	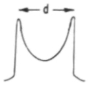	$J_0(\pi\nu d)$	$\frac{0.76}{d}$	0.40	2.30
DOUBLE EXPOSURE	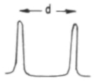	$\cos(\pi\nu d)$	$\frac{0.5}{d}$	1.0	3.00

quality research may not be sufficiently general so that in cases such as badly motion-blurred images the restoration of the signal to something like a typical good image may be helpful even if noise power is also increased. Let us attempt to restore the image to one similar to that created by a well corrected, incoherent imaging system. We note that the filter gain should approach zero where the signal or the MTF of the degraded image is near zero and so we have a band-limited system. In previous work, by ourselves (ref. 8) and others (ref. 9), a number of conditions have been derived which place restrictions on the shapes of transfer functions of incoherent optical systems. We can use these conditions to aid in designing enhancement filters, based upon the criterion that the result is supposed to look like an image from a good, incoherent system. We note that such images will have monotonic edge response functions, which should make low-contrast fine detail less likely to be confused by proximity to high contrast objects.

The restriction on the shape of the transfer function, $|\tau(\vec{\nu})|$, for a system with monotonic edge response can be written in the form:

$$\begin{vmatrix} 1 & \tau(\nu_1-\nu_2) & \tau(\nu_1-\nu_3) & \cdots & \tau(\nu_1-\nu_n) \\ \tau(\nu_2-\nu_1) & 1 & \tau(\nu_2-\nu_3) & \cdots & \tau(\nu_2-\nu_n) \\ \cdot & \cdot & \cdot & & \cdot \\ \cdot & \cdot & \cdot & & \cdot \\ \cdot & \cdot & \cdot & & \cdot \\ \tau(\nu_n-\nu_1) & \tau(\nu_1-\nu_2) & \tau(\nu_n-\nu_3) & \cdots & 1 \end{vmatrix} \geq 0 \qquad (2)$$

where the frequencies ν_i and the size, n, of the determinant are arbitrary. For the case of uniform image motion, this form can be simplified, following reference 8. Assuming that the spatial frequency is normalized by the magnitude of the image motion so that the first zero of $\tau(\nu)$ occurs at $\nu=1$, the ν_i can be chosen as integers, except for $\nu_n=\alpha$, and the determinant (for $n=6$) becomes:

$$\begin{vmatrix} 1 & 0 & 0 & 0 & 0 & \tau(2+\alpha) \\ 0 & 1 & 0 & 0 & 0 & \tau(1+\alpha) \\ 0 & 0 & 1 & 0 & 0 & \tau(\alpha) \\ 0 & 0 & 0 & 1 & 0 & \tau(1-\alpha) \\ 0 & 0 & 0 & 0 & 1 & \tau(2-\alpha) \\ 0 & 0 & 0 & 0 & 0 & 1 \end{vmatrix} \geq 0 \qquad (3)$$

By examining this determinant we can generalize to any even value for n and write an algebraic expression, namely,

$$\tau^2(\alpha)+\sum_{i=1}^{\frac{n-2}{2}} \tau^2(i\pm\alpha)\leq 1 \qquad (4)$$

Integrating equation (4) from $\alpha=0$ to $\alpha=\frac{1}{2}$ and letting $n\rightarrow\infty$, yields:

$$\int_0^\infty \tau^2(\nu)d\nu=N_e\leq\frac{1}{2} \qquad (5)$$

where N_e is Schade's equivalent passband.

Examining the passband of the motion transfer function, one finds it to be exactly one-half for the normalization used. Thus, any linear, stationary operation which increases the passband will inevitably cause negative parts in the line spread, or equivalently, will cause either ringing or ghost images.

With this theoretical limitation in mind, we can choose either of two courses, namely, discard linearity or examine how much edge ringing or ghosts affect practical interpretability. In the following section of this paper, we examine the latter alternative, making use of experimental results.

EXPERIMENTAL RESULTS

In order to examine interpretability of enhanced images, we must choose realistic conditions. Examples of the deblurring of black and white test charts, since they rarely occur in imagery, are not as desirable as the enhancement of a blurred Lunar Orbiter I high resolution photograph. Through a system failure, the original image shown in figure 5 was blurred by almost 100 meters of image motion.

We will examine results from two methods of linear enhancement. The first is the modified inverse filter, while the second is differentiation. The modified inverse filtering technique is an attempt to return the image to what it would be, had it been photographed by a good, incoherent system. Thus the product of the degraded system's MTF and the filter response is made to roll off smoothly with spatial frequency as shown in figure 6. The filter response cannot eliminate the zeros of the MTF, of course, and it is these zeros which we have seen that will cause ghost images. The second method, differentiation, was suggested by Harris (ref. 10). In this method, a single negative ghost image appears, equally as intense as the true image, and displaced by the amount of image motion.

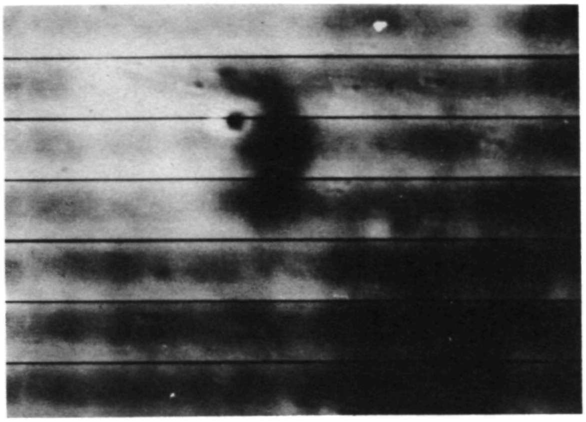

FIGURE 5.—A portion of a motion blurred high resolution frame from Lunar Orbiter I.

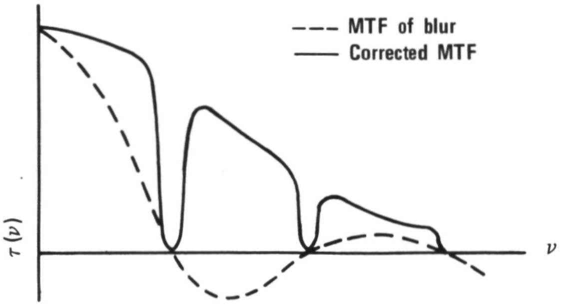

FIGURE 6.—Desired modulation transfer function for an enhanced motion-blurred image.

In addition to the different types of ghost images causing difficulty, the characteristics of enhanced noise are different in each case and lead to different questions about interpretability. Let us examine some experimental results to evaluate these effects. In figure 7, we see the result of differentiating, as Harris suggested, for the case where the motion blur is larger than the object of interest. This example was generated by photographic means,

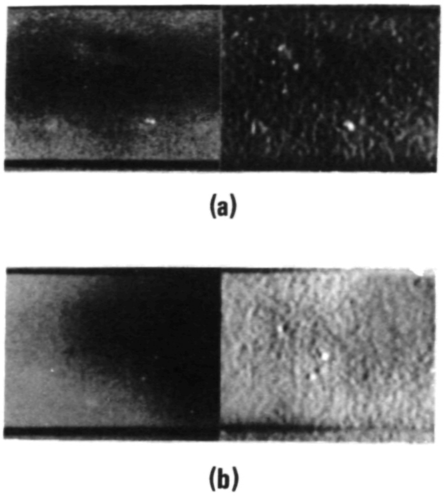

FIGURE 7.—Small area detail enhancement by differentiation. Original blurred image areas (left) and enhanced areas (right). (a) a small crater; (b) flaws in original.

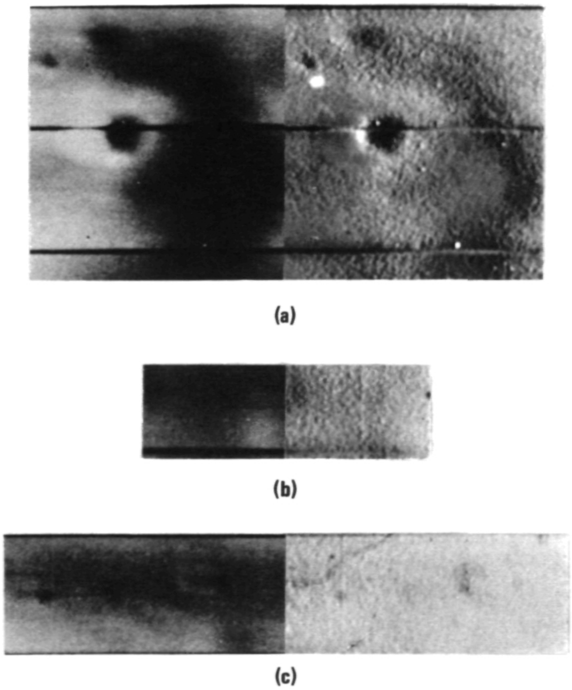

FIGURE 8.—Large area detail enhancement by differentiation. Original blurred image areas (left) and enhanced areas (right). (a) large crater and surrounding areas; (b) flaws in original and (c) area containing suspected ridges.

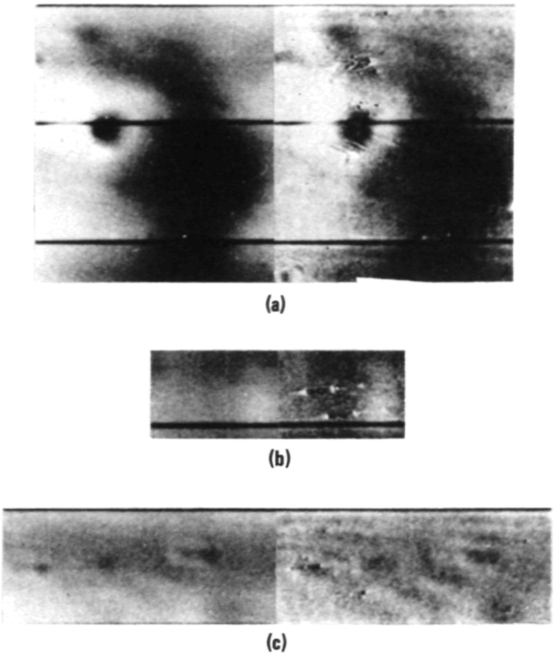

FIGURE 9.—Large area detail enhancement by coherent spatial filtering with a modified inverse filter. Original blurred image areas (left) and enhanced areas (right). (a) large crater and surrounding areas; (b) flaws in original and (c) area containing suspected ridges.

namely, a positive and a negative image of equal contrast were overlaid, displaced relative to each other very slightly in the direction of motion and a print made through the pair. Although this differentiates the density, rather than the exposure, the result is quite similar for low contrast. It can be seen that the object and its negative ghost are well separated, figure 7(a). Each image is clearer than the blurred original. In one sense, we tend to perform a nonstationary filtering by eye when we examine these results in that we essentially block out one image as we examine the other. This process is equivalent to multiplication of the function by an aperture function, which is a nonstationary filtering process (i.e., it does not perform the same operation at every image point). Thus it could be said that in this case the ghost image can easily be eliminated by a nonstationary process, performed by the eye.

Before leaving the discussion of this method for enhancement, we should note its characteristics for enhancement of the noise or introduction of spurious information. The area in figure 7(b) shows the result of a point flaw in the original (dust speck or pinhole). Differentiation yields a black-white pair of points. Although the point shown is clearly noise, this pattern is precisely the characteristic of shadow highlight on a real surface fluctuation. Thus the granular pattern apparent over the general surface may be real surface roughness or it may be simply enhanced grain images. A knowledge of noise characteristics should make us wary of such possibilities in interpretation of filtered images.

Next, consider the same method applied to a region where detail extends over larger areas, as shown in figure 8. At first, the image appears to be considerably sharpened. Upon examination, we cannot find the separate positive and negative images, and we should be suspicious. We cannot be assured which is real detail and which is falsely created by overlap of the real and ghost images. It is this situation in which the high contrast ghost image can create the worst problems. We therefore consider another method of enhancement: the modified inverse filter.

Figure 9(a) shows the same image area, filtered by a modified inverse filter in a coherent optical processing system. At first glance, the image does not appear to be as good as figure 8, but it is clearly sharper than the original. For low contrast of the objects, the ghost images are submerged in the grain noise. There is less need for concern with the ghost images; the apparent detail is mostly real. Turning to the noise structure which might interfere with interpretation of detail, consider the areas shown in figure 9(b). The image of a point flaw appears as a series of spots, either light or dark. While one such spot might appear to be a small crater, the series, separated by multiples of the magnitude of the motion, is a clear indicator of noise rather than signal.

At least two other types of noise can occur and are familiar to those who work with coherent systems. The first of these is the series of diffraction rings created around unfiltered dust specks, such as those on lenses. The other noise structure in the enhanced image is a band pattern resembling a linear interference pattern which might come from a double slit. This structure is probably due to a reflection in the system. Neither of these two types of noise is necessarily present if extreme care is taken in processing, but either or both might occur in any given case. The noise response from flaws in the original, on the other hand, cannot be eliminated in the enhanced image.

One final point should be made with regard to this image. The series of ridges in an area to the right of the large crater are not apparent on the original, but do appear to be real from the enhanced image presented in figure 9(c). This type of enhanced detail leads to serious questions of interpretation. In this case, we must choose between the alternative of another mission to study the area in more detail (in which case the enhancement served only to center attention) or believe the image is real unless we can find a reason to suspect it is noise.

CONCLUSION

We have attempted to show that edge gradient analysis can be used in conjunction with a knowledge of factors such as zero locations in the MTF to identify the type of degradation. In the case of uniform motion, enhancement by linear stationary filters will introduce spurious detail in the form of ghost images, edge ringing or noise enhancement. These effects must be considered in the interpretation of the enhanced images.

In general, of the two linear methods examined, the differentiation technique is preferable for restoration of objects smaller than the magnitude of the motion blur. For extended objects, the high contrast ghost image of the differentiation technique makes it less desirable than a modified inverse filter.

REFERENCES

1. BLACKMAN, E. S.: Effects of Noise on the Determination of Photographic System Modulation Transfer Functions. Photo. Sci. and Eng., vol. 12, no. 5, Sept.–Oct. 1968, p. 244.

2. Kinzly, R. E.; Mazurowski, M. J.; and Holladay, T. M.: Image Evaluation and Its Application to Lunar Orbiter. Appl. Opt., vol. 7, no. 8, Aug. 1968, p. 1577.
3. Jones, Robert A.: An Automated Technique for Deriving MTF's from Edge Traces. Photo. Sci. and Eng., vol. 11, no. 2, Mar.–Apr. 1967, p. 102.
4. Mazurowski, M. J.; and Kinzly, R. E.: The Precision of Edge Analysis Applied to the Evaluation of Motion-Degraded Images. Presented in Session I of this Seminar.
5. Rindfleisch, T.; and Willingham, D.: A Figure of Merit Measuring Picture Resolution. Advances in Electronics and Physics. L. Marton, ed., Academic Press Inc. New York, vol. 22A, 1966, p. 341.
6. Roetling, P. G.; Trabka, E. A.; and Kinzly, R. E.: Theoretical Prediction of Image Quality. J. Opt. Soc. Am., vol. 58, no. 3, Mar. 1968, p. 342.
7. Harris, J. L.: Resolving Power and Decision Theory. J. Opt. Soc. Am., vol. 54, no. 5, May 1964, p. 606.
8. Kinzly, R. E.; Haas, R. C.; and Roetling P. G.: Designing Filters for Image Processing to Recover Detail. Presented at SPIE Seminar on Image Information Recovery, Phila., Pa., Oct. 24–25, 1968.
9. Hildebrand, B. P.: Bounds on the Modulation Transfer Function of Optical Systems in Incoherent Illumination. J. Opt. Soc. Am., vol. 56, no. 1, Jan. 1966, p. 12.
10. Harris, J. L.: Image Evaluation and Restoration. J. Opt. Soc. Am., vol. 56, no. 5, May 1966, p. 569.

AN ANALOG IMAGE PROCESSOR

ROLAND V. SHACK AND WILLIAM SWINDELL
The University of Arizona
Tucson, Ariz.

The analog image processor is a scanning-playback device, rather like a facsimile machine. However, the image is scanned with an extended and spatially varying patch of light rather than a small spot. The transmitted beam is used to reconstruct a restored image. The essential difference between this and other optical processing methods is that the processing is done with incoherent light and takes place in the plane of the blurred image.

THEORY OF OPERATION

The image intensity distribution $i(x, y)$ obtained when an object $o(x, y)$ is imaged in a system with a point spread function $s(x, y)$ is given by

$$i = o * s \tag{1}$$

where * denotes convolution. We assume for the time being that the image is recorded on film (or other medium) which is subsequently processed to a linear positive of transmittance $t(x, y)$. Thus, apart from an inessential constant, we have

$$t = i \tag{2}$$

Alternatively, the object, recording system, and image may be described in terms of spatial frequencies $O(\omega_x, \omega_y)$, $S(\omega_x, \omega_y)$, and $I(\omega_x, \omega_y)$, so equation (1) can be rewritten as

$$I = O \times S \tag{3}$$

To process this image, the transparency is scanned with a beam of light having a cross-sectional variation of intensity $m(x, y)$ (denoted in spatial frequency space by $M(\omega_x, \omega_y)$). The transmitted intensity, $o'(x, y)$, is therefore given by

$$\begin{aligned} o' &= t * m \\ &= i * m \end{aligned} \tag{4}$$

The function $m(x, y)$ is obtained by interposing a mask of transmittance $m(x, y)$ in a uniform beam.

Taking the Fourier transform of both sides of equation (4):

$$\begin{aligned} O' &= I \times M \\ &= O \times S \times M \end{aligned}$$

Ideally, we should like $S \times M$ equal to unity for all object frequencies, thus giving perfect restoration; i.e., $O' = O$. However, S is zero outside the bandpass of the recording system and may be zero at several discrete points within the bandpass. We therefore seek to obtain partial restoration by defining a function L, where

$$L = S \times M \tag{5}$$

which is close to unity for nonzero values of S and zero when S is equal to zero. Thus L describes the net degradation of the object in terms of the spatial frequency content. A suitable function is

$$L = 1 - \exp\{-|S|^2/A\}$$

where A is a free parameter controlling the degree of restoration for small S (fig. 1).

The frequency response M of the required mask is given by $M = L/S$. The technical prob-

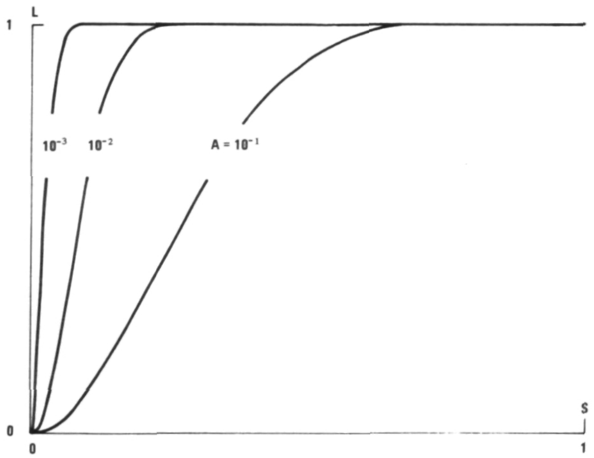

FIGURE 1.—Graph of L vs S, showing how L depends on the free parameter A.

lem is therefore to manufacture a mask whose transmittance m is prescribed as a function of the original degrading spread function, as follows:

$$m = F^{-1}\{L/F(s)\}$$

where F and F^{-1} refer to the Fourier and inverse Fourier transforms. Since s is necessarily real, m is also real but, unlike s, will in general have negative lobes.

DESCRIPTION OF SYSTEM

The calculation in the previous section shows that the required distribution calls for negative intensities. Negative optical intensities or transmissions are not possible, but the required scanning function can be obtained by simultaneously scanning the transparency with two coincident but independent beams. One has a distribution corresponding to the positive parts of the required scanning function, and the other has a distribution corresponding to the negative parts. Each beam falls on a photodetector, and the output of the photodetector, which measures the "negative" beam, is subtracted from the output of the other photodetector.

The analog system was designed as a progressive array of individual modules mounted on an optical bench. Each unit is easily removed for adjustment or modification without disturbing the remaining units. The system is shown in figures 2 and 3.

The first component (left end of figs. 2 and 3) is the scanning head. It contains a ribbon filament light source, each side of which is used. The light beam from each side passes through a condensing lens, a polarizer, and the appropriate mask. The beams are then combined using a beamsplitter so that the masks are imaged in register by the objective lens onto the blurred transparency. The transparency is mounted on the plastic drum which is threaded onto a stationary screw. The drum is belt-driven and thus provides a helical scan path on the drum. The light that passes through the transparency is reflected along the axis of the drum, through condensing lenses, and into a beamsplitter. Each beam leaving the beamsplitter passes through the polarizer to arrive at one of the two photodetectors. The polarizers separate the transmitted beams so that each detector measures only the appropriate signal.

In addition to the blurred transparency, the drum also carries an unexposed film, to be used in the playback operation. A cam on the end of the drum operates a switch that controls a shutter on the light source in the scanning head. This prevents the scan beam from striking the playback film.

The playback head consists primarily of a modulated glow tube (shown at the far side of the unit), an aperture to control the shape of the playback spot, and an optical system to image the aperture on the film.

Fig. 4 shows the control system which is inserted between the output of the differential amplifier and the input to the glow-tube modulator. It consists of a cathode-ray oscilloscope (CRO) whose screen is observed by a photo-multiplier tube (PMT). The PMT output is dc coupled to the Y input of the CRO in such a way that increased light falling on the PMT drives the spot downward. When an opaque mask partially obscures the CRO screen, the system can be adjusted to make the luminous spot sit at the edge of the mask when viewed from the PMT. As the X input is varied, the luminous spot accurately follows the outline of the opaque mask. Thus, the

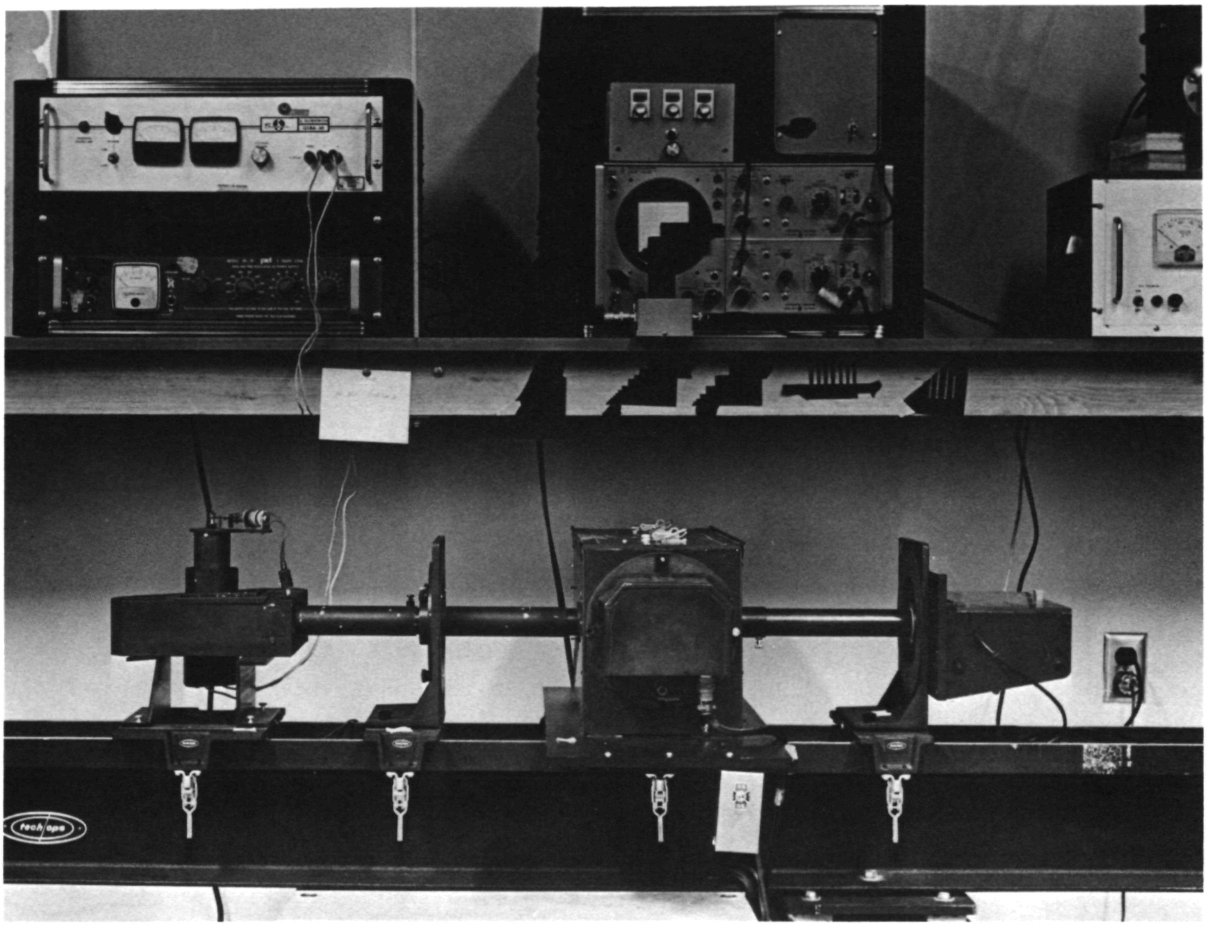

FIGURE 2.—Optical analog image processor. On upper shelf are (left) power supply for lamp and photomultiplier and (right) control device. On optical bench is optical analog image processor with lamp unit at left, scanning replay unit in center, and playback unit at right.

X-input and Y-output terminals of the CRO constitute the input-output terminals of a versatile function generator. There are many uses for this device. In particular, by using a suitable mask, a nonlinear negative may be processed to produce a linear positive transparency. Thus equation (2) can usually be satisfied. In this case, only one beam would be operating, and $m(x)$ would resemble a point transmission function in order to prevent spatial image processing. Other masks permit isophote generation, contrast enhancement, and contrast reversal.

The instrument has been designed to process

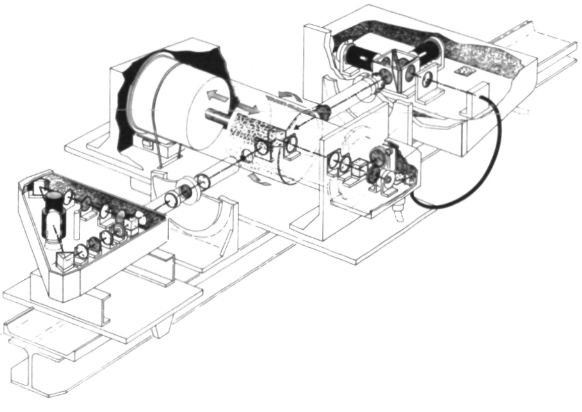

FIGURE 3.—Schematic diagram of optical analog image processor.

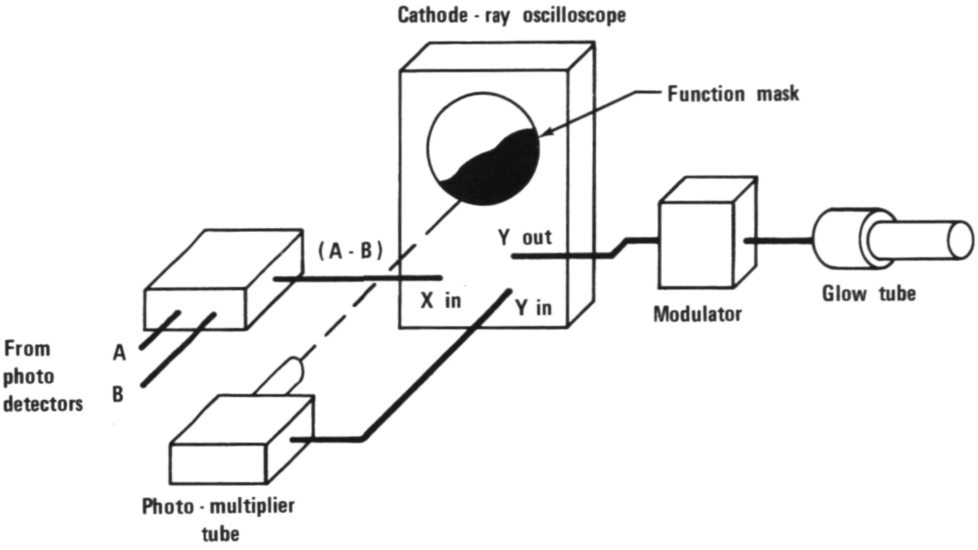

FIGURE 4.—Schematic diagram of control device.

a 4-inch by 5-inch transparency in about 15 minutes with a sampling interval (equal to the pitch of the drive screw) of 0.025 inch. Both these numbers could have been made smaller. However, the instrument is specifically a prototype and these figures reflect the desire to maintain ease and simplicity in the implementation of experiments. It is entirely suitable for investigational work in its present form.

OPTICAL PROCESSING OF MOTION-BLURRED IMAGERY

PHILIP S. CONSIDINE*
Information Technology Corporation
Burlington, Mass.

In the field of analogue image processing the optical-filtering system has the unique capability of processing the large amounts of information content that are common to an optical system. The application of the system to information processing is to utilize its optical transfer function (OTF) properties to manipulate the input-information content in a controllable manner. The advantage of the coherent optical system is that its OTF is the complex amplitude transmittance of the system aperture and hence is controllable in a predictable manner. In other words, a complex transmission mask can be placed in the frequency plane of the optical system to alter selectively the amplitude and phase distribution of the spatial frequencies (ref. 1). Spatial filtering is also possible with incoherent systems though it is somewhat more difficult because the transfer function of the incoherent optical system is the autocorrelation of the complex-amplitude transmittance of the system aperture.

In both cases it is interesting to note that spatial filtering is a reimaging process that in effect is nothing more than a multiplication of the frequency response of the input image with another frequency response. The filtered image output is the resultant image formed by the two cascaded systems, the original taking system and the filtering system. The optical-filtering process is one that can only reorient relative magnitudes of the image frequency response in a passive way. Though image processing can be performed, no harmonic amplification can be effected, and if a uniform frequency response is the desired end of spatial filtering, then it can only be done by decreasing the response of some frequencies to match the response of others.

To implement optical spatial filtering, fabrication of transmission masks is required. The desired mask depends on the system application, and there are several degrees of complexity in types of filters. The simplest to fabricate are blocking filters that have a transmittance of zero or unity and are commonly used as band-limiting filters for removal of half-tone information from imagery, image inversion, and raster removal. The next most complex is the amplitude filter, a transmission mask that is real and positive. Amplitude filters have been used for edge sharpening, image enhancement, and noise filtering, among other applications. Of most interest to this paper is the complex filter that contains both phase and amplitude information. This filter was first applied by Tsujiuchi (ref. 2) for restoration of defocused imagery, and it has since been applied to many problems, in the form of matched and inverse filters, such as image motion compensation, removal of atmospheric blur, and detection filtering. An example of linear blur compensation with an inverse sync filter is shown in figure 1 where the motion blur

---

* This work was performed while the author was at Technical Operations, Inc., with coworkers Richard O'Neil and Richard Profio.

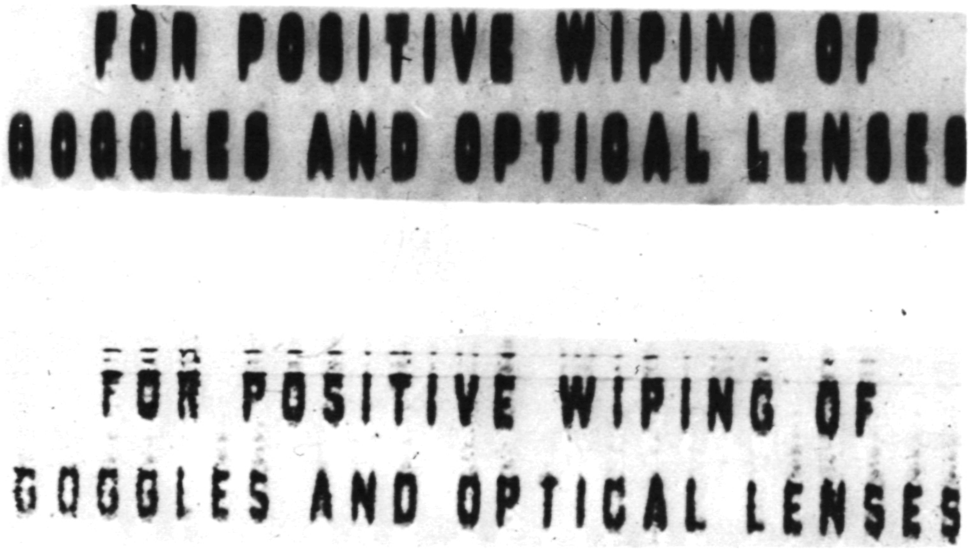

FIGURE 1.—Example of a linearly blurred image (top) and its restored response after in-line optical processing with an inverse sinc filter.

was in the vertical direction. It is apparent that image acuity has been improved.

DIGITAL-ANALOG IMAGE PROCESSING

Both analog and digital data processing of photographic imagery have unique advantages that cannot be supplemented by one processing technique alone. The optical data processing system has the unique capability of handling the large information content of imagery with a minute processing time whereas the computer is best suited for derivation of approximate solutions and for optimization studies. Though the suggestion is not new it is being emphasized here that the proper combination of analog and digital data processing will provide the optimum means of image processing. One solution to the combination of the digital and analog methods is to apply the digital computer to filter generation where only the information of a point spread function and transfer function of an optical system need be processed rather than the scene information. The information derived from the computer can be printed out in the form of a filter with the sensitometrically-calibrated photofacsimile system to be discussed in this paper. Thus the computed filter printout would provide a means to use the optical analogue system for image processing, a task for which it is ideally suited.

There are many basic problems in determining what filter is required for processing because in order to compensate for an aberration, the aberrated point spread function must be known. Most of the image restoration work performed optically has been under laboratory controlled conditions so that the point spread function was recorded separate from the image information or so that it could be gained in one dimension from edge trace analysis. However, the computer provides an excellent method of determining optimum filters for image restoration applications as demonstrated by the work being carried out by Harris at Scripps (ref. 3). For the purposes of this discussion let us accept that the desired filter can be computed by digital techniques; with the photofacsimile system to be dsecribed here the computed filter information can be sensitometrically printed out onto a photographic plate for use as a spatial filter for optical image restoration.

The photofacsimile system is capable of accepting filter transmittance information programmed on IBM cards from an IBM Summary Punch and exposing film in steps as computed.

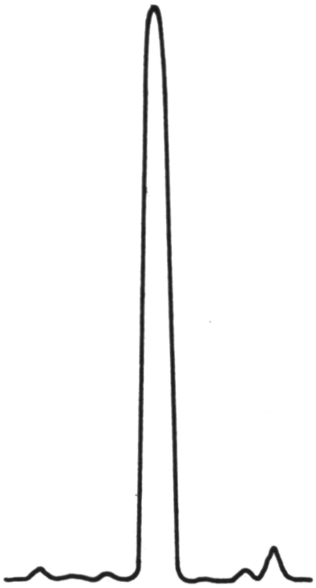

FIGURE 2.—Microdensitometer trace across a restored point spread function after in-line optical processing with a photo-facsimile printer generated filter.

A dc light source, run at a controlled voltage, illuminates a rectangular aperture that is imaged with a microscope lens onto a photographic plate. The brightness of the light illuminating the aperture is controlled by neutral density apertures placed between the light source and the rectangle. The neutral density apertures are mounted on two filter wheels that are driven by servo motors. Their position is controlled by a master commutator that in turn is controlled by the system logic with the signal from the IBM card reader. During the system operation, after the filter wheels have been positioned, the exposure time of the photographic plate is kept constant by a capping and rotating shutter combination. The rotating shutter provides a precise and repeatable exposure time.

The photographic plate is placed on a precision x-, y-movement stage. Each axis is driven by a stepping motion which is controlled and synchronized with the remainder of the system operation by the system logic. For the initial applications of this system a rectangle of constant illumination was used for exposing the photographic plate.

The photofacsimile system is only one component of a total image processing system. The total system would include a scanning microdensitometer that can be used to obtain information from film and provide a digital record of the transmittance information on tape for computer input. The computer output can be retained on tape or IBM cards (the

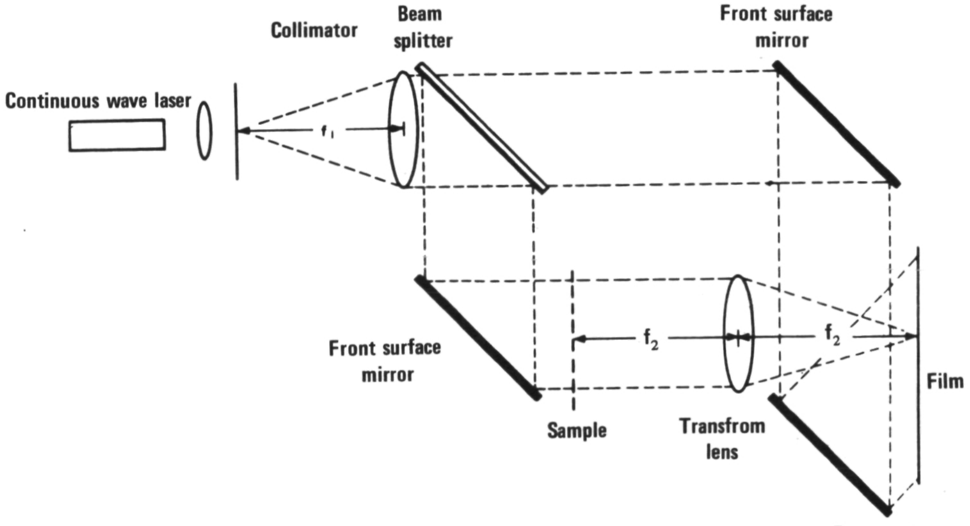

FIGURE 3.—Schematic diagram of a modified Mach-Zehnder interferometer.

latter are sufficient for a slow speed printout device) for use with the photofacsimile system. The filter thus generated is placed into the optical system for restoration of imagery. An example of linear blur compensation with a photofacsimile generated filter is shown in figure 2. This illustration contains a microdensitometer trace of the restored point spread function. The intensity ratio between the central peak and highest side order peak was 30 to 1, and the restored point spread function had a half-intensity width 0.14 that of the blurred point spread function.

HOLOGRAPHIC PROCESSING

Holography, with its capability for recording complex information on a photographic transparency has reduced the task of fabricating complex filters to a straightforward technique. One of the standard ways of fabricating a spatial filtering hologram was first proposed by Vander Lugt (ref. 4) who described a modified Mach-Zehnder interferometer for constructing matched filters. Such filters, which are useful in target recognition, have an output which appears as a bright spot of light in the image plane at the location of the target of interest. Since the original work of Vander Lugt, complex spatial filtering with the use of holographic detection filters in coherent optical systems has been performed by many groups (refs. 5 and 6). More recently Fourier transform holograms have been used to construct inverse filters useful for image enhancement (refs. 7, 8, and 9). A schematic diagram of a Fourier transform interferometer is shown in figure 3 where the transform of a target is recorded at the film plane as noted.

Hologram filters are recorded on photographic transparencies and therefore depend on the response characteristics of films. One of the primary limitations thereby incurred is a limited dynamic range as well as variation in contrast response with dynamic range. The limitation to dynamic range means that one cannot record on film a function greater than the dynamic response of a film. This can be alleviated in part by the functions recording with background illumination that decreases the contrast response. The second limitation—that contrast responds as a function of exposure—can also cause difficulty because the hologram readout is a diffraction phenomenon, and diffraction is a function of the contrast of

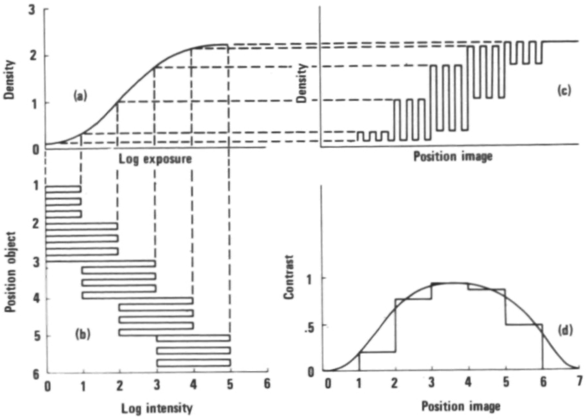

FIGURE 4.—Diagram showing the film response to a modulation input. The hologram output depends on the filter cosine modulation and system diffraction is a function of the recorded modulation.

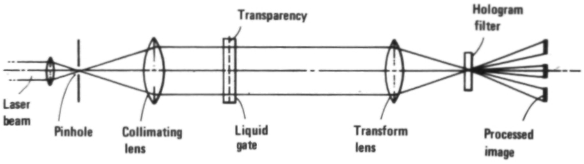

FIGURE 5.—Diagram of the hologram processing system.

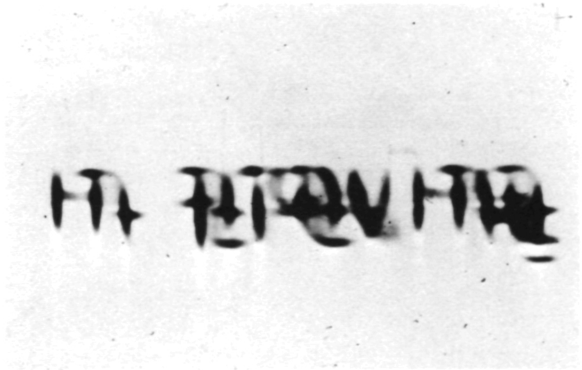

FIGURE 6.—Example of a blurred image where the blur function was Z shaped.

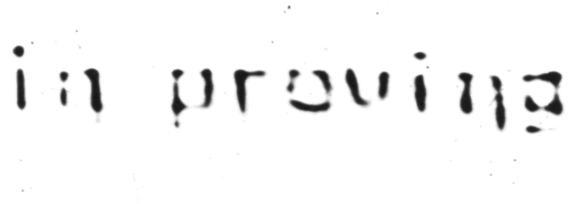

FIGURE 7.—Example of the restored image originally shown in figure 6.

the diffracting medium. Thus if a frequency function (transfer function) exists over a dynamic range, then the film response can cause a spatial filtering effect that varies from frequency to frequency, the variation dependent on the contrast response variation recorded on film as a function of exposure. This is illustrated in figure 4 where the modulation recorded on film shows an inversion because of the film clipping level.

The hologram filter can be used in the system as described in figure 5. The restored image output is obtained from one of the diffracted outputs of the hologram processing system. An example of image reconstruction with the use of a Fourier transform hologram filter is shown with figures 6 and 7, where figure 6 contains a smeared image (the smear was *Z* shaped) and figure 7 contains the partially restored image.

The dependencies that are discussed here are factors that quickly become apparent to the user of a hologram. They must be considered when comparing the value of the hologram filter to in-line optical filters. One major attribute of the in-line filter is that it can be controlled, and its response corrected over the whole dynamic range of interest. Thus in-line filters function well for continuous tone image enhancement where accuracy is needed over the dynamic range. One function for which there is little comparison is the application of filters to target recognition for cases of high selectivity. Hologram filters, because they are formed in an optical system, have the high frequency response of optical systems that is necessary for high selectivity filters.

REFERENCES

1. O'NEILL, E. L.: Introduction to Statistical Optics. Addison-Wesley, Reading, Mass., 1963.
2. TSUJIUCHI, J.: Progress in Optics. vol. II, North Holland Publishing Co., Amsterdam, 1963.
3. HARRIS, J., SR.: J. Opt. Soc. Am., vol., 56, 1966, p. 569.
4. VANDER LUGT, A. B.: Trans. IEEE, vol. It–10 1964, p. 2.
5. CATHEY, W. T., JR.: J. Opt. Soc. Am., vol. 56, 1966, p. 1167.
6. RASO, D. J.: J. Opt. Soc. Am., vol. 58, 1968, p. 432.
7. CUTRONA, L.; ANSLEY, D.; KAY, I.; AND THOMAS, C.: Coherent Light Investigation, Final Report. AF33(615)–2738 (AD–476–825) Conductron Corporation, 1965.
8. LOHMANN, A.; AND WERLICH, H.: Holographic Production of Spatial Filters for Code Translation and Image Restoration. Phys. Letters, vol. 25A, 1967, p. 8.
9. STROKE, G.; INDEBETOUW, G.; AND PUECH, C.: A Posteriori Holographic Sharp Focus Image Restoration from Ordinary Blurred Photographs of Three Dimensional Objects Photographed in White Light. Phys. Letters, vol. 26A, 1968, p. 9.

Page intentionally left blank

Page intentionally left blank

HOLOGRAPHIC PENETRATION OF TURBULENCE

OLOF BRYNGDAHL
IBM Research Division
Los Gatos, Calif.
AND
ADOLF LOHMANN [1]
University of California, La Jolla

Goodman, Huntley, Jackson and Lehmann (ref. 1) recorded a hologram H at a short distance behind a piece of shower glass, which simulated a turbulent layer T (fig. 1). In reconstruction the reference wave R fell again onto the hologram, but with the shower glass T removed. The reconstructed image was a slightly degraded replica of the object, O, although the shower glass was so rough that ordinary imaging through it completely blurred the image. The amount of degradation of images obtained through random media by this holographic technique has been studied by Gaskill (ref. 2).

In applications where a degradation is disturbing it is not practical to place the hologram close behind the turbulence. If, however, the distance to the turbulent layer is known one might simply introduce a lens, which images the plane of the turbulent layer onto the hologram.[2] Thus the case of the distant turbulent layer is reduced to the case of the nearby turbulent layer (ref. 1).

Sometimes the introduction of the relay lens might not be a suitable means for coping with a distant turbulent layer, because the distance may not be known, or a lens of proper dimensions might not be available. For that case we have developed the following three-step holographic method. Close to the object O (fig. 2) is a reference point source, R_0. Light from O and R_0 travels through the turbulent layer to the hologram H_1, where also an undisturbed reference wave R_1 arrives. After developing the hologram H_1, it is illuminated with a replica of the former reference wave R_1, thus recon-

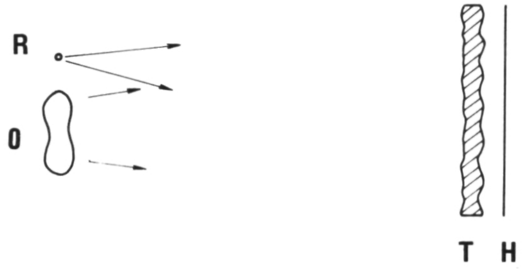

FIGURE 1.—Hologram recording setup of Goodman et al.

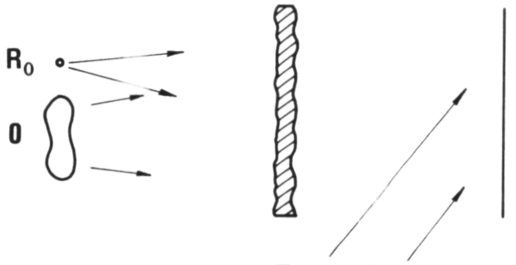

FIGURE 2.—Recording the primary hologram.

---

[1] Work supported in part by ARPA.

[2] Goodman, J. W.: private communication.

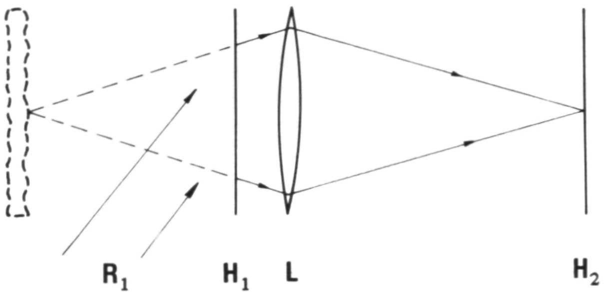

FIGURE 3.—Recording the secondary hologram

structing the wavefield coming from O and R_0 through T. By means of a lens L (fig. 3) we can find the (virtual) location of the turbulent layer T imaged onto a photographic plate H_2.

Since the irradiance falling onto H_2 is the same as the irradiance, which did exist during the primary recording process just behind the layer T, this photograph H_2 is equivalent to a hologram H as recorded by the method according to reference 1. The object O can be reconstructed by illuminating H_2 with a replica of reference wave R_0.

In case of a shower glass as a model of a turbulent layer it is not too difficult to find the image plane H_2 of the turbulent layer. In the plane H_2 (fig. 3) the appearance of the hologram fringes will namely be most regular. Moving away from this plane in either direction will result in wild changes in the irradiance distribution over the hologram and reduction in the hologram areas containing interference fringes. In a more realistic model of a turbulent layer there might not be any sharp gradients. Hence other means must be found to focus the image of a phase object T. Perhaps a knife edge in the rear focal plane of lens L might make it possible to focus since a knife-edge converts a phase object into an amplitude image.

For verifying our proposal we used a transparent cross on an opaque background as object O and a nearby pinhole as reference R_0 (fig. 4(a)). As models of a tubulent layer we used various types of shower glass. The maximal thickness variations of the shower glass were not crucial for the success, but extension of the thickness gradients had to be small enough so that prismatic deflection did not throw large fractions of the light outside of hologram H_1. Reconstruction of our object is shown in figure 4(c) where the strong zeroth order between both first-order reconstructions has been blocked. For comparison an ordinary image of the same object, observed through the shower glass, is shown in figure 4(b).

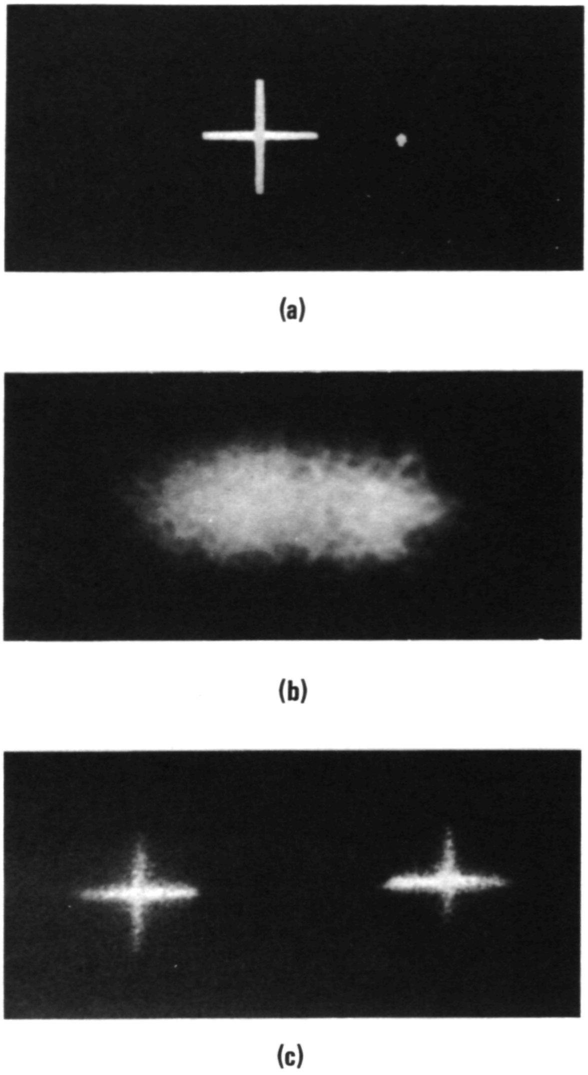

FIGURE 4.—Reconstruction of object which was shielded by a shower glass. (a) the object and reference point source, (b) the object as seen through the shower glass, and (c) reconstruction of the object.

When attempting to perform such an experiment under more realistic conditions, the object O and its own reference R_0 (for example specular reflection from a point of the object periphery) at high altitude would be illuminated by a laser on the ground. Part of the laser beam has to be kept on the ground as reference beam R_1. The reference beam has to be delayed in accordance to the travel time with an accuracy of the wave train duration.

ACKNOWLEDGMENT

We would like to thank H. Werlich for doing the laboratory work.

REFERENCES

1. GOODMAN, J. W.; AND HUNTLEY, W. H., JR.; JACKSON, D. W.; AND LEHMANN, M.; Appl. Phys. Letters, vol. 8, 1966, p. 311.
2. GASKILL, J. D., J. Opt. Soc. Am. vol. 58, 1968, p. 600.

Page intentionally left blank

Page intentionally left blank

COMPENSATION OF MOTION BLUR BY SHUTTER MODULATION

OLOF BRYNGDAHL
IBM Research Division
Los Gatos, Calif.
AND
ADOLF LOHMANN*
University of California, La Jolla

Ordinarily, when making a photographic recording, the shutter is opened for a finite time T, which can be described by a rectangular shutter function (= flux as a function of time). Such a shutter function in connection with linear image motion creates a degradation due to motion blur. If the shutter instead is opened twice as long and modulates the flux by a function $\cos^2(t^2)$, a recording is obtained which has the properties of an "incoherent one-demensional hologram." Hence, compensation of motion blur is achieved by reconstructing a sharp image from the "hologram."

THE PROBLEM

If a moving image shall be recorded on a photographic plate the exposure time has to be short enough in order to avoid disturbing motion blur. However, such a short exposure time is sometimes incompatible with the requirement to place enough energy per unit area onto the photographic emulsion. The motion blur is unavoidable. Several data processing methods are known for compensating a posteriori the effects of motion blur and have been discussed at this symposium.

We wish to present a new method for a posteriori compensation of motion blur. During recording of the moving image, the transmittance of the shutter is time-modulated, for example by a rotating polarizer in combination with a fixed polarizer. The shutter transmittance function $S(t)$ is chosen such that the motion blurred image has essentially all the features of a hologram, although the object radiation might be completely incoherent. The conversion of the motion blurred image into a sharp image is performed like the image reconstruction from a hologram.

THE RECORDING PROCESS

When forming a conventional Fresnel hologram, the light from each object point x', y' is converted into a Fresnel zone pattern (refs. 1 and 2) $\cos^2 [\pi\{(x-x')^2+(y-y')^2\}/a^2]$, where the scale factor a depends on the wavelength and on the geometry of the setup. If the geometry is chosen such that only off-center portions of the Fresnel zone patterns are recorded on the hologram, which usually is achieved by tilting the reference wave (ref. 3), separation of the reconstructed image from the twin image and from the zero-order light is possible.

Somewhat different are "one-dimensional Fresnel holograms" (ref. 3). When forming them, the light from each object point x', y' is

---

*Work supported in part by ARPA.

converted into a one-dimensional Fresnel zone pattern $\delta(y-y')\cos^2[\pi(x-x')^2/a^2]$, which is the same as a horizontal strip out of an ordinary Fresnel zone pattern. Again, the centers of these one-dimensional Fresnel patterns should not fall onto the hologram in order to avoid twin-image confusion. For forming one-dimensional Fresnel holograms it is sufficient if the object points are somehow converted into one-dimensional Fresnel zone patterns. For example, coherent illumination is not necessary (ref. 4). Yet another way for converting an object into a one-dimensional Fresnel hologram is to move the object with constant velocity V in x-direction while it is recorded on a photographic plate. But the temporal transmittance through the lens has to be modulated by a function like $\cos^2(t^2)$.

A detailed form of the shutter transmittance function $S(t)$, which converts the moving object point $\delta(x-Vt-x')\delta(y-y')$ into the motion blurred point image $(1/V)\delta(y-y')\cos^2[\pi(x-x')^2/a^2]$ within $x' \leq x \leq x' + 2VT$ is:

$$S(t) = \cos^2[\pi(Vt/a)^2] \text{ with } 0 \leq t \leq 2T$$

0 otherwise.

This shutter function (fig. 1) has indeed all the necessary properties in order to record a one-dimensional hologram. It is bound between zero and one, and its time integral is the same as for the ordinary rectangular shutter function of duration T:

$$\int_0^{2T} S(t)dt = T$$

if $(2VT/a)^2$ is an integer.

When convolved with the moving object point $\delta(x-Vt-x')$, the shutter function $S(t)$ produces the proper Fresnel blur

$$\int S(t)\delta(x-Vt-x')dt = \frac{1}{V}\cos^2[\pi(x-x')^2/a^2] \text{ in}$$

$$x' \leq x \leq x' + 2VT$$

It contains only the one side of the Fresnel pattern so that the twin image can be eliminated in the holographic reconstruction process.

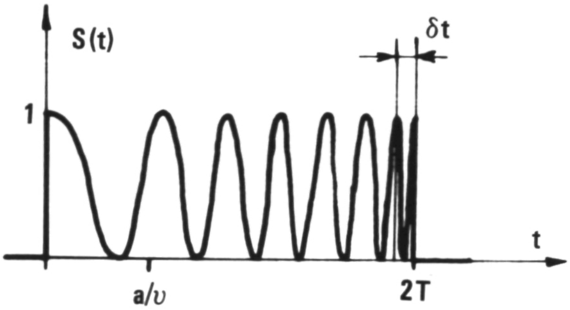

FIGURE 1.—The shutter transmittance function.

THE COMPENSATION PROCESS

A Fresnel zone plate concentrates the incoming light into a focal point. This is the essential effect of the blur compensation process. The blurred record is illuminated by an inherent plane wave. Each motion blurred point image, $\delta(y-y')\cos^2[\pi(x-x')^2/a^2]$, on the blurred record acts like a narrow horizontal strip of a cylinder lens with vertical cylinder axis, and with focal length $f = a^2/2\lambda$. Two actual cylinder lenses are needed for producing an output with sharp image points. The one cylinder lens with a horizontal cylinder axis focuses the blurred point images from the blurred record into the output plane (fig. 2(a)). The other cylinder lens with vertical cylinder axis (fig. 2(b)) fulfills two functions. In its rear focal plane, the light portions, which belong to the real image, the twin image, and the zeroth order, respectively, are separated laterally. A screen rejects the unwanted portions. Furthermore this second cylinder lens forms an image of the Fresnel-focus plane (at distance f behind the motion blurred record) onto the output plane.

The functions of the two cylinder lenses are simple in concept, but difficult in practice, because cylinder lenses are less corrected than spherical lenses of comparable price. Hence in the actual experiment we used a strong spherical lens for doing the bulk of the focusing job, and a weak cylinder lens for introducing the proper difference of focal powers for vertical and horizontal object lines. Figure 3 shows the original object (a), the record with linear motion blur (b), the record with spatially modulated motion blur (c), and the reconstruction from the motion compensation process

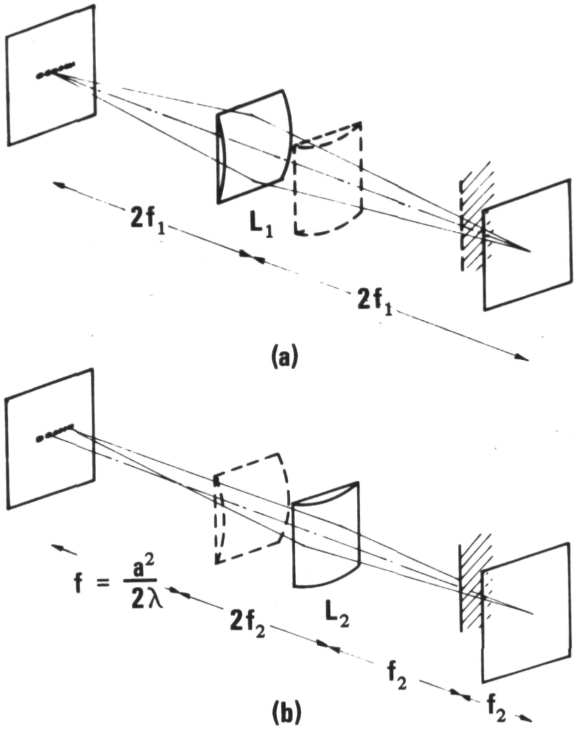

FIGURE 2.—The holographic compensation process. (a) The horizontal cylinder lens L_1 images the blurred record into the output plane. (b) The linear Fresnel pattern focuses the light at a distance f, from where it is imaged by the vertical cylinder lens L_2 into the output plane.

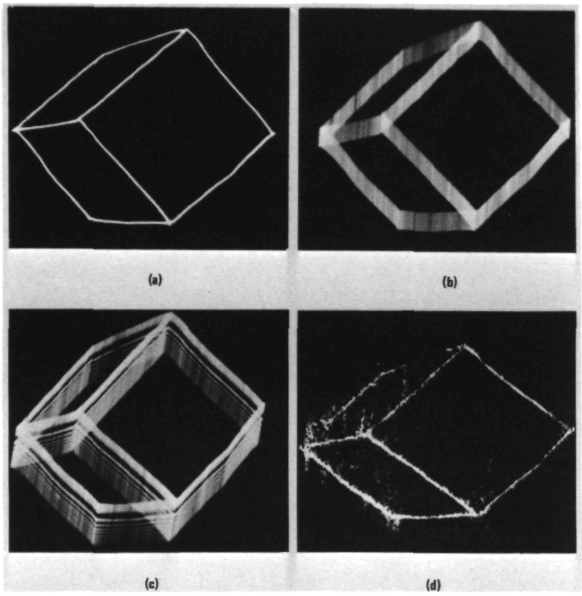

FIGURE 3.—(a) The object; (b) the object with ordinary motion blur, (c) the recording where the motion blur is spatially modulated into one-dimensional Fresnel-zone pattern; (d) reconstructed image from (c).

(d). The most critical part of the experiment was to record the blurred image on the linear portion of the photographic T–E curve (amplitude transmittance versus exposure). For this purpose a small amount of uniform pre-exposure is needed.

THE RESOLUTION OF THE COMPENSATED IMAGE

The blurred point image or linear Fresnel pattern has a width $2VT$, and a focal length $f=a^2/2\lambda$. Considered as a lens it has an F-number, $F=f/2VT=a^2/4\lambda VT$. When such a lens is illuminated with a coherent plane wave, the point image at a distance f behind the lens will have the width $F=a^2/4VT$. This is the best possible resolution we can expect in the output plane, assuming that the two cylinder lenses (fig. 2) do not degrade the image in any way.

For judging the success of our compensation method we compare the resolution $\lambda F=a^2/4VT$ with the resolution VT one gets in an ordinary motion blurred image, exposed during the interval T, while the object is moving with velocity V. The ratio $\lambda F/VT=(a/2VT)^2 \triangleq 1/N$ indicates the improvement in resolution. At the same time N indicates the number of maxima of the shutter function $S(t)$ during the exposure from $t=0$ till $t=2T$ (fig. 1). Yet another relation exists between the resolution λF and the structure of the shutter function $S(t)$. The δt of the narrowest maximum is about $\delta t=a^2/4TV^2$ (fig. 1). Hence, the total width δx of the narrowest maximum of the linear Fresnel pattern or blurred point image is $\delta x=V\delta t=a^2/4TV$, which is the same as the resolution λF in the compensated final image.

ACKNOWLEDGMENT

We would like to thank A. Nafarrate for doing the laboratory work.

REFERENCES

1. ROGERS, G. L.: Nature, vol. 166, 1950, p. 237.
2. GABOR, D.: Proc. Roy. Soc., London, vol. A197, 1949, p. 454.
3. LEITH, E. N.; AND UPATNIEKS, J.: J. Opt. Soc. Am., vol. 52, 1962, p. 1123.
4. BRYNGDAHL, O.; AND LOHMANN, A.: J. Opt. Soc. Am., vol. 58, 1968, p. 625.

U.S. GOVERNMENT PRINTING OFFICE: 1969 O—351-160

NATIONAL AERONAUTICS AND SPACE ADMINISTRATION
WASHINGTON, D. C. 20546

OFFICIAL BUSINESS

POSTAGE AND FEES PAID
NATIONAL AERONAUTICS AND
SPACE ADMINISTRATION

FIRST CLASS MAIL

POSTMASTER: If Undeliverable (Section 158
Postal Manual) Do Not Return

> *"The aeronautical and space activities of the United States shall be conducted so as to contribute . . . to the expansion of human knowledge of phenomena in the atmosphere and space. The Administration shall provide for the widest practicable and appropriate dissemination of information concerning its activities and the results thereof."*
>
> —NATIONAL AERONAUTICS AND SPACE ACT OF 1958

NASA SCIENTIFIC AND TECHNICAL PUBLICATIONS

TECHNICAL REPORTS: Scientific and technical information considered important, complete, and a lasting contribution to existing knowledge.

TECHNICAL NOTES: Information less broad in scope but nevertheless of importance as a contribution to existing knowledge.

TECHNICAL MEMORANDUMS: Information receiving limited distribution because of preliminary data, security classification, or other reasons.

CONTRACTOR REPORTS: Scientific and technical information generated under a NASA contract or grant and considered an important contribution to existing knowledge.

TECHNICAL TRANSLATIONS: Information published in a foreign language considered to merit NASA distribution in English.

SPECIAL PUBLICATIONS: Information derived from or of value to NASA activities. Publications include conference proceedings, monographs, data compilations, handbooks, sourcebooks, and special bibliographies.

TECHNOLOGY UTILIZATION PUBLICATIONS: Information on technology used by NASA that may be of particular interest in commercial and other non-aerospace applications. Publications include Tech Briefs, Technology Utilization Reports and Notes, and Technology Surveys.

Details on the availability of these publications may be obtained from:

SCIENTIFIC AND TECHNICAL INFORMATION DIVISION
NATIONAL AERONAUTICS AND SPACE ADMINISTRATION
Washington, D.C. 20546